Titel der Arbeit:
Humidity Studies on ATLAS ITk Strip Sensors

Dissertation zur Erlangung des akademischen Grades
doctor rerum naturalium
(Dr. rer. nat.)
im Fach Physik: Spezialisierung:
Experimentalphysik
eingereicht an der
Mathematisch-Naturwissenschaftlichen Fakultät der Humboldt-Universität zu Berlin
von
M.Sc. Ilona-Stefana Ninca

Präsidentin der Humboldt-Universität zu Berlin
Prof. Dr. Julia von Blumenthal

Dekan der Mathematisch-Naturwissenschaftlichen Fakultät
Prof. Dr. Emil List-Kratochvil

Gutachter:

1. Prof. Dr. Heiko Lacker
2. Prof. Dr. Steven Worm
3. Prof. Dr. Heinz Graafsma

Tag der mündlichen Prüfung: 12.12.2025

Declaration

I declare that I have completed the thesis independently using only the aids and tools specified. I have not applied for a doctor's degree in the doctoral subject elsewhere and do not hold a corresponding doctor's degree. I have taken due note of the Faculty of Mathematics and Natural Sciences PhD Regulations, published in the Official Gazette of Humboldt-Universität zu Berlin no. 42/2018 on 11/07/2018.

Humidity Studies on ATLAS ITk Strip Sensors

Ilona-Stefana Ninca

Abstract

Silicon strip sensors developed for the ATLAS Inner Tracker Upgrade have shown a strong dependence of the breakdown voltage on varying levels of relative humidity (RH). The solution to this humidity sensitivity has so far been to store and test the sensors in a dry environment ($RH \leq 10\,\%$). This mitigates the effects of humidity but does not attempt to understand the underlying issue. For the design of future sensors, it is important to investigate what processes in the surface and bulk of the silicon sensor trigger this effect.

To understand the silicon strip sensor humidity sensitivity, silicon diodes from the same wafer as the strip sensor were investigated using Technology Computer-Aided Design (TCAD) from Synopsys and the Top-Transient Current Technique (Top-TCT). The silicon diodes were characterized using a probe station. The full depletion voltage, active thickness, and effective silicon doping concentration were derived from Capacitance-Voltage (CV) measurements. The mobility of charge carriers was derived based on Current-Voltage (IV) characteristics.

TCAD simulations for different relative humidity values (0 %, 30 %, and 40 %) were performed at a high bias voltage (900 V) to study the electric field, charge transport, and onset of early breakdown in humid conditions. TCAD proved to be a useful tool in assessing the effect of passivation openings on the leakage current and surface charge transport as a function of the relative humidity. It was observed that the geometry with no passivation openings performed similarly to previous investigations of silicon strip sensors in the presence of humidity [1]. Further simulations were conducted for three different values of the fixed oxide charge concentration to investigate their influence on the electric field and charge transport.

For the first time, the Top-Transient Current Technique was used to study the charge transport in the guard ring region of silicon diodes from the same wafer as the ATLAS strip sensor by generating localized free charge carriers near the surface with picosecond pulses of red laser light. The induced transient currents were measured as a function of the relative humidity and bias voltage to determine how these factors influence the prompt current and charge profile.

Zusammenfassung

Siliziumstreifensensoren, die für das ATLAS Inner Tracker Upgrade entwickelt wurden, haben eine starke Abhängigkeit der Durchbruchsspannung von der relativen Luftfeuchtigkeit (RH) gezeigt. Die Lösung für diese Feuchtigkeitsempfindlichkeit bestand bisher darin, die Sensoren in einer trockenen Umgebung ($RH \leq 10\,\%$) zu lagern und zu testen. Dadurch werden die Auswirkungen der Feuchtigkeit gemildert, aber es wird nicht versucht, das zugrunde liegende Problem zu verstehen. Für die Entwicklung künftiger Sensoren ist es wichtig zu untersuchen, welche Prozesse an der Oberfläche und im Inneren des Siliziumsensors diesen Effekt auslösen.

Um die Feuchtigkeitsempfindlichkeit des Siliziumstreifensensors zu verstehen, wurden Siliziumdioden aus dem gleichen Wafer wie der Streifensensor mit Hilfe von Technology Computer-Aided Design (TCAD) von Synopsys und der Top-Transient Current Technique (Top-TCT) untersucht. Die Siliziumdioden wurden mit einer Prüfstation charakterisiert. Die volle Verarmungsspannung, die aktive Dicke und die effektive Silizium-Dotierungskonzentration wurden aus Kapazitäts-Spannungs-Messungen (CV) abgeleitet. Die Mobilität der Ladungsträger wurde anhand der Strom-Spannungs-Charakteristik (IV) ermittelt.

TCAD-Simulationen für verschiedene Werte der relativen Luftfeuchtigkeit (0 %, 30 % und 40 %) wurden bei einer hohen Vorspannung (900 V) durchgeführt, um das elektrische Feld, den Ladungstransport und das Einsetzen des frühen Durchbruchs unter feuchten Bedingungen zu untersuchen. TCAD erwies sich als nützliches Werkzeug zur Bewertung der Auswirkungen von Passivierungsöffnungen auf den Leckstrom und den Oberflächenladungstransport in Abhängigkeit von der relativen Luftfeuchtigkeit. Es wurde festgestellt, dass die Geometrie ohne Passivierungsöffnungen ähnlich wie frühere Untersuchungen von Siliziumstreifensensoren in Gegenwart von Feuchtigkeit funktioniert. Weitere Simulationen wurden für drei verschiedene Werte der festen Oxidladungskonzentration durchgeführt, um deren Einfluss auf das elektrische Feld und den Ladungstransport zu untersuchen.

Zum ersten Mal wurde die Top-Transient-Current-Technik verwendet, um den Ladungs-transport in der Schutzringregion von Siliziumdioden aus demselben Wafer wie der ATLAS-Streifensensor zu untersuchen, indem lokalisierte freie Ladungsträger nahe der Oberfläche mit Pikosekundenpulsen von rotem Laserlicht erzeugt wurden. Die induzierten transienten Ströme wurden in Abhängigkeit von der relativen Luftfeuchtigkeit und der Vorspannung gemessen, um festzustellen, wie diese Faktoren den Promptstrom und das Ladungsprofil beeinflussen.

Contents

List of Figures

List of Tables

Acknowledgments

"Many of life's failures are people who did not realize how close they were to success when they gave up."

— Thomas Edison

Like any meaningful project, this thesis would not have been possible without the support of many people. I would like to start by thanking Ingo Bloch, Heiko Lacker, and Steven Worm for giving me the wonderful opportunity to contribute to the ATLAS ITk upgrade project. I am beyond happy to have completed my PhD thesis work at DESY Zeuthen, where I worked in an international collaboration, learned how to operate complex devices, participated in testbeam campaigns, performed TCAD simulations, and did many other intriguing activities.

I want to express my heartfelt gratitude to Christian Scharf, who guided me throughout my PhD. When I began working on the humidity studies, Christian was the one who answered all my questions, and he has continued to do so since.

A warm thank you goes to Ben Brüers, who supervised my ATLAS qualification task locally. This PhD thesis does not focus on my qualification task; however, working on a quality control device for electronics has equipped me with practical knowledge of diagnostic tools and quality control methodologies.

I would like to extend my appreciation to Martin Renzmann and Carl Beichert for their assistance with mechanical and electrical tasks. I would not have been able to perform any electrical characterizations on the sensors without their help.

I am thankful to Callan Jessiman for our extensive conversations on TCAD simulations, which always inspired me to try new things in the simulation. Thank you, Callan, for your support and friendship throughout my PhD.

A very special thanks goes to Vlad Berlea, for whom there are not enough words in the English vocabulary to express my gratitude. For far too long, and yet not long enough, we have been discussing physics, from things that we don't know to what we are excited to discover. Thank you, Vlad, for always listening to me, for your endless care, and for being by my side.

Last but not least, I want to thank my mom, Angelica Ninca, and my dad, Ioan Ninca, for their unwavering support. It may not come as a surprise, but I want to dedicate my thesis to you both.

Chapter 1

Introduction

The ATLAS detector is one of the major experiments at the Large Hadron Collider (LHC) that measures the byproducts of proton-proton collisions. It has a layered structure with the Inner Detector (ID) being the closest system to the interaction point. To increase the statistical power of these interactions, the luminosity of the LHC will be increased. The current ATLAS detector was not designed to operate at the radiation levels foreseen for the High-Luminosity LHC (HL-LHC); therefore, it needs to be upgraded. One of the challenges of the ATLAS upgrade is replacing the inner detector with an all-silicon inner tracker (ITk). The inner tracker will consist of a pixel and a strip detector. During the pre-production phase of ATLAS, some silicon strip sensors showed a dependence of the breakdown voltage on exposure to ambient humidity. To prevent performance degradation or failure of the strip sensors due to humidity exposure, they are stored in a dry environment ($RH \leq 10\,\%$) upon reception at the assembly sites. Furthermore, the sensors are electrically tested only in humidity-controlled setups. Humidity will not pose a risk to the ATLAS experiment since the detector will operate in a controlled environment. However, to prepare for the design of future detectors, it is important not only to mitigate the effects of humidity, but also to understand the mechanisms onset by humidity at the surface of silicon sensors.

Humidity refers to the amount of water vapor present in the air. While pure water is a poor electrical conductor, in practice, it contains ions that make it conductive. It is well understood that when liquid water enters a circuit, it can create unintended pathways, which may result in a short circuit. However, the mechanisms through which humidity influences the charge transport at the surface of silicon sensors still require further investigation.

This study aims to investigate the impact of relative humidity (RH) on charge transport at the surface of test structures, namely, n-in-p silicon diodes fabricated on the same wafer as the strip sensor. The test structures were first characterized using a probe station. Taking Current-Voltage (IV) characteristics at different relative humidity values consisted of a preliminary test to assess the electrical stability of the test structures in humid conditions for Top-Transient Current Technique (TCT) scans. The Top-TCT uses a red laser to generate electron-hole pairs at the surface of silicon. The transient current generated by the drift of charge carriers under the influence of the electric field toward the collecting electrode is then recorded. The charge profile and the prompt current can be extracted from the transient current. The prompt current can give an indication of the electric field at the edge of the diode, which has a direct impact on the charge transport.

To support the Top-TCT scans, Technology Computer-Aided Design (TCAD) simulations of the same test structure were performed in both dry and humid conditions. The effect of the relative humidity on the electric field, impact ionization, and carrier densities was investigated. It is important to study the electric field because it influences charge transport at the sensor's surface and inside the silicon bulk. If the electric field is strong enough, it can accelerate charge carriers such that they can gain enough energy to create secondary ionization. As a result, the carrier density increases, changing the current density. The electron and hole densities can also showcase the charge distribution at the surface of the sensor as a function of RH.

The second chapter begins with a summary of the Standard Model (SM). This is a theoretical framework that describes the fundamental particles and their interactions, unifying the electromagnetic, weak, and strong nuclear forces. The ATLAS detector was built to probe the predictions of the Standard Model and to explore new physics. An overview of each individual subsystem of the ATLAS detector is provided, with a focus on the ITk strip detector.

The third chapter introduces conductors, semiconductors, and insulators from the perspective of the band structure model. Phenomena related to charge transport, such as carrier drift, diffusion, recombination, and generation, are further discussed. These are important to understand carrier dynamics and derive the continuity equations, which are the basis of Technology Computer-Aided Design simulations.

The fourth chapter explains the formation of a p-n junction, focusing on the origin of the depletion region, the behavior of charge carriers, and current flow under bias conditions. The processing of a single-crystal semiconductor device is then explained step by step, including growing techniques, photolithography, etching, doping methods, oxidation, metalization, and lastly, passivation deposition. This chapter also delves into the mechanisms through which photons interact with matter: pair production, Compton scattering, and the photoelectric effect. Silicon strip sensors are introduced as an application for particle detection. Finally, the chapter highlights early studies on the humidity effect and mitigation methods from the literature.

The fifth chapter presents the experimental techniques employed to electrically characterize the silicon sensors. The probe station used for taking Current-Voltage (IV) measurements in both dry and humid conditions is presented, along with examples of IV characteristics. The Top-Transient Current Technique (Top-TCT) setup is introduced as a method to study the charge transport at the surface of sensors. Details about the calibration of laser intensity are also presented. The experimental results are discussed later in this chapter. First, an example of a two-dimensional scan of the charge collected in the corner of an n-in-p silicon diode is showcased. An example of the charge profile and prompt current at the edge of silicon diodes as a function of relative humidity (RH) is shown as well. Furthermore, the variation of charge collection with applied voltage is examined. Subsequently, the presence of hysteresis is investigated. The final results discussed in this chapter consist of an example of a long-term stability measurement.

The sixth chapter describes the implementation of a two-dimensional model for a silicon diode in TCAD from Synopsys. The technical details of the geometry and the models used for charge transport are discussed initially. Four passivation opening schemes are investigated to study their effects in humid conditions. The electric field, impact ionization, and carrier densities are presented as a function of the relative humidity for a silicon diode without passivation openings. Finally, the influence of the concentration of

fixed oxide charges at the interface between silicon and silicon dioxide (SiO_2) is studied. The results are presented for all concentration values at 30 % RH.

The last chapter starts with a brief overview of the current study. It continues with a side-by-side analysis of the electric field distribution and the prompt current to understand the differences between the two. The chapter concludes with a proposal for future studies, outlining potential directions to refine simulations.

The Appendix focuses on the precision production of sensor distributions, describing the steps used to build the silicon strip modules, as well as the quality control methods employed: visual inspection, metrology, hybrid burn-in, and cold cycling. It includes a comprehensive list of TCAD results, starting with the results as a function of RH for the passivation opening schemes that were not discussed in Chapter 6. Next, the results are presented as a function of the fixed oxide charge concentration for all RH values, which were not included in the previous chapter dedicated to TCAD simulations.

Chapter 2

The ATLAS Inner Tracker

2.1 A Brief Introduction to the Standard Model

The Standard Model of Particle Physics (SM) is a theoretical framework that describes elementary particles and their interactions. The discovery of the Higgs boson [2]–[4] by the ATLAS [5] and CMS [6] experiments at the Large Hadron Collider (LHC) at the European Council for Nuclear Research (CERN) in Geneva confirmed the Higgs mechanism postulated independently by three groups of physicists: Peter W. Higgs [7]; François Englert and Robert Brout [8], and Gerald Guralnik, Carl R. Hagen, and Tom Kibble [9]. The Higgs mechanism explains how gauge bosons acquire mass through spontaneous symmetry breaking.

A visual representation of the SM is shown in Fig. 2.1. A first classification of particles consists of fermions and bosons. Fermions are particles with half-integer spin that follow the Pauli exclusion principle [10], which states that two or more particles with half-integer spin cannot occupy the same quantum state within a system. Bosons are particles with integer spin that follow the Bose-Einstein statistics. Unlike fermions, an infinite number of bosons can occupy the same energy state in a system.

Fermions are grouped into quarks and leptons. There are six leptons, three with electric charge: electron (e), muon (μ) and tau (τ) and their respective neutrinos: electron neutrino (ν_e), muon neutrino (ν_μ) and tau neutrino (ν_τ) which have no electric charge and no mass in the SM. For neutrinos to acquire mass through the Yukawa coupling [11], neutrinos require the existence of right-handed counterparts. However, under the SM gauge interactions, the right-handed counterparts are singlets and do not interact weakly, which makes it difficult to detect them experimentally. Quarks manifest in six flavors: up (u), down (d), charm (c), strange (s), top (t) and beauty (b). Quarks, unlike leptons, have color charge and follow the color confinement phenomenon, which explains how quarks are held together by gluons, with the force that holds them together increasing as they move apart, preventing them from being isolated. Due to this phenomenon, quarks are strongly bound together, forming mesons and baryons, e.g., a quark together with an antiquark forms a meson, while three quarks bound together to form a baryon. The lightest baryons are protons and neutrons.

Bosons can be divided into gauge bosons (vector bosons) and scalar bosons. There are four gauge bosons: the gluon (g), photon (γ), Z boson (Z), and W boson (W). Gauge bosons are considered force carriers and mediate the interactions between particles. Photons mediate the electromagnetic interactions. Gluons bind quarks together and mediate the strong interactions. The $W^{\pm}$ boson, together with the Z boson, mediates weak inter-

actions that occur between fermions. In the SM there is only one scalar boson: the Higgs boson, which enables fermions to acquire mass through the Yukawa couplings [11].

The SM is the current theoretical framework for understanding the elementary particles and their interactions; however, it has certain limitations, such as the neutrino mass problem [12], the unknown nature of dark matter, the unknown origin of dark energy, the mystery of matter-antimatter asymmetry, etc. With so many questions left unanswered, particle detectors were created to probe the SM and study new physics.

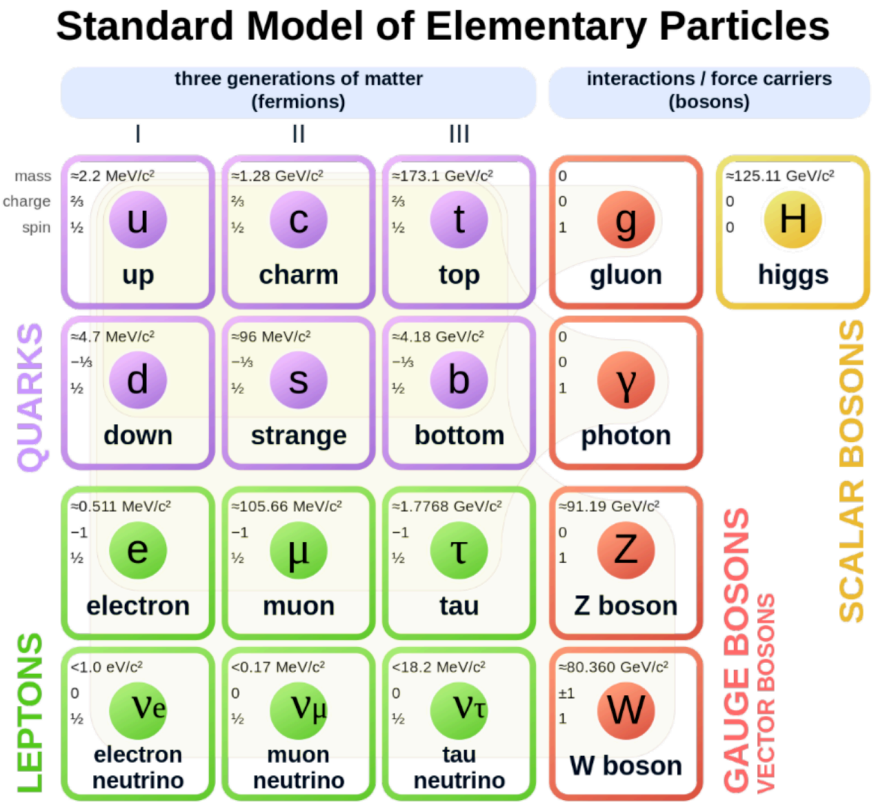

Figure 2.1: Diagram showing the elementary particles of the SM. Particles can be divided into fermions (quarks and leptons) and bosons (gauge bosons and scalar bosons). There are three generations of fermions. Image was taken from [13].

2.2 The ATLAS Detector at LHC

A powerful research tool for probing the SM is the Large Hadron Collider (LHC) at CERN, shown in Fig. 2.2. The LHC is a hadron collider where two counter-rotating proton beams are brought to collision at dedicated interaction points. Protons and heavy nuclei travel in a 26.7 km circular tunnel guided by magnets with a number of accelerating structures that increase their energy along the way. There are four crossing points where particles collide and nine detectors: ATLAS, CMS, LHCb [14], ALICE [15], TOTEM [16], LHCf [17], MoEDAL [18], FASER [19], and SND at the LHC [20], placed around the crossing points. Analysis of the byproducts of these collisions provides physics searches, part of which aim to validate new physics models. So far, the experiments running at the LHC have achieved the discovery of more than 50 new hadrons [21]–[23], allowed in-depth

studies of the properties of the Higgs boson [24], conducted supersymmetry searches [25], etc. Each of the physical processes associated with these phenomena, such as the decay of the Higgs boson, has a low cross section with the number of events generated per second ($\dot{N}_{event}$) [26] at the LHC expressed as:

$$\dot{N}_{event} = L \cdot \sigma_{event}, \tag{2.1}$$

where L is the instantaneous luminosity of the LHC and σ_{event} is the cross section of the process. The instantaneous luminosity is a measure of the collision rate in an accelerator [26] and it is defined by:

$$L = \gamma \frac{n_b N^2 f_{rev}}{4 \pi \beta^* \epsilon_n} R, \tag{2.2}$$

where γ is the particle beam energy in unit of rest mass; n_b is the number of bunches in each beam; N is the number of protons or ions in a bunch; f_{rev} is the revolution frequency; β^* is the beam beta function at the collision point, which describes the size and divergence of the beam; ϵ_n is the transverse normalized emittance quantifying the spread of particles in the transverse plane of the beam, and R is the luminosity geometrical reduction factor, which accounts for geometric inefficiencies in particle collisions.

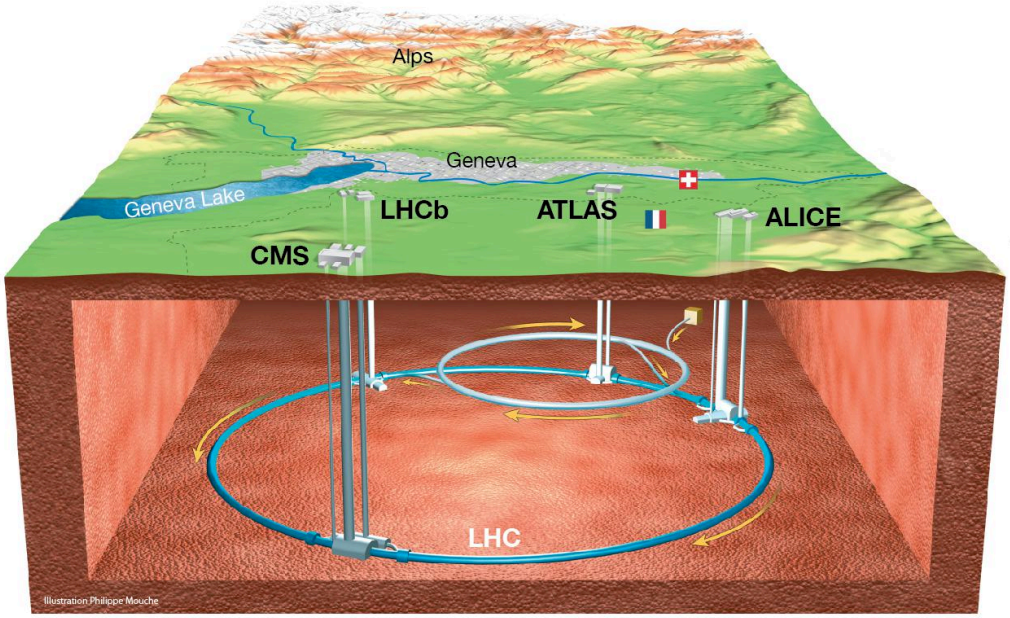

Figure 2.2: Diagram of the LHC two ring hadron collider [27] underneath the Franco-Swiss border, near Geneva. The four main detectors are ATLAS, CMS, ALICE and LHCb.

To increase the statistical power of the searches, the LHC will be upgraded to the High-Luminosity LHC (HL-LHC). The instantaneous luminosity of the machine will be increased from $2 \cdot 10^{34}\,\mathrm{cm}^{-2} \cdot \mathrm{s}^{-1}$ to $5 \cdot 10^{34}\,\mathrm{cm}^{-2} \cdot \mathrm{s}^{-1}$ and as a result the LHC will produce 15 million Higgs bosons per year compared to three million in 2017 [28]. The increase in luminosity implies higher radiation levels, greater heat dissipation suffered by

the guiding magnets and adjacent systems, higher pile-up in the detectors, which occurs when multiple events happen in the same time window, leading to overlapping signals. To overcome these issues, the technical systems, together with the detectors, will be upgraded.

ATLAS is a general-purpose detector providing information on the mass, momentum, energy, and charge of all detectable particles produced at the interaction point. It is a forward-backward symmetric detector with respect to the beam direction. Fig. 2.3 shows a diagram of the ATLAS detector, which is 25 m tall and 44 m long, weighing a total of 7000 tonnes. The four main systems in ATLAS are: the Inner Detector (ID) [29], [30], calorimeters (electromagnetic calorimeter and hadronic calorimeter) [31], [32], muon spectrometers [33], and the magnet system. The ID is the closest detection element relative to the beam pipe. A thin superconducting solenoid magnet surrounds the ID, creating a strong magnetic field which bends the trajectories of charged particles. The radius of the curved tracks is directly proportional to the momentum of a particle and is inversely proportional to the magnetic field strength. The greater the momentum, the less bent the trajectory is, and vice versa. When the curvature of a particle track is measured by a detector, the transverse momentum can be inferred. The transverse momentum, together with additional information such as energy loss, time of flight, etc., leads to particle identification. The tile calorimeters, together with the Liquid Argon (LAr) calorimeters, are placed around the solenoid magnet to measure the energy of particles by absorbing them. Barrel and endcap magnets flank the calorimeters, bending the muon trajectories so that their momentum can be measured. Muon spectrometers are the farthest system from the interaction point, surrounding the rest of the detector. The muon spectrometers detect and measure the transverse momentum, charge, and paths of muons, which pass through the other detector systems.

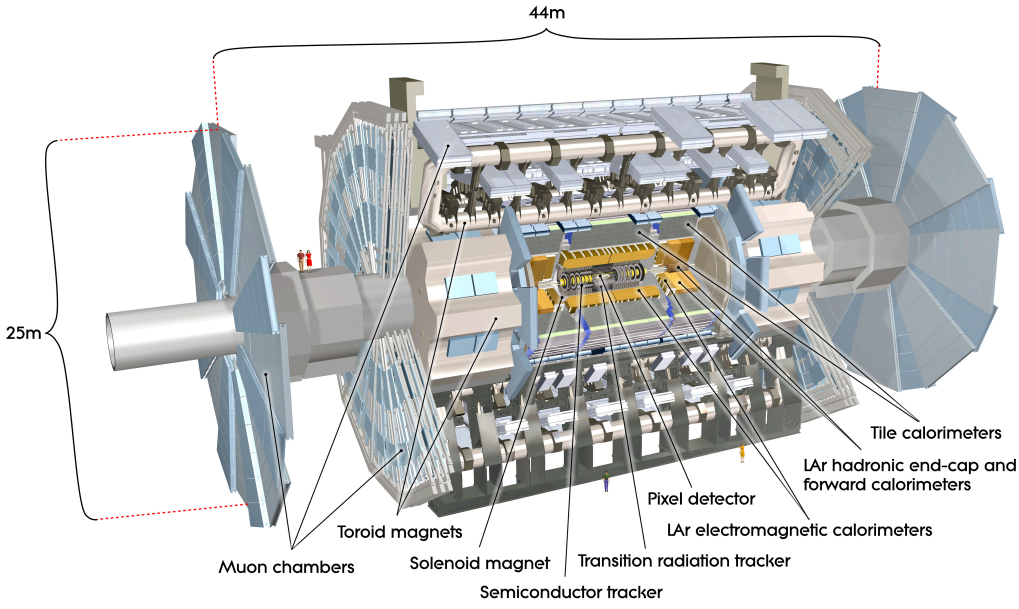

Figure 2.3: Diagram of the ATLAS detector geometry for the LHC Run 3 [34]. The four main detector systems are the ID, the calorimeters (electromagnetic and hadronic calorimeters), the muon spectrometers and the magnet systems.

The muon spectrometers consist of detectors with a timing resolution of less than

4.5 ns. These are fast detectors that provide the orthogonal coordinate of muons. The barrel region is made of Monitored Drift Tubes (MDTs) and Resistive Plate Chambers (RPCs). The MDTs provide high precision in tracking muons, while the RPCs are used for the triggering system. The endcap regions are populated with MDTs, Cathode Strip Chambers (CSCs), and Thin Gap Chambers (TGCs). The CSCs and the TGCs are used in addition to MDTs for triggering purposes because these are optimized to handle the high influx of particles specific to the forward regions.

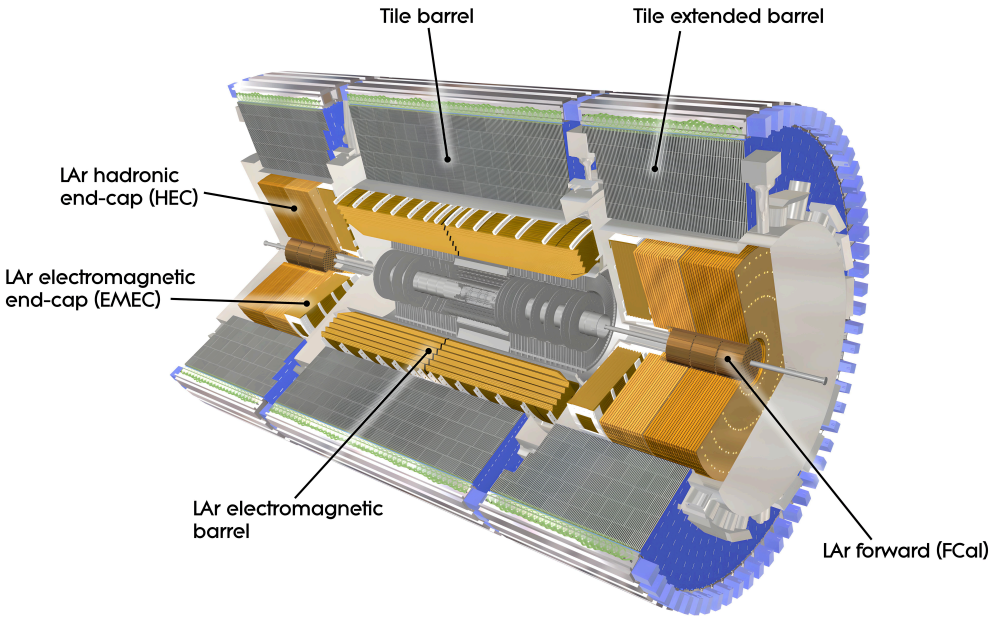

Figure 2.4: Diagram of the ATLAS calorimeter [35]. The calorimeter follows the classical geometry of barrel and endcaps with an electromagnetic and a hadronic calorimeter.

In ATLAS, an electromagnetic and a hadronic calorimeter are employed for measuring the energy of particles produced in proton-proton collisions. The Electromagnetic Calorimeter (ECAL) measures the energy of particles that interact via the electromagnetic force. The ECAL occupies the barrel region, and it extends to the endcaps to cover the full range of polar angles. The ECAL barrel region is split into two identical parts made of 1024 lead stainless steel absorbers, which increase the probability of particle interaction. These are interleaved with an equal number of collecting electrodes with the whole system immersed in LAr.

The Hadronic Calorimeter (HCAL) measures the energy of hadrons and has a similar geometry to the ECAL. The HCAL in the barrel region is made of iron absorbers and plastic scintillation tiles. For the barrel section of the HCAL, iron is used as the absorber material because the radiation levels are lower than in the forward region. There are two independent endcap wheels, each with 32 modules. The wheel closest to the muon spectrometer is made of 25 mm thick copper plates, while the second wheel is made of copper plates twice as thick [36]. Between the copper plates, there are collecting electrodes similar to the ECAL.

The ID is made of three detector regions based on different technologies depending on the distance from the interaction point: the Pixel Detector [30], the Semiconductor Tracker (SCT) [29], and the Transition Radiation Tracker (TRT) [37]. This follows the

same geometry as the other outer-layer subsystems, as illustrated in Fig. 2.5. Pixel Detectors are used closer to the beam line because these provide maximum spatial resolution, which is necessary for tracking particles that originate from high-energy collisions. The pixel detector consists of four barrel layers with 1736 pixel modules and three disks in each endcap with 288 pixel modules. Each module is built with a silicon sensor with 16 readout chips.

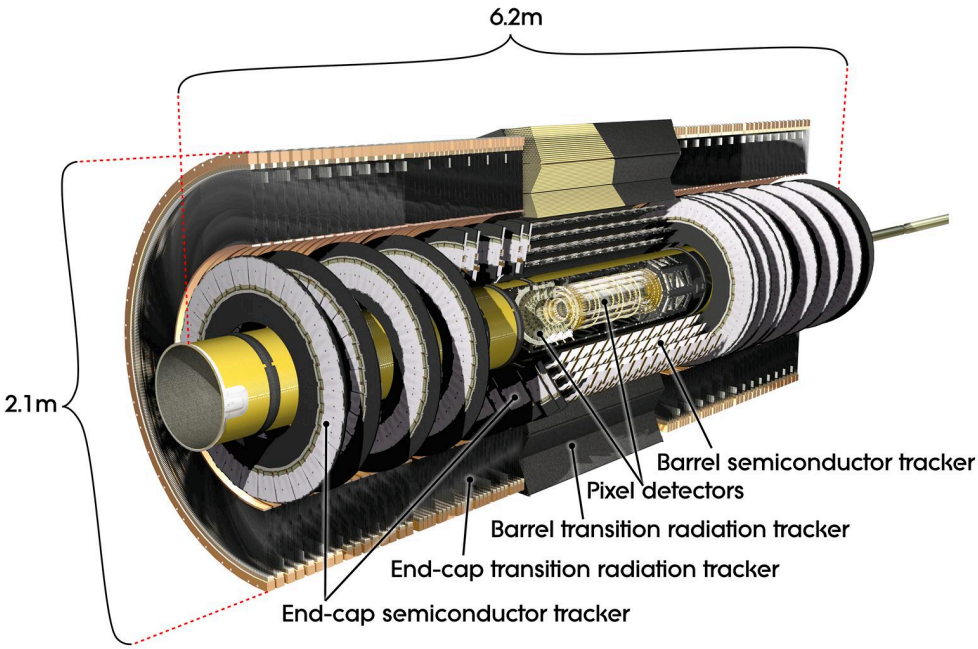

Figure 2.5: Diagram of the ATLAS ID [38]. The ID is made of a pixel detector surrounded by a semiconductor-tracker, and a transition radiation tracker.

For the SCT, silicon strip sensors are used. Although these have a lower spatial resolution, their much lower number of readout channels provides an economical solution for tracking at larger radii of the ID. The SCT is made of five barrel layers and seven disks in each endcap with 4088 silicon microstrip modules. Barrel modules are all identical with a strip pitch of 80 μm, while the endcap has four flavors of modules with the strip pitch varying from 57 μm to 90 μm.

The transition radiation tracker is built of 372 032 drift tubes with an inner diameter of 4 mm filled with a Xe-rich gas mixture. Drift tubes provide a better material budget than silicon because Xe has a high atomic number and a high density, which increases the interaction probability, leading to more ionized electrons. The drift tubes have different lengths depending on their location: 144 cm for barrel and 37 cm for endcap.

2.3 The ATLAS ITk Strip Detector for the HL-LHC

The biggest upgrade planned for ATLAS for the HL-LHC is to replace the ID with an all-silicon Inner Tracker (ITk), which is currently under development. Fig. 2.6 shows a diagram of the ITk, which consists of an inner pixel detector subsystem surrounded by a strip detector subsystem. The strip system consists of four concentric barrel layers with staves and six endcap disks with petals. The first two barrel layers are the inner barrel, while the third and fourth layers make up the outer barrel. The staves and petals are lightweight support elements that hold the strip sensor modules. These have two surfaces: front and back. The support elements have been designed to provide both cooling and electrical power to the strip modules via the End-of-Substructure (EoS) card. For each support element, there are two EoS cards, one for each surface. Fig. 2.7 shows a computer-generated image of a stave and a petal. The stave, a 1400 mm-long rigid structure, houses 14 modules on each surface. For staves, there are two types of modules: the Short Strip (SS) with 2.4 cm strip length and the LS with 4.83 cm strip length. Both barrel modules come with a strip pitch of 75.5 µm. The SS modules are employed in the inner barrel regions, while the LS modules populate the outer barrel.

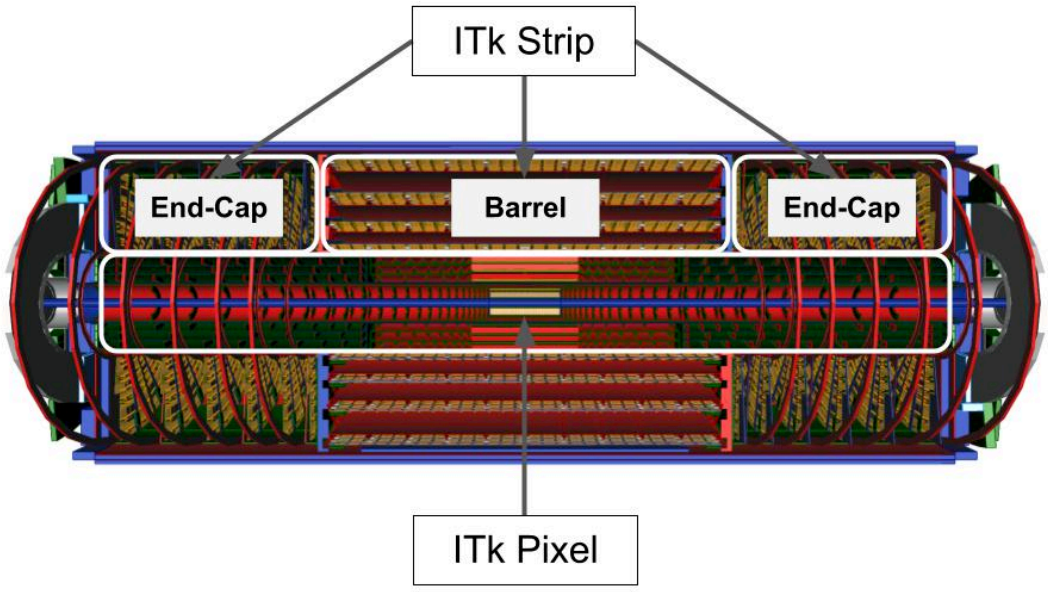

Figure 2.6: Diagram of the future ATLAS ITk [29]. The pixel detector is the closest to the beamline and it is surrounded by the strip detector. The barrel region is flanked by the endcaps on each side.

The petal is a 593 mm radial structure that has been adapted to cover the circular cross-section of the endcap. Following this design, endcap modules can detect particles that pass through the endcap at polar angles not covered by the barrel. There are six types of endcap modules, numbered R0 to R5, with strip pitches between 70 and 80 µm. One petal houses nine different modules on each surface, from R0 to R5. In total, there are 18 000 strip modules between the barrel and the endcaps.

An exploded view of a strip module is presented in Fig. 2.8. All strip modules consist of a sensor, readout, and power electronics. The strip modules have the same components; however, their geometry has been adapted to fit the spatial constraints of the barrel and

endcap. Sensors are read out by "hybrids" - multi-component assemblies that combine readout chips, a control chip, and powering electronics on a Printed Circuit Board (PCB). Hybrids are glued on top of the sensor, and each strip is wirebonded to one corresponding readout channel.

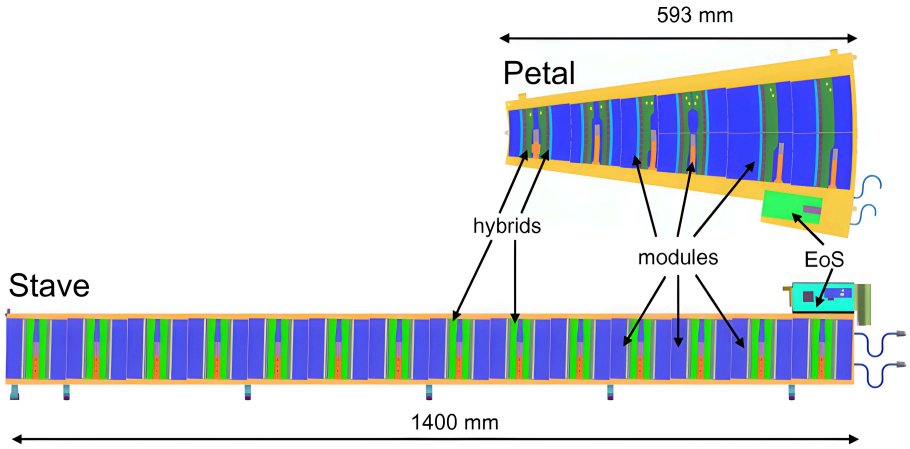

Figure 2.7: Diagram of support structures: petal and stave, populated with modules [29]. The stave is a 1400 mm long structure populated with 14 barrel modules. The petal is a 593 mm long radial structure housing six different endcap modules, from R0 to R5.

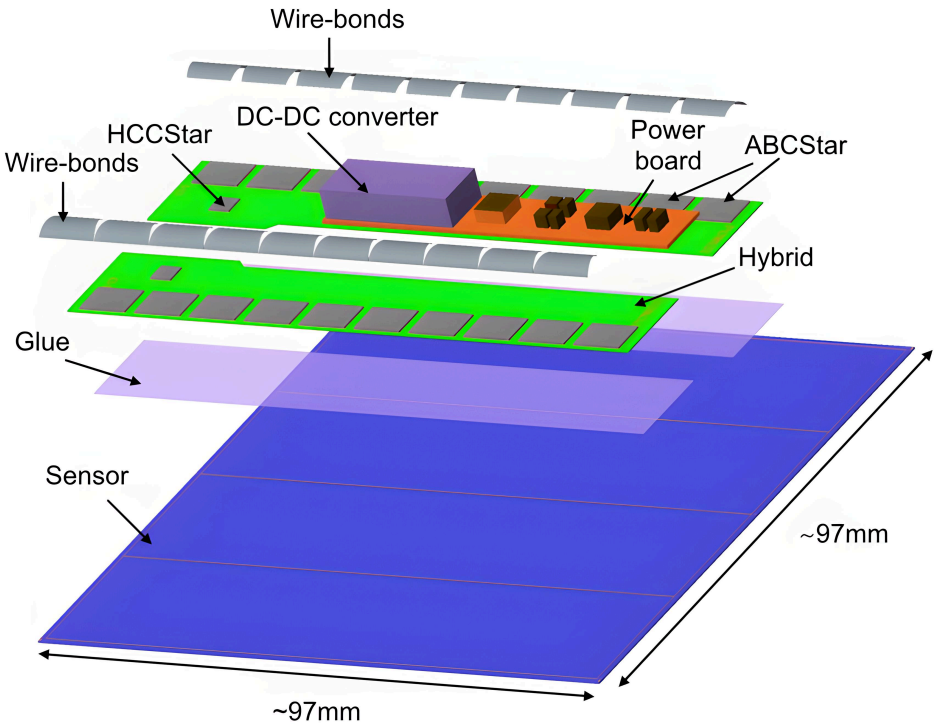

Figure 2.8: Exploded view of the ATLAS ITk barrel module [29]. The main components are the silicon strip sensor, hybrids and the powering electronics.

The signal coming from strips is read out by the ABCStar chip, which is a radiation hard 130 nm feature size chip produced at Global foundry [29]. The ABCStar chip has

256 readout channels, with each channel wirebonded to one strip. There are individual analogue pre-amplifiers and discriminators with independent threshold capabilities for each readout channel. Barrel hybrids have 10 ABCStar chips, while stave hybrids have between seven and 12 readout chips, depending on their flavor. For each hybrid, there is one control chip called the Hybrid Controller Chip Star (HCCStar) chip. The HCCStar chip is built in the 130 nm technology. The architecture of the HCCStar chip is based on a control path, an input channel, and a packet builder. The control path handles the clock and control signals specific to staves and barrels, respectively, and then it sends them to the readout chips.

The powerboard provides electrical power to both the hybrids and the sensor. The powerboard is made of a PCB, a control chip called the Autonomous and Monitoring Control Star (AMACStar) chip, a HV filter, and a Low Voltage (LV) DCDC switch. The AMACStar chip is a radiation-hard chip for powering and control that manages both hybrids and the powerboard and can perform functionality and performance tests on the module.

For the strip module to meet the performance criteria established by the ITk collaboration, each component undergoes strict quality controls before and after module assembly. A brief overview of the quality control methods employed in module production, with a focus on the set-up dedicated to the quality control of hybrids—the hybrid burn-in crate—is given in the Appendix.

Chapter 3

Charge Carrier Transport

The effects described in this chapter are parameterized and used in the Technology Computer-Aided (TCAD) simulation.

3.1 The Band Structure Model

Solid-state materials can be divided into three categories based on their electrical resistivity (ρ): conductors, insulators, and semiconductors. In the International System of Units (SI), electrical resistivity is expressed in $\Omega \cdot \mathrm{m}$. The electrical resistivity of insulators ranges between $10^6\,\Omega \cdot \mathrm{m}$ and $10^{16}\,\Omega \cdot \mathrm{m}$, while the electrical resistivity of conductors is much lower, between $10^{-8}\,\Omega \cdot \mathrm{m}$ and $10^{-6}\,\Omega \cdot \mathrm{m}$ [39]. The value of the electrical resistivity of semiconductors is between insulators and conductors and is sensitive to temperature, illumination, and impurities, a trait exploited in the semiconductor industry. For most applications, the single-crystal form of silicon is used.

A crystal is made of a periodic arrangement of atoms. The primitive cell is the smallest arrangement of atoms that, when repeated in all directions, forms a particular crystal. The silicon atom has 14 electrons with four valence electrons placed in the outer shell (the n = 3 level): two electrons in the 3s subshell and two electrons in the 3p subshell. In a silicon crystal, each atom forms a tetrahedral arrangement with the four neighboring silicon atoms. Each tetrahedral arrangement repeats throughout the entire lattice, fitting into a face-centered cubic lattice.

Depending on the crystal seed orientation, a crystal can have several primitive cell configurations that have an impact on the crystal's electrical and optical properties. These configurations are described by the Miller indices [40], which are a useful method to represent the orientation of a plane in a crystal lattice.

At very low temperatures, $T \simeq 0\,\mathrm{K}$, electrons are bound and are not available for conduction [39]. At higher temperatures, due to thermal excitation, electrons can break the covalent bond, leaving behind a vacancy in the valence band (hole). Both electrons and holes can participate in charge conduction.

Fig. 3.1 shows the band structure diagram of the formation of a silicon crystal from N silicon atoms. The 3s subshells and the 3p subshells of the N silicon atoms amount to 4 orbitals per atom. When N atoms are brought together, due to Pauli's exclusion principle, they split into 8N energy levels. For solids, where N is very large, the individual energy levels are so close together that they form a continuous band of a few eV. The lower-energy electrons occupy the valence band, associated with bonding states. The conduction band consists of higher-energy states that can host electrons excited from

the valence band. For semiconductors, at $T \simeq 0\,\mathrm{K}$, all electrons are situated in the valence band. The energy band between the conduction and valence bands is known as the band gap or forbidden energy band. The band gap energy is equivalent to the energy an electron in the valence band needs to get excited to the conduction band.

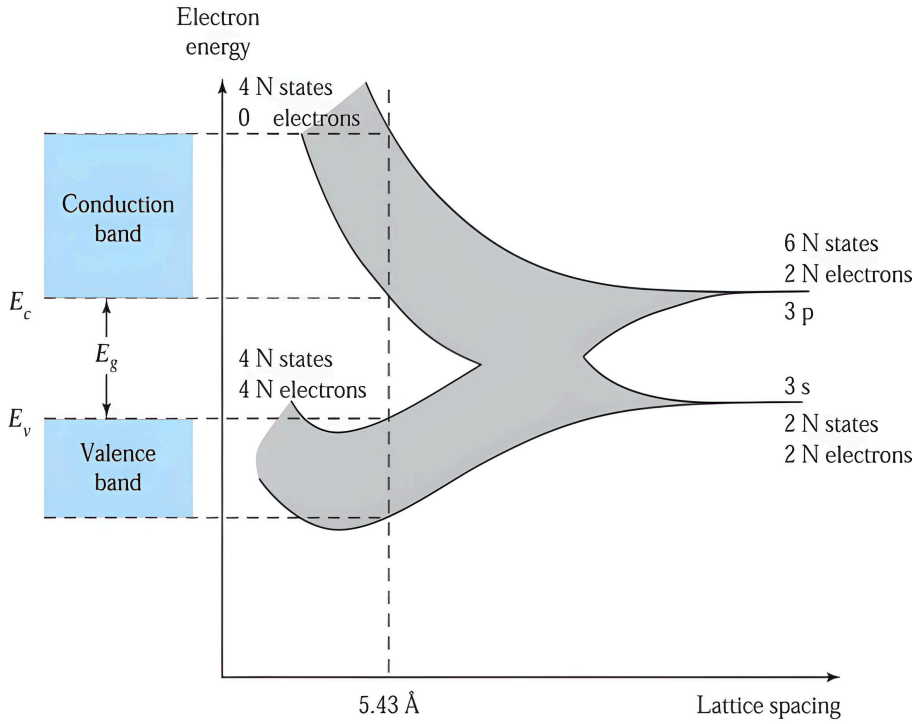

Figure 3.1: Schematic drawing of the formation of energy levels in a silicon crystal by bringing together N silicon atoms. The lattice constant of crystalline silicon is 5.43 Å. The image was taken from [39].

The kinetic energy (E_k) of a free electron [39] is defined by the formula:

$$E_k = \frac{p^2}{2\,m_0}, \tag{3.1}$$

where p is the momentum and m_0 represents the mass of the free electron. In a silicon crystal, the movement of electrons is influenced by the periodic potential of nuclei, leading to the formation of band gaps and energy bands. The electrons in silicon are no longer allowed to have continuous energies, which restricts them to specific energy levels, namely the conduction and valence bands, with forbidden energy levels in between, known as the band gap. To account for this, the mass of the free electron in equation 3.1 is replaced with the effective mass m^*, which is the mass the electrons seem to have under the influence of forces or when they interact with other particles:

$$E = \frac{p^2}{2\,m^*}. \tag{3.2}$$

The energy band diagram for insulators, conductors and semiconductors is shown in Fig. 3.2. Fig. 3.2 (a) illustrates the large band gap ($E_g > 4\,\mathrm{eV}$) characteristic to insulators. In an insulator, valence electrons are strongly bound and there are no free electrons available for current conduction under normal conditions. At $T = 300\,\mathrm{K}$ thermal energy

is not sufficient to excite an electron from the upper levels of the valence band to the conduction band.

Fig. 3.2 (b) shows that for semiconductors the band gap is smaller than for insulators ($0.5\,\text{eV} \leq E_g \leq 3.0\,\text{eV}$). For silicon, the band gap is 1.12 eV at $T = 293\,\text{K}$ [41]. The lattice temperature dependency of the band gap [42] is modeled in TCAD from Synopsys as follows:

$$E_g(T) = E_g(0) - \frac{\alpha T^2}{T + \beta}, \tag{3.3}$$

where $E_g(0)$ is the band gap energy at 0 K, and α and β are material parameters. For silicon, the parameter α is $4.73 \cdot 10^{-4}\,\text{eV} \cdot \text{K}^{-1}$ [39], while β is 636 K [39]. At $T = 0\,\text{K}$, all electrons are situated in the valence band. At $T = 300\,\text{K}$, thermal energy kT, where k denotes the Boltzmann constant, is 0.029 eV [39], which is a fraction of the band gap energy of silicon. The probability of an electron transitioning from the valence band to the conduction band is described by the Boltzmann factor [43]:

$$P = \exp\left(-\frac{E_g}{kT}\right). \tag{3.4}$$

Although at $T = 300\,\text{K}$ the probability of an electron to become thermally excited is small, in silicon there are $5 \cdot 10^{22}\,\text{atoms} \cdot \text{cm}^{-3}$, and therefore, some electrons gain enough energy to transition to the conduction band.

Fig. 3.2 (c) illustrates how, for metals, the conduction band overlaps with the valence band. The electrons situated on the upper levels of the valence band can transition to the conduction band once they gain enough energy. In metals, only a small applied electric field is necessary for electrons to move freely since there are many unoccupied energy states close to the occupied states. That is to say, metals have a low resistivity and they conduct current easily.

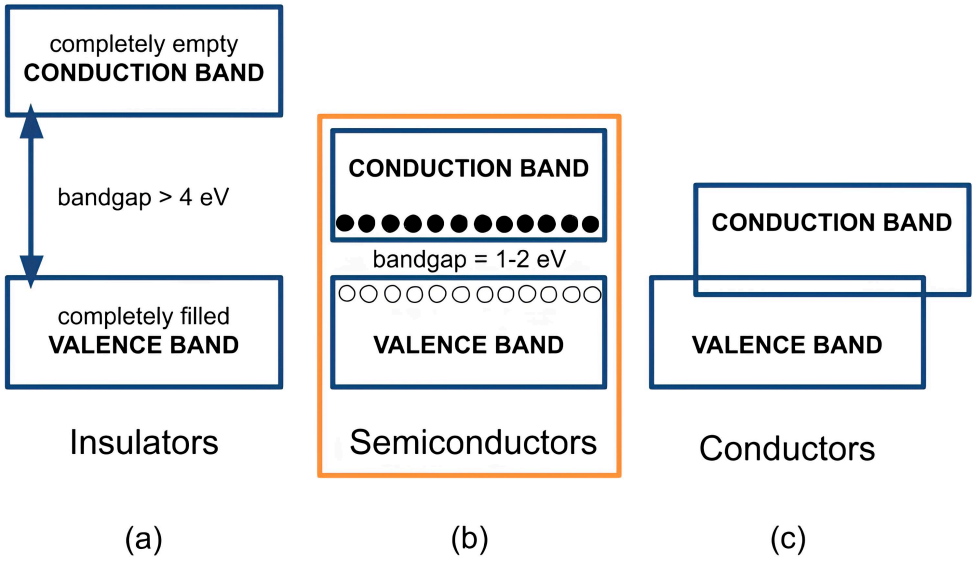

Figure 3.2: Schematic drawing of the band diagram model for different types of materials: conductors (a), semiconductors (b) and insulators (c).

An intrinsic semiconductor is a semiconductor that has not been doped. Doping represents the technological process in which impurities are added to a semiconductor in

order to alter its electrical properties. A characteristic of intrinsic semiconductors is that the electron and hole densities are equal. The first step to determine the electron density $n(E)$ in an intrinsic semiconductor is to determine how many electrons occupy a specific energy level within a narrow range ($\mathrm{d}E$). The electron density [39] is defined by:

$$n(E) = N(E) \cdot F(E)\,\mathrm{d}E, \tag{3.5}$$

where $N(E)$ [39] is the number of available electron states per volume and per energy range at a specific energy ($\mathrm{d}E$):

$$N(E) = M_C \frac{\sqrt{2}}{\pi^2} \frac{\sqrt{m_{de}^3 (E - E_C)}}{\hbar^3}, \tag{3.6}$$

where M_C is the number of equivalent minima in the conduction band, m_{de} is the density-of-state effective mass for electrons, E_C is the conduction band minimum energy, and $\hbar$ is the reduced Planck constant.

The term $F(E)$ is the probability that an electron occupies an available energy state in the given energy range. To derive the electron density in the conduction band, equation 3.5 has to be integrated across all energy levels corresponding to the conduction band:

$$n = \int_{E_C^{min}}^{E_C^{max}} n(E)\,\mathrm{d}E = \int_{E_C^{min}}^{E_C^{max}} N(E) \cdot F(E)\,\mathrm{d}E, \tag{3.7}$$

where n is expressed in cm^{-3}, and $N(E)$ is expressed in $\mathrm{cm}^{-3} \cdot \mathrm{eV}^{-1}$. The term E_C^{min} refers to the minimum energy in the conduction band, while E_C^{max} refers to the maximum energy in the conduction band.

The probability that an electron occupies a certain energy state is given by the Fermi-Dirac distribution function [44]:

$$F(E) = \frac{1}{1 + \mathrm{e}^{(E - E_F)/kT}}, \tag{3.8}$$

where E_F is the Fermi level, which corresponds to the energy level that has a 50 % chance to be occupied by an electron; k is the Boltzmann constant, and T is the absolute temperature. Equation 3.8 can be rewritten depending on the energy range with respect to the Fermi level:

$$F(E) \simeq \mathrm{e}^{-(E - E_F)/kT} \qquad \text{for } (E - E_F) > 3kT, \tag{3.9}$$

$$F(E) \simeq 1 - \mathrm{e}^{-(E - E_F)/kT} \qquad \text{for } (E - E_F) < 3kT. \tag{3.10}$$

For an intrinsic semiconductor, there are very few states occupied in the conduction band, and therefore, the probability for an electron to occupy the valence band is approximately one. In an intrinsic semiconductor, at $T = 0\,\mathrm{K}$, all electrons are situated in the valence band. The Fermi level E_F is situated in the middle of the band gap. At any given temperature, the number of electrons in the conduction band equals the number of holes in the valence band. The Fermi-Dirac distribution must be symmetric with respect to the Fermi level. For equal concentrations of electrons and holes, the Fermi level at any given temperature must be in the middle of the band gap.

When $(E - E_F) \gg 3kT$, the maximum energy of the conduction band can be approximated as infinite [39]. For energies much greater than kT, the probability that

an electron occupies a certain energy state expressed in equation 3.8 becomes extremely small. This means that energies well above the thermal energy scale have a negligible contribution to physical quantities like the electron density:

$$n = \frac{2}{\pi^{3/2}} N_C (kT)^{3/2} \int_{E_C^{min}}^{\infty} (E - E_C)^{1/2} \exp\left(-\frac{E - E_F}{kT}\right) \mathrm{d}E, \tag{3.11}$$

where N_C is the effective density of states in the conduction band for silicon [39], which is defined by:

$$N_C \equiv 12 \left(\frac{2\pi m_n kT}{h^2}\right)^{3/2}, \tag{3.12}$$

where h is Planck's constant and m_n is the electron effective mass. Equation 3.11 can be generalized by defining the conduction band minimum as E_C:

$$n = N_C \exp\left(-\frac{E_C - E_F}{kT}\right). \tag{3.13}$$

Expressing the electron density as a function of the difference between the energy of the conduction band and the Fermi level shows how the band structure influences the availability of states. The hole density can be expressed in a similar way to the electron density:

$$p = N_V \exp\left(-\frac{E_F - E_V}{kT}\right), \tag{3.14}$$

where N_V is the effective density of states in the valence band for silicon [39], and it is defined as:

$$N_V \equiv 2 \left(\frac{2\pi m_p kT}{h^2}\right)^{3/2}, \tag{3.15}$$

where m_p is the hole effective mass.

Adding the electron density in equation 3.13 together with the hole density in equation 3.14 gives the Fermi level for an intrinsic semiconductor [39]:

$$E_F = \frac{E_C + E_V}{2} + \frac{kT}{2} \ln\left(\frac{N_V}{N_C}\right). \tag{3.16}$$

The intrinsic carrier density [39] can be obtained by multiplying the electron density with the hole density, and simplifying the exponents $E_g = E_C - E_V$:

$$np = n_i^2, \tag{3.17}$$

$$n_i^2 = N_C N_V \exp\left(-\frac{E_g(T)}{kT}\right). \tag{3.18}$$

An extrinsic semiconductor is a semiconductor that has been doped with impurities. In the context of doping, there are two types of impurities: acceptor and donor impurities. Acceptor impurities are atoms that have fewer valence electrons than the semiconductor atoms, while donor impurities have a higher number of valence electrons than the semiconductor atoms.

Fig. 3.3 (a) shows a donor impurity atom, an arsenic atom replacing one of the silicon atoms in the covalent bond. Only a small amount of energy is required to free the electron coming from an arsenic atom, which will transition to the conduction band, leaving behind an ionized donor impurity. For each ionized donor impurity, there is an electron in the conduction band, and therefore, charge neutrality is still satisfied. The concentration of delocalized electrons in the conduction band is greater than the intrinsic concentration of electrons. Silicon doped with donor impurities becomes n-type, meaning that the majority of charge carriers are electrons.

Fig. 3.3 (b) shows an acceptor impurity atom, a boron atom replacing one of the silicon atoms in the covalent bond. Silicon that has been doped with acceptor impurities becomes p-type because boron is a trivalent atom that has one electron less than silicon, leading to one of the silicon covalent bonds to remain unsatisfied. This vacancy is similar to the one left behind by an excited electron, i.e., a hole. If the vacancy is filled, the electron that was captured is not as strongly bound as a valence electron would normally be. In p-type semiconductors, the concentration of holes is greater than the intrinsic concentration of holes in the valence band.

The doping atoms interrupt the perfect periodicity of the crystal lattice, adding energy levels within the band gap that were otherwise forbidden. Donor impurities add energy levels closer to the conduction band, while acceptor impurities add energy levels closer to the valence band.

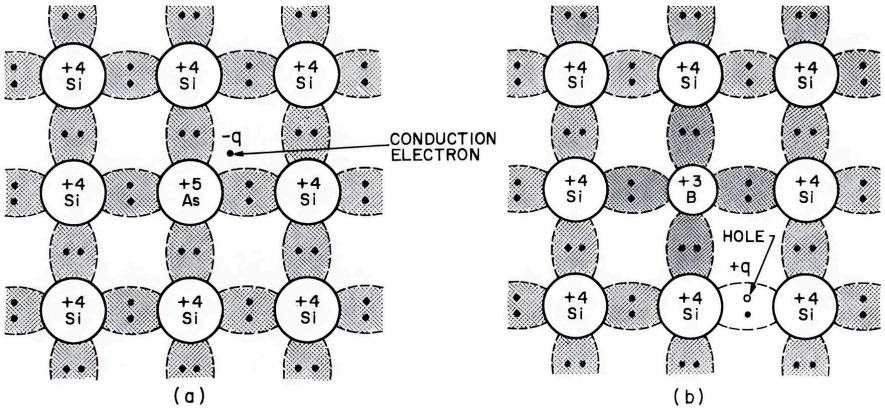

Figure 3.3: Schematic representation of n-type silicon (a) and p-type silicon (b) [45]. Here q^- denotes one conduction electron donated by the arsenic atom, which does not form a covalent bond. Whereas, q^+ denotes a vacancy resulting from the boron atom forming only three covalent bonds with the silicon atom.

Based on the ionization energy, dopant impurities (acceptors or donors) can be divided into shallow and deep. Shallow dopant impurities require minimal ionization energy, usually in the range of thermal energy, to release a charge carrier, enabling the transition of electrons into one of the lower levels of the conduction band or holes to form in the valence band. They introduce energy levels in the band gap closer to the edge of the conduction (donor impurities) or the valence (acceptor impurities) band. Unlike shallow dopant impurities, deep dopant impurities require an ionization energy greater than thermal energy at room temperature, which is less effective at generating free carriers. These introduce energy levels near the middle of the band gap.

In a shallow-doped semiconductor, at room temperature, thermal excitation is usually enough to excite all donor electrons into the conduction band (n-type semiconductor) or

all acceptor electrons into the valence band (p-type semiconductor). This effect is referred to as complete ionization. Under the influence of complete ionization, the majority carrier density (n for electrons, p for holes) is equivalent to the dopant impurity concentration (N_D for donor concentration, N_A for acceptor concentration). In this case, the Fermi level [39] can be obtained in terms of the dopant impurity concentration and the number of available energy levels at the edge of the conduction (N_C) or valence band (N_V) (the effective density of states):

$$E_{C,V} - E_F = kT \ln\left(\frac{N_{C,V}}{N_{D,A}}\right), \tag{3.19}$$

where E_C is the lower edge of the conduction band, E_V is the upper edge of the valence band, and E_F is the Fermi level. If the donor concentration increases, the difference $E_C - E_F$ decreases, which means that the Fermi level moves closer to the bottom of the conduction band. In contrast, if the acceptor concentration increases, the difference $E_C - E_F$ will increase, meaning that the Fermi level moves closer to the top of the valence band.

The equilibrium carrier concentration [39] can be derived in terms of the Fermi level using equation 3.19:

$$n^* = n_i \exp\left(\pm\frac{E_F - E_{C,V}}{kT}\right), \tag{3.20}$$

where n^* is the equilibrium carrier concentration (n for electrons, p for holes) and n_i is the intrinsic carrier concentration. The positive sign corresponds to the electron concentration, while the negative sign corresponds to the hole concentration.

When both impurity types are present in a semiconductor, the majority type will dictate the current conduction. Charge neutrality has to be satisfied, therefore the Fermi level adjusts itself such that the electron concentration equals the hole concentration. Under complete ionization, charge neutrality is defined as:

$$n + N_A = p + N_D. \tag{3.21}$$

Equations 3.17 and 3.18 can be solved for electrons and holes densities:

$$n = \frac{1}{2}\left[N_D - N_A + \sqrt{(N_D - N_A)^2 + 4n_i^2}\right], \tag{3.22}$$

$$p = \frac{1}{2}\left[N_A - N_D + \sqrt{(N_A - N_D)^2 + 4n_i^2}\right]. \tag{3.23}$$

It should be noted that the carrier concentrations can be calculated for arbitrary values of the acceptor and donor concentrations.

3.2 Carrier Drift

In a semiconductor, electrons in the conduction band can be approximated as free electrons because these are free to move everywhere in the crystal lattice; however, unlike electrons in vacuum, electrons in the conduction band will experience the influence of the lattice potential. The kinetic energy of an electron moving in three-dimensional space is equivalent to the thermal energy derived from the equipartition theorem [46]:

$$\frac{1}{2}m_n v_{th}^2 = \frac{3}{2}kT, \tag{3.24}$$

where m_n is the effective mass of an electron, v_{th} is the average thermal velocity, k is the Boltzmann constant, and T is the absolute temperature. In silicon, at $T = 300\,\mathrm{K}$ the average thermal velocity of electrons is $10^7\,\mathrm{cm}\cdot\mathrm{s}^{-1}$ [39]. The movement of free electrons is a collection of random scatterings with lattice atoms, impurity atoms, and other scattering centers, such as ionized impurity scatterings, crystallographic defects, etc. The average distance between collisions is referred to as the mean free path, while the time between collisions is known as the mean free time (τ_c).

In the presence of a low-intensity electric field, the electric field force ($-q\mathcal{E}$) will influence electrons such that their thermal motion between collisions will follow the field lines. An additional velocity component known as the drift velocity (v_n) will contribute to the movement of electrons. Considering the effect of the electrical force on an electron during the mean free time (τ_c) between collisions, the drift velocity can be derived by applying Newton's second law to the electric part of the Lorentz force equation [47]:

$$q\mathcal{E}\tau_c = m_n \cdot v_n. \tag{3.25}$$

From equation 3.25, the drift velocity of charge carriers [48] can be defined as:

$$v = \frac{q\tau_c}{m}\mathcal{E}. \tag{3.26}$$

The drift velocity in equation 3.26 is directly proportional to the applied electric field, and the proportionality factor is known as the low field mobility:

$$\mu_0 = \frac{q\tau_c}{m} = \frac{v}{\mathcal{E}}. \tag{3.27}$$

Mobility quantifies how much the electric field influences the motion of a charged particle. Fig. 3.4 illustrates how the electric field amplitude affects the drift velocity of electrons and holes in silicon at $T = 300\,\mathrm{K}$. The data reported by Canali et al. [49] was used to demonstrate that the observed velocity trends can be described by what is now known as the Canali model for drift velocity saturation. The Canali model is employed in TCAD simulations to model the velocity saturation of carriers with the applied electric field in silicon. The curves in Fig. 3.4 were interpolated to highlight their agreement with the trend given by the Canali model [49]:

$$v = \mu_0 \frac{\mathcal{E}}{[1 + (\mathcal{E}/\mathcal{E}_c)\beta]^{1/\beta}}, \tag{3.28}$$

where μ_0 is the low field mobility, while $\mathcal{E}_c$ and β are fitting parameters. $\mathcal{E}_c$ is related to the saturation drift velocity (v_s) by $v_s = \mu_0\mathcal{E}_c$. At $T = 300\,\mathrm{K}$, $\mathcal{E}_c$ is $7240\ \mathrm{V}\cdot\mathrm{cm}^{-1}$ and β is 1.30.

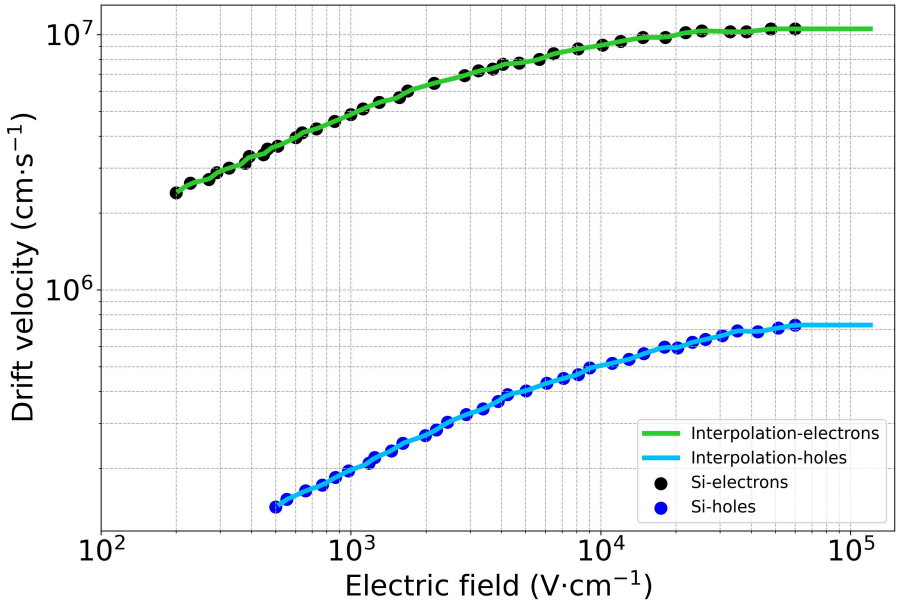

Figure 3.4: Dependence of the drift velocity of electrons and holes in silicon (Si) on the electric field amplitude at $T = 300\,\mathrm{K}$. The plotted data here was taken from [49] and interpolated to show the expected trend.

For values lower than $10^4\,\mathrm{V}\cdot\mathrm{cm}^{-1}$, the drift velocity increases linearly with the electric field according to equation 3.26. At higher electric field values, the drift velocity increases sublinearly and saturates to approximately $10^5\,\mathrm{cm}\cdot\mathrm{s}^{-1}$. This phenomenon is known as velocity saturation. For high electric field values, the drift velocity increases because the electric field exerts a higher force on charged particles, which would increase their acceleration between collisions. Eventually, the frequency with which carriers collide (the scattering event rate) balances out the acceleration gained from the electric field, leading to velocity saturation.

From the first equality in 3.27, it can be noted that mobility is directly dependent on the mean free time between collisions, which is influenced primarily by lattice vibrations and impurities in the semiconductor. Lattice scattering affects the thermal energy of carriers, while impurity scattering alters their pathways.

Lattice scattering (also referred to as phonon scattering) occurs due to the thermal vibrations of atoms when $T > 0\,\mathrm{K}$. The periodicity of the lattice is perturbed, enabling energy transfer between the lattice and charge carriers. When the temperature increases, the lattice vibrations become more frequent, which in turn increases the lattice scattering while decreasing the mobility [48].

Crystalline silicon contains defects, typically impurities and dislocations. Carriers that pass close enough to ionized dopant impurities are scattered such that the Coulomb force changes their trajectories. This phenomenon is known as impurity scattering. The impurity scattering depends linearly on the concentration of impurities and decreases with temperature [48] because, at higher temperatures, carriers move faster, spending less time near impurity centers, which means they interact less with impurities.

The mobility of charge carriers can be expressed in terms of the mobility influenced by impurity scatterings (μ_i) and the mobility influenced by lattice scatterings (μ_l) using

Mathiessen's rule [50]:

$$\frac{1}{\mu} = \left(\frac{1}{\mu_i} + \frac{1}{\mu_l}\right)^{-1}. \tag{3.29}$$

Fig 3.5 shows a schematic comparison between an n-type semiconductor at thermal equilibrium (a) and when a bias voltage is applied (b), together with the band structure diagram for both cases. Here E_C corresponds to the lower edge of the conduction band, E_V corresponds to the upper edge of the valence band, E_F is the Fermi level, and E_i denotes the intrinsic Fermi level, which represents the position of the Fermi level in an intrinsic semiconductor where the concentrations of electrons and holes are equal. In the presence of an electrostatic difference across the semiconductor, electrons will be influenced by the electrical force [39], which can be expressed as the negative gradient of the potential energy:

$$-q\mathcal{E} = -\frac{\mathrm{d}E_i}{\mathrm{d}x}. \tag{3.30}$$

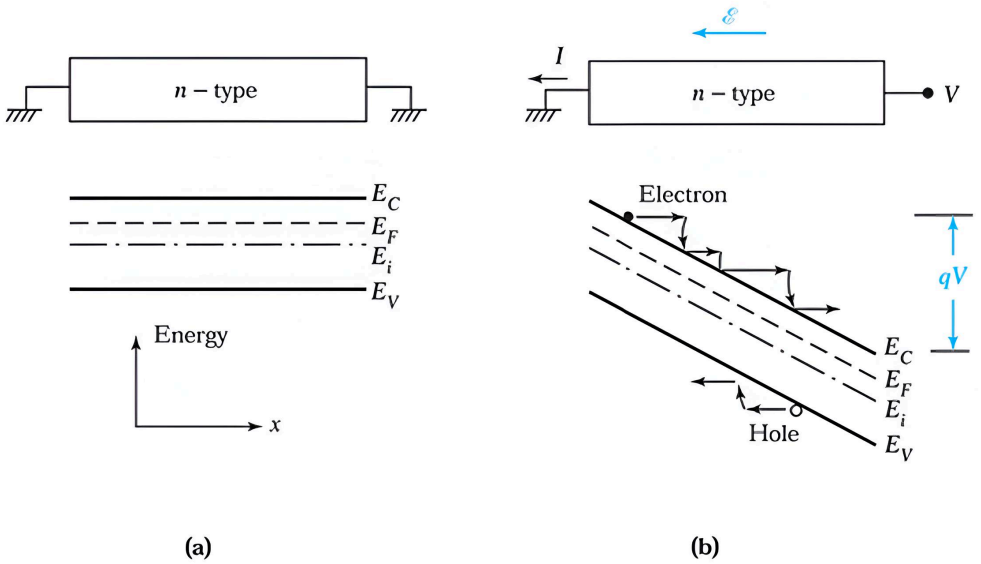

Figure 3.5: Schematic comparison between an n-type semiconductor at thermal equilibrium (a) and when a bias voltage is applied (b). The E_C represents the lower energy level of the conduction band; E_V represents the highest energy level of the valence band; E_i is the intrinsic Fermi level, and E_F is the Fermi level. Image was taken from [39].

The electric field in terms of the electrostatic potential ($\phi = E_i/q$) can be obtained by dividing equation 3.30 by the electric charge:

$$\mathcal{E} = \frac{\mathrm{d}\,\phi}{\mathrm{d}\,x}. \tag{3.31}$$

It can be noted that the electrostatic potential is directly proportional to the intrinsic Fermi level, and both measures decrease linearly with distance. The energy band diagram in Fig. 3.5 (b) shows electrons in the conduction band moving in the opposite direction of the applied electric field. While electrons move against the electric field, they can suffer several collisions where they lose some or all of their kinetic energy to the lattice.

This would return electrons closer to their thermal equilibrium position. In this case, the kinetic energy of electrons corresponds to their position in relation to the edge of the conduction band. Electrons will continue to move in the opposite direction of the electric field while they regain their kinetic energy.

The motion of holes can be visualized similarly, but in the opposite direction due to their positive charge. The motion of carriers under the influence of an electric field generates a current called the drift current. In a semiconductor with cross-sectional area A, length L, and carrier concentration n^* (n for electrons, p for holes), the drift current density $J_{drift(n,p)}$ (n for electrons, p for holes) is given by:

$$J_{drift(n,p)} = \frac{I_{n,p}}{A} = n^* q v_{n,p} = n^* q \mu_{n,p} \mathcal{E}, \tag{3.32}$$

where I_n and I_p represent the electron and hole currents, respectively, with subscripts n and p denoting electrons and holes.
The total drift current density in a semiconductor can be obtained by summing the electron and hole drift current densities:

$$J_{drift} = (nq\mu_n + pq\mu_p)\mathcal{E}, \tag{3.33}$$

where the term $(nq\mu_n + pq\mu_p)$ is the conductivity (σ). In an extrinsic semiconductor, where only one carrier type participates in the current conduction, resistivity [39] can be simplified to:

$$\rho_{n,p} = \frac{1}{qn^*\mu_{n,p}}. \tag{3.34}$$

3.3 Charge Carrier Dynamics

3.3.1 Diffusion

If the carrier concentration varies spatially, carriers will move from regions of higher concentration to regions of lower concentration. This motion is known as diffusion and it is governed by Fick's law [51]:

$$\frac{dn_t}{dt} = -D\nabla^2 n_t, \tag{3.35}$$

where $D = l \cdot v_{th}$ is the charge carrier diffusion coefficient, l is the mean free path, v_{th} is the thermal velocity, ∇^2 is the Laplace operator, and n_t is the particle density (electrons and holes). The diffusion coefficient describes how fast a particle diffuses through a medium and is proportional to the flux of carriers. The diffusion current density generated by the carrier's movement from a higher concentration region to a lower concentration region is defined as:

$$J_{diff} = qD\nabla n_t. \tag{3.36}$$

The Einstein relation [39] correlates the diffusion coefficient (D) with mobility. The general form of the Einstein relation can be obtained starting from the thermal energy equation:

$$\frac{1}{2}mv_{th}^2 = \frac{3}{2}kT, \tag{3.37}$$

and the low field mobility expressed in equation 3.27:

$$D = \frac{kT}{q}\mu. \tag{3.38}$$

The total conduction current density can be written as the sum of the drift and diffusion currents:

$$J_{cond} = q\mu n_t \mathcal{E} + qD\nabla n_t. \tag{3.39}$$

3.3.2 Generation - Recombination Processes

In general, energy is released as a result of recombination processes; however, the type of energy depends on the actual recombination process, e.g., the energy emitted can be in the form of a photon or heat emitted to the lattice. The recombination processes can include band-to-band Auger recombination [52], [53], or indirect mechanisms such as Shockley-Read-Hall (SRH) recombination (also known as trap-assisted recombination) [54], [55], and surface recombination [56].

Generation happens when an electron transitions to the conduction band, leaving behind a hole in the valence band. This process is characterized by the generation rate G_{th}, which represents the number of electron-hole pairs generated in a semiconductor per unit time. When an electron transitions from the conduction band to the valence band, an electron-hole pair is annihilated. This process is called recombination and is characterized by the recombination rate, R_{th}. At thermal equilibrium, the generation rate is equal to the recombination rate.

The recombination rate [39] is directly proportional to the number of electrons in the conduction band and the number of holes in the valence band, as showcased in the following relation:

$$R = G = \beta np, \tag{3.40}$$

where β is a proportionality factor.

For simplicity, the discussion will focus only on the example of charge injection through laser illumination in an n-type semiconductor. This will create electron-hole pairs inside the semiconductor with a generation rate G_L, which would disrupt the charge neutrality equilibrium. Under the influence of charge injection, the generation and recombination rates [39] can be described as:

$$R = \beta(n_{n0} + \Delta n)(p_{n0} + \Delta p), \tag{3.41}$$

$$G = G_{th} + G_L, \tag{3.42}$$

where n_{n0} and p_{p0} are the concentrations of electrons and holes in an n-type semiconductor at thermal equilibrium, while Δn and Δp are the excess charge carriers produced:

$$\Delta n = n_n - n_{n0}, \tag{3.43}$$

$$\Delta p = p_n - p_{n0}. \tag{3.44}$$

In an n-type semiconductor, for processes such as recombination, the behavior of the minority carriers, holes, is important because the n-type semiconductor is already rich in electrons. The net rate of change of the hole concentration [39] can be defined as:

$$\frac{dp_n}{dt} = G - R = G_L + G_{th} - R. \tag{3.45}$$

Under the influence of external factors, e.g., laser illumination, the generation rate (G_L) can become equal to the recombination rate if external factors such as illumination, temperature, bias voltage, etc., remain constant, which means that the system reached a steady state and the net rate of change for the hole concentration becomes zero ($\frac{dp_n}{dt} = 0$):

$$G_L = R - G_{th} \equiv U, \tag{3.46}$$

where U is the net recombination rate. The net recombination rate can be derived by replacing equation 3.40 and 3.41 in equation 3.46:

$$U = \beta(n_{n0} + p_{n0}\Delta p)\Delta p. \tag{3.47}$$

If $\Delta p, p_{n0} \ll n_{n0}$, relation 3.47 can be simplified to:

$$U \equiv \beta n_{n0}\Delta p = \frac{p_n - p_{n0}}{\frac{1}{\beta n_{n0}}}, \tag{3.48}$$

where the denominator, $\frac{1}{\beta n_{n0}}$, is the recombination lifetime of holes (τ_p):

$$U = \frac{p_n - p_{n0}}{\tau_p}. \tag{3.49}$$

Auger recombination [52], [53] is the recombination process between an electron and a hole where the emitted energy is carried by a third charge carrier: either an electron or a hole. Auger recombination is an intrinsic property of silicon, which ultimately limits its performance under high-doping or high-injection conditions [53]. Unlike trap-assisted recombination, which can be reduced by lowering the impurity density, Auger recombination cannot be eliminated. In a low-doped silicon diode ($10^{12}\,\mathrm{cm}^{-3}$) with highly doped implants ($10^{19}\,\mathrm{cm}^{-3}$), Auger recombination may become relevant close to the implants because the recombination rate [42], [53] is dependent on the electron and hole concentrations:

$$R_{Auger} = (C_n n + C_p p)(np - n_{i,eff}^2), \tag{3.50}$$

where $n_{i,eff}$ is the effective intrinsic carrier concentration, n is the electron density, p is the hole density. The effective intrinsic carrier concentration is the adjusted carrier concentration in a semiconductor, accounting for modifications due to doping, temperature variations, etc. The terms C_n and C_p are the temperature-dependent Auger coefficients [42], [53]:

$$C_{n,p}(T) = \left[A_{A,(n,p)} + B_{A,(n,p)}\left(\frac{T}{T_0}\right) + C_{A,(n,p)}\left(\frac{T}{T_0}^2\right)\right]\left[1 + H_{n,p}\exp\left(-\frac{n}{N_{0,(n,p)}}\right)\right], \tag{3.51}$$

where $T = 300\,\mathrm{K}$, and $N_{0,(n,p)}$ is the density of charge carriers ($N_{0,n}$ for electrons, $N_{0,p}$ for holes). The parameters necessary to quantify equation 3.51 specific to silicon [42] are presented in Table 3.1.

Table 3.1: Auger recombination model coefficients in silicon

	$A_A\,[\mathrm{cm}^6\mathrm{s}^{-1}]$	$B_A\,[\mathrm{cm}^6\mathrm{s}^{-1}]$	$C_A\,[\mathrm{cm}^6\mathrm{s}^{-1}]$	H	$N_0\,[\mathrm{cm}^{-3}]$
Electrons	$6.7 \cdot 10^{-32}$	$2.45 \cdot 10^{-31}$	$-2.2 \cdot 10^{-32}$	3.46	$1 \cdot 10^{18}$
Holes	$7.2 \cdot 10^{-32}$	$4.5 \cdot 10^{-33}$	$2.36 \cdot 10^{-32}$	8.25	$1 \cdot 10^{18}$

The lifetime of charge carriers for Auger recombination [53] can be approximated for high-injection conditions to:

$$\tau_{Auger,hi} = \frac{1}{(C_n + C_p)\Delta n^2}, \tag{3.52}$$

and for low-injection conditions to:

$$\tau_{Auger,li} = \frac{1}{C_{n,p} N_{dop}^2}, \tag{3.53}$$

where $\Delta n = n - n_0 = p - p_0$ is the excess carrier density, n_0 and p_0 are the thermal equilibrium concentrations of electrons and holes, while N_{dop} is the net dopant concentration. The net dopant concentration is the concentration of ionized donor atoms in an n-type semiconductor or ionized acceptor atoms in a p-type semiconductor.

SRH recombination [54], [55] is the recombination process facilitated by the presence of traps as presented in Fig. 3.6. A trap is a localized defect or impurity state in the band gap of a semiconductor that can temporarily capture charge carriers. Initially,

the trap is neutral, but once it captures a charge carrier, it can become either positive or negative depending on the carrier's charge type. When an electron from the conduction band becomes trapped: Fig. 3.6 (a), the trap becomes negative. If the electron does not recombine with a hole inside the trap, it is released by the trap back into the conduction band: Fig. 3.6 (b). The same process is valid for holes; when a hole from the valence band is captured by a trap: Fig. 3.6 (c), the trap becomes positive. If the hole doesn't recombine with an electron inside the trap before getting enough thermal energy, the hole will be released back into the valence band: Fig. 3.6 (d).

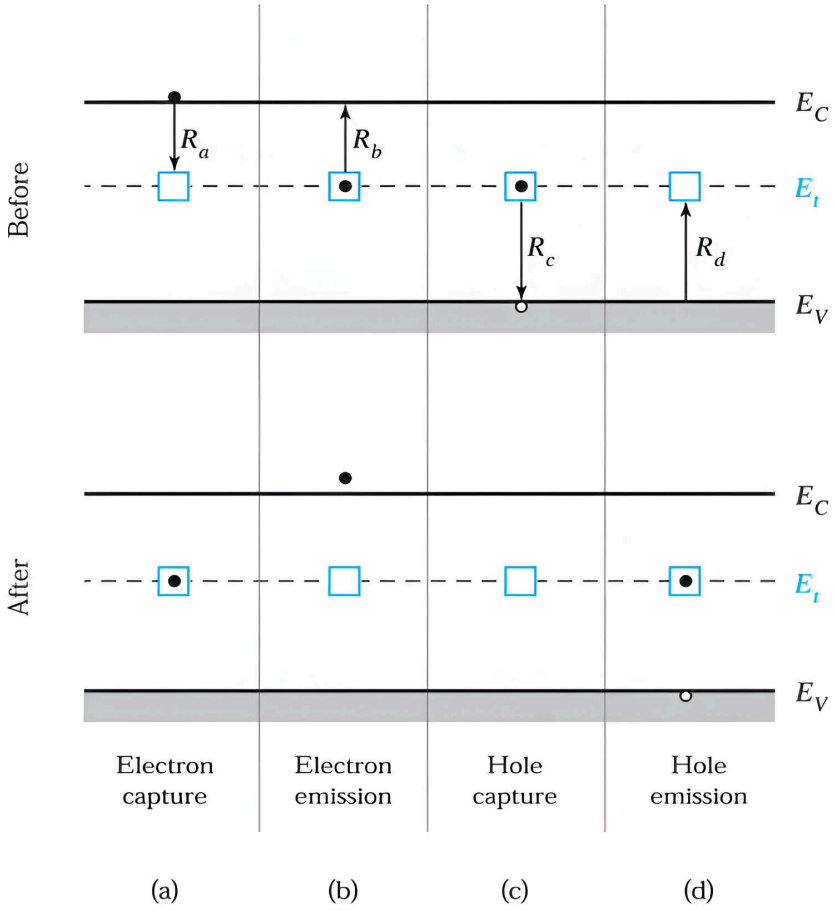

Figure 3.6: Schematic diagram of electrons and holes trap-assisted recombination. A trap may exist in a neutral state, and once it captures a charge carrier, it becomes either positive or negative, depending on whether the carrier has a positive or negative charge. The processes involved in trap-assisted recombination are: (a) electron capture characterized by the number of electrons captured from the conduction band (E_c) to the trap level (E_t) in unit time R_a, (b) electron emission characterized by the number of electrons emitted from the trap level to the conduction band in unit time R_b, (c) hole capture characterized by the number of holes captured from the valence band to the trap level in unit time R_c and (d) hole emission characterized by the number of holes emitted from the trap level to the valence band in unit time R_d. Image was taken from [39].

The SRH recombination rate depends on the concentrations of electrons and holes, the lifetimes of carriers, and the density of trap states. The recombination rate [42] is

given by the following equation:

$$R_{net}^{SRH} = \frac{np - n_{i,eff}^2}{\tau_p(n + n_1) + \tau_n(p + p_1)}, \tag{3.54}$$

where n and p are the densities of electrons and holes. The parameters τ_n and τ_p represent the electron and hole lifetimes. The terms n_1 and p_1 denote the electron and hole concentrations close to a recombination center, which could recombine. The term $n_{i,eff}^2$ is the square of the effective intrinsic carrier concentration. The numerator $(np - n_{i,eff}^2)$ describes the deviation of carrier densities from their equilibrium values. If $np > n_{i,eff}^2$, recombination dominates, and if $np < n_{i,eff}^2$, generation dominates. The parameters $n + n_1$ and $p + p_1$ combined with the electron and hole lifetimes account for carrier capture and release rate. The equilibrium electron and hole concentrations [42] can be expressed as:

$$n_1, p_1 = n_{i,eff} \exp\left(\pm \frac{E_{trap}}{kT}\right), \tag{3.55}$$

where E_{trap} is the energy level of the recombination center relative to the conduction band (for electrons) and the valence band (for holes). The sign plus corresponds to electrons, while the minus corresponds to holes.

The lifetimes of electrons (τ_n) and holes (τ_p) [42], are defined by:

$$\tau_{n,p} = \tau_{dop} \frac{f(T)}{1 + g_{n,p}(\mathcal{E})}, \tag{3.56}$$

where τ_{dop} models the lifetime doping dependence, $f(T)$ models the dependence of the lifetime on temperature, and the term $1 + g_{n,p}(\mathcal{E})$ models the dependence of the SRH lifetime on the applied electric field. The lifetime doping dependence is expressed using the Scharfetter relation [57]:

$$\tau_{dop}(N_{A,0} + N_{D,0}) = \tau_{min} + \frac{\tau_{max} - \tau_{min}}{1 + \left(\frac{N_{A,0} + N_{D,0}}{N_{ref}}\right)^{\delta}}, \tag{3.57}$$

where $N_{A,0}$ and $N_{D,0}$ are the doping concentrations of donors and acceptors, τ_{min} is the minimum lifetime, τ_{max} is the maximum lifetime, and N_{ref} is the doping reference, where the transition between τ_{min} and τ_{max} happens.

The temperature-dependent scaling factor for the lifetime accounts for variations in lifetime with temperature:

$$f(T) = \left(\frac{T}{300\,\mathrm{K}}\right)^{T_\alpha}, \tag{3.58}$$

where T_α determines the rate at which the scaling factor changes with temperature.

Surface recombination occurs due to impurities or defects at the surface or boundary of a semiconductor. At interfaces, an additional formula similar to the one given by the SRH recombination for silicon is used to model carrier loss due to surface recombination [42]:

$$R_{surf,net}^{SRH} = \frac{np - n_{i,eff}^2}{\frac{n+n_1}{s_p} + \frac{p+p_1}{s_n}}, \tag{3.59}$$

where s_n and s_p are the effective surface velocities for electrons and holes. The equilibrium electron (n_1) and hole (p_1) concentrations were defined in equation 3.55.

Oxide Surface Defects

Silicon exposed to air naturally forms four covalent bonds with the oxygen atoms from the atmosphere. This process is called oxidation and creates a silicon dioxide (SiO_2) layer on top of the silicon. For the ATLAS ITk silicon sensors, SiO_2 is intentionally grown in a controlled manner during the manufacturing process as part of the passivation layer. The passivation acts as an insulator, protecting the silicon from contaminants. During the oxidation process, two types of basic oxide charges can appear: interface trap levels and fixed oxide charges [58]. They result from oxidation conditions, annealing, and contaminants.

Interface trap charges are localized electronic states that arise from defects at the interface between silicon and SiO_2, creating energy levels within the semiconductor bandgap. These traps can change their charge state by interacting with mobile carriers in silicon. The charge state depends on its occupancy, which can vary with the bias voltage applied to the electrode. As the bias voltage shifts the trap energy level relative to the Fermi level, the occupancy of the trap can change, and with that, its charge state.

Unlike interface traps, fixed oxide charges have their charge state set and cannot be changed by interacting with mobile carriers. In the context of oxide charges, only the fixed oxide charges may be an issue for the ATLAS ITk strip sensor [59]. These are usually located very close to the interface and represent the remaining charge density after attempting to remove interface trap charges through annealing. The fixed oxide charges are positively charged, which may arise from trivalent silicon or excess oxygen centers in the transition region towards the interface [60]. Trivalent silicon happens when a silicon atom forms only three covalent bonds while the fourth one remains unsatisfied (dangling bond). Under the influence of an electric field, fixed oxide charges are immobile.

3.3.3 The Continuity Equation

The effects of drift, diffusion, and recombination usually occur simultaneously in a semiconductor. The continuity equation accounts for the contributions of all three processes. The first step in deriving the continuity equation is to derive the rate of change in electron concentration in a given volume. Fig. 3.7 illustrates a semiconductor with area A and volume V with the current flow and generation-recombination processes that take place in an infinitesimal slice of the semiconductor with thickness $\mathrm{d}x$. Two mechanisms impact the concentration of electrons in a given semiconductor slice: the net current flow into the slice and the net generation-recombination processes within the slice. The net current flow is the difference between the electrons entering the slice at position x and the electrons leaving the semiconductor slice at position $(x + \mathrm{d}x)$. The rate of change in electron concentration in a given volume [39] can be expressed as:

$$\frac{\partial n}{\partial t} A \mathrm{d}x = \left[\frac{J_n(x)}{-q} - \frac{J_n(x + \mathrm{d}x)}{-q} \right] A + (G_n - R_n) A \mathrm{d}x, \tag{3.60}$$

where A is the cross-sectional area of the slice, $\mathrm{d}x$ is the thickness of the slice, G_n is the generation rate, R_n is the recombination rate, $J_n(x) \cdot (-q)^{-1}$ is the current density flow entering the slice, and $J_n(x + \mathrm{d}x) \cdot (-q)^{-1}$ is the current density flow leaving the

semiconductor slice. To derive the fundamental form of the continuity equation, the current at $(x + \mathrm{d}x)$ can be expanded using the Taylor series:

$$J_n\,(x + \mathrm{d}x) = J_n(x) + \frac{\partial J_n}{\partial x}\mathrm{d}x + \ldots, \tag{3.61}$$

Replacing the Taylor series expansion of $J_n(x + \mathrm{d}x)$ in equation 3.60 gives the simplified form of the continuity equation for electrons and for holes [39]:

$$\frac{\partial n^*}{\partial t} - \frac{1}{q}\frac{\partial J_{n,p}}{\partial x} = G_{n,p} - R_{n,p}, \tag{3.62}$$

where n^* is the carrier concentration (n for electrons, and p for holes).

The left-hand side of equation 3.62 represents the evolution of charge carrier density over time, accounting for the accumulation of charges within a volume and their flow across the boundaries. The right-hand side accounts for the generation and recombination processes. When the generation rate is higher than the recombination rate, the carrier density increases. Conversely, when the generation rate is lower than the recombination rate, the carrier density decreases. The continuity equation shows that any change in carrier density is balanced by a change in carrier dynamics such that charge conservation is satisfied.

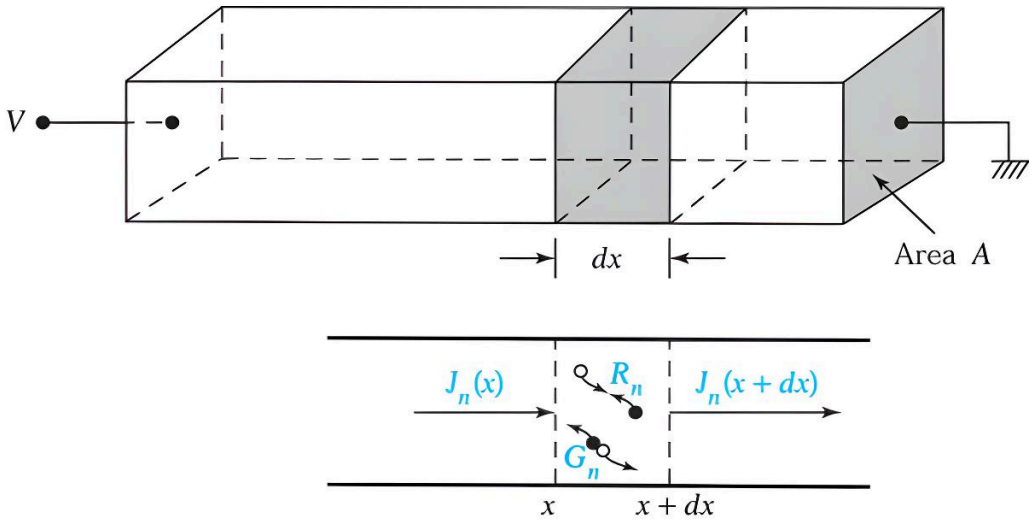

Figure 3.7: Schematic drawing of the current density flow and generation-recombination processes taking place in an infinitesimal slice of a semiconductor with thickness dx [39].

Under low injection, the number of excess carriers Δn and Δp is smaller than the concentration of majority carriers at equilibrium, $\Delta n, \Delta p \ll n_0$. To derive the continuity equation for minority carriers under low injection conditions [39], the total current density for electrons and holes in equation 3.39 together with the net recombination rate expressed in equation 3.49 have to be substituted into the continuity equations for both charge carriers:

$$\frac{\partial {n^*}_{p,n}}{\partial t} = \mu_{n,p}\mathcal{E}\frac{\partial {n^*}_{p,n}}{\partial x} + D_{n,p}\frac{\partial^2 {n^*}_{p,n}}{\partial x^2} + G_{n,p} - \frac{{n^*}_{p,n} - {n^*}_{p0,n0}}{\tau_{n,p}}, \tag{3.63}$$

where $\mu_{n,p}$ is the mobility of charge carriers, $\mathcal{E}$ is the electric field, $\partial {n^*}_{p,n}/\partial x$ is the spatial gradient of the carrier concentration, $D_{n,p}$ is the diffusion coefficient of charge carriers,

$G_{n,p}$ is the generation rate of carriers, ${n^*}_{p0,n0}$ is the equilibrium carrier concentration, and $\tau_{n,p}$ is the charge carrier lifetime.

In order for charge to be conserved, in addition to the continuity equations, Poisson's equation [45] needs to be satisfied. This equation relates the electric field with the charge distribution:

$$\nabla^2\phi = -\nabla \cdot \vec{\mathcal{E}} = -\frac{\rho}{\epsilon_s} = -\frac{q}{\epsilon_s}Q_s, \tag{3.64}$$

where ϕ is the electric potential, ρ is the volume charge density, ϵ_s is the permittivity of the semiconductor, and Q_s is the space charge density. The terms in the Poisson's equation can be explained as follows:
∘ $\nabla^2\phi$ shows the variations in electric potential across a region.
∘ $\nabla \cdot \vec{\mathcal{E}}$ illustrates the variations in electric field.
∘ $\frac{\rho}{\epsilon_s}$ shows how the electric field is connected to the charge density inside a semiconductor.
∘ $\frac{q}{\epsilon_s}Q_s$ correlates the electric field produced by a surface charge to the permittivity of a semiconductor.

The space charge density [45] depends on the distribution of all charged elements:

$$Q_s = p - n + N_D - N_A + Q_t, \tag{3.65}$$

where p is the hole concentration, n is the electron concentration, N_D is the donor concentration, N_A is the acceptor concentration, and Q_t represents the charged defects concentration.

3.3.4 Tunneling

In quantum mechanics, the wave function of an electron is not confined to a fixed space, but it can penetrate into and through a potential barrier of finite height. Tunneling is the process in which electrons pass from one band to another in the presence of an electric field. For low temperatures, tunneling is independent of thermal excitations. From the Schrödinger equation, the wave function of an electron can be expressed as:

$$\frac{\mathrm{d}^2\psi}{\mathrm{d}x^2} + \frac{2m}{\hbar^2}[E - U(x)]\psi = 0, \tag{3.66}$$

where ψ is the Schrödinger wave function, m is the particle mass, $\hbar$ is the reduced Planck's constant, E is the energy of the particle that is associated with motion along the abscissa, and $U(x)$ is the potential energy of the particle. To find the wave function from equation 3.66, the second term will be moved to the right-hand side:

$$\frac{\mathrm{d}^2\psi}{\mathrm{d}x^2} = -\frac{2m}{\hbar^2}[E - U(x)]\psi, \tag{3.67}$$

where $2m[E - U(x)]/\hbar^2$ is denoted with k^2. The wave function is the solution to Schrödinger's equation:

$$\psi = \exp(\pm ikx). \tag{3.68}$$

Considering a rectangular barrier with height U_0 and width W as represented in Fig. 3.8, a particle with wave function ψ_A could tunnel through the barrier changing its

wave function to ψ_B. For the simplest case, the tunneling probability [39] is given by the formula:

$$\begin{aligned} T_t =& \frac{|\psi_B|^2}{|\psi_A|^2} = \left[1 + \frac{U_0^2 sinh^2(|k|W)}{4E(U_0 - E)}\right]^{-1} \\ =& \frac{16E(U_0 - E)}{U_0} \exp\left(-2\sqrt{\frac{2m(U_0 - E)}{\hbar^2}}W\right). \end{aligned} \tag{3.69}$$

The probability that a particle would tunnel through a potential barrier depends on the particle's energy, the height and the width of the potential barrier, and an exponential decay term, $-2\sqrt{[2m(U_0 - E)/\hbar^2]}W$. The tunneling probability increases when the particle energy approaches the potential energy of the barrier and decreases significantly when the energy is much less than the potential energy, $E \ll U_0$. The wider the potential barrier, the less likely it is for a particle to tunnel through. The probability decreases exponentially with the width of the potential barrier. The probability is inversely proportional to the height of the potential barrier. From the exponential decay term, the probability that a particle would tunnel through is lower given that the difference between the potential energy and the particle's energy increases.

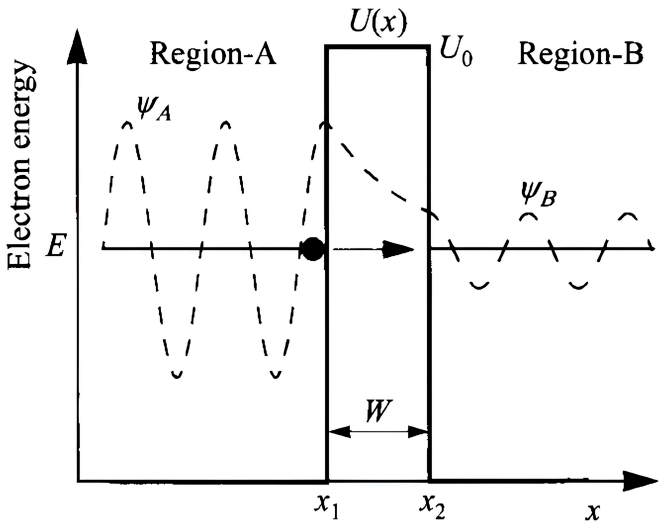

Figure 3.8: Schematic drawing of a rectangular barrier with height, U_0, and width, W [39].

In a silicon sensor, a potential barrier can form at junctions, i.e., between a metal contact and the silicon bulk, leading to barrier tunneling or across a depletion region in a p-n junction, leading to band-to-band tunneling. These barriers can prevent charge carriers from flowing from one region to the other; however, under certain conditions, carriers can tunnel through the potential barrier. The Hurkx tunneling model [61] shows how electrons can tunnel from the valence band directly to the conduction band in the presence of a high electric field ($\geq 7 \cdot 10^5$ Vcm), which reduces the barrier height between the bands. When electrons tunnel into the conduction band, the concentration of free electrons inside silicon may increase, which could increase the recombination with holes.

The recombination rate due to Hurkx tunneling [42] is modeled in TCAD by the following formula:

$$R_{net}^{bb} = A_r \cdot D^* \cdot \left(\frac{\mathcal{E}}{1\mathrm{V} \cdot \mathrm{cm}^{-1}} \right)^P \exp\left(-\frac{B E_g(T)^{3/2}}{E_g(300\,\mathrm{K})^{3/2} \mathcal{E}} \right), \tag{3.70}$$

where $A_r = 3.4 \cdot 10^{21}\,\mathrm{V}^{-2} \cdot \mathrm{cm}^{-1} \cdot \mathrm{s}^{-1}$, $P = 2$, $B = 22.6 \cdot 10^6\,\mathrm{V} \cdot \mathrm{cm}^{-1}$, $\mathcal{E}$ is the electric field, $E_g(T)$ is the band gap energy of the semiconductor as a function of temperature, $E_g(300\,\mathrm{K})$ is the bandgap energy of the semiconductor at $T = 300\mathrm{K}$, and D^* is defined as follows:

$$D^* = \frac{(np - n_{i,eff}^2)}{(n + n_{i,eff})(p + n_{i,eff})}, \tag{3.71}$$

where n is the electron density, p is the hole density, and $n_{i,eff}$ is the effective intrinsic carrier concentration.

Chapter 4

Semiconductor Devices

4.1 The p-n Junction

Single-crystal semiconductor sensors employ both n- and p-type regions, which, when brought into contact, form a p-n junction. Fig. 4.1 (a) shows an n-type and a p-type semiconductor uniformly doped and physically separated. For the n-type semiconductor, the Fermi level is close to the edge of the conduction band, while for the p-type, the Fermi level is close to the edge of the valence band. Fig. 4.1 (b) shows the n- and p-type regions in thermodynamic contact. The difference between the electron concentration in the n-doped semiconductor and the hole concentration in the p-doped semiconductor leads to carrier movement via diffusion. Electrons from the n-type region diffuse to the p-type region, leaving behind immobile positive charges. Once the electrons reach the p-type region, they recombine with holes. At the same time, the holes in the p-type region diffuse to the n-type region, leaving behind acceptor sites that will pick up an extra electron. Due to the diffusion of charge carriers, a negative Space Charge Region (SCR) is formed on the p-side, while a positive SCR is formed on the n-type. The two newly formed regions together are known as the depletion region or the SCR.

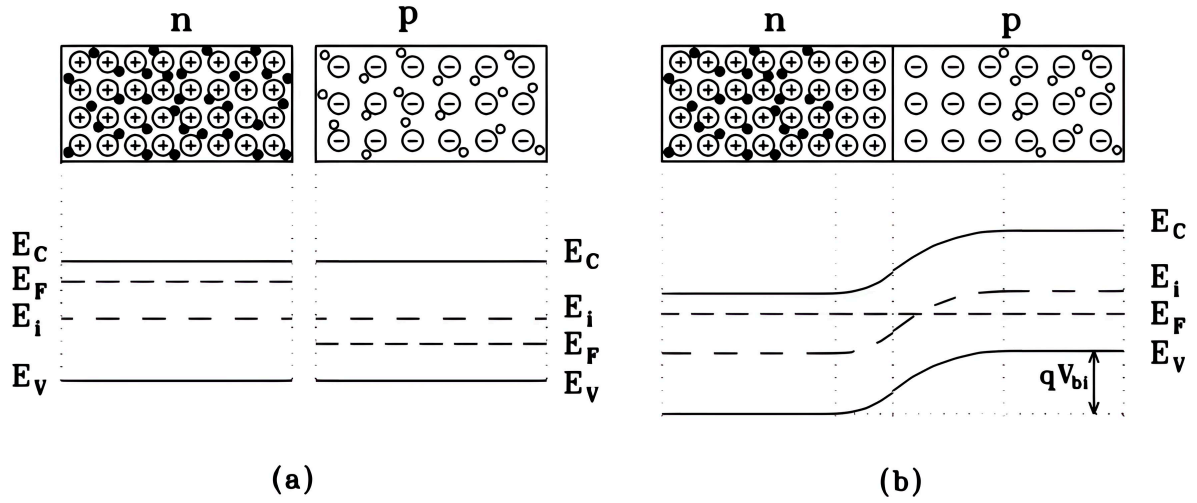

Figure 4.1: Schematic drawing of the initial energy levels of a p- and n-type semiconductor not in contact (a) and the energy levels of a p- and n-type semiconductor in contact (b) [45].

When the donor and acceptor impurities are equal ($N_A = N_D$), symmetrical diffusion happens between the two sides. If $N_A \neq N_D$, the space charge region will extend further into the side with lower doping. In the n-type neutral region, electrons are the majority carriers, whereas in the p-type neutral region, holes are the majority carriers. The net charge within the region of the junction establishes an electric potential difference (ϕ), which can be expressed using Poisson's equation in 3.64. The electric potential difference creates an electric field ($\vec{\mathcal{E}}$) [39], which can be defined as:

$$\mathcal{E} = -\frac{\mathrm{d}\phi}{\mathrm{d}x}. \tag{4.1}$$

The electric field lines go from the n-type region towards the p-type region. The hole and electron drift currents go along the direction of the electric field. In contrast, the charge carriers' diffusion currents go in the opposite direction to the electric field. For an equal concentration of electrons and holes, and no external excitation, the net currents flowing across the junction are zero. This means that the drift currents cancel the diffusion currents. The total electron current density ($J_{n,total}$) [39], can be expressed in terms of the drift ($J_{n,drift}$) and diffusion ($J_{n,diffusion}$) current densities, and likewise for the hole current density:

$$J_{n,total} = J_{n,drift} + J_{n,diffusion} = q\mu_n n\mathcal{E} - qD_n\frac{\mathrm{d}n}{\mathrm{d}x} = 0, \tag{4.2}$$

where q is the electric charge, μ_n is the electron mobility, n is the electron concentration, D_n is the diffusion coefficient given by the Einstein relation in equation 3.38 and $\mathrm{d}n/\mathrm{d}x$ is the spatial derivative of the electron concentration. Substituting the diffusion coefficient from equation 3.38 into equation 4.2 yields the following:

$$J_{n,total} = q\mu_n n\left(\frac{1}{q}\frac{\mathrm{d}E_i}{\mathrm{d}x}\right) - \mu_n kT\frac{\mathrm{d}n}{\mathrm{d}x}, \tag{4.3}$$

where E_i is the intrinsic Fermi level, k is the Boltzmann constant and T is the temperature. Applying the expression of the electron concentration derivative in equation 3.20, the carrier current density (J_n for electrons, J_p for holes) [39] can be defined as:

$$J_{n,p} = \mu_{n,p}n^*\frac{\mathrm{d}E_i}{\mathrm{d}x} - \mu_{n,p}n_i\left(\frac{\mathrm{d}E_i}{\mathrm{d}x} - \frac{\mathrm{d}E_F}{\mathrm{d}x}\right) = \mu_{n,p}n_i\frac{\mathrm{d}E_F}{\mathrm{d}x} = 0, \tag{4.4}$$

where $\mu_{n,p}$ is the carrier mobility, n^* is the concentration of carriers (n for electrons, p for holes), and n_i is the intrinsic concentration of carriers. Based on the carrier current density derived in equation 4.4, the Fermi level remains constant across the junction. This creates a special space charge distribution, which is described by Poisson's equation given in 3.64. For the regions far away from the depletion region, Poisson's equation [39] can be simplified to:

$$\frac{\mathrm{d}^2\phi}{\mathrm{d}x^2} = 0 \Leftrightarrow N_D - N_A + p - n = 0, \tag{4.5}$$

where N_D is the dopant concentration and N_A is the acceptor concentration. The electrostatic potential for n- (ϕ_n) and p-type (ϕ_p) neutral regions [39], where $N_A = 0$ and $n > p$, or $N_D = 0$ and $p > n$, can be expressed as:

$$\phi_{n,p} = -\frac{1}{q}(E_i - E_F) = \pm\frac{kT}{q}\ln\left(\frac{N_{D,A}}{n_i}\right). \tag{4.6}$$

When the electric field is strong enough to prevent carriers from diffusing across the junction, the p-n junction reaches equilibrium. The potential difference between the n-type and p-type regions, as expressed in equation 4.6 is known as the built-in potential (V_{bi}) [39] of a p-n junction:

$$V_{bi} = \phi_n - \phi_p = \frac{kT}{q} \ln\left(\frac{N_A N_D}{n_i^2}\right). \tag{4.7}$$

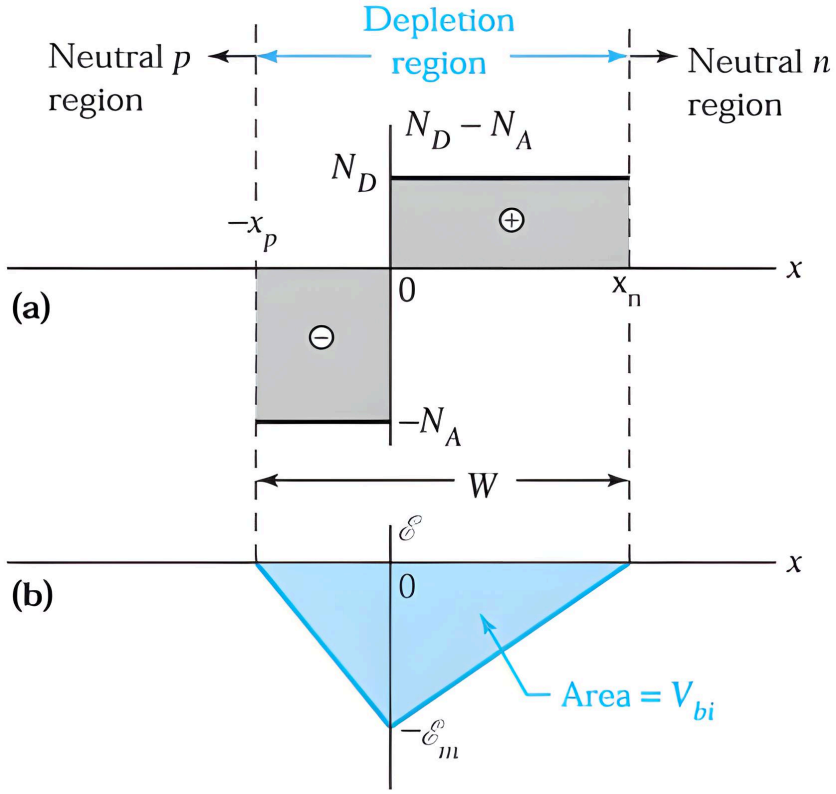

Figure 4.2: Schematic representation of the ideal depletion region of a p-n junction (a) and its electric field distribution (b) [39]. The depletion region goes from $-x_p$ to x_n. The total depletion width W is given by $|-x_p|+|x_n|$. N_A represents the acceptor concentration on the p-side, and N_D represents the donor concentration on the n-side. The net charge density is denoted by $N_A - N_D$. $\mathcal{E}$ represents the electric field distribution while $\mathcal{E}_m$ is the electric field maximum. V_{bi} is the built-in potential, which can be derived as the area under the electric field distribution.

A visual representation of the depletion region of an ideal p-n junction and its electric field distribution is illustrated in Fig. 4.2. The depletion region for an ideal p-n junction is characterized by: no crystallographic defects, an infinitely thin depletion region with a sharp boundary between the n- and p-type semiconductor, uniform charge density within each side of the depletion region, and no recombination processes. This is an approximation because, in reality, at the extremities of the depletion region, there is a transition region towards the neutral region, where the space charge impurity ions are partially compensated by the charge carriers. For this approximation of the depletion region, the Poisson's equation can be simplified to the following form [39]:

$$\frac{\mathrm{d}^2\phi}{\mathrm{d}x^2} = +\frac{qN_A}{\epsilon_s} \qquad \text{for} \quad -x_p \leq x < 0, \tag{4.8}$$

$$\frac{\mathrm{d}^2\phi}{\mathrm{d}x^2} = -\frac{qN_D}{\epsilon_s} \qquad \text{for} \quad 0 < x \leq x_n, \tag{4.9}$$

where ϵ_s is the permittivity of the semiconductor.

Charge neutrality requires:

$$N_A x_p = N_D x_n. \tag{4.10}$$

The depletion region width represented in Fig. 4.2 is the sum between the width in the p-region ($|-x_p|$) and the width in the n-region (x_n):

$$W = |-x_p| + x_n. \tag{4.11}$$

The electric field illustrated in Fig. 4.2 [39] can be calculated by integrating the simplified Poisson equation in 4.8 and 4.9:

$$\mathcal{E}(x) = \frac{\mathrm{d}\phi}{\mathrm{d}x} = +\frac{qN_A}{\epsilon_s}x = +\frac{qN_A}{\epsilon_s}(x + x_p) \qquad \text{for} \quad -x_p \leq x < 0, \tag{4.12}$$

$$\mathcal{E}(x) = -\frac{qN_D}{\epsilon_s}x = -\frac{qN_A}{\epsilon_s}x = +\frac{qN_A}{\epsilon_s}(x - x_n) \qquad \text{for} \quad 0 < x \leq x_n. \tag{4.13}$$

From Fig. 4.2, where the electric field reaches its maximum at $x = 0$, the electric field can be written as:

$$\mathcal{E} = \frac{qN_D x_n}{\epsilon_s} = \frac{qN_A x_p}{\epsilon_s}. \tag{4.14}$$

The built-in potential (V_{bi}) [39] can be calculated by integrating the electric field:

$$V_{bi} = -\int_{x_p}^{x_n} \mathcal{E}(x)\mathrm{d}x \tag{4.15a}$$

$$= \int_{x_p}^{0} \mathcal{E}(x)\mathrm{d}x - \int_{0}^{x_n} \mathcal{E}(x)\mathrm{d}x \tag{4.15b}$$

$$= \frac{qN_A x_p^2}{2\epsilon_s} + \frac{qN_D x_n^2}{2\epsilon_s}, \tag{4.15c}$$

where $x_{n,p}$ [39] can be expressed in terms of the doping concentrations and the depletion width:

$$x_{n,p} = \frac{N_{A,D}}{N_A + N_D} W. \tag{4.16}$$

The depletion width [39] can be defined in terms of the built-in potential:

$$W = \sqrt{\frac{2\epsilon_s}{q}\left(\frac{N_A + N_D}{N_A N_D}\right) V_{bi}}, \tag{4.17}$$

where

$$N_{eff} = \frac{N_A N_D}{N_A + N_D} \tag{4.18}$$

is the effective doping for a p-n junction. If for example $N_D > N_A$, then the depletion width can be expressed in terms of the effective doping (N_{eff}) [39]:

$$W = \sqrt{\frac{2\epsilon_s V_{bi}}{qN_{eff}}}. \tag{4.19}$$

There are two operation modes of a p-n junction: forward and reverse. Forward operation means a positive bias is applied to the p-type region, while a negative bias is applied to the n-type region. If a forward bias is applied to a p-n junction, the holes in the p-type region will move toward the negatively biased region, while the electrons in the n-type region will move toward the positively biased region. In this case, both carriers will move towards the junction, decreasing the depletion region. This will increase the conductivity across the junction while the total electrostatic potential will decrease by $V_{applied}$. In reverse bias, a positive bias is applied to the n-type region and a negative bias on the p-type region. Under the reverse bias, electrons from the n-type region and holes from the p-type region move further from the junction. The reverse bias increases the depletion region, and the total electrostatic potential will increase by $V_{applied}$.

If the built-in potential is replaced by the total electrostatic potential in equation 4.19, the depletion width can be written as:

$$W = \sqrt{\frac{2\epsilon_s(V_{bi} + V_{applied})}{qN_{eff}}}, \tag{4.20}$$

where $V_{applied}$ is positive for forward operation and negative for reverse operation.

Capacitance-Voltage Relation in p-n Junctions

In a p-n junction, the depletion region is flanked by neutral regions, which are not affected by the electric field across the junction. The n- and p-type neutral regions of a p-n junction can be approximated as the plates of a capacitor with the depletion region as the insulator material. For a p-n junction, the capacitance (C) [62] is the variation in the depletion layer charge ($\mathrm{d}Q$) corresponding to an incremental change in the applied bias voltage ($\mathrm{d}V$):

$$C = \frac{\mathrm{d}Q}{\mathrm{d}V}. \tag{4.21}$$

An increase in voltage leads to an increase in charge while charge neutrality remains satisfied. This leads to the widening of the depletion region. The voltage variation [39] directly influences the depletion width and the electric field:

$$\mathrm{d}V = W \cdot \mathrm{d}\mathcal{E}. \tag{4.22}$$

The electric field [63] is influenced by the increase in charge, and it changes according to Poisson's equation in 3.64. If the voltage variation from equation 4.22 and the electric field from equation 3.64 are introduced in equation 4.21, the capacitance can be written

in terms of the permittivity of the semiconductor and the width of the depletion region (W):

$$C = \frac{\epsilon\epsilon_0}{W}A, \tag{4.23}$$

where ϵ is the relative permittivity, ϵ_0 is the permittivity of free space, and A is the cross-sectional area of the p-n junction.

If the expression for W from equation 4.19 is substituted in 4.23, $1/C^2$ can be expressed in terms of the voltage at which the junction becomes fully depleted (V_{FD}) and the applied bias voltage (V_{bias}):

$$\frac{1}{C^2} = \frac{2(V_{bias} - V_{FD})}{q\epsilon\epsilon_0 N_{eff} A^2}, \tag{4.24}$$

where N_{eff} is the effective doping of the semiconductor. In practice, Capacitance-Voltage (CV) measurements can be used to determine the full depletion voltage of a p-n junction. In an ideal diode, when the applied bias is less than the full depletion voltage, $1/C^2$ increases linearly. Once the applied voltage surpasses the full depletion potential, $1/C^2$ starts to saturate. The inflection point corresponds to the numerical value of the full depletion voltage.

4.2 Processing of Single-Crystal Sensors

Detector applications require high-purity crystals. Single-crystal processing yields single-crystal semiconductors with minimal defect densities and good electrical properties. High-quality crystals are produced through the Czochralski technique [64] or the Float Zone (FZ) technique [65].

The Czochralski Technique

Fig. 4.3 shows the Czochralski crystal puller [64], which is a specialized set-up for single crystal production. Inside the Czochralski crystal puller, the atmosphere is inert to prevent contamination of the single crystal during production. The raw material that is melted to form a single crystal is known as the feed material. For silicon production, the feed material is high-purity silicon, e.g., polysilicon obtained from refining processes. The high-purity silicon is placed in a heat-resistant, cylindrical crucible where it is melted using Radio Frequency (RF) or resistance heaters. When the high-purity silicon has been melted, a silicon crystal seed is dipped into the melt. The crystal seed determines the orientation of the lattice of the newly grown single crystal by providing a stable structure for the atoms of the melt to arrange themselves. At the contact between the crystal seed and the melt, a minuscule melt forms. A small part of the crystal seed is remelted to ensure the new single crystal grows smoothly. The crystal seed is slowly pulled upwards from the melt. The melt crystallizes at the interface, slowly forming the new crystal. The seed crystal is rotated to ensure uniform heat distribution, which facilitates uniform crystal growth.

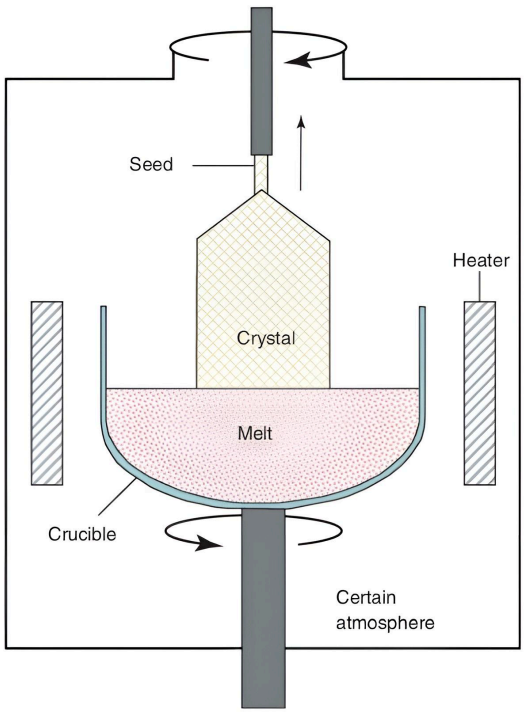

Figure 4.3: Schematic drawing of a Czochralski crystal puller [66].

The Float Zone Technique

The FZ technique [65] is a crucible-free single-crystal growing technique. Fig. 4.4 shows the FZ technique setup, which consists of a floating feed rod in direct contact with a crystal seed. In this case, the floating feed rod is the raw material that is melted to form a single crystal. The feed rod is deposited in a quartz envelope in an inert atmosphere to ensure no contamination from the outside environment. During silicon single crystal growth, the polysilicon feed rod part, which is in direct contact with the silicon seed, is melted using RF heaters while the rod rotates constantly. The silicon atoms from the melted polysilicon adhere to the silicon seed. When cooled, silicon atoms rearrange themselves according to the orientation of the seed, forming a single crystal structure. The heater moves across the whole length of the rod in small increments. As the heater moves forward, the molten silicon behind it cools down and solidifies. During this cooling phase, atoms rearrange themselves into a single crystalline structure, following the pattern of the seed crystal at the beginning of the rod. The silicon sensors produced with the FZ technique have fewer impurities than those produced with the Czochralski technique because the FZ technique is crucible-free, which avoids the risk of contamination due to the material of the crucible.

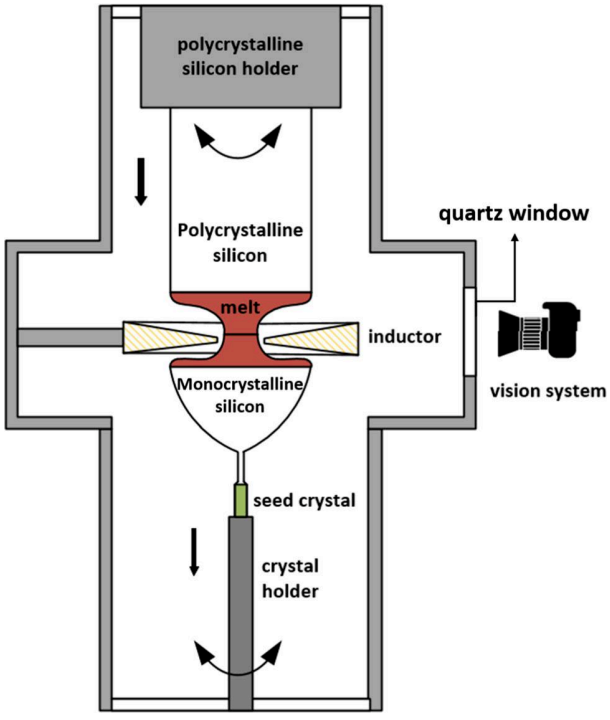

Figure 4.4: Schematic drawing of a FZ crystal growing setup [67].

The silicon sensor for the ATLAS ITk strip detector is grown using the FZ technique. Regardless of the single-crystal growing technique employed, the newly grown crystal (ingot) is cut into thin, flat pieces (wafers) and used as the substrate for the sensor fabrication. The thickness of the wafers is application specific: for ATLAS ITk strip silicon sensors, the wafer thickness is between 300 µm and 320 µm [29]. A 6-inch wafer was selected for the fabrication of the strip sensors. After the ingot is cut into wafers, they are polished to ensure the surface is smooth and defect-free.

Photolithography

Photolithography is the microfabrication process used to create the intricate features of semiconductor devices. Fig. 4.5 shows an example of the process flow of SiO_2 pattern generation on a semiconductor substrate. A thin layer of SiO_2 is first deposited on the semiconductor (4.5 a). Thin layer deposition is usually achieved with the Physical Vapor Deposition (PVD) technique [68] or the Chemical Vapor Deposition (CVD) technique [69]. A light-sensitive polymer (a photoresist) is deposited on top of the SiO_2 layer (4.5 b). There are two types of photoresists: negative photoresist, which hardens when exposed to UV radiation, and positive photoresist, which becomes soluble after UV light exposure. To facilitate good contact between the photoresist and the substrate, the wafer is baked at a moderate temperature. A photomask is used to transfer the pattern using UV radiation (4.5 c). The photomask allows the UV radiation to pass in certain areas, while blocking its passage in other areas. After UV light exposure, the wafer is immersed in a solution (developer) that dissolves the activated photoresist (4.5 d). The regions where the photoresist was developed allow further wafer processing, e.g., etching (4.5 e), doping, etc. Following etching or doping, the remaining photoresist is removed, leaving behind the intended pattern (4.5 f).

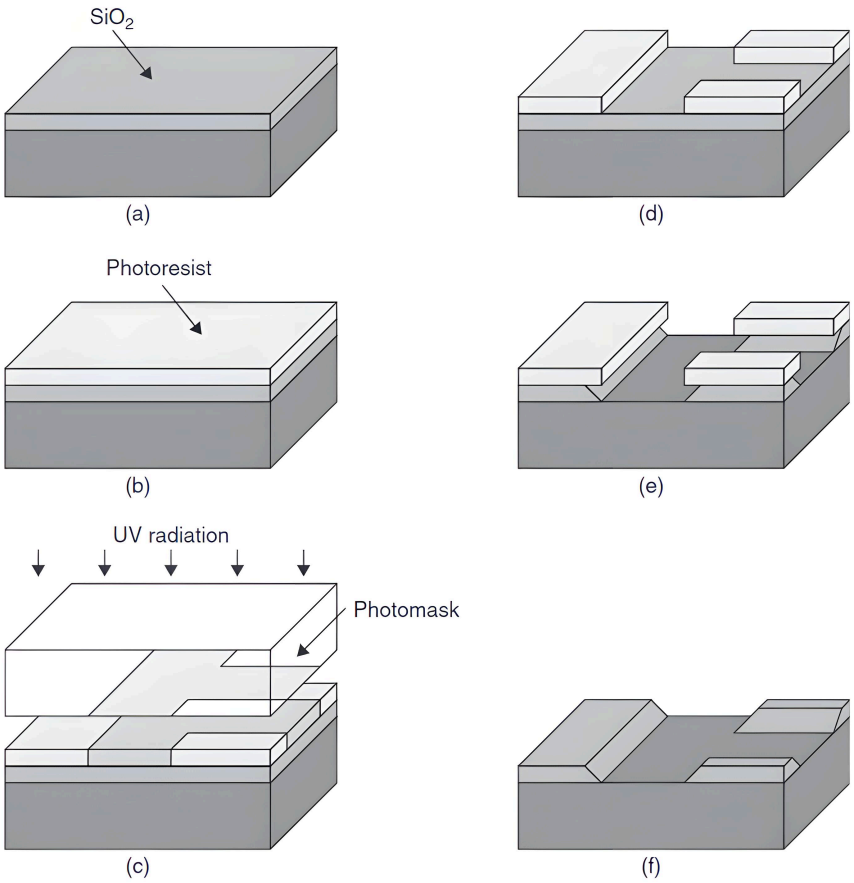

Figure 4.5: Process flow of pattern deposition on SiO_2 [70]. A layer of SiO_2 is deposited on the wafer (a), followed by a layer of photoresist (b). A photomask is used to transfer the desired pattern by exposing some parts of the photoresist to UV radiation (c). The exposed areas of the photoresist are removed using a dissolving solution (d). The exposed parts of SiO_2 are removed through etching (e). The remaining photoresist is removed (f).

Etching

Etching is a microfabrication process used to remove materials not covered in photoresist. The results following the two types of etching, wet and dry (plasma), are illustrated in Fig. 4.6. In wet etching, liquid chemicals (etchants) are selected to dissolve certain materials. The wafer is either immersed in the etchant or the etchant is sprayed uniformly on the wafer surface. Once the etchant comes in contact with the exposed areas, the material is etched away. During wet etching, some material underneath the photoresist can be removed unintentionally, as showcased in Fig. 4.6, which is the main drawback of the wet etching method.

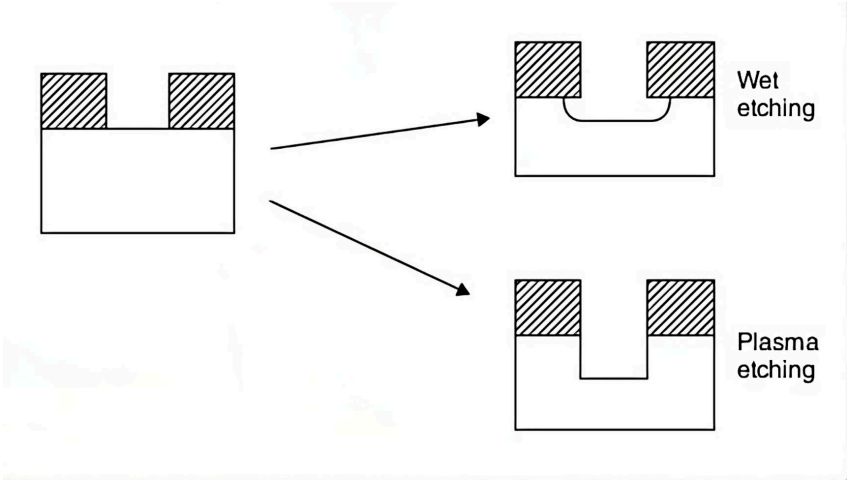

Figure 4.6: Schematic comparison between wet and dry (plasma) etching [70].

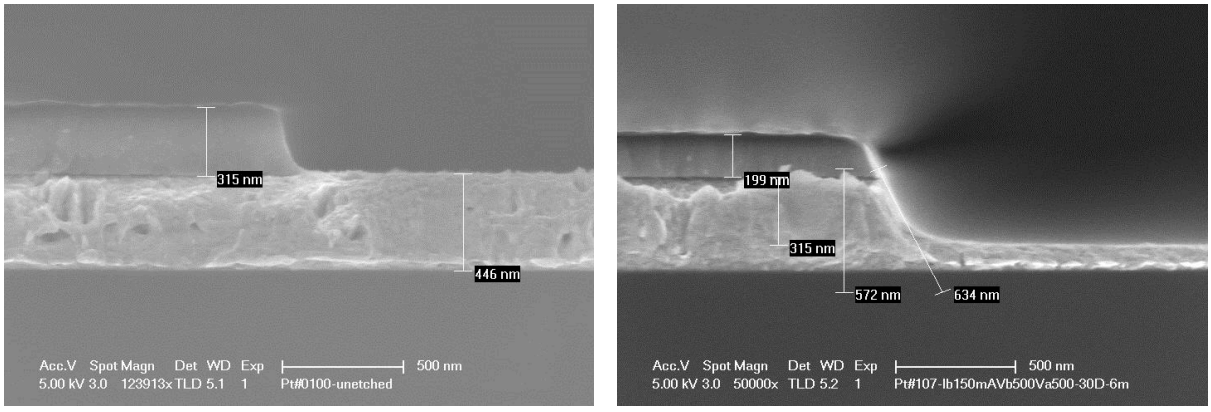

(a) (b)

Figure 4.7: SEM images of a platinum layer with photoresist material on top illustrating the difference before (a) and after dry etching (b) [71].

For dry etching, reactive gases are used to remove the exposed materials. The reactive gases can be ionized in a plasma state that chemically reacts with the exposed material and removes it. Another type of dry etching uses reactive ions, which are bombarded on the exposed material to etch it away. Dry etching with reactive ions provides great precision in removing the exposed materials. This method removes the aluminum not covered by the photoresist, allowing the contacts for sensors to be created. An example

of two Scanning Electron Microscope (SEM) images before and after dry etching is illustrated in Fig. 4.7. It should be noted that Fig. 4.7 (a) and Fig. 4.7 (b) correspond to a different application and are used only as an example. The platinum layer was removed using reactive ion bombardment. From Fig. 4.7 (b), it can be seen that the edge of the remaining platinum material underneath the photoresist is not straight, displaying a slight curvature.

Doping Methods

The electrical properties of a wafer can be changed by intentionally introducing impurities into the semiconductor material. A pure semiconductor has limited electrical conductivity and cannot be used for particle detection. Doping allows for the creation of n- and p-type semiconductors, which are necessary for semiconductor-based devices. The most common dopants are boron (p-type) and phosphorus (n-type). Fig 4.8 shows a side-by-side comparison between thermal diffusion (a) and ion implantation (b), which are two of the most used doping methods.

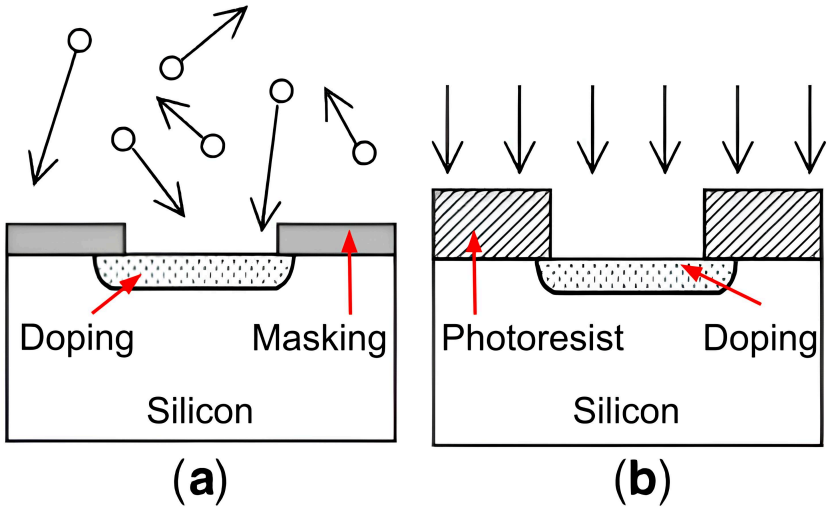

Figure 4.8: Schematic diagram of thermal diffusion (a) and ion implantation (b) used as doping methods [70].

During thermal diffusion, the wafer is exposed to a gas containing the desired dopant in a high-temperature environment. The doping atoms reach the wafer surface, and then they diffuse into the semiconductor. Depending on the kinetic energy of the doping atom, they will diffuse a certain distance inside the semiconductor before replacing some of its atoms. The temperature and dopant concentration directly influence how much the dopant diffuses inside the semiconductor and are adjusted to fit the required needs.

During ion implantation, ions are accelerated in an electric field towards a wafer and implanted inside the semiconductor. Similarly to thermal diffusion, the depth of the ion implantation is influenced by the ion kinetic energy, and therefore, their acceleration in the electric field is easily adjusted depending on the application-specific purpose. This can be used for creating multiple layers of implants.

Ion implantation is preferred over thermal diffusion because it offers better control over the dopant concentration and implant depth, with a wider range of dopants being available. However, ion implantation can introduce unintentional defects in the crystal

lattice (lattice damage, cluster damage, and interstitial vacancy), which can be reduced through high-temperature treatments (annealing).

Regardless of the doping method employed, a high-temperature treatment is applied to arrange the doping atoms into regular lattice positions. The temperature value is carefully adjusted to avoid the lateral diffusion of the dopant. For applications that require doped regions close to each other, lateral diffusion can have a negative impact because it can electrically connect these regions.

Oxidation

When a semiconductor is exposed to the oxygen in the atmosphere, a layer of oxide can form on its surface (oxidation). For silicon devices, such as the ATLAS ITk strip sensor, silicon dioxide (SiO_2) is used as a protective layer due to its insulating properties and non-porous nature. SiO_2 prevents contaminants from reaching the silicon surface and mobile ions from reaching the active area because mobile ions can get trapped inside the oxide instead.

SiO_2 is grown on bare silicon in layers in a high-temperature environment in the presence of an oxidant. First, the wafer is placed in a heated chamber exposed to an oxygen gas. The oxygen adheres to the wafer surface and quickly combines with the silicon, forming an initial layer of SiO_2. To achieve a certain oxide thickness, the oxygen atoms need to travel past the newly formed oxide layer and come in contact with the silicon. For this reason, the oxygen atoms need to diffuse through the oxide to reach the wafer, slowing down the oxide growth rate.

To achieve faster oxidation rates, water vapor ($H^+ - HO^-$) can be used as an oxidant because the hydroxide ion (HO^-) diffuses faster than the oxygen atom through the oxide layer. The oxide layer grown with water vapor is less dense than the one produced with oxygen because some hydrogen atoms get trapped inside the oxide. To eliminate the trapped hydrogen atoms, a high-temperature treatment in an inert atmosphere is applied to the wafer.

During oxidation, the doping atoms situated at the interface relocate: the n-type doping atoms segregate into the silicon rather than adhering to the oxide, while the p-type doping atoms accumulate in the SiO_2 since they diffuse more easily in the oxide layer. This creates an uneven distribution of atoms at the interface between silicon and SiO_2, which can unintentionally change the properties of the device.

One of the requirements for the oxide layer is to be thick enough to avoid induction. This happens when the insulating layer is thin enough to allow charge from the electrodes to build up on the insulating layer. Surface charge build-up can cause a short circuit and undesirable effects in a semiconductor device.

Metallization: Aluminum

Metal layers can be used as contacts to supply voltage to the silicon substrate. Aluminum is one of the most common materials used for metal contacts, and it can be deposited on semiconductors using physical vapor deposition methods.

Fig. 4.9 shows the principle of the physical vapor deposition. The simplest evaporation system is made of a solid target material, an excitation device, substrate holders, a substrate heating system, and a vacuum chamber. During physical vapor deposition, the atoms of the solid target material are excited and then transported to the substrate.

The target can be excited using resistance heaters or electron beam heating. The temperature inside the evaporation chamber is adjusted to maintain the kinetic energy of the aluminum atoms until they reach the wafer surface. The chamber is under vacuum to avoid contamination, e.g., in the presence of oxygen, a layer of Al_2O_3 can form at the surface, which is an insulator and would prevent current from flowing into the silicon.

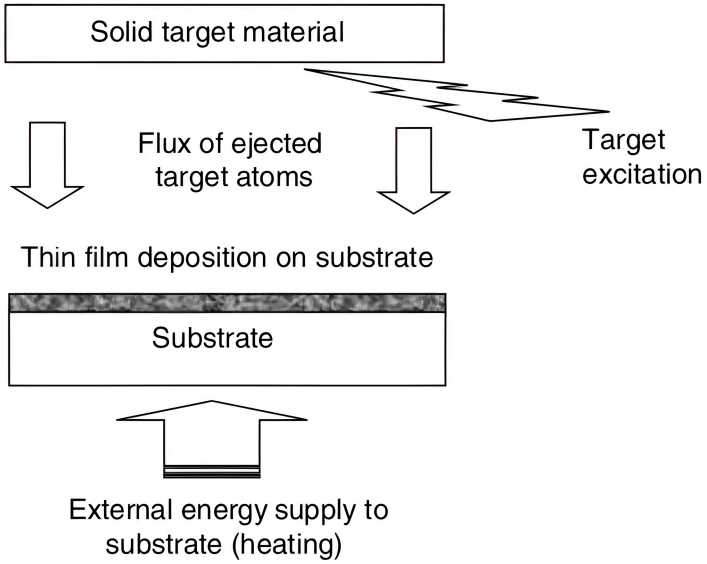

Figure 4.9: Schematic diagram of the working principles of physical vapor deposition [70]. An electron beam is focused on the target material to heat it locally, causing the atoms to gain sufficient thermal energy to evaporate. The vaporized atoms then travel through the vacuum and condense onto a heated substrate, enhancing adhesion to form a thin film.

Fig. 4.10 illustrates a sputtering system, which is not limited to metal deposition. Similarly to the physical vapor deposition system, the sputtering system is placed inside a chamber under vacuum. A simple sputtering system consists of sputtering gas (argon), a plasma discharge system, and a solid target (aluminum). The argon atoms from a glow discharge plasma are accelerated towards an aluminum target and knock off atoms inside the chamber. Then the aluminum atoms diffuse through a collimator until they reach the wafer surface.

Sputtering has better step coverage than evaporation because the aluminum atoms arrive from different angles to coat the semiconductor. The step coverage can be improved further by heating and rotating the wafer. In sputtering, the aluminum atoms have higher kinetic energy, which improves their adhesion to the silicon wafer, leading to a better deposition rate.

During aluminum deposition, a small fraction of the silicon can dissolve, and this needs to be accounted for to prevent substrate losses, which can affect the device's performance. Aluminum spikes can grow inside silicon, and depending on the geometry, the spikes can connect certain features, leading to a short circuit. To prevent aluminum spikes, a thin layer of barrier metal or conducting polysilicon is deposited between the silicon and the aluminum.

Passivation

Passivation protects the wafer from environmental factors such as chemical pollutants, dust, and humidity. To prevent damaging the layers intentionally deposited on the wafer surface, passivation is deposited uniformly at low temperatures. Some common passivation materials are silicon nitride (Si_3N_4), phosphor glass, and polyamide. The passivation for the ATLAS ITk strip sensor consists of a SiO_2 layer and a Si_3N_4 layer. Sometimes, passivation may be undesirable, e.g., when small windows are required for low penetration incoming radiation.

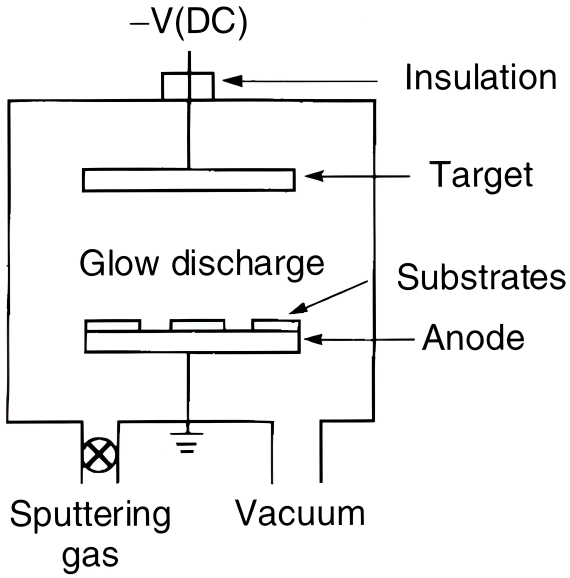

Figure 4.10: Schematic diagram of a DC sputtering system [70]. The cathode is electrically isolated from the chamber's walls. The sputtering gas is introduced inside the vacuum chamber. A high negative bias is applied to the target while the anode is at ground. Under the influence of the electric field, electrons get accelerated toward the anode. The accelerated electrons collide with the sputtering gas atoms, which suffer ionization. The ionized sputtering gas atoms are then accelerated toward the target, and if they hit the target, surface atoms (sputtering atoms) are emitted together with secondary electrons. The secondary electrons maintain the glow discharge while the sputtering atoms move through the chamber and get deposited on the substrates.

4.3 Particle Interactions with Matter

When a particle passes through matter, it can interact with atomic electrons and nuclei depending on its energy and the nature of the interaction. Through the interaction process, the particle loses some or all of its energy inside the target material. The Bethe-Bloch formula [72] gives the average energy loss (E) of an incoming charged particle, propagating with velocity v inside a target with atomic number Z:

$$\left\langle \frac{\mathrm{d}E}{\mathrm{d}x} \right\rangle = -4\pi\hbar^2 c^2 \alpha^2 \frac{nZ}{m_e v^2} \left[\ln\left(\frac{2\beta^2\gamma^2 c^2 m_e}{I_e} \right) - \beta^2 - \frac{\delta(\beta\gamma)}{2} \right], \tag{4.25}$$

where x is the distance the particle traveled, $\hbar$ is the reduced Planck constant, c is the speed of light in vacuum, α is the fine structure constant, n is the number density of atoms, m_e is the electron mass, β represents the ratio v/c, γ denotes the inverse square root of $(1 - v^2/c^2)$, I_e is the effective ionization potential of the material averaged over all atomic electrons, and the term $\frac{\delta(\beta\gamma)}{2}$ denotes the density effect correction, which reduces the stopping power for highly relativistic particles passing through a solid. From equation 4.25, the energy loss is inversely proportional to v^2: the greater the velocity, the lower the energy loss. If the number density of atoms is replaced by: $n = \frac{\rho}{A m_u}$, where ρ is the density of the material, A is the atomic mass, and m_u is the unified atomic mass unit, which is 1/12 the mass of a Carbon atom, then equation 4.25 becomes:

$$\frac{1}{\rho}\left\langle \frac{\mathrm{d}E}{\mathrm{d}x} \right\rangle = -\frac{4\pi\hbar^2 c^2}{m_u m_e v^2} \alpha^2 \frac{Z}{A} \left[\ln\left(\frac{2\beta^2\gamma^2 c^2 m_e}{I_e} \right) - \beta^2 - \frac{\delta(\beta\gamma)}{2} \right]. \tag{4.26}$$

Assuming the number of protons and neutrons are approximately equal, Z/A is approximately constant, which means that the energy loss only depends on the density of the material.

One example of particle-matter interaction is the production of Cerenkov radiation [73]. When a charged particle passes through a material with a speed greater than the speed of light inside the material, it disturbs the local electric field inside the medium, polarizing the molecules inside the target. If the speed of the traversing particle is high enough, the electric field disturbances do not cancel out instantly, leading to the emission of Cerenkov radiation (photons).

Ionization is the primary interaction mechanism of incoming charged particles with matter at low energies. It is a process by which an atom or molecule gains or loses an electron. The resulting atom or molecule is referred to as an ion. There are different types of ionization depending on the particle involved and the interaction mechanism. Photoionization occurs when an atom or a particle absorbs a photon with enough energy to free an electron. Thermal ionization happens when thermal energy is enough to free an electron inside an atom. Impact ionization occurs when a high-energy charged particle collides with an atom and transfers enough energy to free one or multiple electrons from that atom.

In semiconductor devices, impact ionization due to mobile charge carriers determines various characteristics, such as charge multiplication in low-gain avalanche diodes, or unwanted effects, including a low breakdown voltage. For a silicon p-n junction with a breakdown voltage above 8 V, avalanche multiplication due to impact ionization is the leading factor of electrical breakdown [74]. In contrast, for a p-n junction with a breakdown voltage below 5 V, quantum tunneling causes the electrical breakdown. For a

p-n junction with a breakdown voltage between 5 V and 8 V, both impact ionization and tunneling influence the electrical breakdown.

Impact ionization occurs only when the electric field has raised the kinetic energy of the particle above the threshold ionization energy E_{ion}. The number of e-h pairs generated by a carrier per distance is called the ionization rate α. It depends on the probability that a carrier can gain enough energy to reach or surpass the threshold ionization energy. In TCAD from Synopsys, the default ionization rate is given by the van Overstraeten – de Man Model [42], [75], which is based on the Chynoweth law [76]:

$$\alpha(\mathcal{E}, T) = \gamma(T)\exp\left(-\frac{\gamma(T)b}{\mathcal{E}}\right), \tag{4.27}$$

where $\mathcal{E}$ is the electric field, T is the temperature, a and b are coefficients derived by van Overstraeten and de Man [75], and $\gamma(T)$ models the temperature dependence of the impact ionization process:

$$\gamma = \tanh\left(\frac{\hbar\omega_{op}}{2kT_0}\right)\left[\tanh\left(\frac{\hbar\omega_{op}}{2kT}\right)\right]^{-1}, \tag{4.28}$$

where $\hbar\omega_{op}$ is the optical phonon energy, k is the Boltzmann constant, and $T_0 = 300\,\mathrm{K}$. The van Overstraeten and de Man [75] model is valid for electric fields with an amplitude starting from $1.75{\cdot}10^5\,\mathrm{V{\cdot}cm^{-1}}$ to $6{\cdot}10^5\,\mathrm{V{\cdot}cm^{-1}}$. The numerical values for the parameters to calculate the ionization rate for low ($< 4 \cdot 10^5\,\mathrm{V \cdot cm^{-1}}$) and high ($> 4 \cdot 10^5\,\mathrm{V \cdot cm^{-1}}$) fields are listed in Table 4.1.

Table 4.1: Parameters of the van Overstraeten – de Man model for silicon [42], [75].

Symbol	**Electrons**	**Holes**	**Unit**	**Valid Range**
a_{low}	$7.03 \cdot 10^5$	$1.58 \cdot 10^6$	$\mathrm{cm^{-1}}$	$1.75 \cdot 10^5\,\mathrm{V \cdot cm^{-1}}$ to $\mathcal{E}_0$
a_{high}	$7.03 \cdot 10^5$	$6.71 \cdot 10^5$	$\mathrm{cm^{-1}}$	$\mathcal{E}_0$ to $6 \cdot 10^5\,\mathrm{V \cdot cm^{-1}}$
b_{low}	$1.23 \cdot 10^6$	$2.03 \cdot 10^6$	$\mathrm{V \cdot cm^{-1}}$	$1.75 \cdot 10^5\,\mathrm{V \cdot cm^{-1}}$ to $\mathcal{E}_0$
b_{high}	$1.23 \cdot 10^6$	$1.69 \cdot 10^6$	$\mathrm{V \cdot cm^{-1}}$	$\mathcal{E}_0$ to $6 \cdot 10^5\,\mathrm{V \cdot cm^{-1}}$
$\mathcal{E}_0$	$4 \cdot 10^5$	$4 \cdot 10^5$	$\mathrm{V \cdot cm^{-1}}$	-
$\hbar\omega_{\mathrm{op}}$	0.06	0.06	eV	-
β_{low}	0.81	0.67	a.u.	$1.75 \cdot 10^5\,\mathrm{V \cdot cm^{-1}}$ to $\mathcal{E}_0$
β_{high}	0.67	0.67	a.u.	$\mathcal{E}_0$ to $6 \cdot 10^5\,\mathrm{V \cdot cm^{-1}}$

For charged particles with energies higher than the threshold energy ($E_c = 800\,Z^{-1}\,\mathrm{MeV}$), bremsstrahlung [77] becomes the dominant energy loss mechanism in matter. Bremsstrahlung radiation, also known as braking radiation, is produced when a charged particle with $E > E_c$ scatters off a nucleus, emitting a photon.

Photons interact with matter through different mechanisms depending on the photon energy. Fig. 4.11 illustrates the interaction mechanisms of photons as a function of atomic number (Z) and energy (E). At lower energies ($E < 0.1\,\mathrm{MeV}$), the photoelectric effect (photoabsorption) dominates the interaction cross-section, and at high energies ($E > 10\,\mathrm{MeV}$), pair production is the leading interaction mechanism. For intermediate energies, Compton scattering is the main interaction process.

The photoelectric effect consists of the emission of an electron as a result of the interaction between a photon and an atomic electron, as illustrated in Fig. 4.12 (a). When

the photon interacts with the target atom, its entire energy is absorbed by the atom, and then an electron is emitted. The emitted electron kinetic energy [78] can be expressed as:

$$E_{e^-} = h\nu - E_b, \tag{4.29}$$

where $h\nu$ is the energy of the photon and E_b is the binding energy of the electron. Once the target atom emits one of its electrons, a vacancy is created, which can be filled by electrons from higher energy levels or free electrons. The photoelectric effect is the predominant interaction mechanism of photon interaction with matter at low energies of the photon and has a power-law dependence on the atomic number Z of the absorber material.

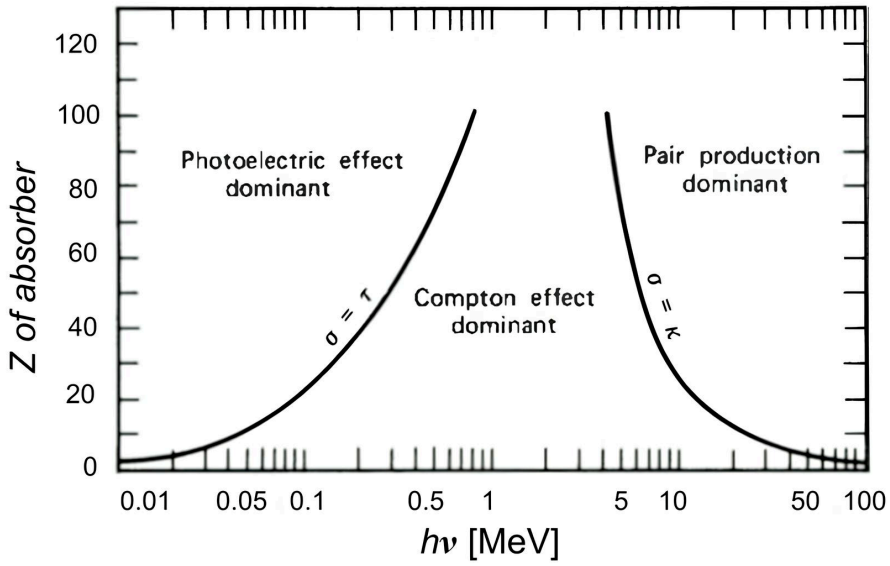

Figure 4.11: Schematic diagram of the photon interactions mechanisms as a function of the incident photon energy E expressed in MeV and the atomic number Z of the absorber material [78]. The photoelectric effect is dominant at low energies ($< 0.1\,\text{MeV}$) and exhibits a power-law dependence on Z. The Compton scattering is dominant for $0.1\,\text{MeV} < E < 10\,\text{MeV}$ and it is directly proportional to the atomic number Z. Pair production is dominant at high energies ($> 10\,\text{MeV}$) and exhibits a Z^2 dependence.

Compton scattering is the interaction process between an incident photon and an atomic electron as represented in Fig. 4.12 (b). The photon interacts with the atomic electron, losing some of its energy. Because of the interaction, the trajectory of the photon changes by an angle θ. The energy transferred to the electron [78] can be expressed in terms of the scattering angle (θ) as follows:

$$h\nu' = \frac{h\nu}{1 + \frac{h\nu}{m_0c^2}(1 - \cos\theta)}, \tag{4.30}$$

where $h\nu$ is the energy of the incident photon and m_0c^2 is the rest mass of the electron. Even in extreme cases when $\theta = \pi$, the photon still keeps a part of its energy. The probability of photons interacting through Compton scattering depends on the number of electrons the target atom has, and it increases with the increase in the atomic number Z of the target material.

Pair production occurs when the entire energy of an incident photon is converted into an electron-positron pair as represented in Fig. 4.12 (c). This occurs only for energies of the incident photon at least double the energy equivalent to the rest mass of an electron ($h\nu > 2m_0c^2$). Pair production exhibits a quadratic dependence on the atomic number Z.

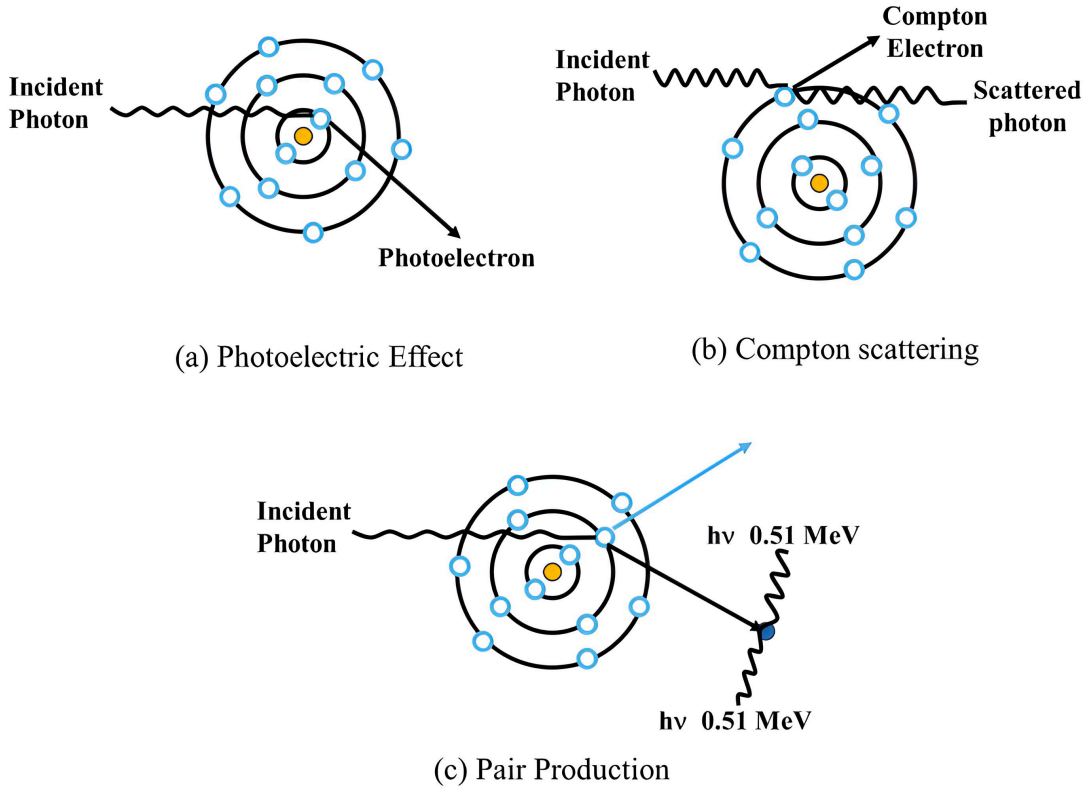

(a) Photoelectric Effect

(b) Compton scattering

(c) Pair Production

Figure 4.12: Graphical representation of the photon interaction processes: photoelectric effect (a), Compton scattering (b) and pair production (c) [79]. Pair production happens when a photon with energy $>$ 1.022 MeV, typically near a nucleus, converts into an electron-positron pair. The term $h\nu = 0.51$ MeV is the rest mass energy of an electron or positron.

4.4 Strip Sensors

For HL-LHC experiments, particle tracking is a key input to the data analysis process. This is achieved using detectors, which can provide information on the position of the charged particle's interactions. Fig. 4.13 shows a cross-sectional view of an n-type silicon strip sensor fabricated by Enertec (Strasbourg). There are 25 aluminum strips, each 1800 µm wide and placed 200 µm apart, each with a p-type implant underneath. The passivation layer on top consists of SiO_2. Ionizing particles that reach the top surface of the sensor can interact with the silicon, creating electron-hole pairs. The amount of charge generated inside the sensor is proportional to the energy of the ionizing particle, assuming full energy deposition and linear response. The charge is accelerated by the electric field, which is generated by the potential difference across the sensor. Then, the charge is collected and delivered to an amplifier. In this case, the signal collected from a particular strip already gives information related to the approximate position where an ionizing particle interacted with the silicon.

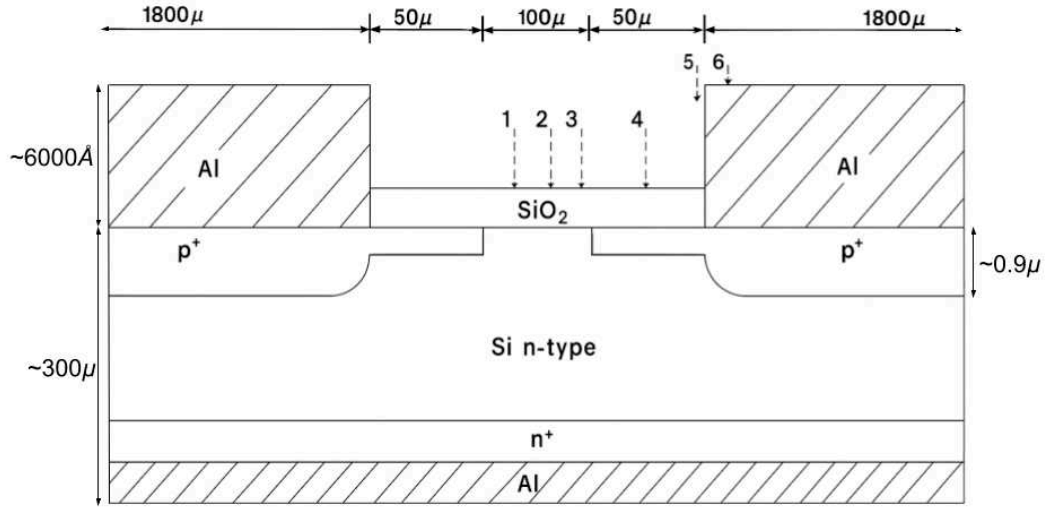

Figure 4.13: Sketch diagram of a strip detector fabricated by Enertec (Strasbourg) [80]. The bulk is n-doped; underneath the aluminum strips, there is a p^+ implant, and on the backside, there is a n^+ implant. A SiO_2 layer acts as the passivation between strips.

If a uniform charge distribution and a binary readout are assumed, the spatial resolution of a sensor is related to the strip pitch as:

$$< \Delta x^2 >= \frac{1}{p} \int_{-\frac{p}{2}}^{\frac{p}{2}} x^2 \mathrm{d}x = \frac{p^2}{12}, \tag{4.31}$$

where x is the true coordinate of the event and p is the strip pitch. To improve the spatial resolution, the strip pitch should be smaller such that the signal can be reconstructed from the interpolation of several strips. For this, the strip pitch has to match the width of the charge cloud. If the pitch is too large, some of the charge may not be collected by nearby strips, reducing measurement precision. If the pitch is too small, unnecessary readout channels are used without improving accuracy. Capacitive charge division [45] is a technique that allows for charge collection across a wider area than would be possible

based solely on charge diffusion inside a semiconductor. The strip pitch is a limiting factor because, for signal interpolation, the strip pitch has to match the diffusion width.

Fig. 4.14 shows the two methods of coupling: capacitive coupling (left-strip) and direct coupling (right-biased electrode). For capacitive coupling, the metal strip is not in electrical contact with the silicon. The SiO_2 acts as a dielectric material while both the strip and the implant act as the metal plates of a capacitor. The capacitive coupling allows only the induced AC signal to be read out while shielding the DC signal, which can lead to pedestal shifts [45]. For direct coupling, the biasing electrode is in direct contact with the implant. The ATLAS ITk strip sensor comes with capacitive-coupled strips (AC coupled), which help with noise reduction and signal isolation.

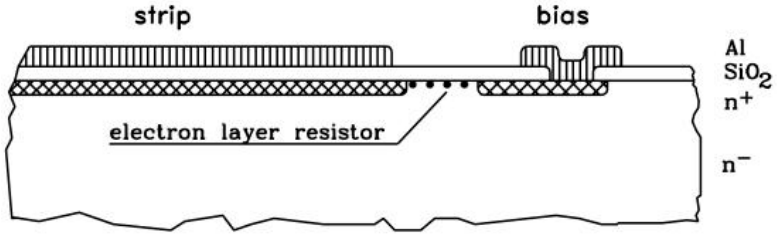

Figure 4.14: Example sketch of a silicon strip detector with the substrate n^- and n^+ implants. A layer of silicon dioxide SiO_2 is deposited on top of the silicon. The strip and the bias electrode are made of Aluminum (Al). The electron layer resistor acts as a resistive path and is typically made of doped polysilicon. On the left side, the strip is capacitively coupled to the silicon, while on the right side, the bias electrode is directly connected to the silicon. The image was taken from [45].

Positive charges can get trapped at the interface between silicon and SiO_2 during oxidation. Fig. 4.15 (a) illustrates a silicon strip sensor with n^+ implants underneath the strips and SiO_2 passivation on top of silicon. Under the influence of an applied electric field, an electron accumulation layer forms between the strips because electrons are attracted toward the positive oxide charges. This creates a conductive channel between the strips, which can lead to a short circuit. This issue can be mitigated in three distinct ways that are presented in Fig. 4.15 (b)-(d).

The first method consists of depositing a wide p-type compensation implant as illustrated in Fig. 4.15 (b), which would compensate for the trapped charges and prevent the formation of an electron layer. The width of the compensation implant needs to be chosen carefully because wide implants generate high electric fields, which might lead to localized electrical breakdown at the edge of the strips.

The second method employs the deposition of a p-stop between the strips as represented in Fig. 4.15 (c). A p-stop consists of a p-type implant between electrodes with n^+ implants. In this case, the p-stop does not prevent electrons from accumulating between the strips, but it prevents the formation of a conductive channel. The ATLAS ITk strip collaboration opted for implementing a p-stop to prevent the build-up of a conductive channel between the strips.

The third method consists of the deposition of a metal between the strips, which together, with the SiO_2 layer and the silicon, would create a metal–oxide–semiconductor (MOS) [58] structure as presented in Fig. 4.15 (d). Applying a moderate negative bias voltage, lower than the bias for the n-type strips, would prevent electrons from accumulating underneath. However, if a high enough bias voltage is applied on the oxide, then

holes can accumulate there.

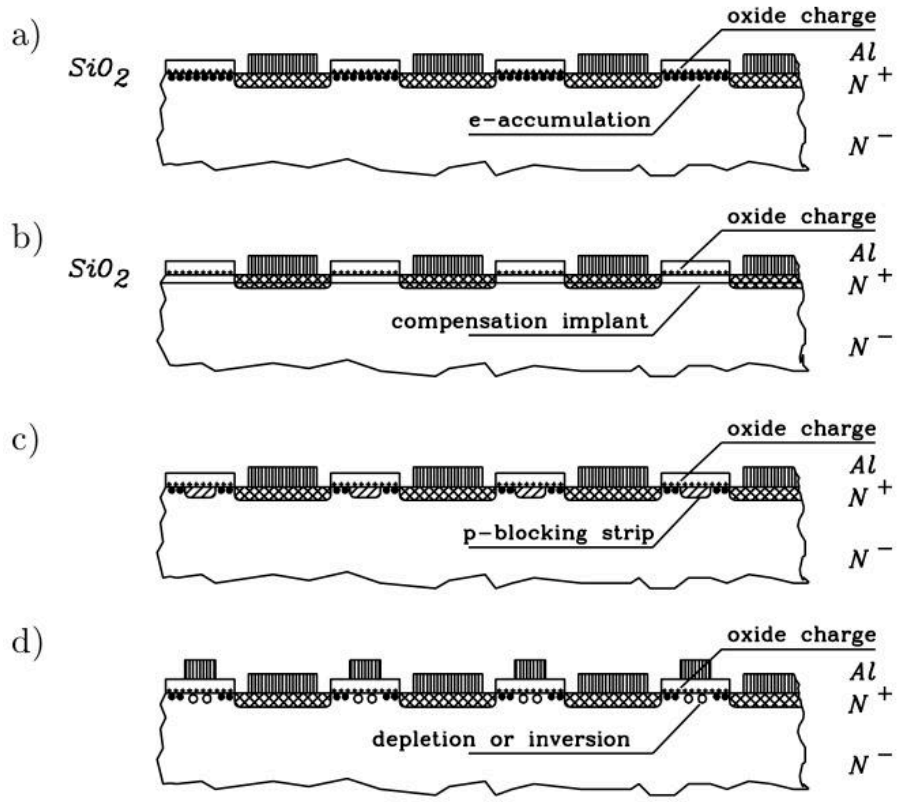

Figure 4.15: Example of different silicon strip sensors geometries [45]. The silicon is n^- doped (N^-), while the Aluminum strips are n^+ doped (N^+). a) Strips divided by SiO_2 regions where an inversion layer builds up. b) Strips with a compensation implant in between. c) Strips divided by a p-stop. d) Strips where a metal is deposited on top of the SiO_2 to form a negatively biased (with respect to the n^+ strips) MOS like-structure [45].

4.5 Humidity Studies Motivation

In the previous section, the relative humidity (RH) has not been considered when discussing the mitigation methods to prevent electrons from accumulating between the strips due to being attracted to the positive oxide charges. An early study conducted by Atalla et al. [81] investigated the effects of RH on silicon p-n junctions with SiO_2 passivation. First, the leakage current as a function of the applied reverse bias was measured for a p-n junction in dry conditions. Then, the p-n junction was exposed to $RH = 60\,\%$ with no bias applied. Periodically, a fixed bias was applied for only a few seconds, and the leakage current was measured. Over a period of 24 hours, no changes were observed in the leakage current due to the presence of humidity.

Following that, the leakage current was measured for bias voltage values ranging from 5 V to 30 V, as a function of humidity ($RH = 35\,\%, 50\,\%, 60\,\%$). It was observed that the leakage current increased with the increase in bias voltage and RH until it reached a plateau after waiting some time (see Fig.3 in [81]). To explain this phenomenon, Atalla has proposed a new charge transport model at the surface of silicon p-n junctions with SiO_2 passivation. If a p-n junction is exposed to humidity and is reverse-biased, positive charges accumulate on the surface near the p-region, while negative charges accumulate near the n-region. These surface charges introduce localized electric fields, which alter the electric field distribution inside the p-n junction. The depletion region may widen near the surface, changing the potential barrier that carriers need to overcome. If the concentration of surface charges is high enough, an inversion channel will form inside the silicon close to the surface. Initially, when the bias voltage increases, more surface charges accumulate near the p- and n-sides, and the leakage current rises. Eventually, the surface charges reach equilibrium, and their effect saturates such that a further increase in bias voltage at a given RH does not lead to additional increases in leakage current, leading to a plateau. Shockley et. al. [82] has verified the Atalla charge transport model at the surface of silicon p-n junctions with SiO_2 passivation in humid conditions [81].

Schroen [83] investigated how surface treatments impact ion accumulation and charge transport on the surface of silicon diodes with SiO_2 passivation. Different surface treatments were applied to a planar n^+-p diode, and the surface potential was measured as a function of time in humid conditions. When the bias voltage is applied to the diode, positive ions accumulate at the surface close to the p-type region, and negative ions accumulate near the n-type region. The ion distribution was frozen at the surface of the diode using dry nitrogen. A Kelvin probe [84], which operates on the vibrator capacitor principle, was used to measure the contact potential difference across the diode's surface [82].

Fig. 4.16 shows the evolution of the surface potential measured between the contact tip of a Kelvin probe and the p- or n-side before and after heat treatments (a) and the application of Kodak Photo Resist (KPR) (b). During the heat treatment(s), the silicon diodes were baked at 600°C for 1800 s in the presence of nitrogen in vacuum (10^{-6} Torr). It can be observed in Fig. 4.16 (a) that after the second heat treatment, the surface potential decreased for both positive and negative ions and continued to decrease for the entire measuring time. After the third heat treatment, the surface potential was close to 0 V and almost constant while measurements were taken. Heat treatments are a useful treatment after the fabrication process is finished, especially if sensors are affected by humidity.

Fig.4.16 (b) shows the surface potential measured between the tip of a Kelvin probe

and the p- or n-side of a p-n diode before and after treatment with KPR (a photoresist material). It can be seen that after the KPR treatment, the surface potential decreased to 0 V and remained constant throughout the measurement period. The KPR treatment can be used as part of the passivation process for future devices designed to operate in humid conditions.

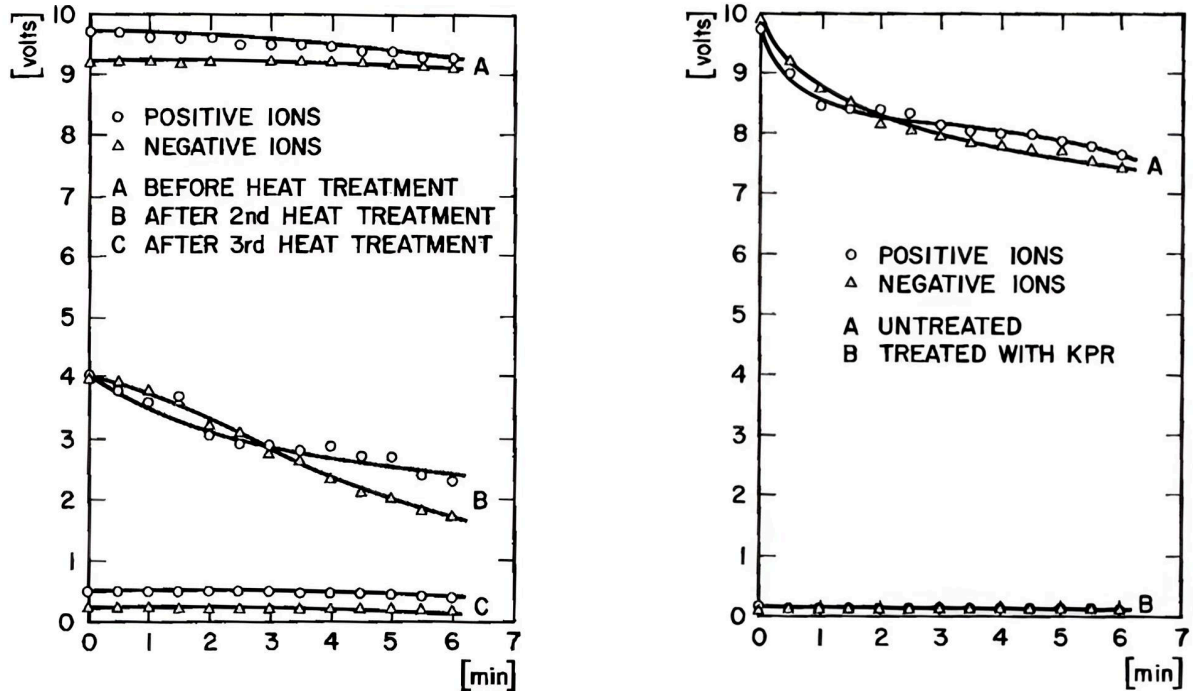

Figure 4.16: Surface potential evolution measured between the tip of a Kelvin probe and the p- or n-side of a silicon p-n junction before and after heat treatments (a) and the application of Kodak Photo Resist (KPR) (b) [83].

Impact of Humidity on ATLAS ITk Strip Sensor

The ATLAS ITk strip sensors come in many flavors, as previously mentioned in section 2.2. Fig. 4.17 shows each wafer type with the main sensors and test structures for both barrel and end-cap. Each type of sensor is produced on individual 6-inch wafers by Hamamatsu Photonics. The sensor is placed in the middle of the wafer, while the remaining space is populated with test structures dedicated to the quality assurance and control of the sensor's properties. The ATLAS ITk strip sensor is an n^+-in-p silicon sensor produced using the Float Zone (FZ) technology with the silicon p-doped. The edge of the strip sensor is presented in Fig. 4.18. Moving from the outer region towards the active area, the structures include the Edge Ring (ER) with a p-implant, the Guard Ring (GR) and the bias ring, both with n-doping. The backside (not shown in Fig. 4.18) is p^+-doped, with an aluminum metal layer deposited on it. The interstrip isolation is achieved with a p-stop. The passivation consists of a SiO_2 layer and a Si_3N_4 layer. The thickness of the passivation has been measured within the ATLAS ITk Strip collaboration ($\sim 0.6\,\mu m$ for SiO_2 and $\sim 0.6\,\mu m$ for Si_3N_4), however these values have not been published.

During the prototyping phase of the ATLAS ITk strip detector, some silicon strip sensors showed signs of a lowered breakdown voltage when exposed to an $RH \geq 20\,\%$

[1]. Fig. 4.19 shows multiple Current-Voltage (IV) distributions measured between the backplane and the bias ring for different RH values. First, the sensor was tested at $RH = 10\,\%$ and no sign of early breakdown was visible even for $V_{bias} \geq 1000\,\mathrm{V}$. Then the sensor was tested in humid conditions, at $RH = 40\,\%$ and $RH = 60\,\%$. At $RH \geq 40\,\%$, the leakage current was high for $V_{bias} \leq 800\,\mathrm{V}$. When RH was reduced back to $10\,\%$, the leakage current was still high for $V_{bias} \leq 700\,\mathrm{V}$.

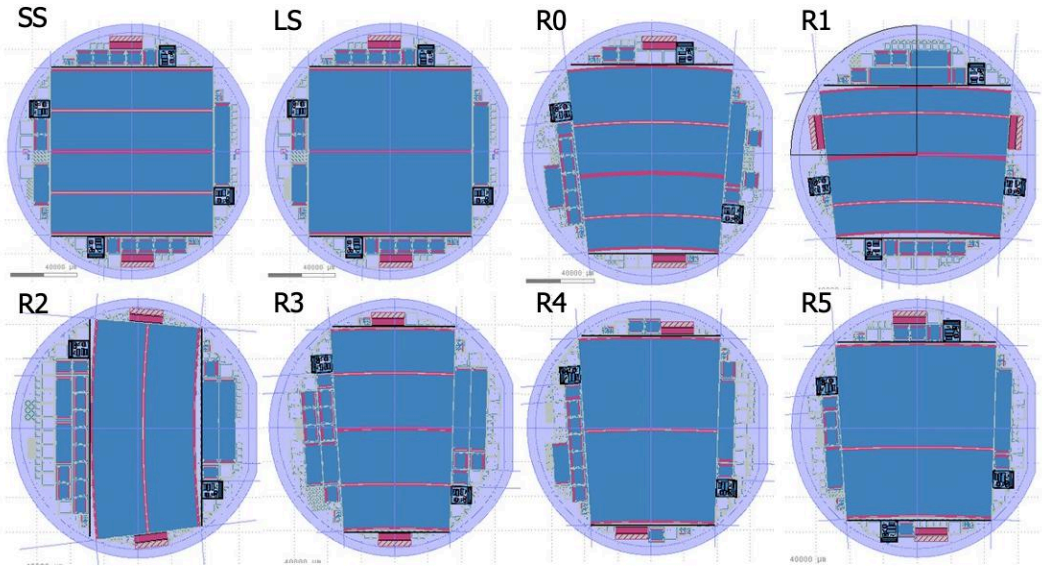

Figure 4.17: Schematic view of barrel and end-cap wafers [85]. The main sensors are in the middle of the wafer while the rest of the space is populated with test structures for quality assurance purposes.

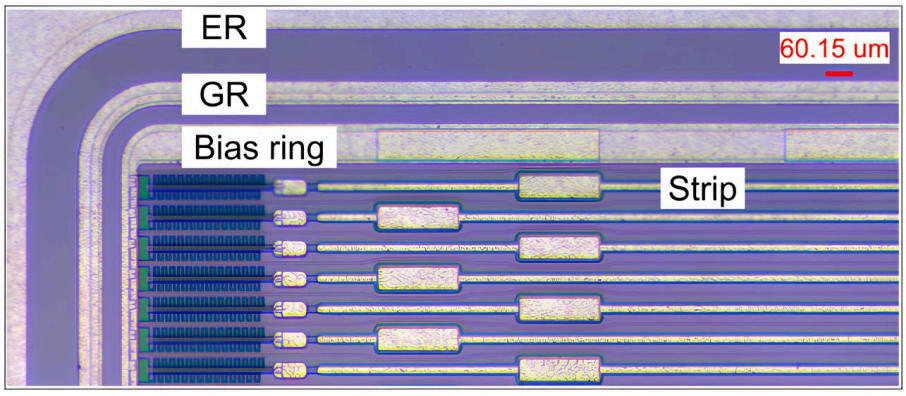

Figure 4.18: Microscope image of the ATLAS ITk strip sensor edge [86]. From the outer region to the active area, the structures consist of the Edge Ring (ER), the Guard Ring (GR), the bias ring and the strips which are connected via a polysilicon resistor with the bias ring.

A commercial CMOS camera [87] was used to cross-check the location of the avalanche breakdown in the edge region of test structures. Fig. 4.20 shows an example of a 4 mm by 4 mm n-in-p silicon diode operated in electrical breakdown. Similarly to the edge geometry of the strip sensor, the outermost aluminum ring is called the ER and has a

p-implant, then there is the GR and the pad metal with an n-implant each. The bias voltage was applied on the backside, which has a conductive coupling to the ER via the undepleted region along the dicing edge. The GR and pad were kept at ground. Under humid conditions, in a high biased sensor, electrons are accelerated in the strong electric field present in the edge region of the diode. When the accelerated electrons lose their excess energy, photons with a wavelength in the near-infrared are emitted from that region [88], [89]. This process can be observed in Fig. 4.20 by the presence of a white spot encircled with red in the edge region of the sensor.

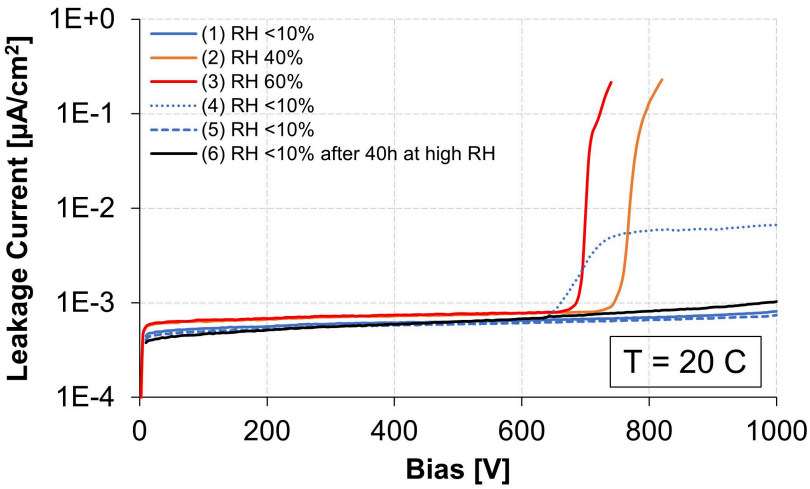

Figure 4.19: Example of IV measurements of an un-irradiated silicon strip sensor for different RH values at $T = 20^\circ\,\mathrm{C}$ [90]. The first measurement (blue curve) is taken in dry conditions, $RH = 10\,\%$. The second and third curves (orange and red) were taken in humid conditions at $RH \geq 40\,\%$. Then the sensor is tested again in dry conditions (dotted and dashed blue lines). Finally, the sensor is kept in a dry environment for 40 h and retested at $RH = 10\,\%$.

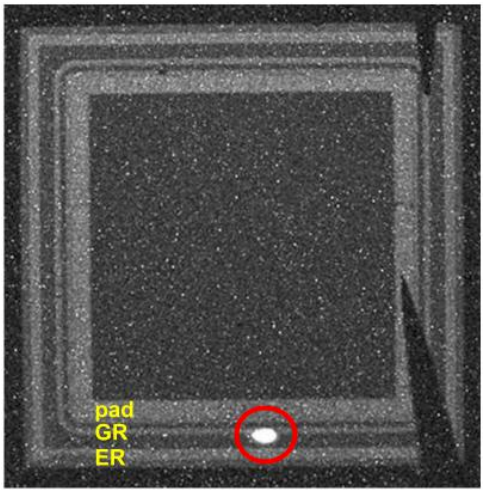

Figure 4.20: Microscope picture of a 4 mm by 4 mm ATLAS ITk n-in-p silicon diode operated in avalanche breakdown [91]. The photon emission during avalanche breakdown [92] is visible as a bright spot encircled with red. The measurement was performed at $RH \simeq 50\,\%$. The breakdown current between the backside and the GR was $\mathcal{O}(1)$ µA.

To understand how the surface properties impact the humidity-induced electrical breakdown, a special batch of sensors with the final design [93] was requested from the vendor [90]. For this, some sensors had surface treatment, thicker passivation, special masking, a p-spray addition, or further treatment. A p-spray addition is a shallow, low-dose ($10^{11}\,\mathrm{cm}^{-2}$) p-type ion implantation. The sensors were electrically tested in dry and humid conditions (between 20 % and 60 % RH). At $RH = 60\,\%$, the ATLAS breakdown voltage requirement of at least 500 V was met only by the sensor with the thicker passivation layer or p-spray addition. This seemed to confirm that a thicker passivation layer could prevent the accumulation of positive charges on the surface.

To mitigate the humidity sensitivity of strip sensors, they are stored in a dry environment, $RH \leq 10\,\%$. Electrical tests are performed in humidity-controlled setups at $RH \leq 10\,\%$ to avoid electrical failures due to the effect of humidity on sensors. Humidity could become an issue when sensors are mounted on support structures, staves, and petals because these are assembled and tested over extended periods in large cleanrooms, where air drying of large volumes is not feasible ($50\,\% \leq RH \leq 70\,\%$). Since the long-term effects of humidity on strip sensors were unknown, a long-term humidity exposure study looked at the electrical behavior of 32 sensors from different delivery batches. The sensors had different initial electrical performance levels on reception and required different recovery procedures [94]. The recovery methods include dry storage, ionizing gas treatment, UV light irradiation, and high-temperature exposure.

Dry storage: Sensors are stored in humidity controlled cabinets at $RH \leq 10\,\%$. Dry air is flushed inside the cabinets to keep the RH below 10 %. In dry storage, moisture on the sensor's surface evaporates, which means that there is less water to facilitate corrosion reactions between metals and oxygen.

Ionizing gas treatment: A high-intensity flow of ionized gas (e.g., air, nitrogen) is applied to the sensor's surface. The gas molecules neutralize surface charges by transferring charge to the surface. For example, if the surface is positively charged, it attracts gas molecules that can donate electrons, neutralizing the positive charge while repelling the positive molecules; the opposite is true if the surface is negatively charged. The ionizing gas treatment is applied using an ionizing air blower for approximately 30 minutes [95].

UV light irradiation: Photons in the UV range, typically with wavelengths between 100 nm and 400 nm have energies ranging from 12.4 eV (for 100 nm) to 3 eV (for 400 nm). The SiO_2 energy bandgap is 8.9 eV, corresponding to a wavelength of approx. 139.3 nm, therefore, only photons in the deep UV range can generate electron-hole pairs in SiO_2. Photons with higher wavelengths (lower energies) can still contribute to the release of trapped charges through secondary processes such as multiphoton absorption or thermal excitation. There are two types of UV light treatments: irradiation with UV-A ($\lambda \in [315, 400]\,\mathrm{nm}$) with exposure between 2 and 8 hours and irradiation with UV-C ($\lambda \in [100, 280]\,\mathrm{nm}$) with exposure of 60 seconds [95].

High-temperature treatment: Water molecules can be absorbed onto surfaces or in porous materials. High-temperature exposure quickly evaporates moisture from the sensor's surface. Additionally, a high-temperature treatment promotes the rearrangement of surface atoms such that some of the interface states can be passivated, improving the electrical behavior of the sensor. Sensors are baked inside industrial ovens at high temperatures for more than 16 hours at 150° C [95].

The recovery methods can be tried individually or in combination. In a recent long-term humidity exposure of ATLAS18 ITk strip sensors study conducted by V. Fadeyev et al., [94], it was shown that sensors exposed for long periods to high humidity recovered

their nominal behavior when the sensors were tested in dry conditions. This finding confirms that the sensor's technology is compatible with extended periods of exposure to humidity as long as the sensors are operated in dry conditions. However, the sensors' humidity sensitivity could become an operational problem if they are electrically tested after being accidentally exposed to $RH > 10\,\%$, as there is always the risk of deviation in case the laboratory infrastructure fails. Once installed, the ITk will be in a controlled, dry environment, so humidity sensitivity is not an issue during the ATLAS operation.

The mechanisms behind the early breakdown of sensors in humid conditions are not yet fully understood. To gain insight into the physical processes that trigger the early breakdown of sensors due to exposure to humidity, charge transport in the edge region of the sensor was investigated by generating localized free charge carriers near the surface with picosecond pulses of laser light, i.e., the Top-Transient Current Technique (Top-TCT). The electrical behavior of test structures was simulated using Technology Computer-Aided Design (TCAD) from Synopsys [96] to support the experimental data.

Fig. 4.21 shows the device investigated in this study, an 8 mm by 8 mm, n-in-p silicon diode called the monitor diode (MD8). This type of diode comes from the same ATLAS18 ITk wafer as the strip sensor presented in Fig. 4.22. The geometry of the MD8 is similar to the diode illustrated in Fig. 4.20, but it has a special feature of a p-stop between the GR and the pad metal, which is more representative of the strip sensor. A p-stop is an additional p^+ implant, which introduces an isolation between the GR and the pad.

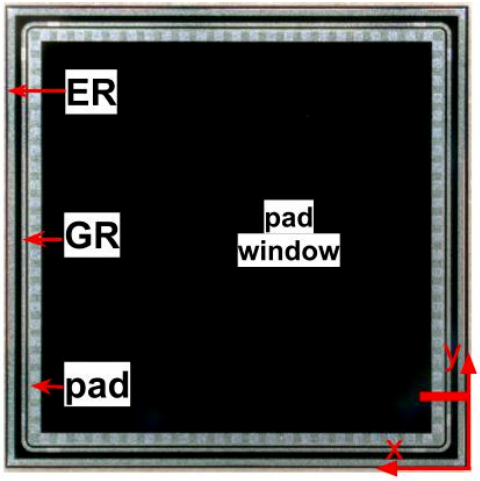

Figure 4.21: Microscope image in the visible spectrum of an 8 mm by 8 mm n-in-p silicon diode from the ATLAS18LS wafer. From left to right, there is an ER with a p-implant, a GR with an n-implant and a pad metal with a n-implant. There is a p-implant on the backside. The central part of the diode area is without aluminum metal.

Capacitance-Voltage (CV) measurements were performed on two different MD8 diodes to extract the full depletion voltage (V_{FD}), active thickness (W), and the effective silicon bulk doping (N_{eff}). An example of a CV characteristic is presented in Fig. 4.23. The bias voltage was plotted as absolute values. For CV measurements, the bias voltage was applied to the backside using a Keithley 2400 source meter [97], while the GR was at ground. The capacitance was measured on the pad metal using an Agilent E4981A LCR-meter [98].

The depletion region of a p-n junction acts approximately as a plate capacitor of area A, and W as the distance between the two electrodes plates. The capacitance depends

on the depletion depth as shown in equation 4.23.

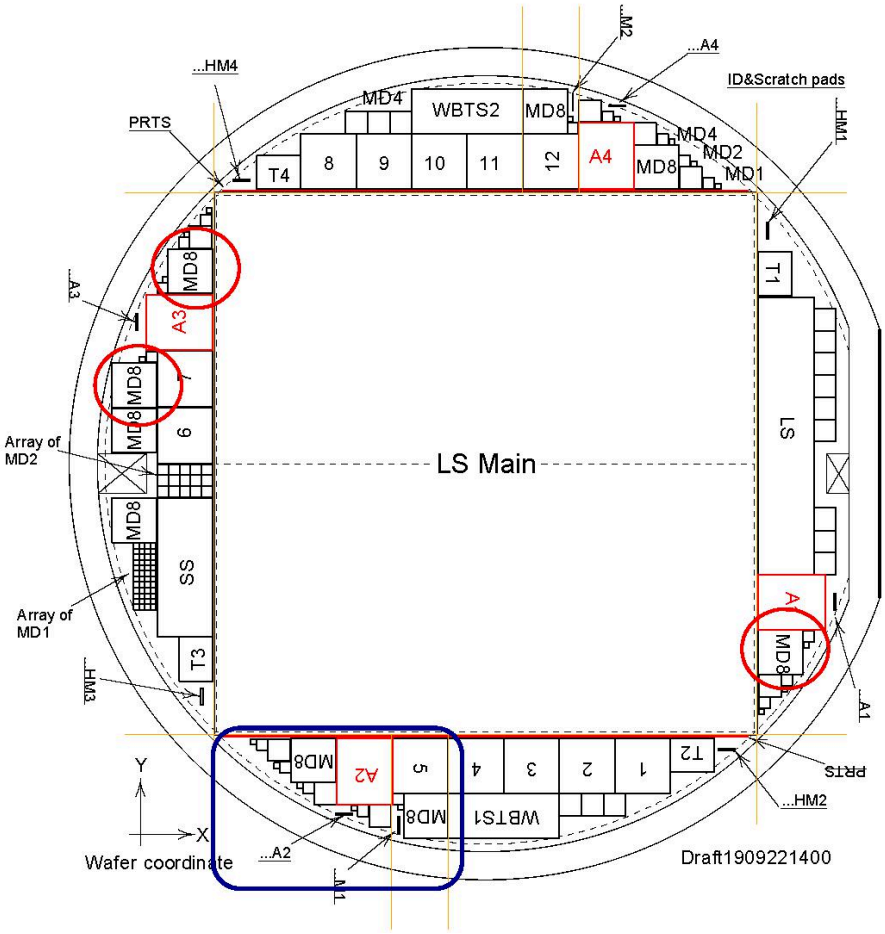

Figure 4.22: Design of the ATLAS ITk Long Strip (LS) wafer [93]. The LS sensor is placed in the middle of the wafer. Test structures with the same properties as the main sensor, but different layouts and sizes are placed in the corners.

For a p-n junction, the depletion width is given in equation 4.20, which for $V_{\text{bias}} \gg V_{\text{bi}}$ simplifies to

$$W \propto \sqrt{V_{\text{bias}}}.$$

Thus, the capacitance behaves as

$$C \propto \frac{1}{\sqrt{V_{\text{bias}}}}.$$

Once the full depletion (V_{FD}) is reached, the entire active region is depleted, and any further increase in bias voltage would not change the active thickness significantly. Therefore, the capacitance saturates:

$$C \approx \text{constant for } V_{\text{bias}} \geq V_{\text{FD}}.$$

It can be seen that for the CV characterization presented in Fig. 4.23, $1/C^2$ has a distinctive behavior depending on the voltage range:

- From 0 V to 80 V, $1/C^2$ increases almost linearly. The deviation from a linear increase could potentially come from a conductive channel forming between the

GR and pad. The conductive channel forms because electrons are attracted at the surface by the positive fixed oxide charges at the interface between silicon and the SiO_2. As the voltage increases, the lateral electric field dissipates the accumulation layer.

- From 80 V to 280 V, $1/C^2$ increases linearly, which is the expected behavior.
- From 280 V to 350 V, $1/C^2$ starts to saturate. Only in an ideal diode, when the diode reaches the full depletion voltage, will $1/C^2$ become constant immediately after reaching the inflection point.
- From 350 V to 450 V, $1/C^2$ becomes constant because the diode is fully depleted.

To obtain the full depletion voltage, the data was fitted using two methods:

- A linear fit was applied between 80 V and 260 V because in this range $\frac{1}{C^2}$ stabilizes and increases linearly with the applied bias voltage. The fitted function is given by: $y = ax + b$, where $a = (9.377 \pm 0.004) \cdot 10^{18}\, 1/(\mathrm{F}^2 \cdot \mathrm{V})$ is the slope and $b = (4.778 \pm 0.073) \cdot 10^{19}\, 1/\mathrm{F}^2$ is the intercept obtained from regression analysis. The linear regression was performed using a least-squares fitting method. The uncertainties in the slope and intercept were calculated from the residuals of the linear regression, representing the standard errors that quantify how well the fit aligns with the data points given their scatter. For the CV characteristic, the error bar calculation begins with the average of three repeated capacitance measurements taken at each bias voltage. The standard deviation of these values is then computed and subsequently propagated through the $1/C^2$ using standard error propagation.
- A constant fit was applied between 350 V and 450 V, which is the region where the capacitance saturates. The constant fit is given by $y = c$, where $c = (2.720 \pm 0.001) \cdot 10^{21}\, 1/\mathrm{F}^2$ is the average $1/C^2$ in the selected range with an uncertainty calculated from the standard error of the mean. The uncertainty is calculated from the spread of the data points between 350 V and 450 V, divided by the square root of the number of points.

The full depletion voltage is determined as the intersection point between the linear fit and the constant fit: $c = aV_{FD} + b$. From the CV measurement presented in Fig. 4.23, $V_{FD} = 285.04\,\mathrm{V} \pm 0.2\,\mathrm{V}$, where the error estimation was calculated based on the Gaussian error propagation of the two fits.

To calculate the active thickness of the diode (W), equation 4.23 can be rearranged to:

$$W = \frac{\epsilon \epsilon_0 A_{pad}}{C}, \tag{4.32}$$

where ϵ is the relative permittivity given as $\epsilon = 11.9$ for silicon [60] and ϵ_0 is the permittivity of free space. The term A_{pad} corresponds to the area of the pad window, extended to the middle of the p-stop. This estimation was made to account for the extension of the full depletion region beyond the pad metal. The area was calculated based on microscope measurements of the pad window, pad metal, the radius of the pad metal, etc. In addition, to ensure the reliability of the averaged capacitance, two CV characteristics were measured. Introducing the numerical values from Table 4.2 in equation 4.32, the average active thickness was calculated as 286.66 µm and approximated to 287 µm for an easy implementation in TCAD simulations. For reference, the diode thickness is ~ 295 µm.

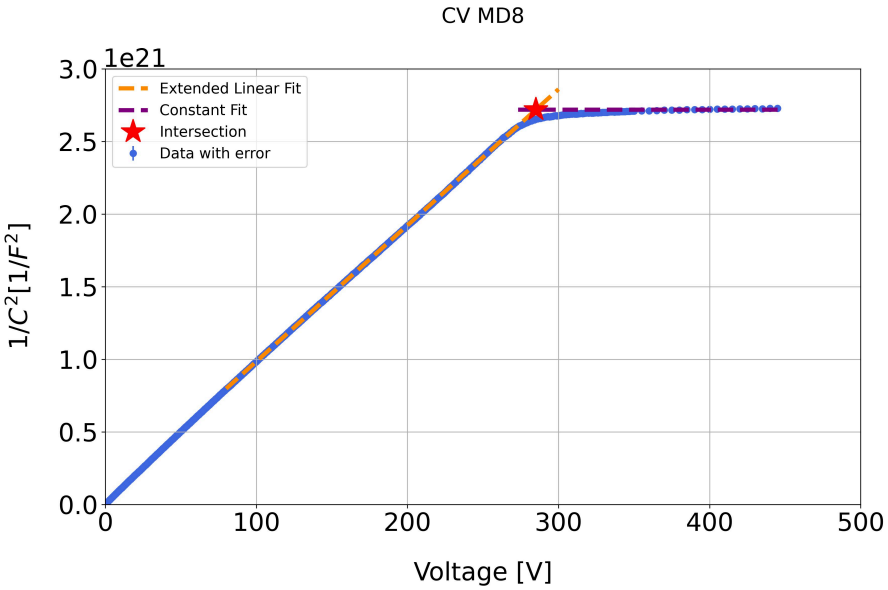

Figure 4.23: CV characteristic for an MD8 diode from the ATLAS18LS wafer illustrating the full depletion voltage. The bias voltage was applied on the backside, while the GR was at ground. The capacitance was measured across the pad metal.

Table 4.2: Active Thickness Parameters

Avg. C [F]	ϵ_0 [F/m]	ϵ	Area [µm^2]	W [µm]
$1.92 \cdot 10^{-11}$	$8.85 \cdot 10^{-12}$	11.9	51988110.55	285.16
$1.90 \cdot 10^{-11}$	$8.85 \cdot 10^{-12}$	11.9	51988110.55	288.16
			Average:	286.66

Once the full depletion voltage is reached, the depletion region extends to the entire active thickness. The effective doping N_{eff} [60] can be determined based on the active thickness and the full depletion voltage using the following formula:

$$N_{eff} = \frac{2\epsilon\epsilon_0}{qW^2} V_{FD}. \tag{4.33}$$

The error for the effective doping was determined based on the uncertainty propagation in the full depletion voltage and active thickness. Introducing the numerical values from Table 4.3 into equation 4.33, the effective doping was calculated to be $4.56 \cdot 10^{12}\,\mathrm{cm}^{-3}$.

An alternative method for calculating the effective silicon bulk doping [99] uses the formula:

$$N_{eff} = \frac{2}{\epsilon\epsilon_0 A^2 q} \frac{1}{\Theta}, \tag{4.34}$$

where Θ is the slope of the linear fit in Fig. 4.23. The numerical values of the parameters to compute equation 4.34 are listed in Table 4.4. The same slope value, $9.37 \cdot 10^{19}\,\mathrm{F}^{-2}$, was obtained for both CV characteristics measured; therefore, the values in Table 4.4 were not repeated. Using this method, the effective doping was derived as $4.68 \cdot 10^{12}\,\mathrm{cm}^{-3}$.

Table 4.3: Effective Doping Parameters (Method 1)

Parameter	1st Value	2nd Value	Unit
Avg. C	$1.92 \pm 0.01 \cdot 10^{-11}$	$1.90 \pm 0.01 \cdot 10^{-11}$	F
ϵ_0	$8.85 \cdot 10^{-12}$	$8.85 \cdot 10^{-12}$	F/m
ϵ	11.9	11.9	a.u.
A_{pad}	51988110.55	51988110.55	μm^2
W	286.66	286.66	μm
V_{FD}	285.04	285	V
N_{eff}	$4.56 \cdot 10^{12}$	$4.56 \cdot 10^{12}$	cm^{-3}
		Average:	$4.56 \cdot 10^{12}\,cm^{-3}$

Table 4.4: Effective Doping Parameters (Method 2)

Parameter	Value	Unit
q	$1.60 \cdot 10^{-19}$	C
ϵ_0	$8.85 \cdot 10^{-12}$	F/m
ϵ	11.9	a.u.
A_{pad}	51988110.55	μm^2
Θ	$9.37 \cdot 10^{19}$	F^{-2}
N_{eff}	$4.68 \cdot 10^{12}$	cm^{-3}

Chapter 5

Charge Transport Studies

For the ATLAS ITk strip, it was seen that some prototype silicon sensors had a lower breakdown voltage in humid conditions ($RH \geq 20\,\%$). It was observed that the avalanche breakdown localizes in the edge region of the sensors. This chapter presents the experimental methods used to study charge transport in the edge region of n-in-p silicon diodes and the results obtained. The IV characteristics as a function of RH were measured using a probe station setup. Charge transport studies in humid conditions were performed using a Top-Transient Current Technique (Top-TCT) setup.

5.1 Current-Voltage Measurements

Current-Voltage (IV) measurements were performed using a probe station PA200 from Cascade Microtech, which is presented in Fig. 5.1 with a close-up image of a diode positioned on the thermal chuck included in Fig. 5.2. The probe station is equipped with a Motic PSM1000 Series microscope [100] for a magnified view of the samples. A consumer astronomy camera with a CMOS sensor from Sony (IMX183CQJ-J) is attached to the microscope for imaging the localized avalanche breakdown. The CMOS sensor has a 15.86 mm diagonal and 20.2 megapixels. Fig. 5.3 presents the Quantum Efficiency (QE) of the sensor, which covers a portion of the Near-infrared (NIR) spectrum such that the photon emission coming from the edge region of the device can be detected. The camera was operated at room temperature as the Signal-to-Noise Ratio (SNR) was sufficiently high to ensure reliable pictures.

The sensors were placed on the thermal chuck, which is a round metal plate that can move in 0.5 µm increments in both x and y directions. The chuck is equipped with holes for vacuum sealing, which allow a secure grip on the bare sensor(s).

The needle holders shown in Fig. 5.1 and Fig. 5.2 are also part of the probe station setup. Each needle holder is equipped with a needle made out of tungsten with a 7 µm wide sharp tip. Once a needle contacts the desired electrode, the holders can be fixed in place, and the bias voltage can be applied.

The RH inside the probe station can be decreased using dry air, or it can be increased using an electronic humidifier such as the Magna 3.0 from Cigar Oasis [101] shown in Fig. 5.1. This humidifier works using expanding water beads, which absorb and retain the liquid, in this case, distilled water. A fan disperses the moisture trapped inside the beads. This method aimed to prevent water droplets from being spread on the surface of diodes. The RH was varied from 10 % to 50 %. A PT1000 and a GY-21 HTU21 sensor were used to read the temperature and RH inside the setup.

To facilitate the control and monitoring of *RH* during IV measurements, the probe station was always closed.

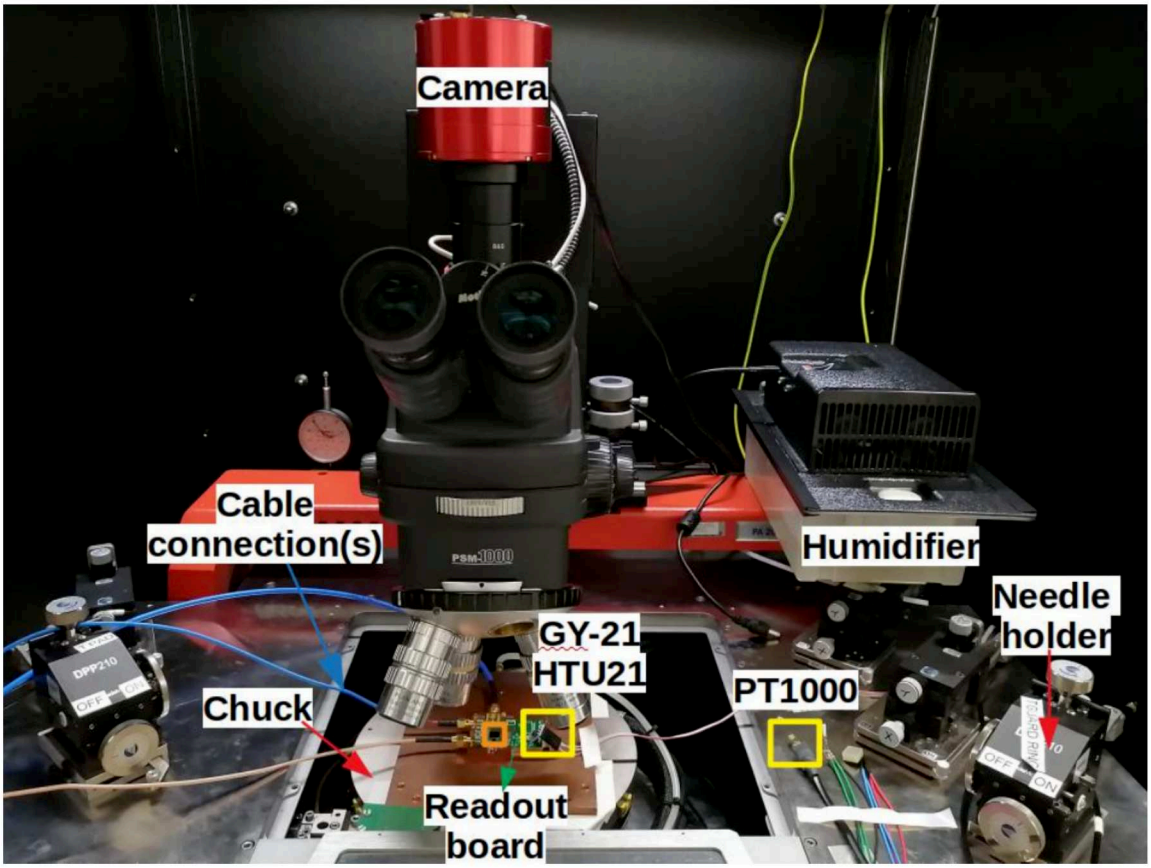

Figure 5.1: Image of the probe station setup from Cascade Microtech at DESY Zeuthen. An astronomy camera is attached on top of a Motic PSM1000 Series microscope. An n-in-p silicon diode (highlighted by an orange square) glued and wirebonded on TCT PCB is placed on top of the thermal chuck. The *RH* is controlled using dry air and a humidifier. Temperature and *RH* are monitored using a GY-21 HTU21 and a PT1000 sensor (indicated by yellow squares).

Preliminary tests of the experimental setups were conducted with 4 mm by 4 mm n-in-p silicon diodes (MD4). Initially, the MD4 diodes were positioned directly on the thermal chuck inside the probe station and secured using vacuum sealing. The needles were used to establish electrical contact. First, the surface was scratched because the MD4 diodes do not have passivation openings. For IV measurements, the bias voltage was applied to the backside metal, which is in electrical contact with the Edge Ring (ER), using the thermal chuck that was connected to a Keithley-2410 source meter [97]. The Guard Ring (GR) and pad metal were each connected using needles to Keithley-6485 amperemeters [102]. It should be noted that the photon emission during avalanche breakdown can be imaged only when the GR leakage current is $\geq 1\,\mu A$. Fig. 5.4 shows an example microscope image of an MD4 diode connected with needles and operated in avalanche breakdown in humid conditions. The photon emission during avalanche breakdown is localized near the pad needle. The needle can alter the localized electric field, triggering the avalanche breakdown in this region. As a consequence, the following investigations were performed with the diodes glued and wirebonded on a readout board.

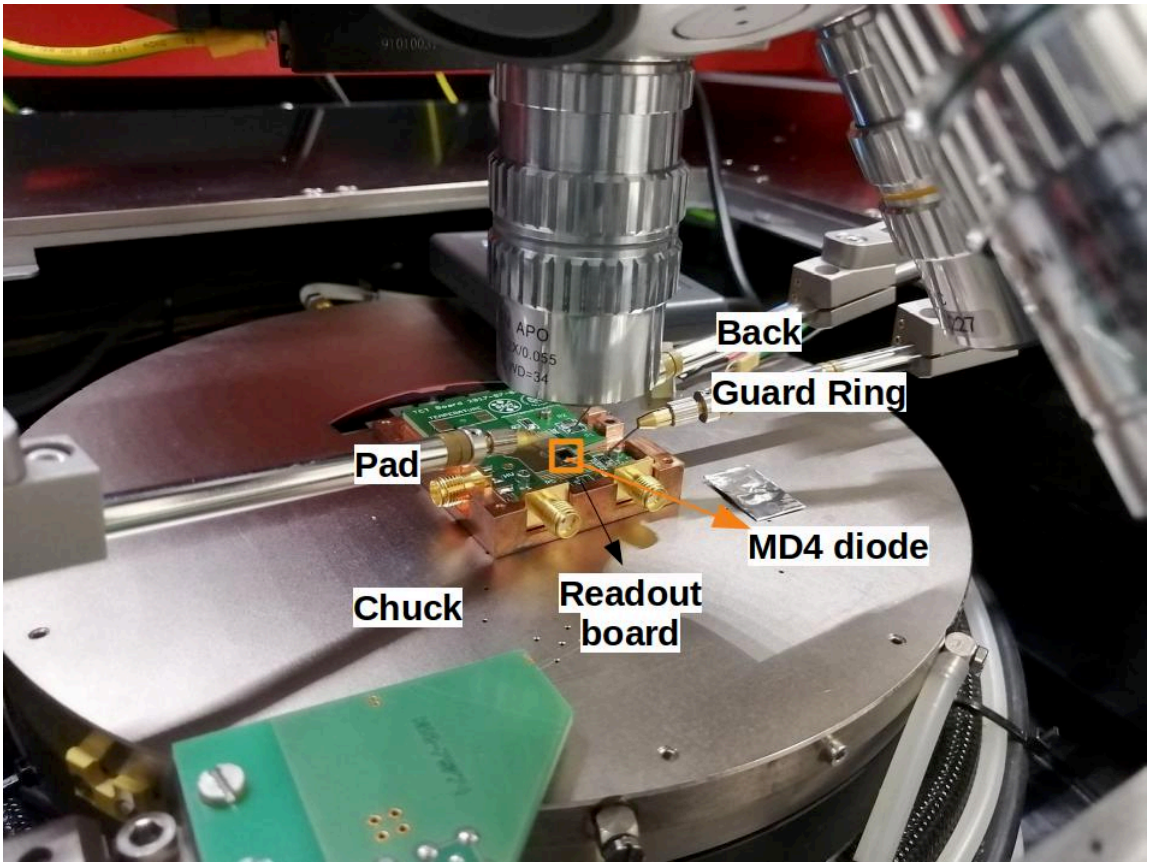

Figure 5.2: Close-up view of a diode glued and wirebonded on a TCT PCB placed on the thermal chuck, which is electrically connected to the measuring devices using the probe station needles.

Fig. 5.1 and Fig. 5.2 show the test structures glued with electrical conductive paste on the readout board (a Printed Circuit Board (PCB) for Top-TCT measurements). The Top-TCT PCB is equipped with a high voltage channel, which enables bias voltage to be applied to the backside metal. The GR and the pad are wirebonded to individual readout channels. In Fig. 5.2, the needles are in contact with the metal lines on the PCB. Since the MD4 diode lacks passivation openings for electrical contacts, wirebonding the GR and the pad to the readout board can still trigger avalanche breakdown. For this reason, diodes with passivation openings were used for further investigations.

Unlike the MD4 diode, the MD8 diode, which was first introduced in section 4.5, has passivation openings on the GR and pad, which can be used to facilitate electrical contact with the probing needles or through wirebonding. Fig. 5.5 shows a digital microscope picture of the corner of an MD8 diode. The GR opening is approx. 20 µm and the pad opening is roughly 150 µm.

The MD8 diode is twice as wide as the MD4, and for this reason, it cannot be captured in one picture, which requires the chuck to be moved. If the chuck is moved during measurements to image the localized avalanche breakdown, the needle, intended to contact the metal lines or the SubMiniature version A (SMA) connectors, might slide across the surface of the diode, potentially causing damage. For this reason, the MD8 diode glued to the Top-TCT PCB was connected using cables to the desired electrical measuring devices. Additionally, the TCT PCB is fixed on a copper plate to ensure mechanical support inside the probe station during the movement of the chuck.

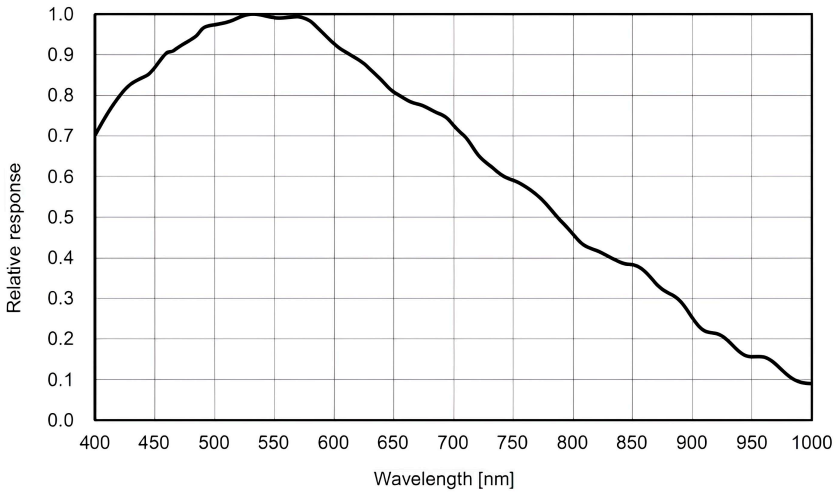

Figure 5.3: Quantum Efficiency (QE) curve of the IMX183CQJ-J CMOS sensor from Sony [87] as a function of the photon wavelength. The plot shows the relative response across the visible and near infrared spectrum.

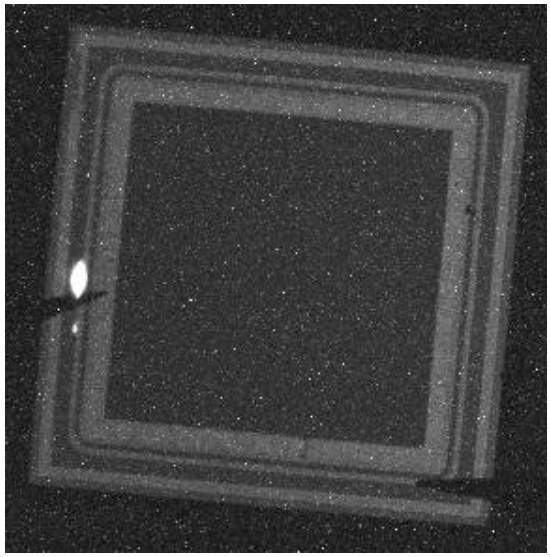

Figure 5.4: Microscope picture of an n-in-p silicon diode operated in avalanche breakdown [103]. Photon emission due to avalanche breakdown is visible as a bright spot. The measurement was performed at $RH \simeq 50\,\%$. The breakdown current between the backside metal and the GR was $\mathcal{O}(1)$ µA.

While it is known that surface defects can influence the localized electric field and trigger the avalanche breakdown, scratched diodes have been investigated to cross-check the maximum bias applied to the device. Fig. 5.6 (b) shows the edge region of an MD8 diode with surface scratches.

Fig. 5.6 (a) shows an IV characteristic of an MD8 diode at $RH = 36\,\%$ and $T = 25^\circ$ C. The bias voltage is displayed as its magnitude. Before data taking, the diode was biased such that the GR leakage current would not reach values higher than 1 µA. The leakage current behaves erratically at bias voltages lower than 20 V, which may be caused by a conductive channel forming between the GR and the pad, effectively short-circuiting

them. This effect has been previously studied for the isolation between the strips for silicon sensors in [104]; however, it can also be applied to the GR and pad metal for the investigated diodes. The conductive channel forms because electrons are attracted at the surface by the positive fixed oxide charges at the interface between silicon and the SiO_2 layer. As the voltage increases, the lateral electric field dissipates the accumulation layer. The diode supported a bias of 990 V until the GR leakage current reached values close to 1 µA. Fig. 5.6 (b) shows a microscope image of an MD8 diode operated in avalanche breakdown at 990 V. The photon emission during avalanche breakdown is visible as a bright spot in the scratched region. From the IV characteristic, it can be seen that the GR leakage current started increasing rapidly at 825 V, while the pad leakage current was 10^4 times lower. The leakage current is higher for the GR than the pad because the electric field near the GR is stronger, which draws more carriers to be collected there.

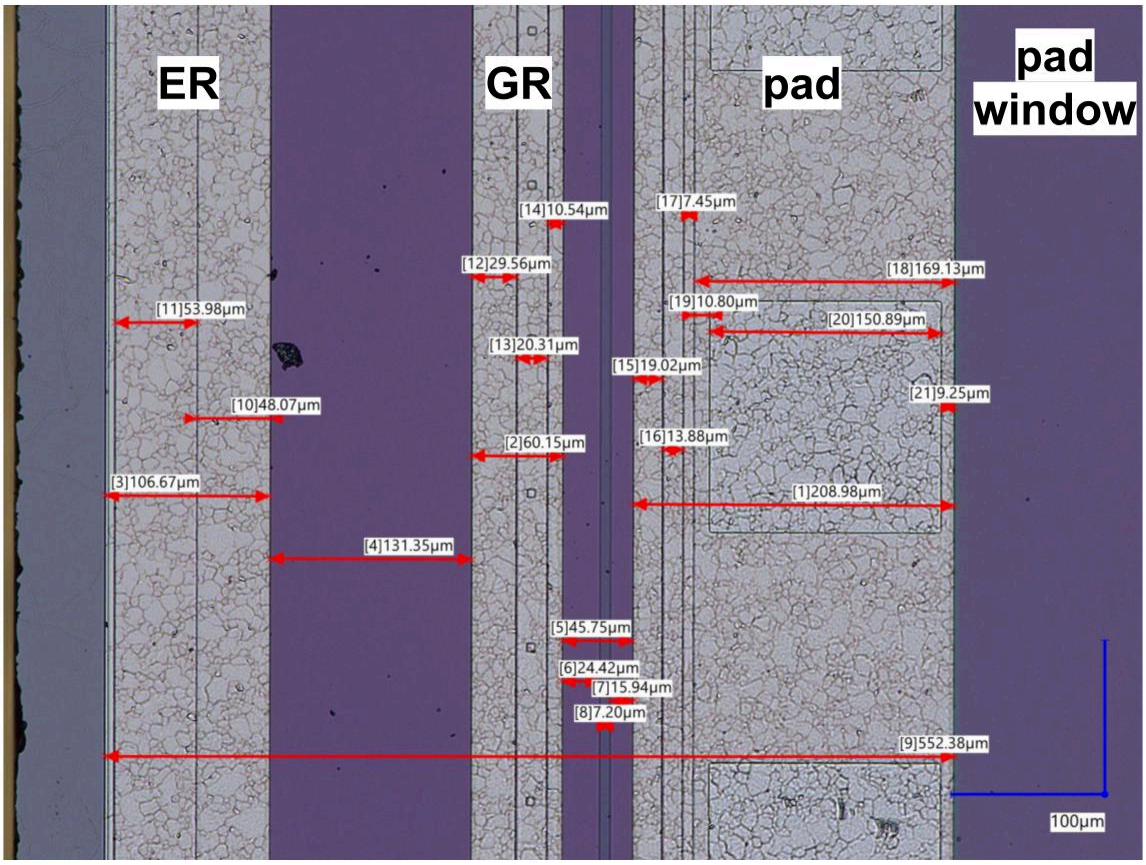

Figure 5.5: Image of a corner of an MD8 diode taken with a Keyence VHX digital microscope. The following parameters have been measured: ER width = 106.67 µm, ER implant = 53.98 µm, ER-GR distance = 131.35 µm, GR width = 60.15 µm, GR implant = 20.31 µm, GR-pad distance = 45.75 µm, pad width = 208.98 µm, and the pad implant = 169.13 µm.

From initial tests performed on MD4 and MD8 diodes, it was observed that the photon emission during avalanche breakdown can be imaged only if the GR leakage current is $\geq$ 1 µA, and therefore, the bias voltage was applied until the GR leakage current reached similar values. It was also observed that a bias voltage higher than 1000 V can electrically damage the samples, because some diodes that broke down at high bias voltages had considerably lower breakdown voltages on subsequent tests. For these devices, dry storage and UV treatments did not improve the breakdown voltage. To

avoid damaging the devices due to high voltage application, the maximum bias voltage applied was 1000 V with a 1 µA limit for the current.

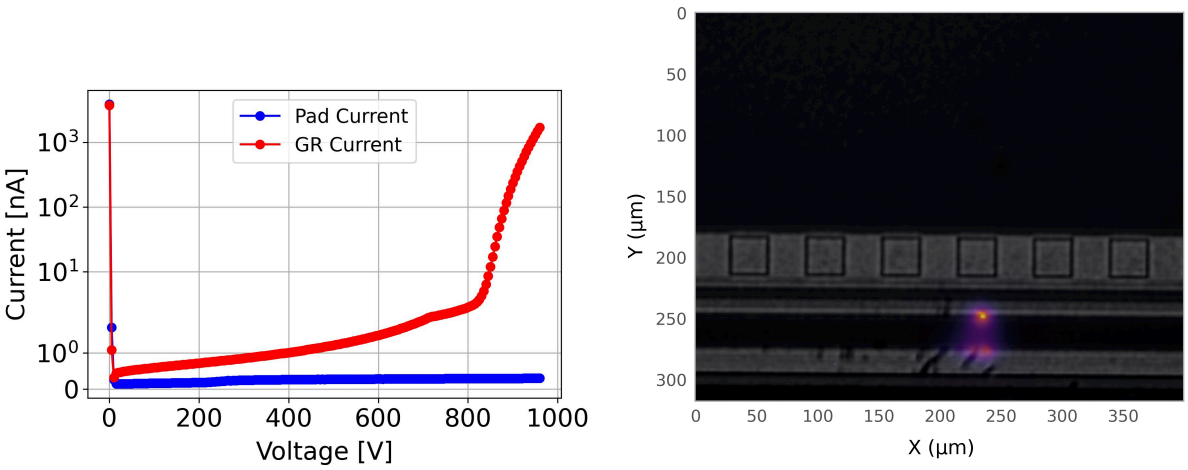

(a) (b)

Figure 5.6: GR and pad leakage currents as a function of bias voltage for an MD8 diode exposed to $RH = 36\,\%$ and $T = 25°\,\mathrm{C}$ (a). Breakdown happens at 825 V. The photon emission during avalanche breakdown was imaged at $V_{bias} = -990\,\mathrm{V}$ (b).

While these initial tests were necessary for evaluating the electrical behavior of the monitoring diodes, the primary focus of this study is understanding how humidity affects the silicon sensors. Multiple MD8 diodes were tested and reverse IV characteristics were taken for several RH values (10 %, 20 %, 30 %, 40 %, 50 %). To avoid hysteresis effects [81], electrical measurements were performed starting from the lowest target RH (10 %). Once the target RH was achieved, bias voltage was applied on the backside metal, −10 V/10 s, while 0 V were applied on the GR and pad. Following the bias voltage and current limit, and investigating only diodes without visible surface defects, the GR leakage current never reached the 1 µA limit during IV measurements. As a consequence, imaging of the photon emission was not possible.

An example of multiple IV characteristics measured for the GR as a function of RH is presented in Fig. 5.7. The GR leakage current is an important parameter because it is the closest electrode to the edge of the diode that can give a quantitative measurement of the electrical breakdown. One IV measurement takes approx. 40 minutes during which the diode is ramped down from 1000 V to 0 V. For all IV characteristics, a slow increase in the GR leakage current can be observed when the bias voltage reaches 700 V. The leakage current continues to increase slowly until the bias voltage reaches 970 V, then it starts increasing rapidly. This follows an exponential trend, which is indicative of a soft electrical breakdown. Considering that the leakage current remains below 1 µA, the MD8 diodes maintained a high breakdown voltage. With respect to RH, it was observed that only for the IV characteristic presented in Fig. 5.7, RH has a monotonous nonlinear impact. It can be seen that the leakage current has similar values for $RH \leq 40\,\%$. However, an increase can be observed when $RH = 50\,\%$, because the humidity effect activates at this value. Previous studies have shown that small structures like mini sensors [93] or diodes show less humidity sensitivity than large ones [90], such as the ATLAS ITk strip sensors. Although for 8 mm by 8 mm silicon n-in-p diodes, it was not possible to observe a clear dependence between the leakage current and RH, they helped to identify a threshold

effect ($RH > 40\,\%$) for which surface conduction starts.

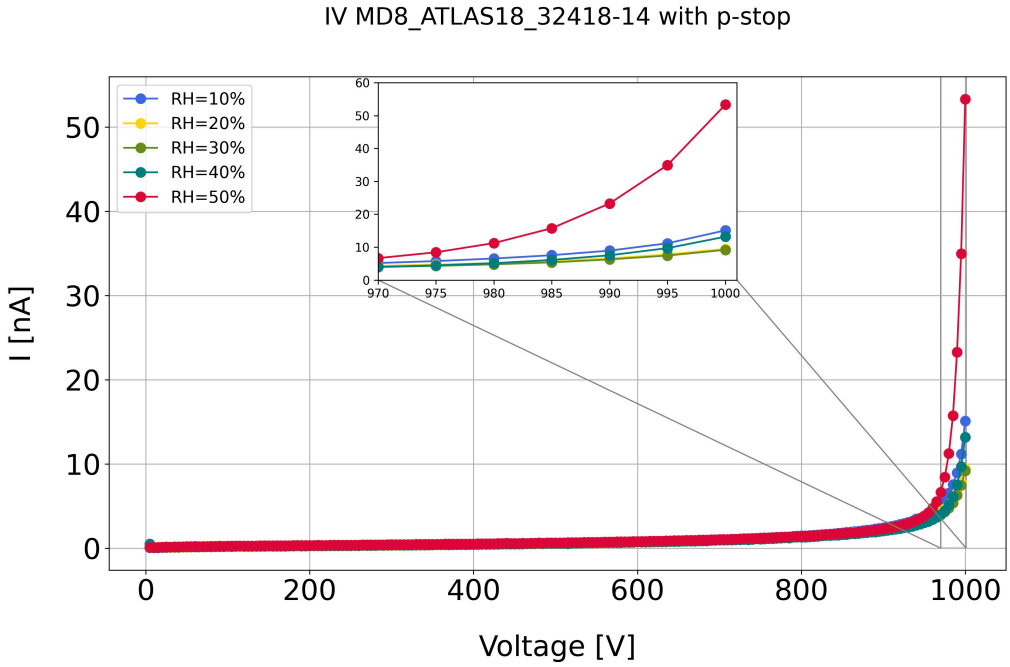

Figure 5.7: GR IV characteristics for an n-in-p 8 mm by 8 mm silicon diode (MD8-32418-14) as a function of RH. IV measurements were first performed at $RH = 10\,\%$, and subsequently the RH was increased $10\,\%$ for each subsequent measurement.

5.2 The Top-TCT Measurements

The following section is based on Ninca, I. S., et al., TCAD simulations of humidity-induced breakdown of silicon sensors, Nuclear Instruments and Methods in Physics Research Section A: Accelerators, Spectrometers, Detectors and Associated Equipment (2024): 169729 [91]. The work presented in the aforementioned article has been shown at the 13th International Hiroshima Symposium on the Development and Application of Semiconductor Tracking Detectors (HSTD13), Vancouver, Canada.

5.2.1 The Top-TCT Setup

The Transient Current Technique (TCT) is an investigation method in which the charge carriers generated by the presence of short laser pulses within a semiconductor drift under the influence of an electric field created by a potential difference, and the resulting transient current is measured. The Top-TCT is a variation of the transient current technique, in which short laser pulses enter the sensor from the top surface.

The Top-TCT was used to study the charge transport in the GR region of silicon diodes by generating localized free charge carriers near the surface with picosecond pulses of red laser light. The induced transient currents were measured as a function of RH to determine how humidity impacts the surface electric field in this region, which can be roughly estimated from the prompt current and charge profile. The prompt current refers to the initial rise of the transient current immediately after charge carrier generation. The charge profile refers to the integral of the transient current over the entire duration of the signal as a function of position.

Fig. 5.8 shows the Top-TCT setup, which is a commercial setup from Particulars, Advanced Measurement Systems [105]. The Top-TCT uses a red laser with a wavelength of 660 nm, which has an absorption length in silicon of approx. 4 µm (see Fig. 5.9). The absorption of photons in a material is described by the Beer-Lambert law [106]:

$$I = I_0 \mathrm{e}^{-\alpha(\lambda)\cdot l}, \tag{5.1}$$

where, I is the transmitted intensity, I_0 is the initial intensity of the photon, α is the absorption coefficient of the material, and l is the absorption length. The Beer-Lambert law shows that absorption is dependent on the properties of the material and the wavelength of the photons.

A photon with a wavelength of 660 nm has an energy of 1.88 eV. Fig. 4.11 shows that for a photon with an energy of 1.88 eV, the dominant interaction mechanism is the photoelectric effect. When a photon with an energy of 1.88 eV reaches the surface of a silicon diode, it may interact with an atomic electron as shown in Fig. 4.12 (a). The entire energy of the photon is absorbed by the atom, causing an electron to be emitted and creating a hole. The laser from Particulars [107] offers short pulses with the pulse width ranging from 350 ps to 4000 ps. The laser intensity corresponds to the creation of electron-hole pairs in silicon of a few Minimum Ionizing Particles (MIP) [108].

The optical system is presented in Fig. 5.10 and consists of an optical fiber, a fiber collimator, a beam expander, a plano-convex lens, and an iris. The generated laser light is transmitted through an optical fiber at an angle that enables total internal reflection to a fiber collimator (Thorlabs F220FC-850 [109]). This aligns the laser light in parallel lines. The collimated beam is then fed to a beam expander (Thorlabs GBE15-B [110]), which increases its diameter 15 times while maintaining the collimation. A plano-convex

lens converges the parallel lines to a focal point to focus the beam on the Device Under Test (DUT). Then the width of the beam can be adjusted using the iris. The optical system is attached to a vertical stage (Standa 8MT175-100 [111]).

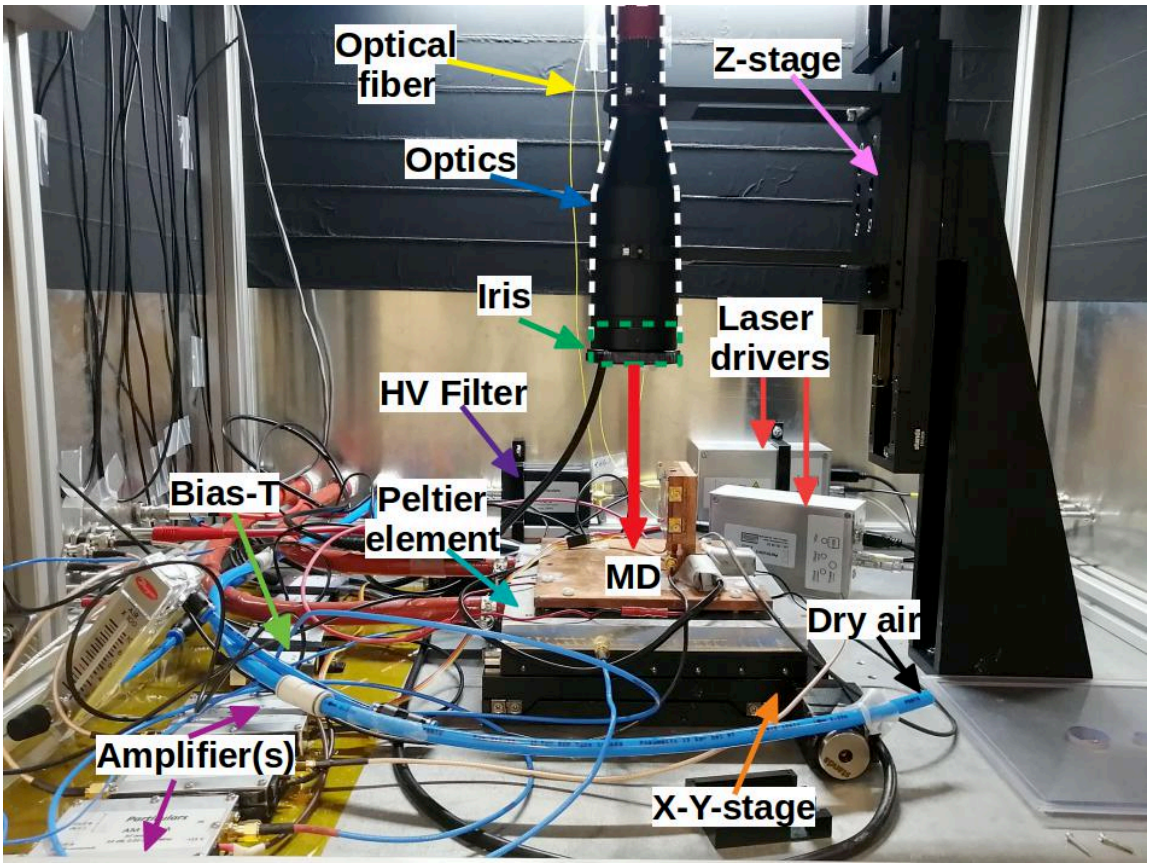

Figure 5.8: Image of the Top-TCT setup at DESY Zeuthen. The optical fiber (yellow cable) is connected to the optical system attached to a vertical stage. Samples are fixed on a copper plate placed on an x-y stage. The temperature can be controlled using a chuck placed underneath the copper plate. The *RH* can be modified using dry air (blue pipe) and desiccants (not visible).

The samples are mounted on the Top-TCT PCB as shown in Fig. 5.11. The diode is then mechanically fixed on a copper plate as shown in Fig. 5.8. Underneath the plate, there is a Peltier element connected to a Huber mini-chiller 300 [112]. Samples can be tested between -20° C and 40° C. A horizontal stage (Standa 8MTF-102LS05 [113]) supports the Peltier element together with the DUT. The range for both the horizontal and the vertical stage is 100 mm with a maximum speed of 10 mm/s, and a resolution of 2.5 µm for a full step. The *RH* inside the Top-TCT setup can be controlled as presented in section 5.1.

The electrical connection for Top-TCT measurements is presented in Fig. 5.12. Bias voltage was applied on the backside of the diode using a Keithley-2410 voltmeter source [97] or a Keithley 6517B electrometer [114]. The Keithley-2410 voltmeter source provides a bias of ± 1000 V with a digital resolution of -50 mV. The Keithley 6517B electrometer measures currents between 1 µA up to 1 A with a digital resolution of 10 pA.

A High Voltage (HV) filter (Particulars F-01 A [115]) is connected between the DUT and the voltage source to filter out high-frequency distortions. The DUT is also connected to a Bias-T (Particulars BT-01 [116]), which is a device that enables bias voltage

application and the measurement of the transient currents at the same time. The GR and pad are connected to ground.

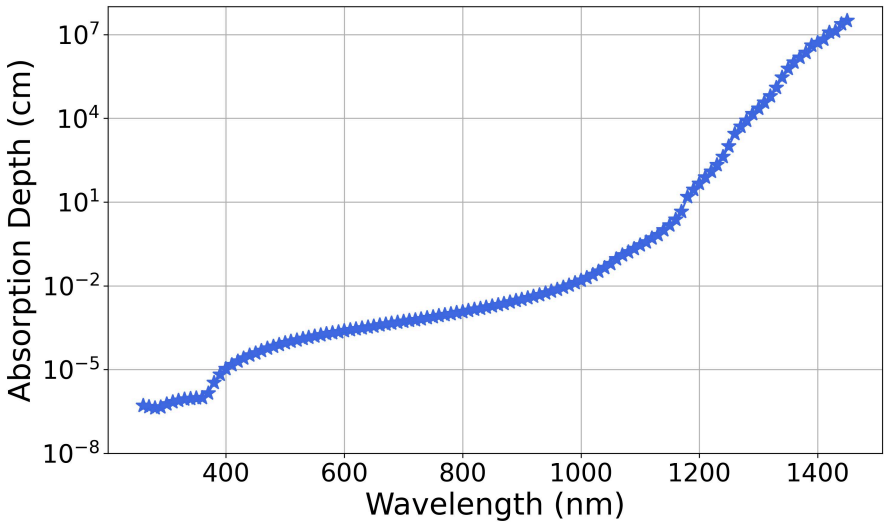

Figure 5.9: Representation of the absorption depth in silicon as a function of the photon wavelength at 300 K. The data was reconstructed from [117].

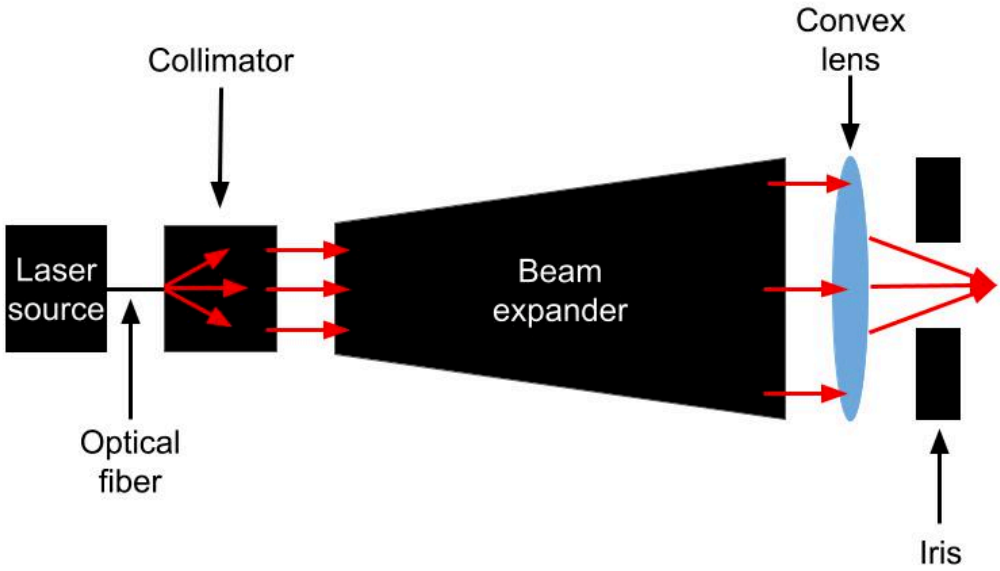

Figure 5.10: Sketch of the optical system employed in the Top-TCT setup. A collimator is used to align the laser light in parallel lines. A beam expander increases the diameter of the parallel beam. A convex lens converges the parallel lines through a focal point to focus the beam through the iris and then onto the sensor.

A Rohde and Schwarz RTO1024 oscilloscope [118] with a sampling rate of 10 Gsample/s and a bandwidth of 2 GHz was used to acquire the transient currents. The signal is pre-amplified using AM-02 amplifiers [119], which are connected between the readout channels and the oscilloscope. The maximum amplification is 53 dB at the maximum operating voltage of the amplifier (13 V). The Top-TCT requires the laser pulse duration to

be shorter than the drift time of the carriers to measure the transient currents accurately. The acquisition time is mainly restricted by the DUT's capacitance and the operational bandwidths of the oscilloscope, amplifiers, and Bias-T.

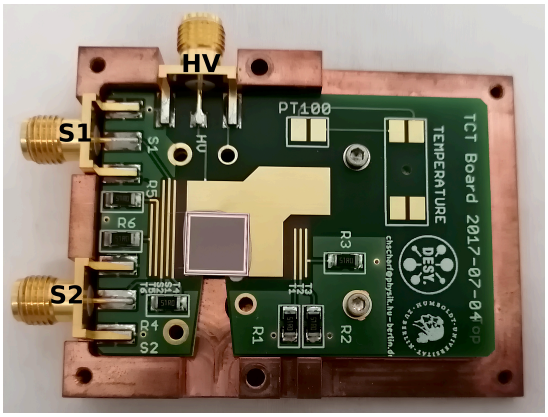

Figure 5.11: Picture of an n-in-p silicon diode glued on the Top-TCT PCB, and mechanically fixed inside a copper support case. The backside of the diode is directly connected to the HV channel. The GR is wirebonded to the S1 channel, and the pad is wirebonded to the S2 channel.

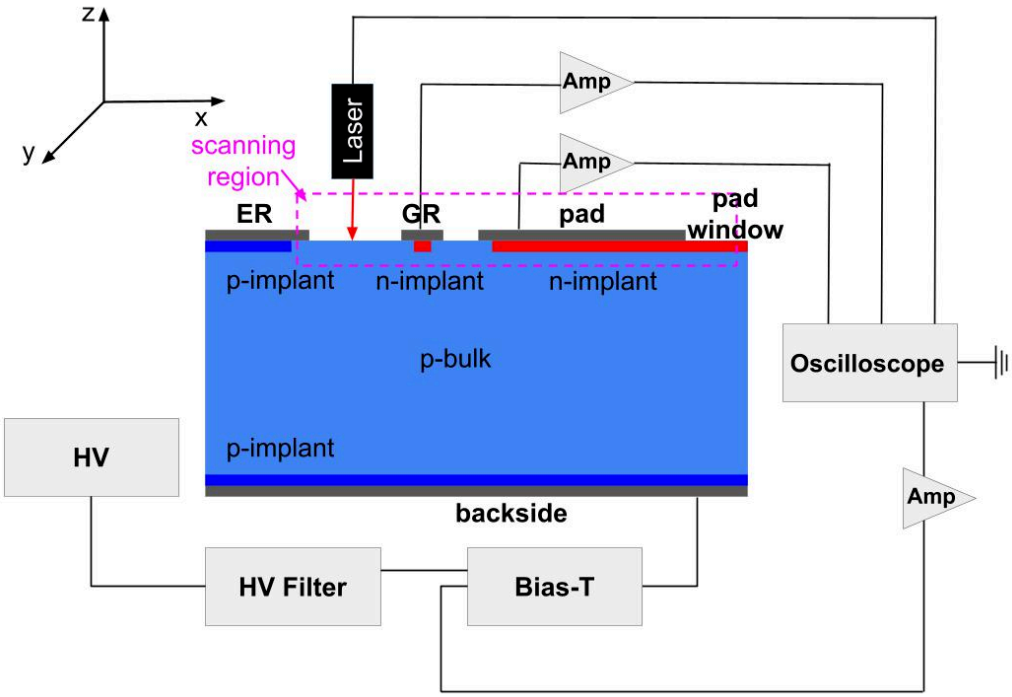

Figure 5.12: Sketch of the electrical setup for the Top-TCT measurements. A red laser is moved along the edge of the silicon diode, generating electron-hole pairs at the surface. The bias voltage is applied on the backside of the diode, which is electrically connected to the ER through the dicing edge. A Bias-T enables the application of a bias voltage on the backside and the collection of current. The GR and pad are connected to ground. An oscilloscope is used to monitor and measure the transient currents.

The driver that controls the current passage to the laser diode correlates laser power

with pulse duration. As represented in Fig. 5.13, the pulse duration is inversely proportional to the current applied to the laser diode. For a high current, the pulse width reduces and vice versa. The beam width gives the scanning resolution for the Top-TCT measurements, which should be as small as possible to detect smaller changes or features in the data collected. The threshold setting is controlled using the Digital-to-Analog Converter (DAC), which is expressed in units of mV. The maximum threshold corresponds to a DAC value of 3300 mV when no photons should pass through the optical system. From the laser control software [120], the frequency and the pulse width of the laser can be adjusted.

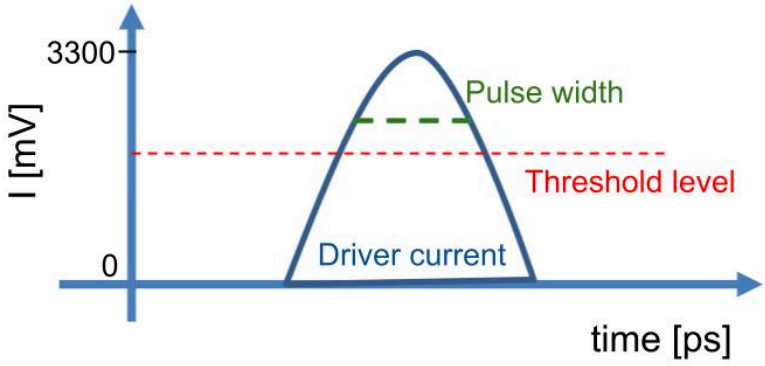

Figure 5.13: Schematic diagram illustrating the laser driver current [121]. The pulse width and power decrease with an increase in the threshold level. At the maximum threshold, 3300 mV, no photons should pass through the optical system.

5.2.2 Determining the Laser Focus

The laser beam intensity profile can be simplified to a Gaussian distribution as shown in Fig. 5.14 with the largest photon concentration near the center of the beam. From the paraxial Helmholtz equation [122], the intensity of the laser beam can be obtained as a function of the position along the propagation direction z and the radial coordinate r:

$$I(r,z) = I_0 \left(\frac{w_0}{w(z)}\right)^2 \exp\left(-\frac{2r^2}{w(z)^2}\right), \tag{5.2}$$

where I_0 is the intensity at the center of the beam; w_0 is the beam waist; $w(z)$ is the beam radius at which the intensity drops to $1/e^2$ of the peak value, and r is the radial distance from the center of the beam.

The radius of the beam at any position on the propagation direction can be obtained as a function of the beam waist [122]:

$$w(z) = w_0\sqrt{1+\left(\frac{z-z_0}{z_R}\right)^2}, \qquad \text{with} \qquad w_0 = \sqrt{\frac{z_R\lambda}{\pi n}}, \tag{5.3}$$

where z_0 is the location of the beam waist, z_R is the Rayleigh length, λ is the wavelength, and n is the refractive index. The Rayleigh length defines the distance starting from the beam waist to the point on the propagating direction where the beam width is $\sqrt{2}$ of the

beam waist: $w(z_0 \pm z_R) = \sqrt{2}w_0$. An expression for the Rayleigh length can be derived from equation 5.3:

$$z_R = \frac{\pi n w_0^2}{\lambda}, \tag{5.4}$$

where it can be seen that for a known refractive index and wavelength, the Rayleigh length depends only on the beam waist. The double of the Rayleigh length is denoted by b.

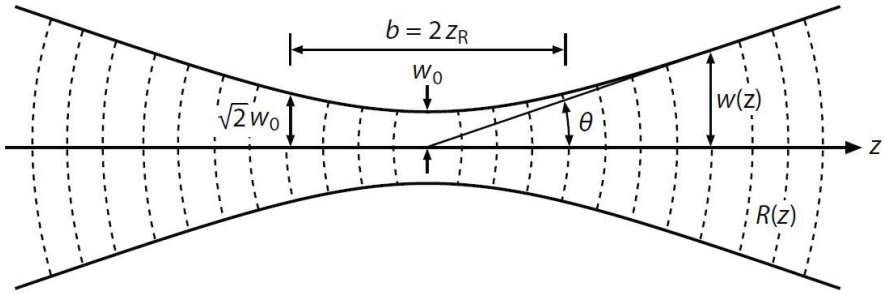

Figure 5.14: Schematic illustration of a Gaussian beam propagation along the z-direction [122]. The radius $w(z)$ and beam wavefront curvature $R(z)$ change along z. The width of the beam becomes $\sqrt{2}$ times greater than the waist of the beam at a distance from the waist of the beam equal to the Rayleigh distance z_R.

The width of the beam can be expressed in terms of the full width at half maximum (FWHM) using the following relation:

$$w(z) = \frac{\mathrm{FWHM(z)}}{\sqrt{2\ln 2}}. \tag{5.5}$$

At large distances from the beam center, larger than the Rayleigh length $z \gg z_R$, equation 5.3 simplifies to:

$$w(z) = w_0 \frac{z}{z_R}. \tag{5.6}$$

If $z \gg z_R$, the beam width expands linearly with z.

The expansion of the propagating beam is described by the divergence angle θ [122]:

$$\theta = \lim_{z \gg z_R} \frac{w(z)}{z} = \frac{\lambda}{\pi w_0}. \tag{5.7}$$

For the experiment at hand, the laser beam propagates in a silicon diode. Considering this is a solid material when expressing the intensity profile of the beam, light absorption needs to be taken into account as follows:

$$I'(r,z) = I_0 \left(\frac{w_0}{w(z)}\right)^2 \exp\left(-\frac{2r^2}{w(z)^2}\right) \exp\big(-\alpha(\lambda) n z\big), \tag{5.8}$$

where n is the refractive index of the medium and $\alpha(\lambda)$ is the absorption coefficient.

The laser beam waist should be as small as possible to perform precise, position-dependent measurements of the transient currents using the Top-TCT. This can be achieved by doing a focus scan following the steps described in [123]. The first step

is to set a scanning range in the x- or y-direction and z-direction. The Top-TCT setup is equipped with a vertical and a horizontal stage. The laser is attached to the vertical stage and can be moved up and down along the z-direction. The samples are placed on a copper plate and fixed on the horizontal stage, which can move in the x- and y-directions. For the following measurements, the x-direction was chosen as the horizontal scanning axis, while the y-axis was kept constant. The scanning range in the x-direction includes points on the metal, where no signal is expected, and points on the active area. The z-range contains points where the beam width is maximum and points where it is minimum, as illustrated in Fig. 5.15. In practice, a focus scan can be started using the Data Acquisition (DAQ) software [124] provided by Particulars, which saves the transient currents for each point.

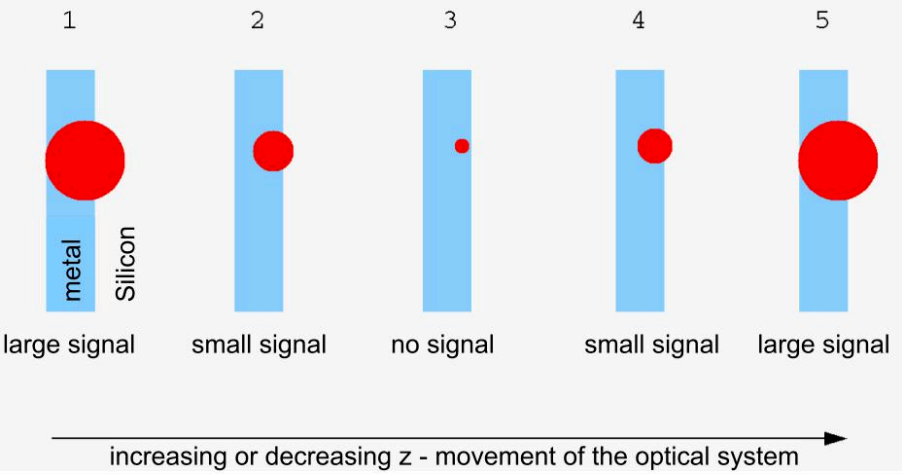

Figure 5.15: Schematic sketch of how the laser beam width changes with the distance of the optical system [125].

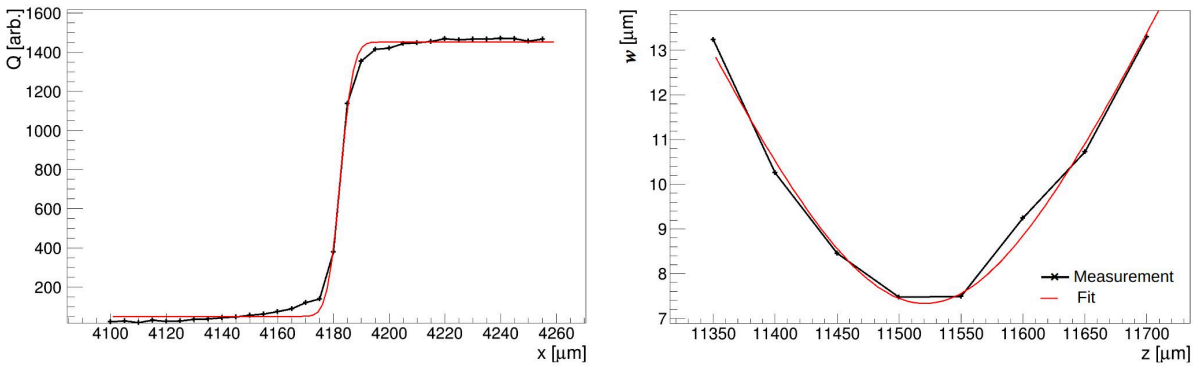

(a) (b)

Figure 5.16: Representation of the maximum collected charge along the abscissa at $z = 15500\,\mu\text{m}$ (a) and the width of the beam as a function of the z-position (b). The position of the focused laser is found at $z = 11520 \pm 2.45\,\mu\text{m}$.

Fig. 5.16 shows an example of the collected charge along the abscissa for $z = 15500\,\mu\text{m}$ (a) and the beam width as a function of the z-position (b). The one-dimensional charge distribution collected along the abscissa reveals three distinct regions. From $4100\,\mu\text{m}$ to $4175\,\mu\text{m}$, the collected charge is ≤ 138 a.u. because the majority of the laser beam

reached only the metal. Between 4195 µm and 4260 µm a rapid increase can be observed in the charge collected from 138 a.u. to 1446 a.u., which shows that the beam width of the laser progressively overlapped with the active area. The entire beam width reached the active area starting from $x = 4205$ µm. The laser beam waist dependence on the laser position and the total induced charge Q is modeled by an S-shaped curve, as shown in Fig. 5.16 (a):

$$Q(x) = \frac{Q_{max}}{2}\left(1 + \mathrm{erf}\left(\frac{\sqrt{2}(x - x_0)}{\omega(z)}\right)\right), \tag{5.9}$$

where Q_{max} is the maximum induced charge in the active region, x is the position along the scanning axis, and x_0 is the position of the metal electrode. Fitting the data along the x-axis corresponding to each laser position on the z-axis, a dependence of the laser beam waist on the z-position can be obtained as presented in Fig. 5.16 (b).

To obtain the z-coordinate where the beam width is the smallest, equation 5.3 is used to fit the data in Fig. 5.16 (b). The value that gives the focused laser is found at $z = 11520 \pm 2.45$ µm and the width of the laser beam ($\omega(z)$) is 7.33 µm $\pm$ 0.16 µm.

5.2.3 Laser Intensity Optimization

The laser intensity was optimized to ensure the laser beam does not shield the electric field, distorting the charge profile. Preliminary tests were conducted using a DAC value of 2550 mV. This was considered to correspond to 100 % of the laser intensity. To investigate how the laser intensity influences the shape of the charge profile, it was first decreased to 68 %, 50 %, and 28 % of the initial level. Then it was increased to 243 % and 262 % above the initial intensity used.

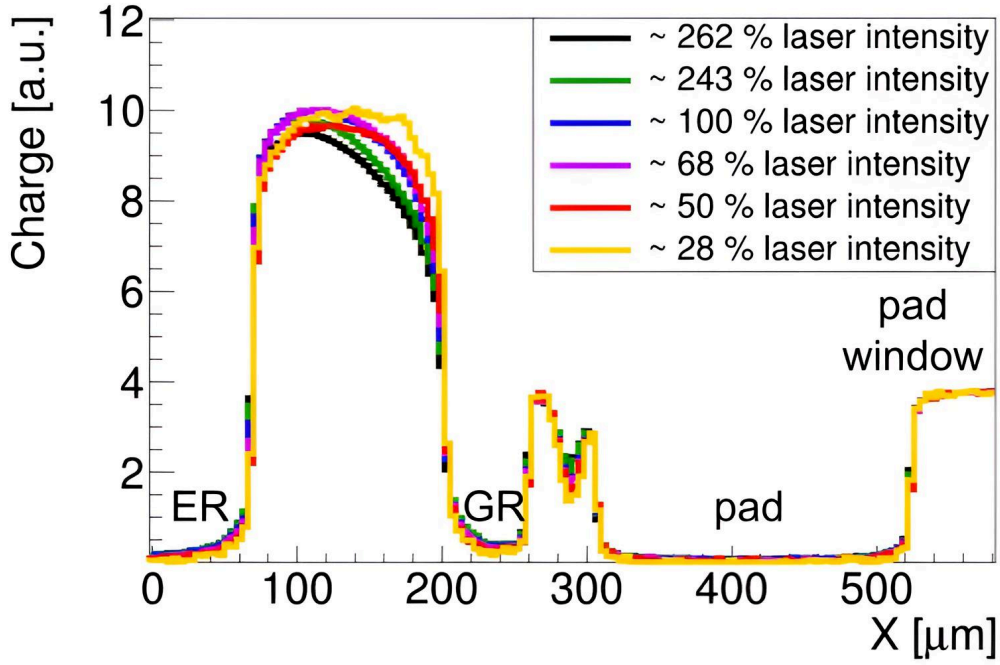

Figure 5.17: Normalized collected charge between the ER and pad window at $RH < 10$ %, $V_{bias} = -1000$ V and different laser intensities. The collected charge was normalized to the charge collected in the pad window, which starts at $x \simeq 520$ µm, for each laser intensity.

Fig. 5.17 shows the charge profiles measured with different laser intensities for an 8 mm by 8 mm n-in-p silicon diode with a p-stop (MD8). The bias voltage was applied to the backside metal, which is connected via the dicing edge to the ER, $-10\,\mathrm{V}/10\,\mathrm{s}$. The GR and pad metal were connected at ground. During the measurements, the bias voltage remained constant at $-1000\,\mathrm{V}$. The RH inside the Top-TCT setup was $< 10\,\%$ throughout the scanning period. The laser was scanned across the diode starting from the ER to the pad window at constant y ($y = 5820\,\mu\mathrm{m}$). The transient currents were recorded on the backside metal of the diode. The charge profiles were obtained by integrating the transient currents for the whole duration of the signal. The data was normalized with respect to the charge collected in the pad window to facilitate a comparison between the shapes of the charge profiles for different values of the laser intensity.

The charge profile is close to zero in the regions with metal: the ER (from $x = 0\,\mu\mathrm{m}$ to $x \simeq 73\,\mu\mathrm{m}$), the GR (from $x \simeq 203\,\mu\mathrm{m}$ to $x \simeq 263\,\mu\mathrm{m}$) and the pad metal (starting from $x \simeq 310\,\mu\mathrm{m}$ to $x \simeq 520\,\mu\mathrm{m}$) because the generated photons from the red laser are mostly reflected by the aluminum. The charge is non-zero in the non-metalized regions because the red laser is absorbed in silicon and generates electron-hole pairs inside the material.

The charge profile is expected to have an approximately rectangular shape in the ER-GR region and in the pad window, because the electric field in the central part of the depletion region of an over-biased p-n junction can be approximately uniform. The charge profile between the GR and pad exhibits a non-rectangular shape, which may be an effect of the p-stop in this region.

The charge profile between the GR and the pad metal (from $263\,\mu\mathrm{m}$ and $310\,\mu\mathrm{m}$), and in the pad window, remains constant across all laser intensity changes. This is because the electric field here does not have values high enough to accelerate the laser-induced carriers such that they gain enough energy to create impact ionization.

In contrast, the charge profile in the ER-GR region changes with the laser intensity. It can be observed in Fig. 5.17 that for laser intensities higher than 68 %, the charge profile between the ER and GR region presents a shark fin shape [126]. This is a consequence of the laser shielding the electric field near the GR. If the laser intensity is reduced to 28 %, the charge profile has an approximately rectangular shape. For further measurements, the laser intensity was therefore reduced to 28 %.

To perform a comparison with high-energy applications, the MIP equivalent to the laser-induced signal was determined. For the calculation, the charge collected in the pad window was considered, as the electric field in the pad window is not high enough to facilitate charge generation from impact ionization. The number of MIPs [127] was calculated using the following formula:

$$MIPs = \frac{Q_{pad} \cdot 10^{-3}}{f_s \cdot Z \cdot \frac{V_{out}}{V_{in}} \cdot Q_t \cdot W}, \qquad \text{where} \tag{5.10}$$

- Q_{pad} is the charge collected in the pad window. The charge is obtained by integrating the transient currents for the whole duration of the signal ($\simeq 15\,\mathrm{ns}$). Given that the transient currents were collected in units of mV and not V, the charge was multiplied by 10^{-3} to convert from mV to V.

- f_s denotes the sampling rate of the oscilloscope, which is 10 Gsamples/s [118].

- Z stands for the oscilloscope impedance, which is $50\,\Omega$ [118].

- $\frac{V_{out}}{V_{in}}$ is the amplification factor of the amplifier. The gain of the amplifier is 53 dB [119]. Using the formula for gain:

$$Gain(\text{dB}) = 20\log 10\frac{V_{out}}{V_{in}}, \tag{5.11}$$

the amplification factor is obtained as 446 a.u.

- Q_t is the the total charge deposited by 1 MIP in 1 µm thick silicon ($73{\cdot}1.602{\cdot}10^{-19}$ C [128]).

- W is the active thickness of the diode, which was calculated to be approximately 287 µm.

The conversion between the number of MIPs generated by the laser in silicon and the electron-hole pairs is based on the ionization energy: $I_0 = 3.62\,\text{eV}$ [45] and the energy loss of a MIP [129]:

$$\frac{\text{d}E}{\text{d}x} = 3.87\,\frac{\text{MeV}}{\text{cm}}. \tag{5.12}$$

The number of electron-hole pairs produced per µm can be derived using the formula:

$$N_{eh} = \frac{\frac{\text{d}E}{\text{d}x}\cdot W}{I_0} = \frac{3.87\cdot 10^6\cdot 0.0287}{3.62} = 30682. \tag{5.13}$$

Table 5.1 records the charge collected in the pad area in a.u., the calculated MIP equivalent together with the e-h pairs produced for each laser intensity.

Table 5.1: Injected charge as a function of laser intensity.

Intensity (%)	Q_{pad} (a.u.)	MIPs	e-h pairs
262 % I	1707	2.31	$7.09\cdot 10^4$
243 % I	1520.6	2.06	$6.32\cdot 10^4$
100 % I	624.3	0.85	$2.59\cdot 10^4$
68 % I	420.2	0.57	$1.75\cdot 10^4$
50 % I	322.5	0.44	$1.34\cdot 10^4$
28 % I	180.5	0.24	$7.50\cdot 10^3$

5.2.4 Measurement Preparation and Data Analysis

Silicon n-in-p diodes from the ATLAS17LS and the ATLAS18LS wafer were investigated in humid conditions using the Top-TCT. Before starting the Top-TCT scans, IV characteristics as a function of RH were measured. Then, each diode was moved to the Top-TCT setup, and it was electrically connected, as shown in Fig. 5.12. The setup was closed, and the pressurized air was used to dry the TCT box to the desired RH. Once the target RH was reached, a minimum of 10 minutes was allowed for the RH to stabilize at the target value. During Top-TCT scans RH variations of $\pm\,3$ % were encountered. Only the edge region of the diodes, starting from the ER and moving toward the pad window, was investigated. For 1-dimensional scans, a scanning range was set on the x-axis, while the y- and z-axis were fixed. For 2-dimensional scans, a scanning range was set for both the x- and y-axis, while the z-axis was fixed.

Similarly to IV measurements, the bias voltage was applied on the backside metal, 10 V/10 s, while the GR and pad were connected to ground. When the full bias voltage was reached, the Top-TCT measurement was started. The same scanning procedure was followed for each RH value (10 %, 20 %, 30 %, 40 %, 50 %). The measurements were performed starting from the lowest RH value to avoid hysteresis effects, which can occur when the sensor is biased at high humidity and the humidity is subsequently lowered, freezing a possible charge at the surface [81]. Hysteresis defines the phenomenon in which the electrical response of a sensor depends on the previous testing conditions, e.g., biasing, environmental conditions, etc. When a sensor is electrically tested in humid conditions, ions can accumulate at the surface. If the relative humidity is subsequently lowered and the sensor is tested again, the redistribution of these ions would take longer than the measurement time. Consequently, when the humidity is changed from high values to lower, the observed characteristics do not retrace the same path; instead, they exhibit hysteresis.

The current induced by the drift of a charge carrier hitting the read-out electrode of the diode can be expressed using the Shockley-Ramo formula [130], [131]:

$$I_{e,h} = e \cdot \mu_{e,h}(\vec{\mathcal{E}}) \cdot \vec{\mathcal{E}} \cdot \vec{\mathcal{E}_w} \tag{5.14}$$

where e is the elementary charge, $\mu_{e,h}$ is the mobility, $\vec{\mathcal{E}}$ is the electric field and $\vec{\mathcal{E}_w}$ is the weighting field. The weighting field is the electric field when only 1 V is applied on the electrode of interest, while any other electrodes are at 0 V. Equation 5.14 is representative for the current induced by a single charge carrier.

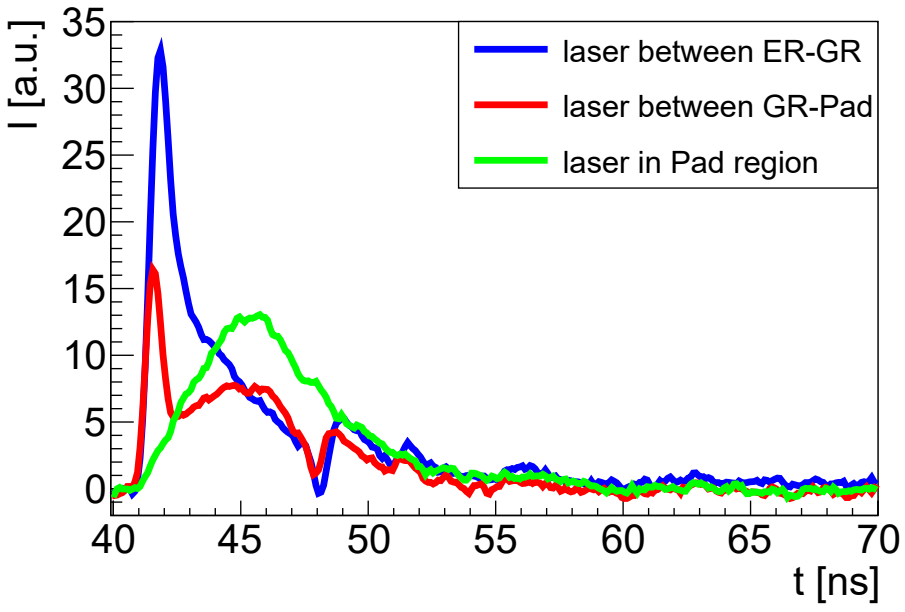

Figure 5.18: Example of measured transient currents at the backside metal for three different laser positions on an MD8 diode: between ER and GR (blue curve), between the GR and pad (red curve), and in the pad window (green curve).

The DAQ software records the average of multiple waveforms for each point along the scanning region. In this case, the waveforms are the transient current variation(s) over time measured on the backside electrode. On average, a scan along the x-direction has

≥ 100 registered waveforms. Fig. 5.18 shows only one waveform for each sensitive region (between the ER and GR, between the GR and the pad metal, and inside the active window). On the abscissa, the duration of the signal (t) is represented in ns, while on the ordinate, the amplitude of the signal is represented in a.u. The steep rise of the signal mainly corresponds to the fast collection of electrons, while the descent of the signal corresponds to some of the holes being collected on the backside metal. This is because the holes have a lower mobility than electrons, and they need to travel across the diode towards the backside. Moving the laser from the ER towards the pad region seems to lower the amplitude of the signal because, in the pad window, there is a 2.2 µm implant and the electric field within the implant region is close to zero.

The induced charge can be obtained by integrating the transient current for the total duration of the signal [132]:

$$Q = \int_{t_i}^{t_f} I dt, \tag{5.15}$$

where Q is the induced charge, I is the transient current, t_i is the time when the signal starts rising, and t_f is the time when the signal goes to zero a.u. The charge profiles presented in the following section were obtained by integrating the transient currents for $\simeq$ 15 ns to ensure that all the charge collected contributes to the signal.

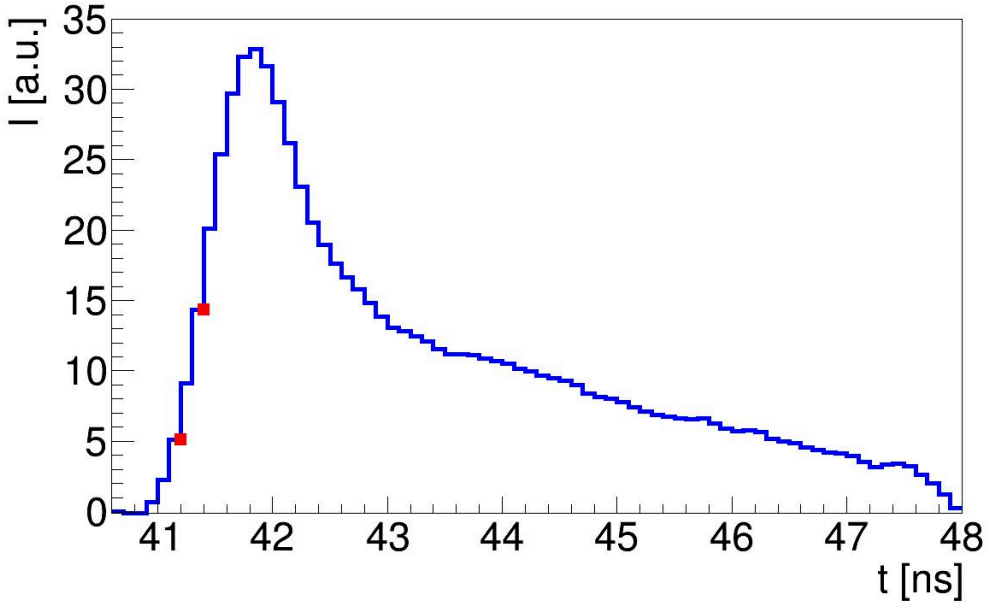

Figure 5.19: An example of a single transient current showing the integration window for the prompt current derivation with two red markers, one at 41.2 ns and the second at 41.4 ns.

The prompt current technique [132] was used to gain insight into the electric field. The prompt current technique focuses on the analysis of the initial rise of the transient current produced by the drift of charge carriers in the electric field. The analysis of the initial rise of the transient current ensures that the recombination or trapping of charge carriers does not affect the signal. If charges are lost due to recombination or trapping, the signal may have a different signature, e.g., lower amplitude, different shape, or delayed

rise time, which can lead to a different interpretation of the electric field. In the prompt current technique, the prompt current refers to the initial rise of the transient current. In practice, the prompt current is obtained by integrating the measured transient current for a short time (200 ps) shortly after the carrier generation at the surface of the diode [132]. Although it is called a current, it is formally a prompt charge. The rising edge of the transient current is proportional to the electron and hole drift velocity, as shown by the Ramo-Shockley theorem:

$$I_i(x,t) = \sum_{i=1}^{N} \sum_{j=1}^{n} e \left[\vec{v}_e\big(x_i(t_j)\big) + \vec{v}_h\big(x_i(t_j)\big) \right] \cdot \vec{\mathcal{E}}_w(x), \tag{5.16}$$

where I_i is the current generated by electron-hole pairs drift, also known as the transient current, e is the elementary charge, $\vec{v}_{e,h}(x(t))$ is the velocity of carriers, and $\vec{\mathcal{E}}_w(x)$ is the weighting field. The term $n = \frac{t_2 - t_1}{\delta t}$ denotes the total number of time steps. The term N consists of the total number of generated carriers. Considering that the integration window is small enough, the carriers travel a small distance inside the sensor, ensuring that the variations in the electric field and weighting field are small enough. Therefore, equation 5.16 can be simplified to:

$$I_i(x,t) = e \cdot N(x) \cdot \left[\vec{v}_e\big(x_i(t_j)\big) + \vec{v}_h\big(x_i(t_j)\big) \right] \cdot \vec{\mathcal{E}}_w(x). \tag{5.17}$$

Fig. 5.19 shows an example of a transient current. The red marker at 41.2 ns was taken as t_1, while the marker at 41.4 ns was taken as t_2. All prompt currents were obtained using the same integration window of 200 ps.

5.3 Discussion of Charge Profiles and Prompt Currents

5.3.1 XY Scan

Fig. 5.20 shows an example of the charge collected in the corner of a 4 mm by 4 mm n-in-p silicon diode (MD4) without a p-stop. A negative bias voltage of $-440\,\mathrm{V}$ was applied on the backside electrode while the GR and pad were at ground. The Top-TCT scan was performed in humid conditions ($RH > 20\,\%$) and at room temperature. The color map illustrates the normalized charge that has been collected. Dark blue represents areas where no charges are collected because the aluminum metal reflects the laser, while other structures allow the laser to penetrate the silicon.

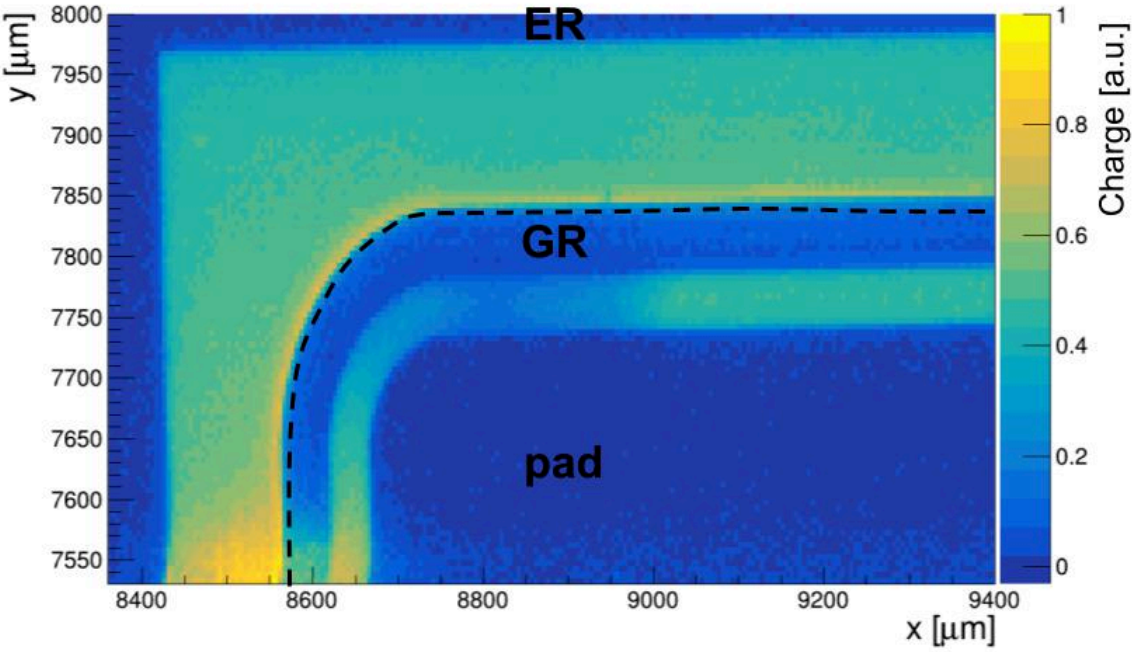

Figure 5.20: Example of a 2D charge distribution of a 4 mm by 4 mm n-in-p silicon diode without a p-stop, fully depleted ($V_{bias} = -440\,\mathrm{V}$). The step size of the Top-TCT scan is $5\,\mu\mathrm{m}$ in both x- and y-directions. The measurement was performed at room temperature and $RH > 20\,\%$. The color map represents the normalized charge in a.u.

It can be seen that in the ER-GR region, the charge is greater near the GR (along the black dotted line). This is indicative of a high electric field near the GR, which coincides with the region where photon emission during avalanche breakdown was captured in Fig. 5.4 and 5.6 (b). Given that the ER is at the same potential as the backside metal because it is electrically connected via the dicing edge, and the GR is at ground, an electric field proportional to the bias voltage is expected in this region.

The charge measured between $x = 8450 - 8720\,\mu\mathrm{m}$ and $y = 7530 - 7580\,\mu\mathrm{m}$ is significantly higher than in the neighboring regions. Considering that the diode was tested at $RH > 20\,\%$, the elevated charge collected in this region could be caused by charge multiplication between the ER and GR.

5.3.2 X-Scan: Variation of Charge with Relative Humidity (RH)

The laser was scanned along the x-direction of MD8 diodes with the y-direction held constant ($y = 5050\,\mu m$) at constant bias voltage in dry and humid conditions to study the dependence of the charge profile and prompt current on the relative humidity. Fig. 5.21 shows an example of the charge profiles, while Fig. 5.22 shows an example of the prompt currents as a function of RH. The tested diode (MD8-32415-13) was stored at ambient laboratory conditions before conducting investigations with the TCT laser. The biasing scheme followed the one shown in Fig. 5.12. The bias voltage was applied $-10\,V/10\,s$ until reaching $-900\,V$. The bias voltage remained constant throughout all Top-TCT scans and RH changes. This prevents changes in the electric field between the ER-GR region caused by voltage variations, such as ramping during RH changes. The laser intensity was set to 28 % according to section 5.2.3 to ensure that the laser does not shield the electric field near the GR. The Top-TCT measurements started from the lowest target RH (10 %) in order not to be affected by hysteresis [82], which is investigated in section 5.3.4.

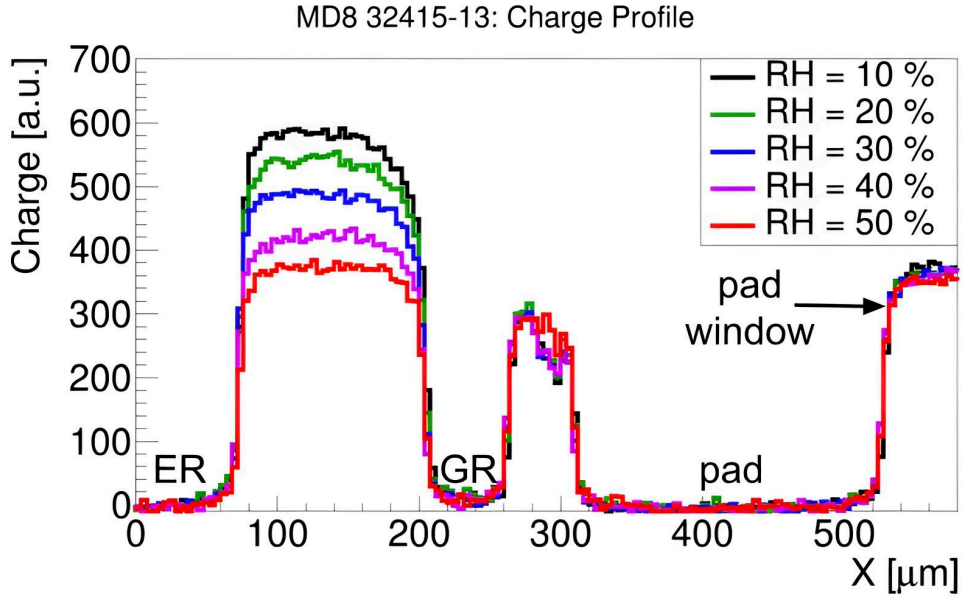

Figure 5.21: Representation of charge profiles for an MD8 diode as a function of RH and $V_{bias} = -900\,V$.

Charge Profile Variations with RH

From Fig. 5.21 it can be seen that between the ER and the GR, the charge profile decreases non-linearly with the increase in RH. In the GR-pad metal region and in the pad window, the charge collected is constant and has a smaller amplitude because the electric field here is smaller.

From the TCAD simulations, it was observed that the electric field near the GR is high enough $\geq 300\,kV \cdot cm^{-1}$ at $-900\,V$ (see Fig. 6.6) to promote secondary charge generation. This is efficient if the concentration of charge carriers is sufficiently small not to shield the electric field [133], [134]. In TCAD simulations, it has been observed that both electrons and holes are present with comparable density values between the ER and GR (see Fig. 6.9 (d) and 6.10 (d)). This pattern suggests that there will be an increase in charge recombination and a decrease in the efficiency of charge transport for the carriers

induced by the laser with the increase in humidity, leading to a reduced TCT signal. To cross-check this hypothesis, a TCAD simulation of the laser scanned along the edge of the diode toward the pad window is needed and should be the focus of future studies.

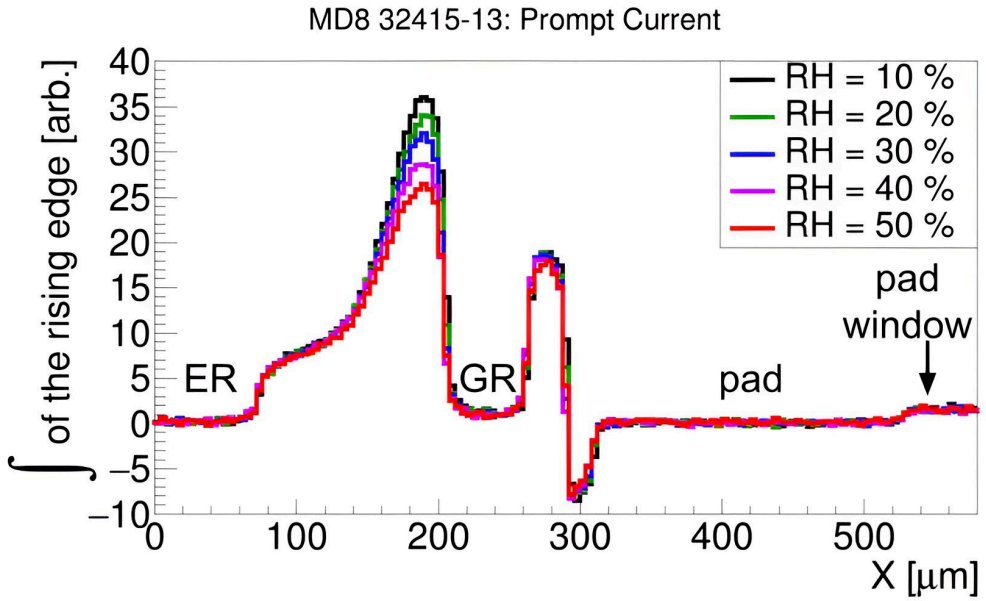

Figure 5.22: Representation of prompt currents for an MD8 diode as a function of RH and $V_{bias} = -900\,\mathrm{V}$.

General Shape of the Prompt Current

The prompt currents along the abscissa and $y = 5050\,\mu\mathrm{m}$ under the influence of RH are presented in Fig. 5.22. Similar to the charge profiles, the prompt current is zero in the metalized regions and non-zero in the sensitive regions. Shining the red laser from the ER towards the GR, it is apparent that the prompt current has a maximum peak near the GR. Between the GR and pad, the prompt current has a positive peak near the GR and a negative peak close to the pad metal. As previously stated, this may be an effect of the p-stop. Fig. 5.23 shows the transient currents for a few points between the GR and pad metal (from $x = 263\,\mu\mathrm{m}$ to $x = 310\,\mu\mathrm{m}$). The p-stop starts roughly at $x = 287\,\mu\mathrm{m}$ and ends at $x = 294\,\mu\mathrm{m}$. It can be seen that the transient current corresponding to a laser position before the p-stop ($x \leq 287\,\mu\mathrm{m}$) has a positive amplitude. Meanwhile, when the laser approaches the p-stop, the transient current amplitude decreases, and it becomes negative. Once the laser is no longer positioned on the p-stop, the transient current amplitude increases.

The prompt current indicates the presence of a strong electric field near the GR. A strong electric field can accelerate charge carriers such that they produce secondary charge generation, which leads to charge multiplication. For a tracking detector like the ATLAS ITk strip, charge multiplication should not be a concern. However, in calorimetry, charge multiplication can disrupt the linearity between the energy deposited and the signal amplitude.

The prompt current also decreases with the increase in RH. The charge profile and prompt current dependence on RH are not yet fully understood; therefore, simulating

the charge injection in TCAD should be the next step to verify if this dependency can be reproduced, which might help with understanding the underlying causes.

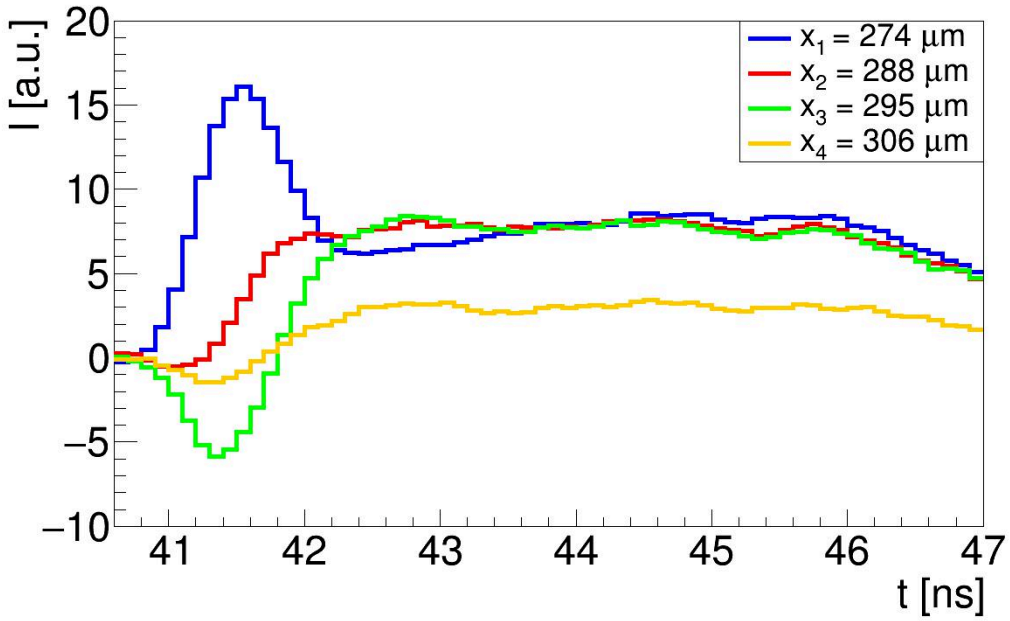

Figure 5.23: Example of position dependent transient currents between the GR and pad metal.

5.3.3 Variation of Charge with Applied Bias

To evaluate how the charge profile and prompt current depend on the applied bias voltage, 8 mm by 8 mm n-in-p silicon diodes were tested for different bias voltages as a function of RH. The MD8 diodes were scanned across a wide range of voltages, starting from $-300\,\mathrm{V}$ down to $-1000\,\mathrm{V}$ with a step of $-100\,\mathrm{V}$. For each voltage change, the humidity was kept constant. The voltage scans were repeated across the full range of RH values, from the lowest to the highest values, without any other investigations performed in between measurements. The biasing scheme followed the one illustrated in Fig. 5.12. The bias voltage was applied on the backside metal, $-10\,\mathrm{V}/10\,\mathrm{s}$ until the target voltage was reached. For each voltage, the laser was scanned across the diode, starting from the ER moving toward the pad window with the ordinate constant ($y = 5820\,\mu\mathrm{m}$). The laser intensity was reduced to 28 % according to the results obtained in section 5.2.3.

An example of the charge profiles and prompt currents as a function of the bias voltage and for different RH values is illustrated in Fig. 5.24-5.33. The charge profiles have been normalized with respect to the signal collected in the pad window.

The charge profiles in the GR-pad metal region and the pad window remain constant with the applied bias because carriers are being generated and collected in areas where the surface electric field is already established and independent of the bulk properties. In contrast, the charge profile between the ER and the GR increases with the applied voltage for values $\geq 800\,\mathrm{V}$. This is a consequence of the electric field increasing with the applied voltage. As the bias voltage increases, the electric field strengthens, which can promote carrier acceleration such that they gain enough energy to create impact ionization, leading to secondary charge generation.

The prompt current remains constant in the GR-pad metal region and in the pad window for all voltage changes. This is because the electric field in these regions is not significantly altered by the increase in bias voltage. It can be seen that the prompt current in the pad window is significantly lower than in the ER-GR or GR-pad metal region because the electric field in this area is lower. Similarly to the charge profiles, the prompt current in the ER-GR region increases with the bias voltage, and it decreases with the increase in RH.

To facilitate a better understanding of the charge profile and prompt current dependence on the applied bias, their peak values were selected from the ER and GR region and represented as a function of RH in Fig. 5.34-5.35. The voltage values were recorded as absolute values. It is apparent that the collected charge and prompt current increase with the applied bias for $V_{bias} \geq 800\,\mathrm{V}$. A significant increase in the collected charge is observed at a bias voltage higher than 900 V, with the charge increasing by a factor of 1.4 at $V_{bias} = -900\,\mathrm{V}$ and by a factor of 1.8 at $V_{bias} = -1000\,\mathrm{V}$.

For a fully depleted sensor, the drift of carriers in the generated electric field is one of the primary processes that affects the charge collection. From equation 4.22, the electric field increases with the increase in bias voltage. Under the influence of a high electric field i.e. $V_{bias} \geq 900\,\mathrm{V}$ carriers can gain enough energy to cause secondary ionization events leading to an avalanche multiplication effect, which could explain the charge collected increase by a factor of 1.4 at 900 V and by a factor of 1.8 at 1000 V.

From Fig. 5.34-5.35, it can be seen that the charge profile and prompt current decrease with the increase in RH. At $RH = 50\,\%$, the charge collected in the ER-GR region remains constant regardless of voltage variations.

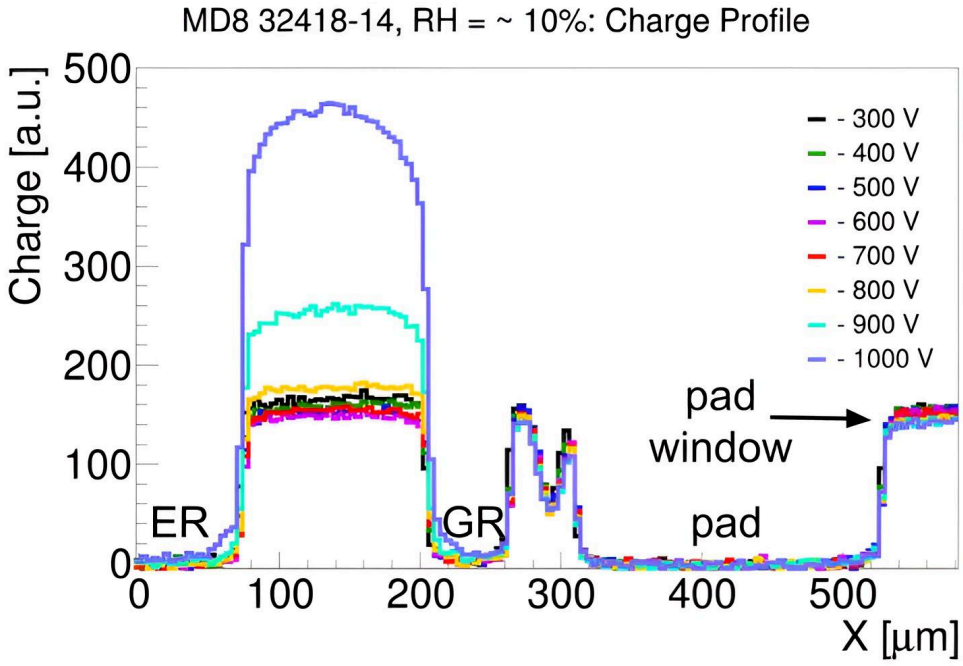

Figure 5.24: Representation of charge profiles for an MD8 diode as a function of voltage and $RH = 10\,\%$.

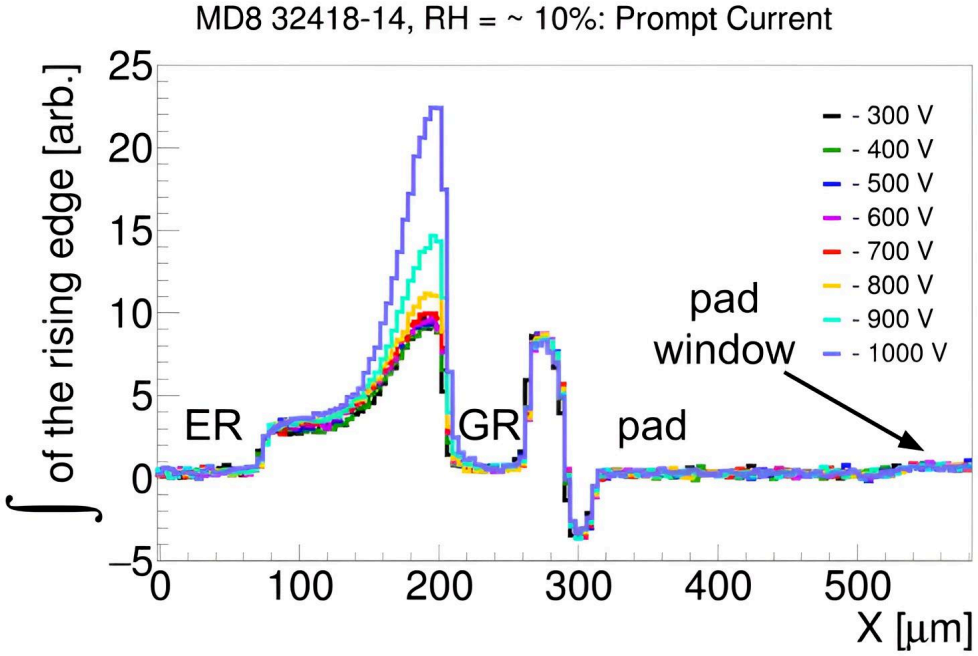

Figure 5.25: Representation of prompt currents for an MD8 diode as a function of voltage and $RH = 10\,\%$.

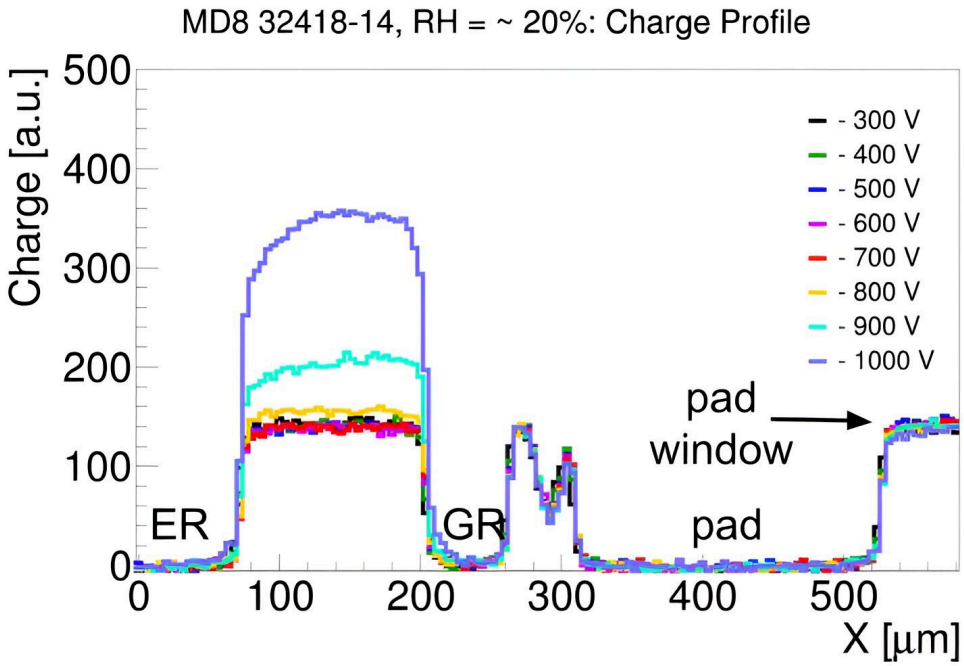

Figure 5.26: Representation of charge profiles for an MD8 diode as a function of voltage and $RH = 20\,\%$.

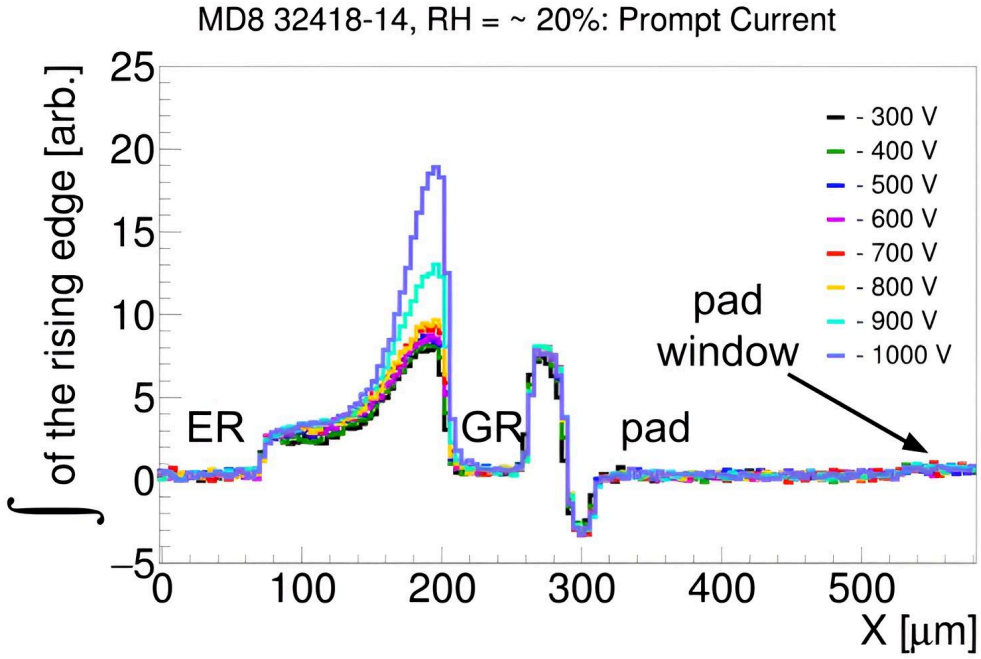

Figure 5.27: Representation of prompt currents for an MD8 diode as a function of voltage and $RH = 20\,\%$.

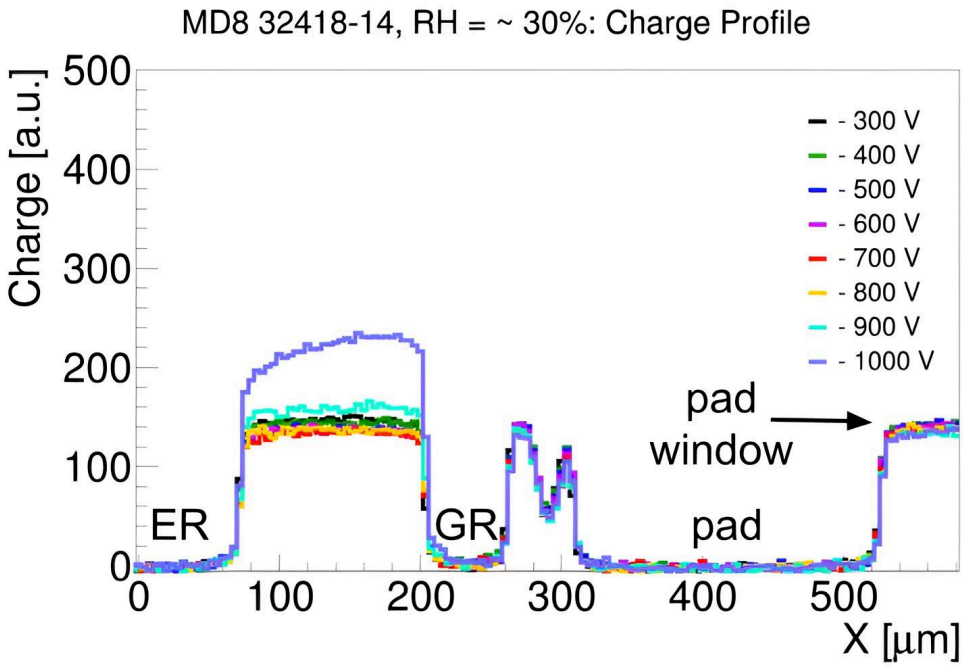

Figure 5.28: Representation of charge profiles for an MD8 diode as a function of voltage and $RH = 30\,\%$.

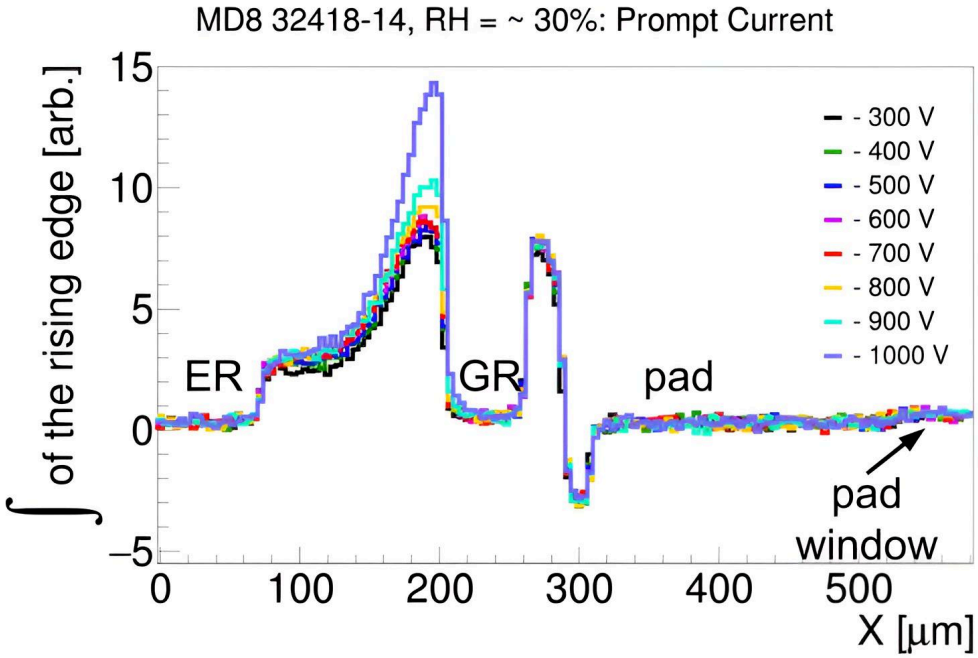

Figure 5.29: Representation of prompt currents for an MD8 diode as a function of voltage and $RH = 30\,\%$.

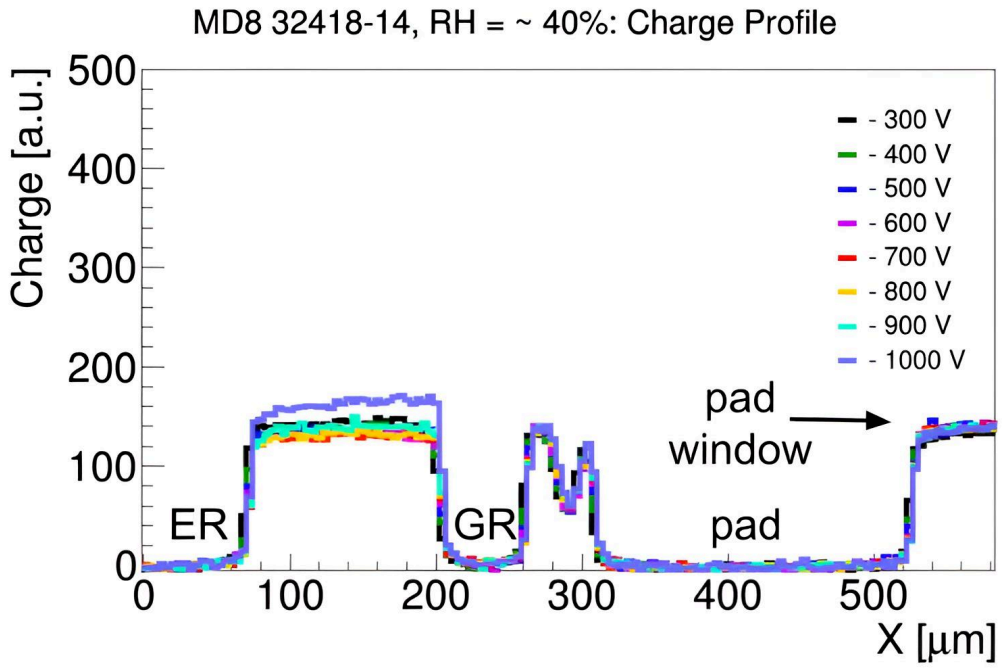

Figure 5.30: Representation of charge profiles for an MD8 diode as a function of voltage and $RH = 40\,\%$.

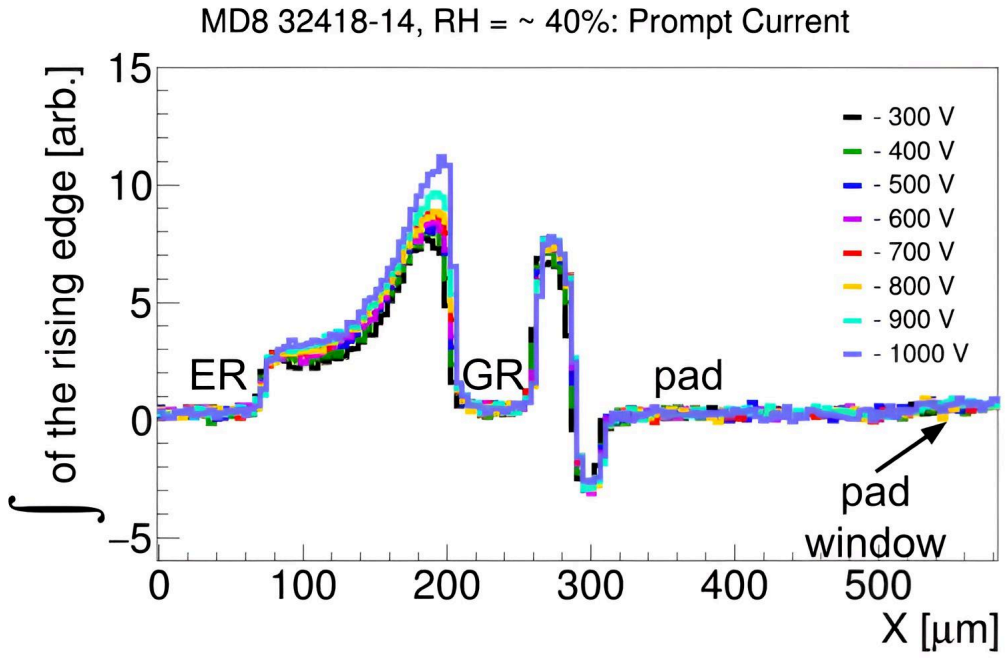

Figure 5.31: Representation of prompt currents for an MD8 diode as a function of voltage and $RH = 40\,\%$.

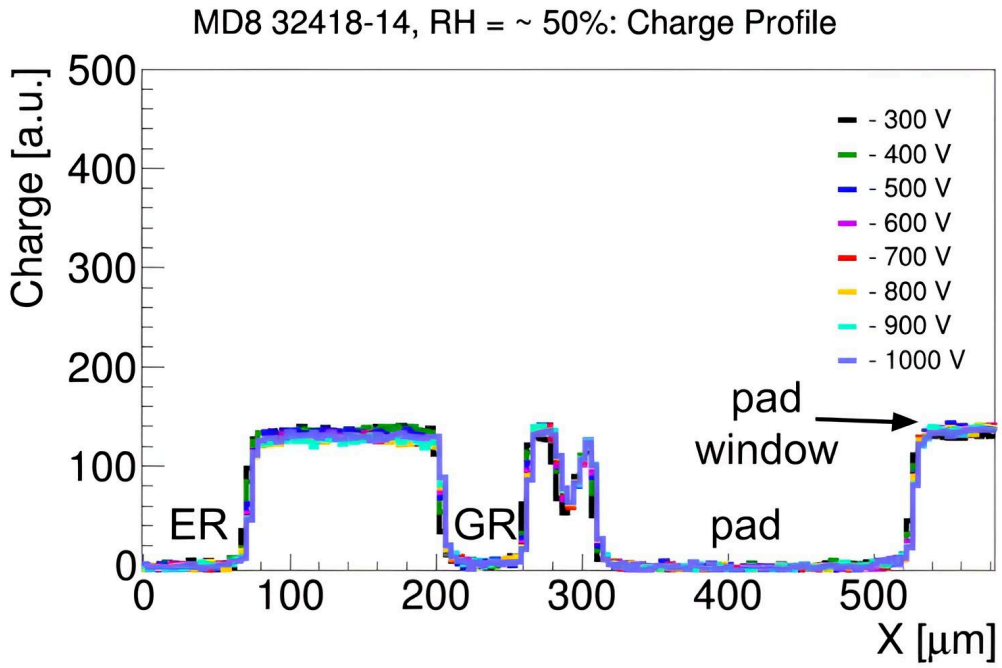

Figure 5.32: Representation of charge profiles for an MD8 diode as a function of voltage and $RH = 50\,\%$.

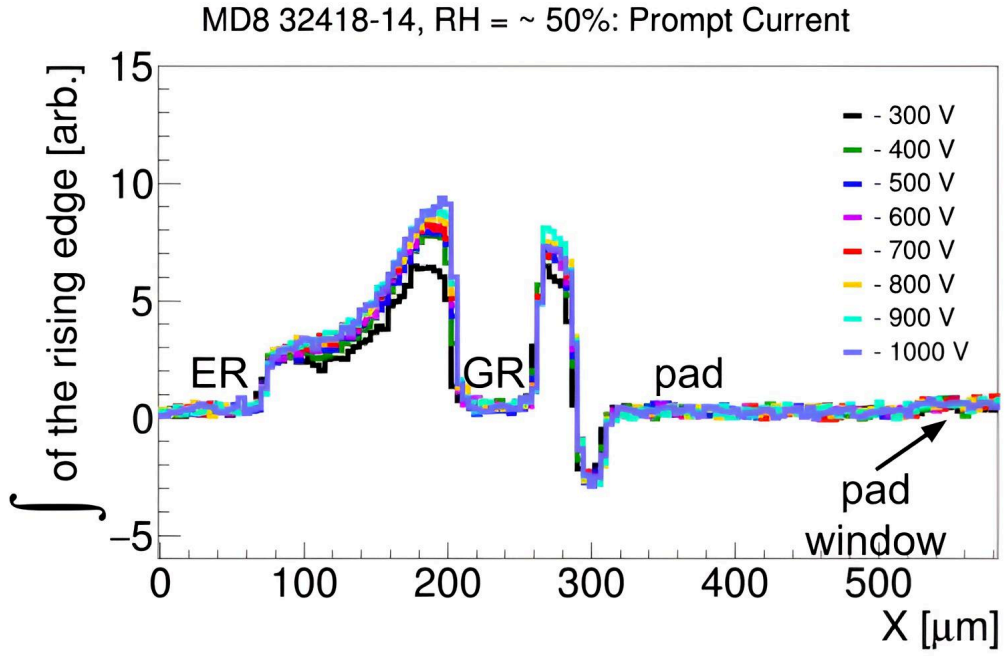

Figure 5.33: Representation of prompt currents for an MD8 diode as a function of voltage and $RH = 50\,\%$.

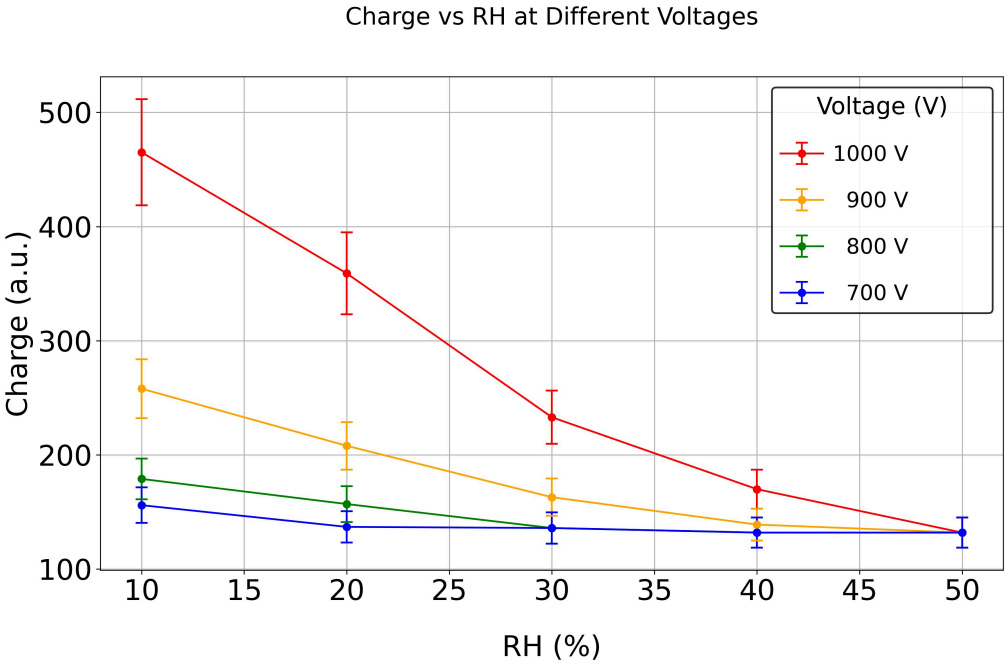

Figure 5.34: Representation of the maximum charge value in the ER-GR region as functions of RH and bias voltage. The error bars were calculated as 10 % of each value represented on the ordinate.

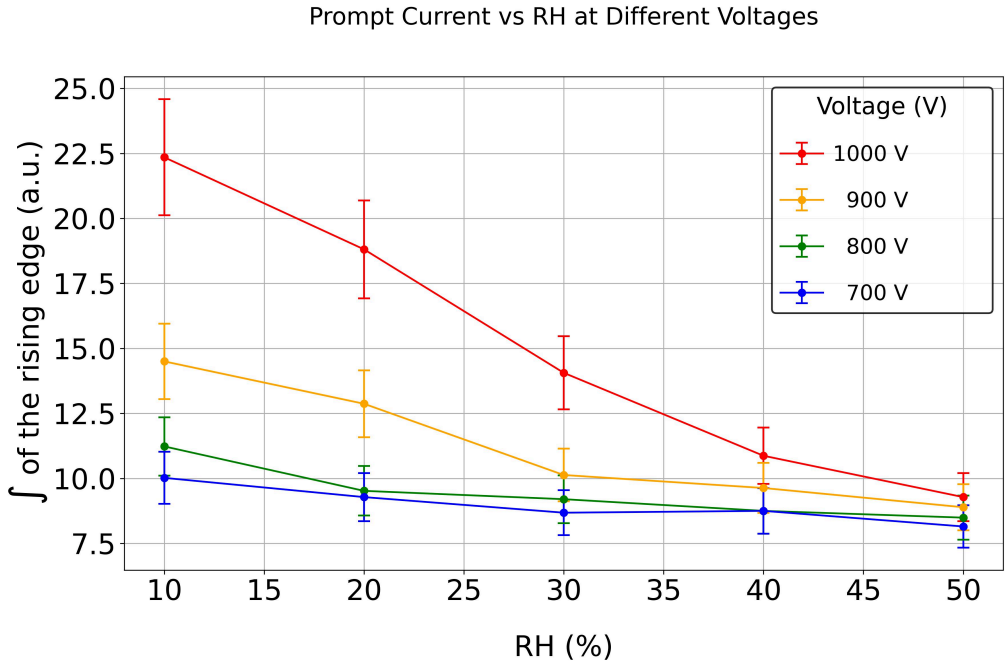

Figure 5.35: Representation of the maximum prompt current in the ER-GR region as functions of RH and bias voltage. The error bars were calculated as 10 % of each value represented on the ordinate.

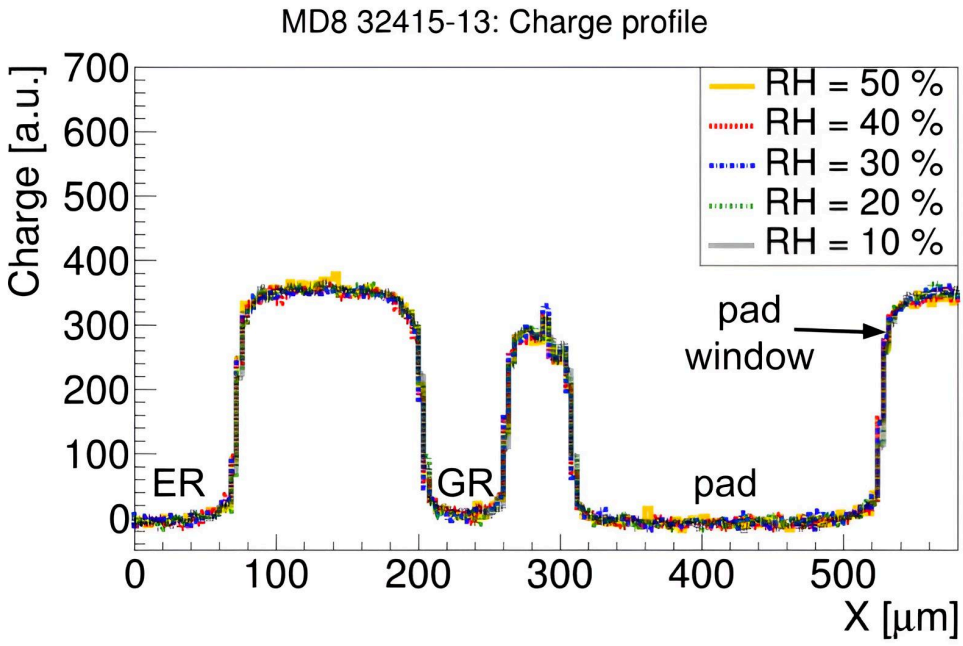

Figure 5.36: Representation of charge profiles as a function of RH at $V_{bias} = -900\,\mathrm{V}$. The measurements were performed starting from the highest target RH to the lowest value with steps of 10 %.

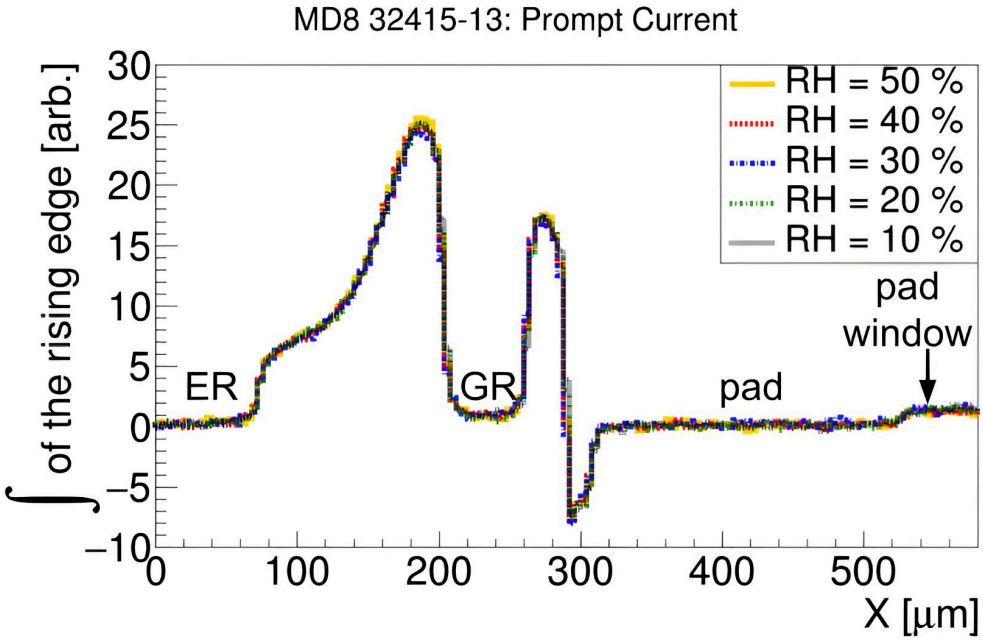

Figure 5.37: Representation of prompt currents as a function of RH at $V_{bias} = -900\,\mathrm{V}$. The measurements were performed starting from the highest target RH to the lowest value with steps of 10 %.

5.3.4 Characterizing Hysteresis for Silicon Diodes

Hysteresis is the dependence of a system on previous changes. For a diode, hysteresis would occur when the figures of merit that would typically vary in response to external conditions become fixed as a result of prior exposure to those conditions. To cross-check if hysteresis affects the charge profiles and prompt currents, following the Top-TCT scan at $RH = 50\,\%$ as shown in Fig. 5.21 and Fig. 5.22, the RH was decreased with a step of $10\,\%$ for each new scan, while the bias voltage was maintained constant at $-900\,\mathrm{V}$. A considerable time of at least 10 min was allowed for the RH to stabilize to the target value. Fig. 5.36 shows the charge profiles and Fig. 5.37 shows the prompt currents as a function of RH when scans are performed starting from the maximum value to the minimum value.

If the charge collected at a lower RH value than the previous measurement is affected by hysteresis, this will be apparent only for the charge collected in the ER and GR region. It can be seen in Fig. 5.36 that the charge profiles in the interest region are fixed at the same amplitude obtained at the highest RH. This shows that the charge profile is affected by hysteresis. The prompt current depends on the collected charge as described by equation 5.14, and therefore, if the charge profiles are affected by hysteresis, the prompt current will exhibit the same behavior as shown in Fig. 5.37.

5.3.5 Variation of Charge with Time

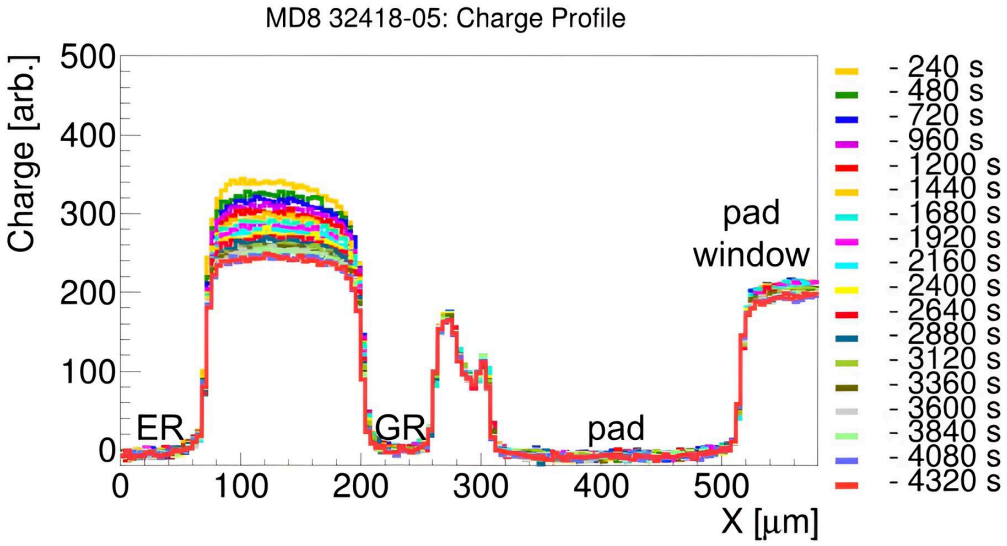

Figure 5.38: Representation of charge profiles as a function of time at $V_{bias} = -900\,\mathrm{V}$ and $RH = 40\,\%$.

The charge profile and prompt current for different timestamps were investigated using an MD8 diode. To enable a comparison between Top-TCT measurements and TCAD simulations, the MD8 diode was tested at $RH = 40\,\%$ and $V_{bias} = -900\,\mathrm{V}$. The biasing scheme was identical for both the simulation and the experiment, following the one illustrated in Fig. 5.12. Under these conditions, the TCAD simulations predict that the leakage current would increase slowly starting from 1450 s after the full bias voltage

was reached. The laser was scanned starting from the ER toward the pad window multiple times for a total of 4320 s.

The charge profiles and prompt currents at different timestamps after the scan started are presented in Fig. 5.38 and Fig. 5.38. It can be observed that the charge collected in the GR-pad metal region and the pad window has no significant variations with time. In contrast, the charge profile in the ER-GR area decreases over time. A similar trend can be observed for the prompt current shown in Fig. 5.39. In regions with a high electric field, the charge cloud can dissipate quickly, which leads to less recombination. However, the opposite effect is observed, which points to a gain reduction. This might be caused by the plasma of carriers shielding the electric field near the GR. To validate the accuracy of the measured induced currents, the laser scanning process should be incorporated in TCAD to model the laser beam profile and its interaction with the MD8 diode. This simulation will allow us to validate the electric field shielding hypothesis.

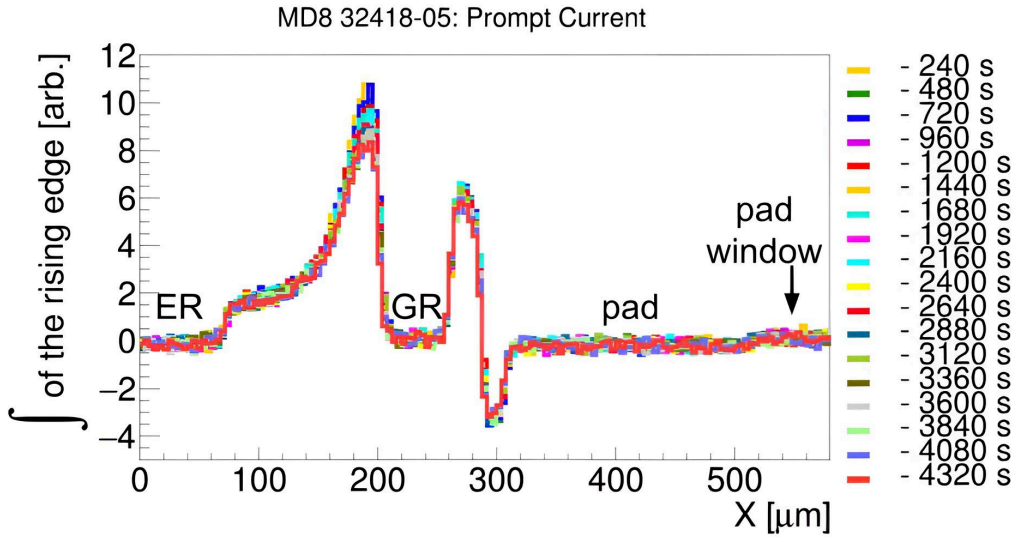

Figure 5.39: Representation of prompt currents as a function of time at $V_{bias} = -900\,\mathrm{V}$ and $RH = 40\,\%$.

Chapter 6

Technology Computer-Aided Design Simulations

Technology Computer-Aided Design (TCAD) is a powerful tool to simulate the electrical behavior of silicon sensors. This study made use of Sentaurus TCAD from Synopsys [96], a commercial suite of software that offers a straightforward way to implement the geometry of sensors and model physics processes that take place in semiconductors, e.g., silicon.

TCAD has been used to evaluate charge transport between the Edge Ring (ER) and Guard Ring (GR) region of monitor diodes (MD8s) in humid conditions. It simulates the most important figures of merit: the electric field, generation of electron-hole pairs from impact ionization, and electron and hole densities. The electric field is studied because it is an important driver of charge transport inside silicon, as shown in the total drift current density equation 3.33. The charge carriers accelerated inside the electric field can gain enough energy to create secondary ionization inside silicon, leading to charge multiplication. As a result, the carrier density will increase, which changes the current density.

The two software tools used are the Structure Device Editor (SDE) [135] and the Sentaurus Device (SDevice) [42]. The SDE software enables device implementation, especially when processing details are missing, while the alternative, i.e., Sentaurus Process, simulates the process. The SDevice software simulates the behavior (fields and carrier transport) of the device. It facilitates an easy way to set parameters, e.g., temperature, concentration of impurities, etc., and physics models, e.g., charge transport models, etc.

6.1 Geometry Implementation

SDE is a tool for implementing 1D, 2D or 3D structures for TCAD simulations. It is advantageous to create the geometry when fabrication details are missing. When the processing steps are known, these can be implemented instead of the sensor's geometry. Two options are available to generate the structure of the device: manually placing each element using the graphical user interface (GUI) or executing the equivalent commands in the Scheme programming language [42]. A combination of the two methods is also possible.

This study took advantage of the Scheme programming language to generate the edge geometry of the MD8 diode in TCAD. Sentaurus Visual (SVisual) [136] was used to visualize the model generated together with the results obtained.

The cross-section of the MD8 is shown in Fig. 6.1, focusing on the structures deposited on the top of the diode. The total thickness of the sensor was calculated from Capacitance-Voltage (CV) measurements (see Fig. 4.23) to be approx. 287 µm (details about the parameters used are presented in Table 4.2). The silicon bulk is uniformly doped with boron atoms. The doping concentration was calculated from CV measurements to be approx. $4.68 \cdot 10^{12}$ cm^{-3}, as presented in section 4.5. The implants were implemented in TCAD as doping profiles described by Gaussian functions, which serve as an approximation for the dopant distribution after ion implantation. The shape of the electrodes is based on Scanning Electron Microscope (SEM) images of similar devices, as shown in Fig. 4.7. The passivation consists of a silicon dioxide (SiO_2) layer and a Silicon nitride (Si_3N_4) layer. The SiO_2 layer is in direct contact with the silicon and goes beneath the overhangs of the aluminum electrodes.

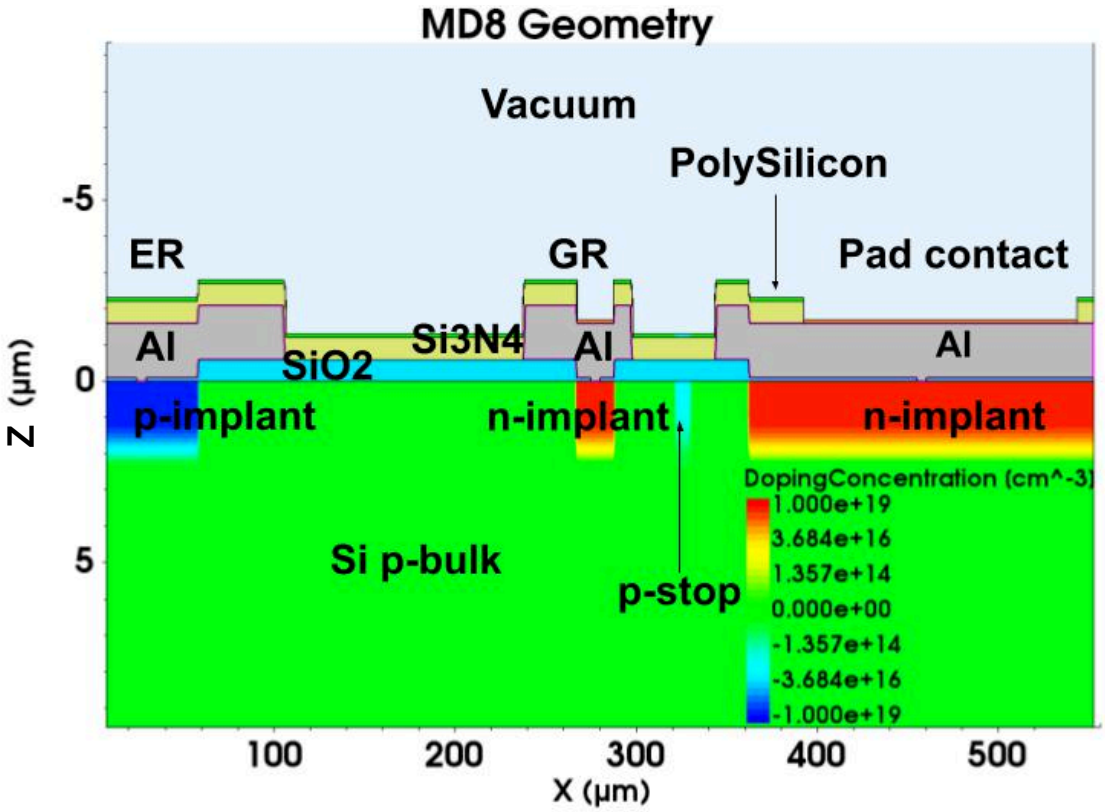

Figure 6.1: View of the diode geometry used in TCAD. The p-implant on the backside (not shown) is at $z = 289.2$ µm and extends along the abscissa. The aspect ratio is 20:1.

The concentration of fixed oxide charges at the interface between the silicon bulk and SiO_2 has been measured to be $1 \cdot 10^{11}$ cm^{-2} [137], and it was implemented in TCAD to obtain more realistic results. However, it should be noted that the concentration of fixed oxide charges varies from batch to batch. Depending on which value is implemented, different results may be obtained. The effects of the concentration of fixed oxide charges are presented in section 6.4.

To model the effects of a resistive layer hypothesized to form on the passivation under humid conditions, a 0.1 µm highly resistive layer was added on top of the passivation, as described in [138]. In TCAD, it is formally called polysilicon. In humid environments, the sheet resistance of the passivation decreases with increasing RH, as measured in

[139]. Under such conditions, moisture can accumulate on the passivation layer, and water molecules may dissociate into positive ions and negative ions [83]. These ions act as additional charge carriers, thereby increasing the surface conductivity and reducing the sheet resistance. To model the effects at a specific RH, the carrier mobility was adjusted to reproduce the sheet resistance values reported in the literature.

To determine the carrier mobility corresponding to a particular sheet resistance, a simple geometry consisting of a polysilicon layer connected to two aluminum electrodes was implemented in TCAD, as shown in Fig. 6.2.

To infer the sheet resistance based on the variation of the mobility, the Current-Voltage (IV) characteristics were simulated. A bias voltage starting from $-100\,\mathrm{V}$ to $100\,\mathrm{V}$ was applied to one of the aluminum electrodes, while the other was kept at ground. Fig. 6.3 shows one example of a TCAD simulated IV characteristics. The following formula was used to derive the sheet resistance:

$$R_s(0.1\,\mu\mathrm{m}) = \frac{1}{\mathrm{slope}} \cdot \frac{1\,\mu\mathrm{m}}{100\,\mu\mathrm{m}}, \tag{6.1}$$

where the factor $\frac{1\,\mu\mathrm{m}}{100\,\mu\mathrm{m}}$ accounts for the ratio between the effective layer thickness and the distance between the contacts (i.e., the device geometry, where W is the width and L is the length of the active region). As seen in Fig. 6.3, the current varies linearly with the applied bias voltage. A linear fit of the form:

$$y = a\,x + b$$

was applied to the data, yielding a slope of

$$a = (1.03 \pm 0.0001) \cdot 10^{-18}\,\Omega^{-1}$$

and an intercept of

$$b = (9.37 \pm 0.94) \cdot 10^{-20}\,\mathrm{A}.$$

The uncertainties were obtained via Gaussian error propagation.

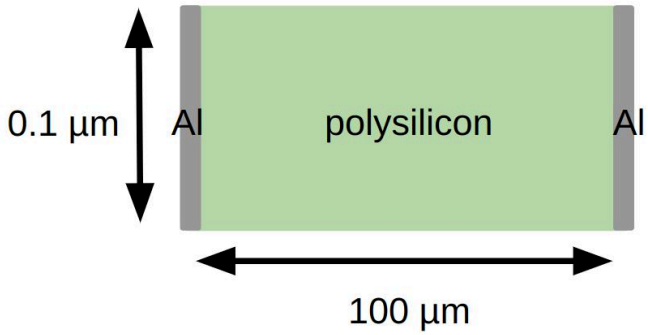

Figure 6.2: Schematic of a simple geometry consisting of a highly resistive layer connected to two aluminum contacts.

In order to maintain a constant sheet resistance for a given device configuration, the device dimensions were fixed (e.g., the channel length was set to $10\,\mu\mathrm{m}$). For a mobility of $4.39 \cdot 10^{-3}\,\mathrm{cm^2\,V^{-1}\,s^{-1}}$, the same sheet resistance was obtained, which serves as an additional confirmation that the simulation works as expected. The mobility values

corresponding to $RH = 40\,\%$ and $RH = 30\,\%$ are summarized in Table 6.1. Note that experimental measurements were performed only for $RH \geq 30\,\%$. Since a comparison between dry and humid conditions is desired, it was assumed that at $RH = 0\,\%$, the sheet resistance would be extremely high, and hence the mobility was set to zero.

Table 6.1: Mobility Parameters for Different RH Conditions

RH (%)	R_s(exp) (Ω)	Slope (Ω^{-1})	R_s(det) (Ω)	μ ($\mathrm{cm^2\,V^{-1}\,s^{-1}}$)
40	$9.7 \cdot 10^{15}$	$1.03 \cdot 10^{-18}$	$9.69 \cdot 10^{15}$	$4.39 \cdot 10^{-3}$
30	$6.6 \cdot 10^{16}$	$1.51 \cdot 10^{-19}$	$6.60 \cdot 10^{16}$	$6.42 \cdot 10^{-4}$

Once the geometry and contacts have been defined, the mesh can be created. The mesh refers to a discretized network of points for which the Poisson equation (presented in equation 3.64) and the carrier continuity equations (discussed in section 3.3.3) are solved for each element of the triangulation of the points. An adaptive meshing technique has been used featuring finer points at the interfaces with a minimum mesh element size of 0.01 µm, and coarser points in the silicon bulk with a maximum distance of 1.05 µm. The areas with denser mesh points can better reflect variations in the gradients of the potential, electric field, and charge carrier concentration.

The simulation is constrained by the accuracy of the parameters implemented, together with the models enabled. The values used for the main geometry parameters implemented in TCAD are listed in Table 6.2.

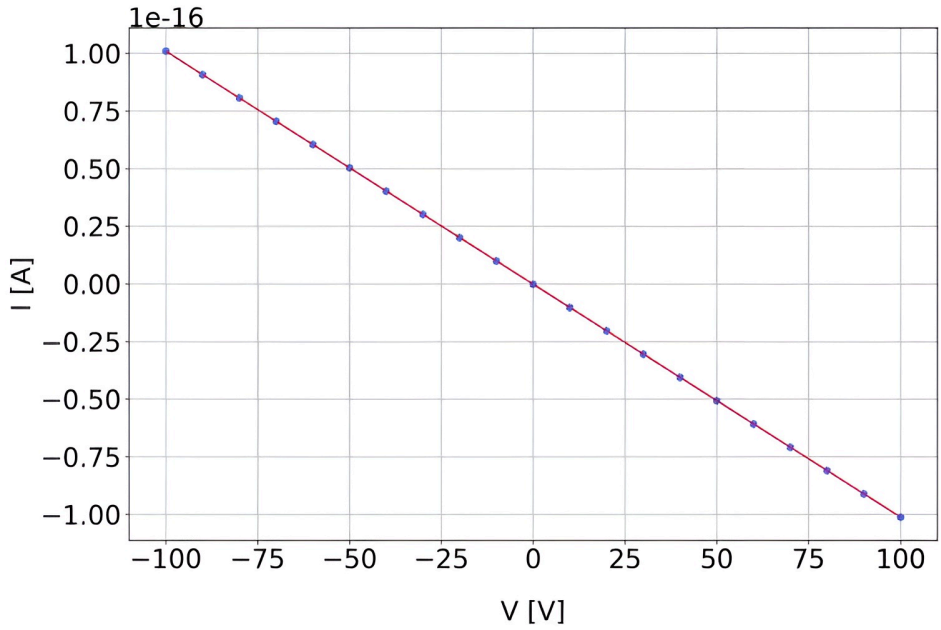

Figure 6.3: Example of an IV characteristic for the simple geometry shown in Fig. 6.2. One electrode was biased between −100 V and 100 V while the other was at ground. Blue markers represent the simulated data points, and the continuous red line indicates the linear fit.

Table 6.2: TCAD Parameters

Parameter	Value	Unit
Si p-bulk thickness	287	µm
Si p-bulk doping	$4.68 \cdot 10^{12}$	cm^{-3}
p-implant doping	$1 \cdot 10^{19}$	cm^{-3}
n-implant doping	$1 \cdot 10^{19}$	cm^{-3}
p-stop doping	$1 \cdot 10^{14}$	cm^{-3}
Fixed oxide charges	$1 \cdot 10^{11}$	cm^{-2}
SiO_2 thickness	0.6	µm
Si_3N_4 thickness	0.6	µm
Poly-Si thickness	0.1	µm
Al electrodes thickness	1.5	µm

6.2 Modeling Mobile Charge in TCAD

After the mesh is generated by SDE, SDevice is used to simulate the electrical behavior of the MD8 diode. The voltage ramping procedure is defined according to the ATLAS Inner Tracker (ITk) Strips Quality Assurance and Quality Control procedure: the bias voltage is applied on the backside and the ER from 0 V in steps of −10 V every 10 s until −900 V are reached.

The carrier mobility was described using the Canali model [49]. The Canali model is based on the Caughey–Thomas formula [140] with temperature-dependent parameters up to 430 K. For the Canali model, the mobility is the following [42]:

$$\mu(F) = \frac{(\alpha+1)\mu_{low}}{\alpha + \left(1 + \left(\frac{(\alpha+1)\mu_{low}F_{hfs}}{\nu_{sat}}\right)^{\beta}\right)^{-\frac{1}{\beta}}}, \tag{6.2}$$

where μ_{low} is the mobility for low electric fields, ν_{sat} is the saturation velocity for high electric fields, F_{hfs} is the driving field force, and α and β are model specific parameters.

The temperature dependence of the saturation velocity in a semiconductor [42] is defined as:

$$\nu_{sat} = \nu_{sat,0}\left(\frac{300\,\mathrm{K}}{T}\right)^{\nu_{sat,exp}}, \tag{6.3}$$

where $\nu_{sat,0}$ is the reference velocity at 300 K, $\nu_{sat,exp}$ quantifies the changes in velocity with temperature T. The numerical values used for $\nu_{sat,0}$ and $\nu_{sat,exp}$ are shown in [42].

The driving field force for electrons is determined by the spatial variations of the quasi-Fermi potential [42]:

$$F_{hfs,n} = |\nabla\phi_n|. \tag{6.4}$$

By default, the electric field replaces the gradient of the quasi-Fermi potential within the mesh elements touching a contact [42]:

$$F_{hfs,n} = |\vec{\mathcal{E}}|. \tag{6.5}$$

The parameter β [42] is temperature dependent and it is defined as:

$$\beta = \beta_0\left(\frac{T}{300\,\mathrm{K}}\right)^{\beta_{exp}}. \tag{6.6}$$

The values for α and β for electrons and holes in silicon can be found in [42].

The recombination lifetime of carriers inside the silicon bulk [39] was calculated using the formula:

$$\tau = \frac{q \cdot n_i \cdot A \cdot W}{I_{FD}}, \tag{6.7}$$

where q is the elementary charge, n_i is the intrinsic carrier concentration, A is the pad area, W is the active thickness, and I_{FD} is the full depletion current. The full depletion current refers to the leakage current after full depletion is achieved. The full depletion voltage was derived from CV measurements in section 4.5.

It should be noted that in calculations, the pad area was extended to the p-stop to avoid edge effects that could affect the measurements [99]. The active thickness was obtained from CV measurements as discussed in section 4.5.

The full depletion current was derived based on IV measurements of the pad current. For this, the pad current was used because it is more stable than the GR current. One example of an IV characteristic for the pad current in dry conditions ($RH = 10\,\%$) is presented in Fig. 6.4. The full depletion current was calculated as the average value of the leakage current corresponding to the voltage range between 285 V and 305 V. As previously mentioned, after 285 V, the diode is fully depleted. The voltage range was extended up to 305 V to average out statistical effects. The averaged full depletion current obtained was $(1.74 \pm 0.01) \cdot 10^{-10}$ A. The error was calculated based on the standard error of the mean of the current values in the $285 - 305$ V range.

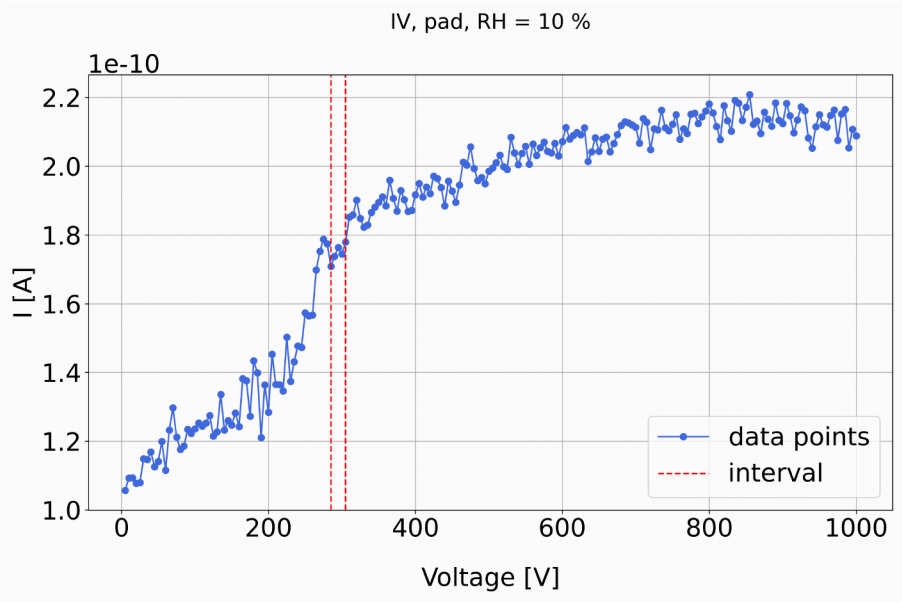

Figure 6.4: IV characteristic of an MD8 diode from the ATLAS18LS wafer, showing the pad current as a function of the applied bias. The bias voltage was applied to the backside metal, while the GR was kept at ground. The red dotted lines indicate the voltage range used to calculate the full depletion current.

The intrinsic carrier concentration was calculated using equation 3.17:

$$n_i(T) = \sqrt{N_c(T)\, N_v(T)} \times \exp\left(-\frac{E_g(T)}{2\, k_B\, T}\right), \tag{6.8}$$

where $k_B = 8.61 \times 10^{-5}$ eV/K is the Boltzmann constant.

The effective density of states were calculated using the formulas:

$$N_c(T) = N_c(300\text{ K}) \times \left(\frac{T}{300}\right)^{3/2}, \tag{6.9}$$

$$N_v(T) = N_v(300\text{ K}) \times \left(\frac{T}{300}\right)^{3/2}, \tag{6.10}$$

where:

- $N_c(300\ \text{K}) = 2.81 \times 10^{19}\ \text{cm}^{-3}$ [141],
- $N_v(300\ \text{K}) = 3.10 \times 10^{19}\ \text{cm}^{-3}$ [141].

The temperature-dependent bandgap energy for silicon can be approximated by:

$$E_g(T) = E_g(0) - \frac{\alpha T^2}{T + \beta}, \tag{6.11}$$

where:

- $E_g(0) = 1.17$ eV (bandgap at 0 K) [50],
- $\alpha = 4.73 \times 10^{-4}$ eV/K [39],
- $\beta = 636$ K [39],
- T is the absolute temperature in Kelvin.

The numerical values for the parameters used for calculating the recombination lifetime are listed in Table 6.3. The average value is 0.1 s.

Table 6.3: Recombination Lifetime Parameters

Parameter	MD8 1	MD8 1	MD8 2	MD8 2	Unit
RH	10	20	10	20	%
T	295.66	295.83	295.86	295.79	K
I_s	$1.51 \cdot 10^{-10}$	$1.21 \cdot 10^{-10}$	$1.75 \cdot 10^{-10}$	$1.76 \cdot 10^{-10}$	A
q	$1.60 \cdot 10^{-19}$	$1.60 \cdot 10^{-19}$	$1.60 \cdot 10^{-19}$	$1.60 \cdot 10^{-19}$	C
A	$5.20 \cdot 10^{-1}$	$5.20 \cdot 10^{-1}$	$5.20 \cdot 10^{-1}$	$5.20 \cdot -1$	cm^2
W	$2.86 \cdot 10^{-2}$	$2.86 \cdot 10^{-2}$	$2.86 \cdot 10^{-2}$	$2.86 \cdot 10^{-2}$	cm
$E_g(T)$	1.12	1.12	1.12	1.12	eV
$N_c(T)$	$2.74 \cdot 10^{19}$	$2.75 \cdot 10^{19}$	$2.75 \cdot 10^{19}$	$2.75 \cdot 10^{19}$	cm^{-3}
$N_v(T)$	$3.03 \cdot 10^{19}$	$3.03 \cdot 10^{19}$	$3.03 \cdot 10^{19}$	$3.03 \cdot 10^{19}$	cm^{-3}
n_i	$7.22 \cdot 10^{9}$	$7.33 \cdot 10^{9}$	$7.35 \cdot 10^{9}$	$7.30 \cdot 10^{9}$	cm^{-3}
τ	$1.14 \cdot 10^{-1}$	$1.45 \cdot 10^{-1}$	$1.00 \cdot 10^{-2}$	$9.87 \cdot 10^{-2}$	s

6.3 Effects of Passivation Openings

6.3.1 Passivation Openings: IV-const Characteristics

Passivation openings are regions on the sensor's surface where the passivation is etched away. These are placed in key areas where only the regions of interest are exposed to the ambient atmosphere, while the parts at risk are still protected against environmental contaminants. The main purpose of passivation openings is to facilitate electrical contact. For this reason, they are placed on the readout electrodes to create contacting pads, which give easy access to tasks such as wirebonding. Without contacting pads on the readout electrodes, the passivation has to be removed manually after fabrication to make an electrical connection, which can damage the sensor depending on its layout.

The MD8 diodes have passivation openings on the GR, pad metal, and in the corners on the ER. The passivation openings on the GR and the pad metal were measured using optical microscopy. Fig. 5.5 shows an example of a digital microscope picture of the edge of the MD8 diode, where the passivation opening on the GR was measured as 20.31 µm, while the passivation opening on the pad metal was measured as 150.89 µm. For the ER, a small passivation opening of 3.5 µm is seen at the outer edge.

Fig. 6.5 shows the simulated GR leakage current as a function of time at constant temperature ($T = 295.6\,\mathrm{K}$) corresponding to different passivation opening schemes in the presence of humidity (0 %, 30 %, 40 %). During the first 900 s, the bias voltage is applied on the sensor, $-10\,\mathrm{V}/10\,\mathrm{s}$. Afterward, the bias voltage is constant at $-900\,\mathrm{V}$.

The GR leakage current obtained during ramping has the same behavior for passivation openings at the ER, GR, and pad - Fig. 6.5 (a); ER - Fig. 6.5 (c), and no passivation openings - Fig. 6.5 (d). However, the leakage current suffers a decrease at 10 V for passivation openings at the GR and pad - Fig. 6.5 (b). This behavior is not yet understood.

Fig. 6.5 (a) shows the IV-const characteristics for the GR leakage current as a function of time for an MD8 with passivation openings on the ER, GR, and the pad metal. For IV-const characteristics, on the abscissa the time is shown, while on the ordinate the leakage current is plotted. Here, the first 900 s correspond to the voltage application, which, based on the biasing procedure, can be interchanged with voltage. The term "const" emphasizes that after 900 s, the voltage remains constant within the chosen time window of 4050 s for all RH values after the target bias voltage has been reached. Under the influence of humidity, inside the resistive layer, positive charges accumulate on top of the ER, while negative charges accumulate on top of the GR [81]. The positive and negative carriers accumulate with a lower concentration and nonuniform distribution on top of electrodes when passivation openings are present on all electrodes ($\geq 4.6 \cdot 10^{12}\,\mathrm{cm}^{-3}$) (see Fig. 6 - 7 in Appendix). In comparison, when passivation openings are missing, carriers accumulate on top of the electrode without passivation openings with a higher concentration and uniform distribution ($10^{16}\,\mathrm{cm}^{-3}$). Over time and in the presence of humidity, the charge accumulation on top of the electrode(s) with no passivation openings starts to spread beyond the electrode. This changes the electric field locally. However, when the concentration of positive and negative charges is nonuniform and constrained on top of the electrodes, they do not influence the electric field over time; therefore, the leakage current remains constant.

Fig. 6.5 (b) presents the IV-const for passivation openings on the GR and the pad metal. For $RH \leq 30\,\%$, the GR leakage current remains constant after the ramping period for the chosen time window. At $RH = 40\,\%$, the leakage current starts to increase

at $t \simeq 4723\,\mathrm{s}$ ($I \simeq 2.32 \cdot 10^{-11}\,\mathrm{A}$). When the resistive layer is capacitively coupled to the ER and under the influence of high humidity ($RH \geq 40\,\%$), the positive charges that have accumulated on top of the ER with a high concentration $\geq 1 \cdot 10^{16}\,\mathrm{cm}^{-3}$ (see Fig. 15 (d) in Appendix) spread beyond the electrode with time such that their influence on the localized electric field starts to become non-negligible at $t \simeq 4723\,\mathrm{s}$, which in turn increases the leakage current.

Fig. 6.5 (c) and (d) show the IV-const characteristics for an MD8 with passivation openings on the ER, and for the case without passivation openings, respectively. For these two passivation opening schemes, the GR leakage current increases with the increase in RH. These two cases model the electrical behavior of the MD8 diode as a function of RH, closer to the results shown in [90] because the leakage current increases with RH. A greater contribution to the leakage current is triggered by the resistive layer being capacitively coupled to the GR. Because of this, negative charges accumulate on top of the GR, which is at $0\,\mathrm{V}$ ($\geq 1 \cdot 10^{16}\,\mathrm{cm}^{-3}$, see Fig. 6.9 (d) and Fig. 11 (d) in Appendix), changing the localized electric field, which contributes more to the increase in leakage current than the changes caused by the resistive layer being capacitively coupled to the ER.

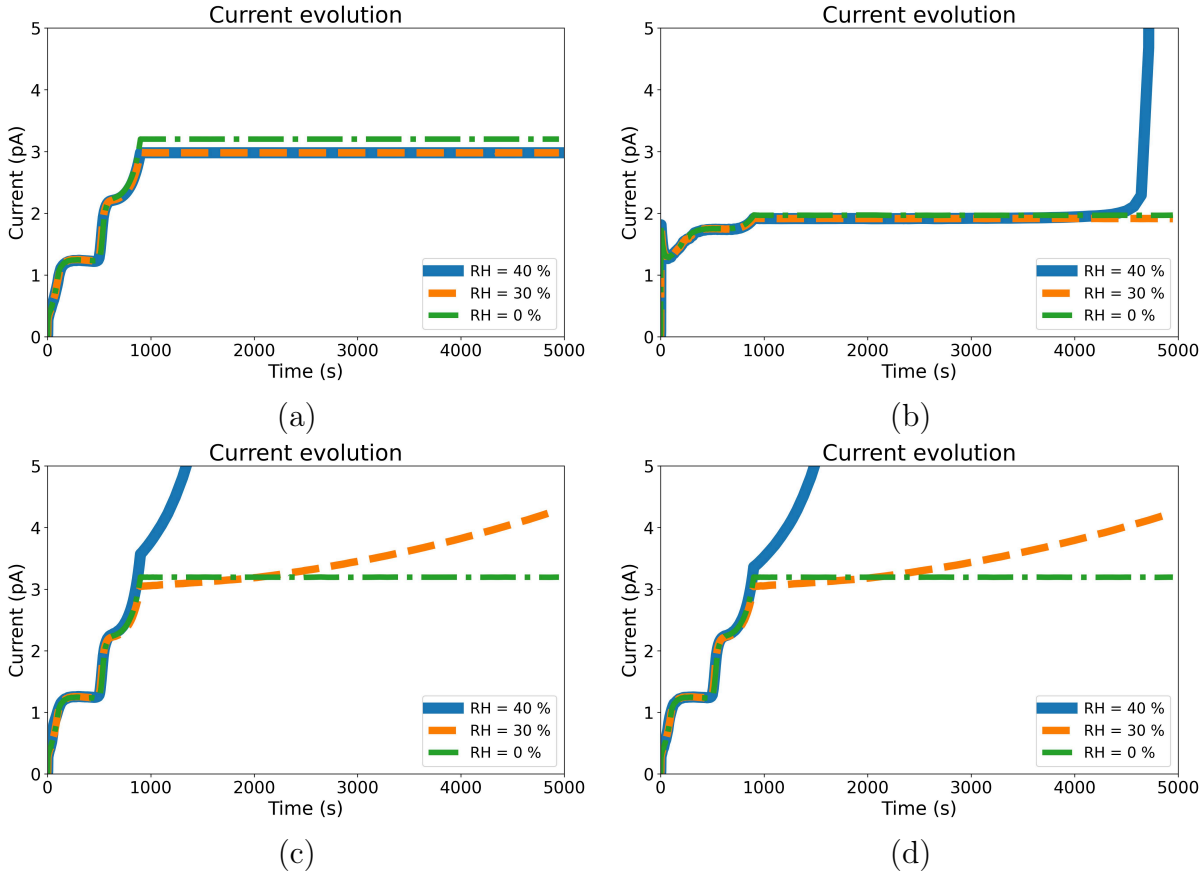

Figure 6.5: Simulated GR leakage current vs. bias voltage at $T = 295.6\,\mathrm{K}$ as a function of RH and different passivation opening schemes: at the ER, GR, and pad metal (a); at the GR and pad metal (b); at the ER (c); and with no passivation openings (d). The first 900 s correspond to the ramping time: $-10\,\mathrm{V}/10\,\mathrm{s}$, and afterwards the bias voltage remains constant ($-900\,\mathrm{V}$).

6.3.2 Passivation Openings: Electric Field Cutlines

It is important to study the electric field's spatial distribution and evolution in time to understand its impact on the drift current and the velocity of carriers. In Sentaurus TCAD from Synopsys, for a 2D model, there are two options to display figures of merit, such as the electric field: as a 1D distribution (showing variations for a fixed coordinate with respect to the other) or as a 2D distribution.

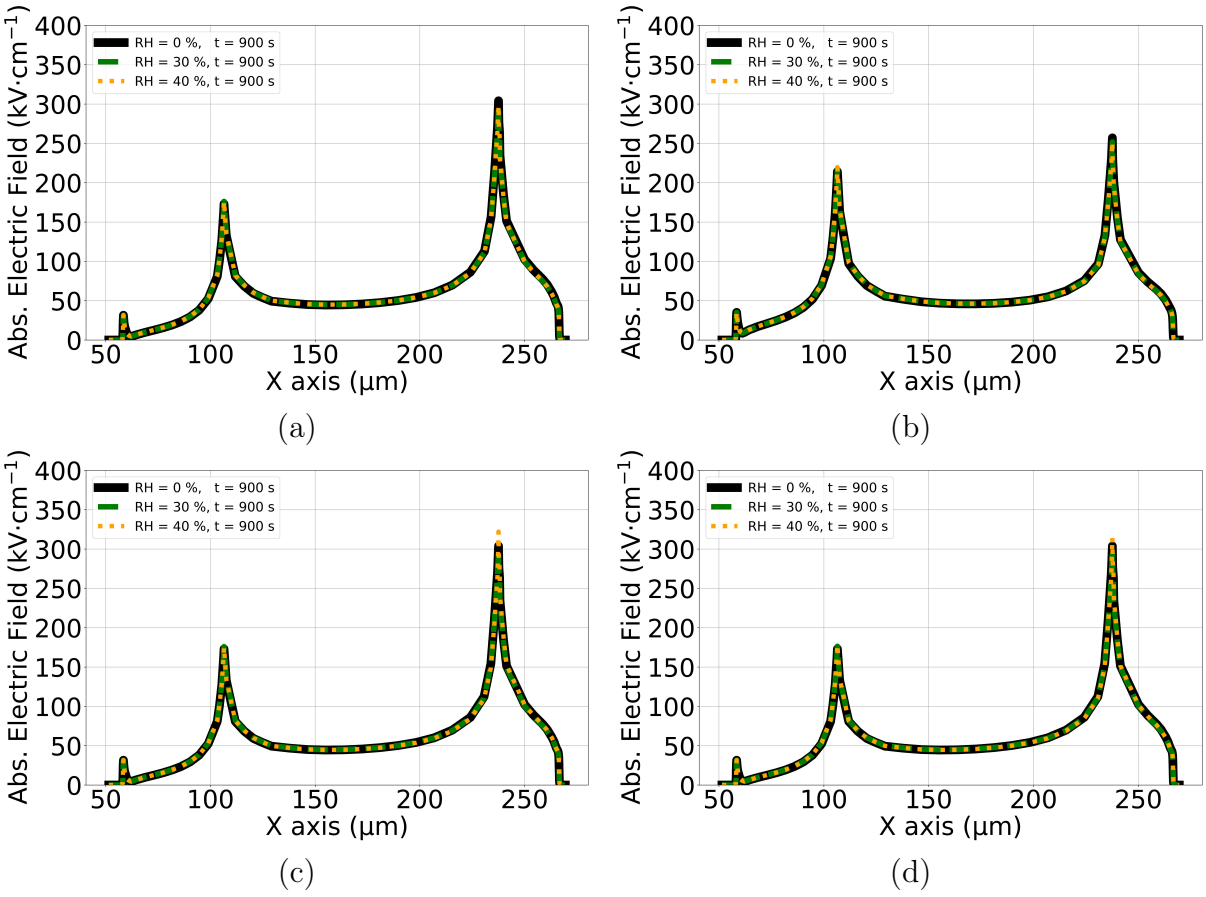

Figure 6.6: Electric field profile for $z = 100\,\text{nm}$ along the abscissa as a function of RH at $V_{bias} = -900\,\text{V}$ and $t = 900\,\text{s}$ for different passivation openings: at the ER, GR, and pad metal (a); at the GR and pad metal (b); at the ER (c); and with no passivation openings (d).

Fig. 6.6 shows the electric field values at $z = 100\,\text{nm}$ below the Si-SiO_2 interface along the abscissa as a function of RH at constant bias voltage $-900,\text{V}$ and $t = 900\,\text{s}$ for different passivation opening schemes. The abscissa and ordinate represented in Fig. 6.6 are the same as in Fig. 6.1. The point on the ordinate was selected to be near the surface, as the goal is to examine the factors that influence charge transport at the sensor's surface. From imaging the photon emission during avalanche breakdown shown in Fig. 4.20, 5.4, and 5.6, it is apparent that a high electric field is expected in the ER-GR region, and therefore, the focus is on this region, between $x = 50\,\mu\text{m}$ and $x = 250\,\mu\text{m}$. The ER starts at $x = 0\,\mu\text{m}$ and ends at $x = 106\,\mu\text{m}$, while the GR starts at $x = 237\,\mu\text{m}$ and ends at $x = 287\,\mu\text{m}$. In Fig. 6.6, it can be seen that for all passivation opening schemes the electric field profile is characterized by the presence of two electric field peaks: one near the ER at $x = 106.49\,\mu\text{m}$, and one near the GR at $x = 237.62\,\mu\text{m}$. These electric field

regions may be caused by the edge geometry of the electrodes, as suggested by a previous study [142]. An example of a metal overhang is shown in Fig. 4.7.

The amplitude of the two electric field peaks is similar across all cases except for the one with passivation openings at the GR and pad metal (Fig. 6.6 (b)). In this case, the electric field peak near the ER is slightly higher, at $\simeq 217\,\mathrm{kV \cdot cm^{-1}}$, compared to approximately $\simeq 176\,\mathrm{kV \cdot cm^{-1}}$ for the other three cases. Meanwhile, the electric field peak near the GR is slightly lower, measuring about $260\,\mathrm{kV \cdot cm^{-1}}$ instead of $305\,\mathrm{kV \cdot cm^{-1}}$ observed for the other cases.

The electric field profiles for passivation openings at the ER, GR, and pad metal shown in Fig. 6.6 (a); and at the GR and pad metal shown in Fig. 6.6 (b) do not change with the increase in RH immediately after ramping. This might be due to the charge dissipating through the passivation openings, with not enough time passing for effects to occur from the charge that could accumulate on the ER in cases where the resistive layer is capacitively coupled to it.

For the case with passivation openings at the ER presented in Fig. 6.6 (c), and with no passivation openings in Fig. 6.6 (d), the electric field peak near the GR has a slight increase at $RH = 40\,\%$. It can also be seen based on the electric field profile that the capacitive coupling of the resistive layer to the GR has a significant contribution to changes in the localized electric field, i.e., an increase at $RH = 40\,\%$ immediately after ramping. This might be caused by electrons accumulating on top of the positively biased electrode, which at high enough RH values contribute to changing the electric field.

The timestamp of 2500 s is chosen as a representative point to analyze the evolution of the figure of merit with respect to RH. This timestamp consists of an intermediate point where the leakage current corresponding to $RH = 40\,\%$ is already slowly increasing but remains in the pA range, while the leakage current for $RH = 30\,\%$ begins to rise. If the leakage current becomes high ($>$ nA), then the diode goes into breakdown; however, the purpose of this study is to understand what triggers the humidity-induced breakdown. This timestamp enables a comparison between the near onset of humidity-induced effects and established ones without the diode being in hard breakdown.

Fig. 6.7 shows the electric field values at $z = 100\,\mathrm{nm}$ along the abscissa as a function of RH at constant bias voltage $-900\,\mathrm{V}$ and $t = 2500\,\mathrm{s}$ for different passivation opening schemes. Similarly to the IV characteristics as a function of RH, there are no changes in the electric field profile for passivation openings at the ER, GR, and pad metal as seen in Fig. 6.7 (a).

For the passivation openings at the GR and pad metal included in Fig. 6.7 (b), the electric field changes only at $RH = 40\,\%$: the electric field peak near the ER increases from approx. $217\,\mathrm{kV \cdot cm^{-1}}$ to approx. $253\,\mathrm{kV \cdot cm^{-1}}$. It seems that under the influence of high humidity ($\geq 40\,\%$), when the resistive layer is capacitively coupled to the ER, positive charges with a high concentration ($\geq 1 \cdot 10^{16}\,\mathrm{cm^{-3}}$) extend past the ER such that they strengthen the electric field peak in that region as shown in Fig. 15 (c) in Appendix.

For passivation openings at the ER shown in Fig. 6.7 (c), and for no passivation openings shown in Fig. 6.7 (d), the electric field at $RH \leq 30\,\%$ has very small variations with time. This might be caused by the concentration of charges not extending beyond the electrodes, where they accumulated at $RH \leq 30\,\%$ such that these could have a significant impact on the electric field regions. At $RH = 40\,\%$, the electric field increases in both cases with a significant increase measured at the electric field peak near the GR. It seems that for higher humidity values, the charge concentration on top of the sensor's surface extended enough to impact the electric field strength. However, it is apparent in

Fig. 6.7 (d), that due to the resistive layer being capacitively coupled to both the ER and the GR, the electric field near the ER increases more in this case, although the greatest increase is still observed for the electric field near the GR ($\simeq 400\,\mathrm{kV}\cdot\mathrm{cm}^{-1}$). Therefore, the case with no passivation openings was selected for further presentation. It should be noted that this study is qualitative, and the aim is to understand what happens at the surface of the sensors in humid conditions.

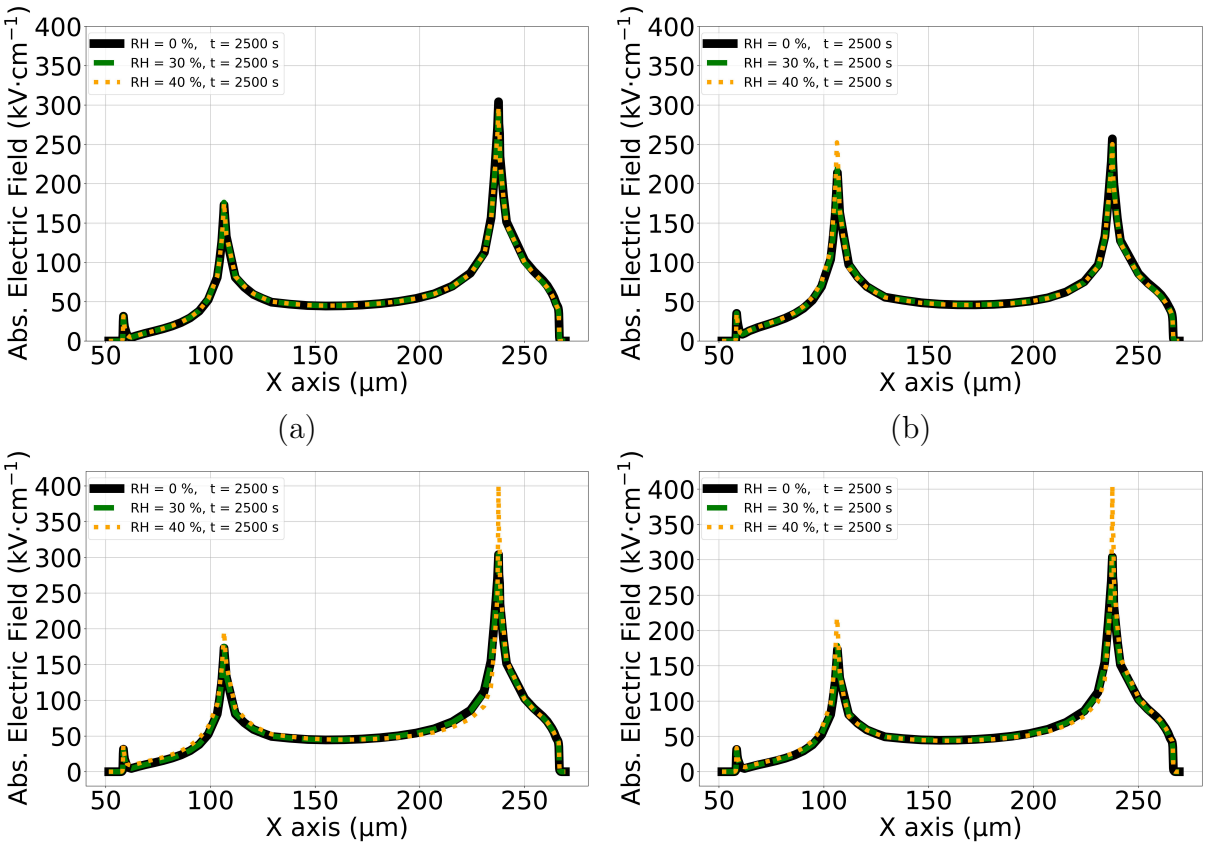

Figure 6.7: Electric field profile for $z = 100\,\mathrm{nm}$ along the abscissa as a function of RH at $V_{bias} = -900\,\mathrm{V}$ and $t = 2500\,\mathrm{s}$ for different passivation openings: at the ER, GR, and pad metal (a); at the GR and pad metal (b); at the ER (c); and with no passivation openings (d).

6.3.3 No Passivation Openings: Electric Field

The 2D plots of the electric field distribution for an MD8 diode with no passivation openings at $V_{bias} = -900\,\text{V}$ after waiting some time ($t = 2500\,\text{s}$) for different RH values are shown in Fig. 6.8. To understand how charge transport at the sensor's surface changes with RH, only the first $\pm 4\,\mu\text{m}$ on the ordinate was represented. The color scheme for TCAD simulation results was chosen to resemble a heat map: dark blue corresponds to regions where the electric field is minimum, while red is used to represent the maximum values. The maximum amplitude of the electric field was set to 150 $\text{kV} \cdot \text{cm}^{-1}$ because, at this value, changes in the electric field peaks are most visible.

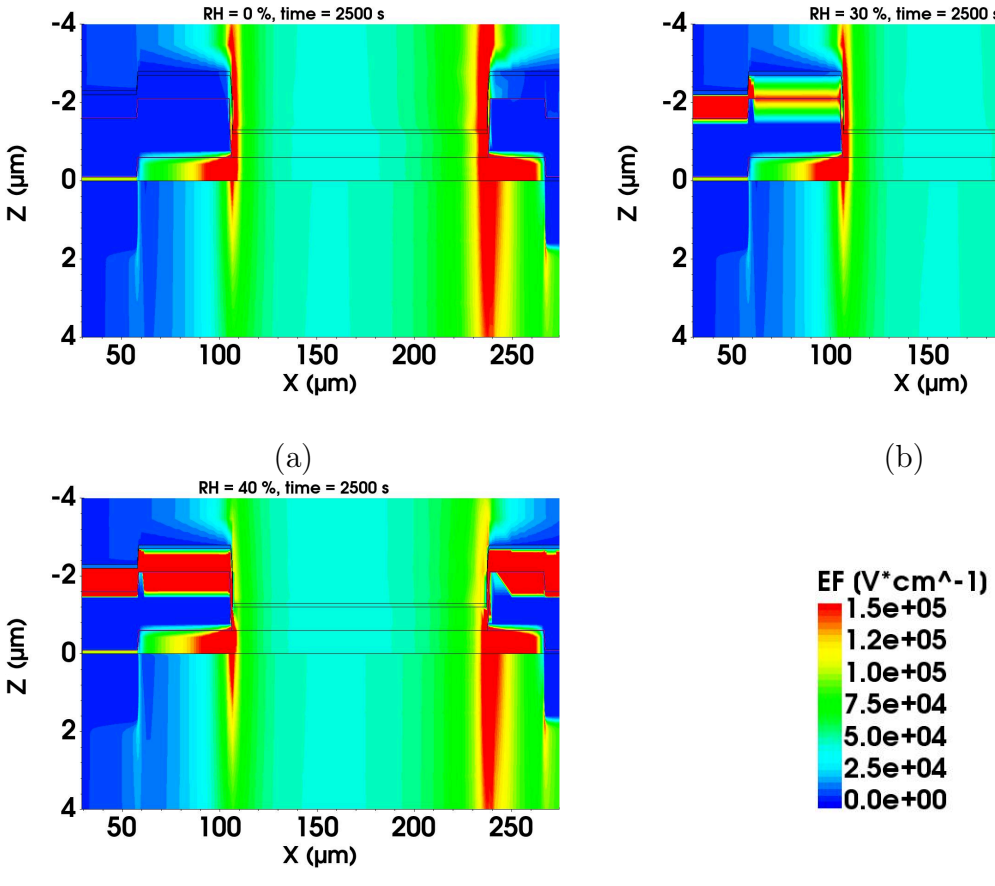

(a) (b) (c)

Figure 6.8: 2D representation of the absolute electric field at $V_{bias} = -900\,\text{V}$ and $t = 2500\,\text{s}$ for an MD8 diode with no passivation openings, and for different RH values: 0 % (a), 30 % (b), and 40 % (c).

The two high electric field peaks identified in Fig. 6.6 are also visible in Fig. 6.8 regardless of RH. One high electric field region is localized near the ER, while another is near the GR. The electric field distribution at $RH \leq 30,\%$ is similar to that at $RH = 0\,\%$. However, when RH reaches 40 %, the electric field peaks near the ER and GR exhibit an amplitude decrease outside of the sensor. As a result of increased humidity, electrons accumulate on top of the GR, while holes accumulate on top of the ER within the highly resistive layer on top of the passivation. Once the leakage current starts to increase, the electron and hole accumulation on top of the passivation move past the GR and ER, respectively. As a result, the electric field is shielded inside the sensor. Furthermore, the

electric field near the ER increases inside the silicon bulk.

6.3.4 No Passivation Openings: Electron Density

The 2D profiles of the electron density for an MD8 diode with no passivation openings with a focus on the ER-GR region at constant bias ($V_{bias} = -900\,\mathrm{V}$) and $t = 2500\,\mathrm{s}$ for different RH values are presented in Fig. 6.9. The electron density ranges from $10^6\,\mathrm{cm}^{-3}$, represented with dark blue to $10^{16}\,\mathrm{cm}^{-3}$, represented with red. It can be seen that for all RH values, between the two electrodes, underneath the passivation, there is a non-negligible inversion layer with a concentration of $\geq 10^7\,\mathrm{cm}^{-3}$. This might contribute to the increase in leakage current over time. Ideally, in an over-biased sensor ($V_{bias} \gg V_{FD}$), there should be no inversion layer in the depletion region. However, some electrons are attracted to the positive fixed oxide charges at the interface of the Si-SiO_2. This could become an operational problem if the concentration of electrons exceeds the silicon bulk doping, creating a conductive channel between the two electrodes and potentially leading to electrical breakdown.

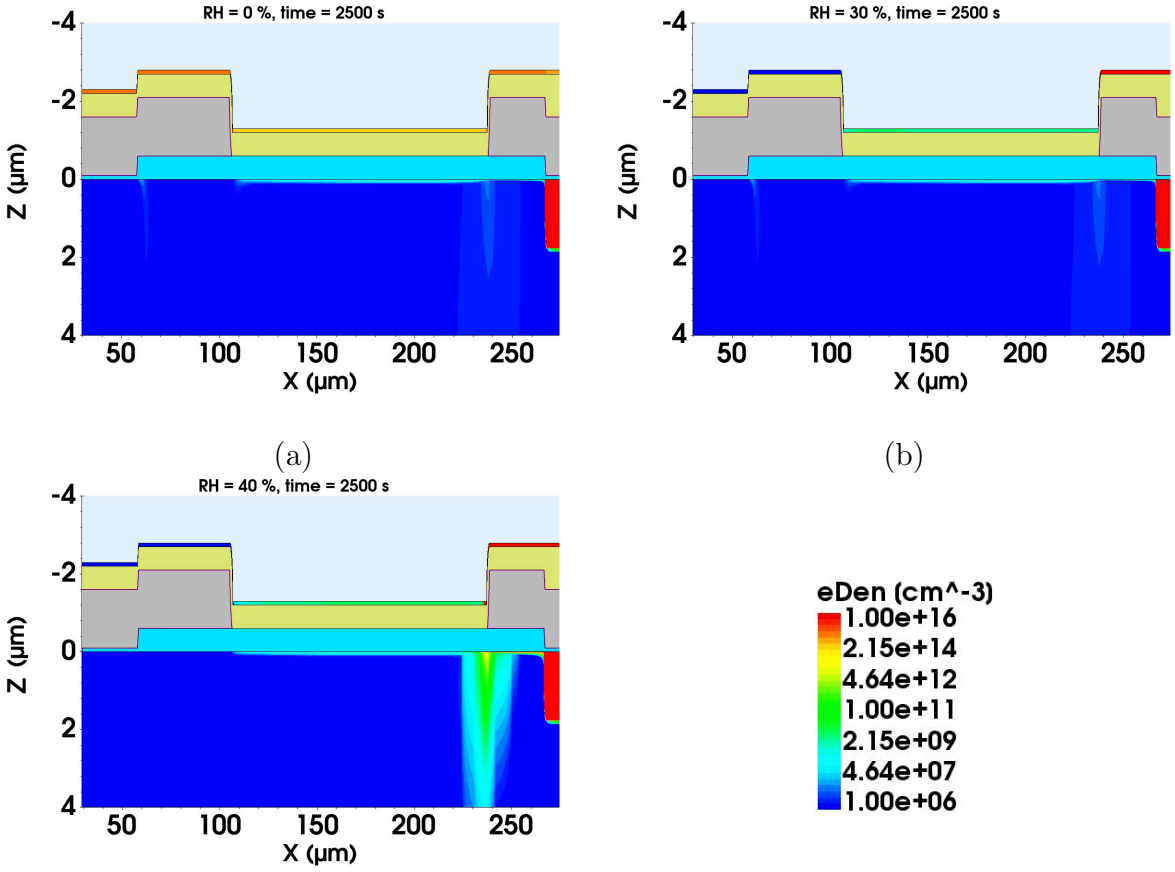

(a) (b) (c)

Figure 6.9: 2D representation of the electron density at $V_{bias} = -900\,\mathrm{V}$ and $t = 2500\,\mathrm{s}$ for an MD8 diode with no passivation openings, and for different RH values: 0 % (a), 30 % (b), and 40 % (c).

When $RH \geq 30\,\%$, a high density of electrons ($\geq 1 \cdot 10^{16}\,\mathrm{cm}^{-3}$) accumulates inside the highly resistive layer on top of the passivation, because they are attracted to the positive

bias voltage (the GR is at ground). This seems to agree with the Atalla model [81], which predicts that in humid conditions, negative charges accumulate on top of the electrode with an n-type implant, while positive charges accumulate on top of the electrode with a p-type implant. Conversely, in dry conditions, the electron concentration inside the resistive layer on top of the passivation is spread uniformly.

In contrast, at $RH = 40\,\%$, the electron accumulation on top of the GR spreads enough laterally such that it strengthens the electric field peak here, which becomes high enough to generate secondary charge ionization as seen by the electrons accumulating with a concentration $\geq 1 \cdot 10^{11}\,\mathrm{cm}^{-3}$ underneath the edge of the GR. This would explain the high leakage current measured at $RH = 40\,\%$.

6.3.5 No Passivation Openings: Hole Density

The spatial distributions of the hole density for an MD8 diode with no passivation openings at $t = 2500\,\mathrm{s}$ and constant bias ($V_{bias} = -900\,\mathrm{V}$) as a function of RH are presented in Fig. 6.10. The minimum hole density ($10^{6}\,\mathrm{cm}^{-3}$) is represented with dark blue, while the maximum ($10^{16}\,\mathrm{cm}^{-3}$) is represented with red.

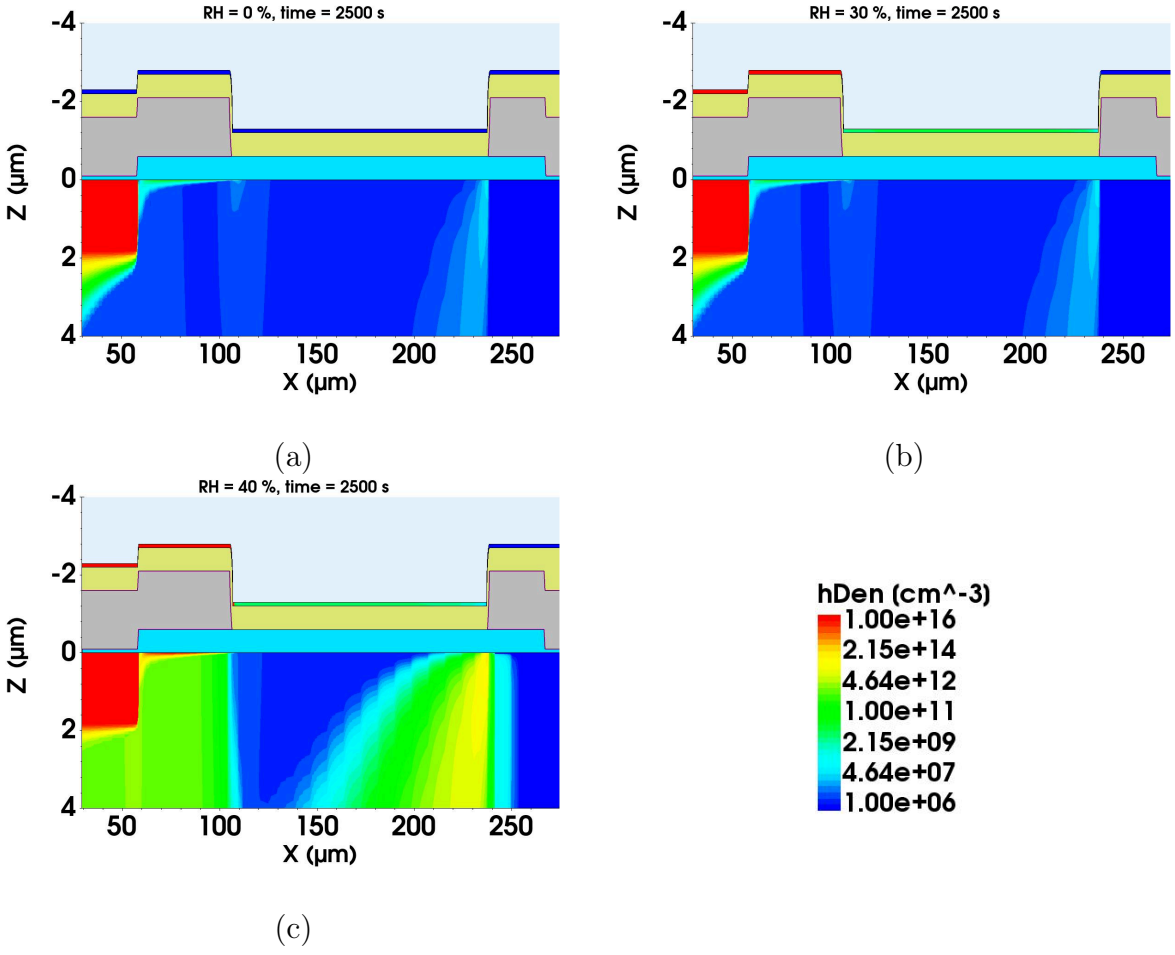

(a) (b) (c)

Figure 6.10: 2D representation of the hole density at $V_{bias} = -900\,\mathrm{V}$ and $t = 2500\,\mathrm{s}$ for an MD8 diode with no passivation openings, and for different RH values: 0 % (a), 30 % (b), and 40 % (c).

When $RH \leq 30\,\%$, holes with a concentration $\geq 10^{7}\,\mathrm{cm}^{-3}$ accumulate near the p-implant and in the vicinity of the GR. In dry conditions, holes are spread evenly inside

the highly resistive layer on top of the passivation. However, when $RH \geq 30\,\%$, a high concentration of holes ($\geq 1 \cdot 10^{16}$) accumulates on top of the ER because they get attracted by the negative bias voltage.

At $RH = 40\,\%$, the hole accumulation on top of the ER extends laterally beyond the electrode. This behavior is similar to the electron accumulation on top of the GR, which also extends past the GR at high humidity. The lateral extension of the charge accumulation on top of these electrodes is believed to be the driving factor of the humidity effect. Humidity lowers the sheet resistance of passivated silicon sensors, as shown in [139]. When the sheet resistance is lowered, the mobility of charge carriers increases. The corresponding mobility for the sheet resistance measured at $RH = 30\,\%$ increases by a factor of 10 compared to that at $RH = 40\,\%$ based on the values derived in Table 6.1. In the TCAD simulation, the effect of humidity in facilitating charge movement is observed through the accumulation and lateral extension of positive charges on top of the ER and negative charges on the GR.

Furthermore, holes with a concentration of $\geq 1 \cdot 10^{12}\,\mathrm{cm}^{-3}$ have accumulated between the two electrodes because charges get accelerated in the electric field regions near the ER and the GR, which can gain enough energy to create impact ionization and generate free carriers. This could also explain the high leakage current measured at $RH = 40\,\%$.

6.3.6 No Passivation Openings: Impact Ionization

The 2D distributions of the generation rate of free carriers from impact ionization at constant bias $V_{bias} = -900\,\mathrm{V}$ and $t = 2500\,\mathrm{s}$ as a function of RH, are plotted in Fig. 6.11.

The generation rate is defined as follows:

$$U = \frac{n_i}{\tau}, \tag{6.12}$$

where n_i is the generation rate usually expressed in $\mathrm{cm}^{-3} \cdot \mathrm{s}^{-2}$, and τ is the SRH lifetime expressed in seconds. The intrinsic charge carriers generation rate was defined in equation 3.17.

For $T = 295.6\,\mathrm{K}$, the main parameters of the intrinsic charge carriers generation rate have the following values:

$$E_g \simeq 1.12\,\mathrm{eV}, \tag{6.13}$$
$$N_c \simeq 2.74 \cdot 10^{19}\,\mathrm{cm}^{-3}, \tag{6.14}$$
$$N_v \simeq 3.03 \cdot 10^{19}\,\mathrm{cm}^{-3}, \tag{6.15}$$
$$k_B = 1.38 \cdot 10^{-23}\,\mathrm{J/K}. \tag{6.16}$$

Introducing the numerical values from 6.13 to 3.17, the intrinsic charge carriers generation rate value is calculated to be $7.22 \cdot 10^9\,\mathrm{cm}^{-3}$. Replacing the intrinsic charge carriers' generation rate with its numerical value, the generation rate is obtained as:

$$U = 7.22 \cdot 10^{10}\,\mathrm{cm}^{-3} \cdot \mathrm{s}^{-1}. \tag{6.17}$$

In Fig. 6.11, the color scale starts from $7.22 \cdot 10^{10}\,\mathrm{cm}^{-3} \cdot \mathrm{s}^{-1}$, which is the generation rate of the bulk derived in equation 6.17. The maximum was set to $10^{21}\,\mathrm{cm}^{-3} \cdot \mathrm{s}^{-1}$, which is the maximum value of impact ionization. For $RH \leq 30\,\%$, impact ionization regions occur near the ER with a magnitude of $\geq 1 \cdot 10^{15}\,\mathrm{cm}^{-3} \cdot \mathrm{s}^{-1}$, and near the GR with a higher magnitude of $\geq 5 \cdot 10^{15}\,\mathrm{cm}^{-3} \cdot \mathrm{s}^{-1}$. In contrast, at $RH = 40\,\%$, the impact

ionization regions extend further laterally, and a new maximum is present near the GR ($\geq 10^{21}\,\mathrm{cm}^{-3}\cdot\mathrm{s}^{-1}$). It is expected that these impact ionization regions correspond to the high electric field peaks. Free carriers are generated in these regions, which leads to their accumulation between the electrodes, and a significant increase in leakage current for high humidities ($RH \geq 40\,\%$).

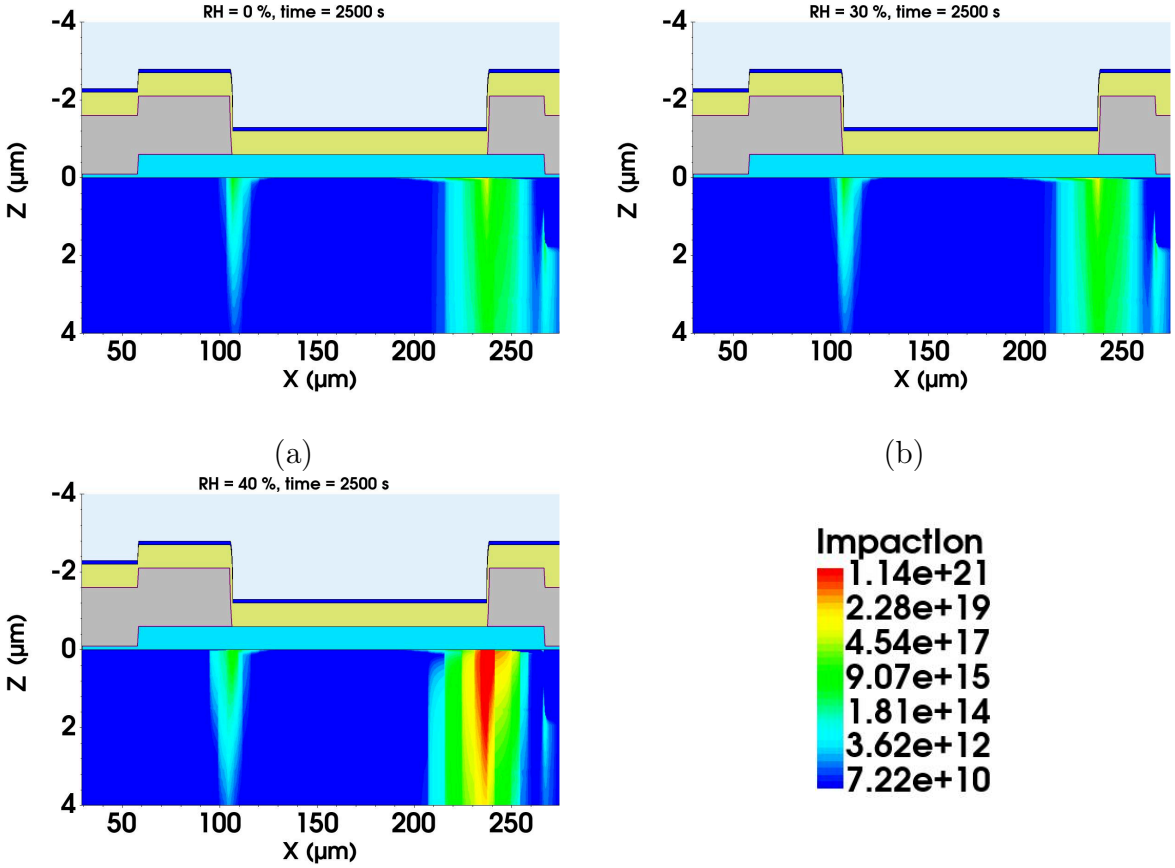

(a) (b) (c)

Figure 6.11: 2D representation of the generation rate of free charge carriers from impact ionization at $V_{bias} = -900\,\mathrm{V}$ and $t = 2500\,\mathrm{s}$ for an MD8 diode with no passivation openings, and for different RH values: 0 % (a), 30 % (b), and 40 % (c).

6.4 Fixed Oxide Charge Concentration Effects

6.4.1 Fixed Oxide Charge Concentration: IV Characteristics

During the thermal growth of silicon dioxide at the surface of silicon, fixed oxide charges can occur at the interface between the two. The process of thermal oxidation requires high temperatures, which can facilitate an irregular arrangement of the atomic structure of silicon and silicon dioxide. If oxygen atoms are missing from their sites, then oxygen vacancies can be created, leading to the creation of fixed oxide charges. Fixed oxide charges can alter the electric field locally, which can influence the recombination rate of carriers and the leakage current.

One negative impact induced by the fixed oxide charges is the presence of an electron inversion layer near the surface between the ER and the GR even after a high bias voltage was applied ($V_{bias} \gg V_{FD}$), which can be observed in the electron density distributions (see Fig. 6.9). Electrons with a concentration of $1 \cdot 10^7\,\mathrm{cm}^{-3}$ are attracted by the positive fixed oxide charges at the interface. This could become an operational issue if the concentration of electrons is high enough to create a conductive channel between the two electrodes, which could lead to an electrical breakdown. The fixed oxide charge concentration (Q_{ox}) for the ATLAS strip sensors has been measured to be approx. $1 \cdot 10^{11}\,\mathrm{cm}^{-2}$ [59]. However, variations in the Q_{ox} occur from batch to batch. To understand the cumulative effects on the breakdown voltage of humidity and Q_{ox}, TCAD simulations of an MD8 diode with no passivation openings were done for three values of the Q_{ox}: $1 \cdot 10^{10}\,\mathrm{cm}^{-2}$, $5 \cdot 10^{10}\,\mathrm{cm}^{-2}$, and $1 \cdot 10^{11}\,\mathrm{cm}^{-2}$.

The IV-const characteristics of an MD8 diode without passivation openings, as a function of Q_{ox} at $T = 295.6\,\mathrm{K}$ and $V_{bias} = -900\,\mathrm{V}$ for three RH values, are presented in Fig. 6.12. The leakage current is shown for the GR. The bias voltage was applied similarly to the IVs presented in Fig. 6.5. The IV characteristics during the ramping period exhibit a similar behavior for all Q_{ox}. After the full bias voltage was reached, the GR leakage current increased with RH for all Q_{ox} values. The GR leakage current increases inversely with the concentration of fixed oxide charges. An increase in fixed oxide charges would attract more electrons close to the interface, which would increase the leakage current. Examining the electron density distributions, it seems that a lower concentration of fixed oxide charges ($1 \cdot 10^{10}\,\mathrm{cm}^{-2}$) spatially attracts more electrons close to the surface (see Fig. 6.17 (a)) than a higher concentration ($1 \cdot 10^{11}\,\mathrm{cm}^{-2}$).

For $Q_{ox} = 1 \cdot 10^{10}\,\mathrm{cm}^{-2}$, at $RH \leq 30\,\%$, immediately after ramping, the leakage current increases to values $\geq 5\,\mathrm{pA}$, however remaining in the range of pA, which is lower than the ATLAS requirement for unirradiated diodes of $1\,\mu\mathrm{A}$. At $RH = 40\,\%$, the leakage current starts increasing rapidly from $t = 1164\,\mathrm{s}$. As previously mentioned, it was observed in the electron density profiles (see Fig. 6.17-6.18) that the electron inversion layer is marginally more dispersed in space for $Q_{ox} = 1 \cdot 10^{10}\,\mathrm{cm}^{-2}$ than for higher values. The electrons in the inversion layer may be accelerated in the high electric field regions near the ER and the GR such that they gain enough energy to produce impact ionization, leading to free carriers generation. The production of more free carriers would lead to an increase in the leakage current.

For $Q_{ox} = 5 \cdot 10^{10}\,\mathrm{cm}^{-2}$ and $Q_{ox} = 1 \cdot 10^{11}\,\mathrm{cm}^{-2}$, in dry conditions, the leakage current remains relatively stable during the 4050 s after ramping shown in Fig. 6.12, with a difference between the two of $\simeq 2\,\mathrm{pA}$. From section 6.3, it was observed that the effects of humidity are connected with the lateral spread of the charge accumulation inside the

resistive layer on top of the ER and the GR. In dry conditions, electrons and holes inside the resistive layer on top of the passivation do not accumulate to the GR and ER, respectively. Without the effect of humidity, the electric field would not increase enough to produce impact ionization. Given that for $Q_{ox} \geq 5 \cdot 10^{10}\,\mathrm{cm}^{-2}$, the inversion layer at the surface is less prominent, and the electric field is not high enough to generate free carriers through impact ionization, the free electrons in the inversion layer do not significantly contribute to the leakage current.

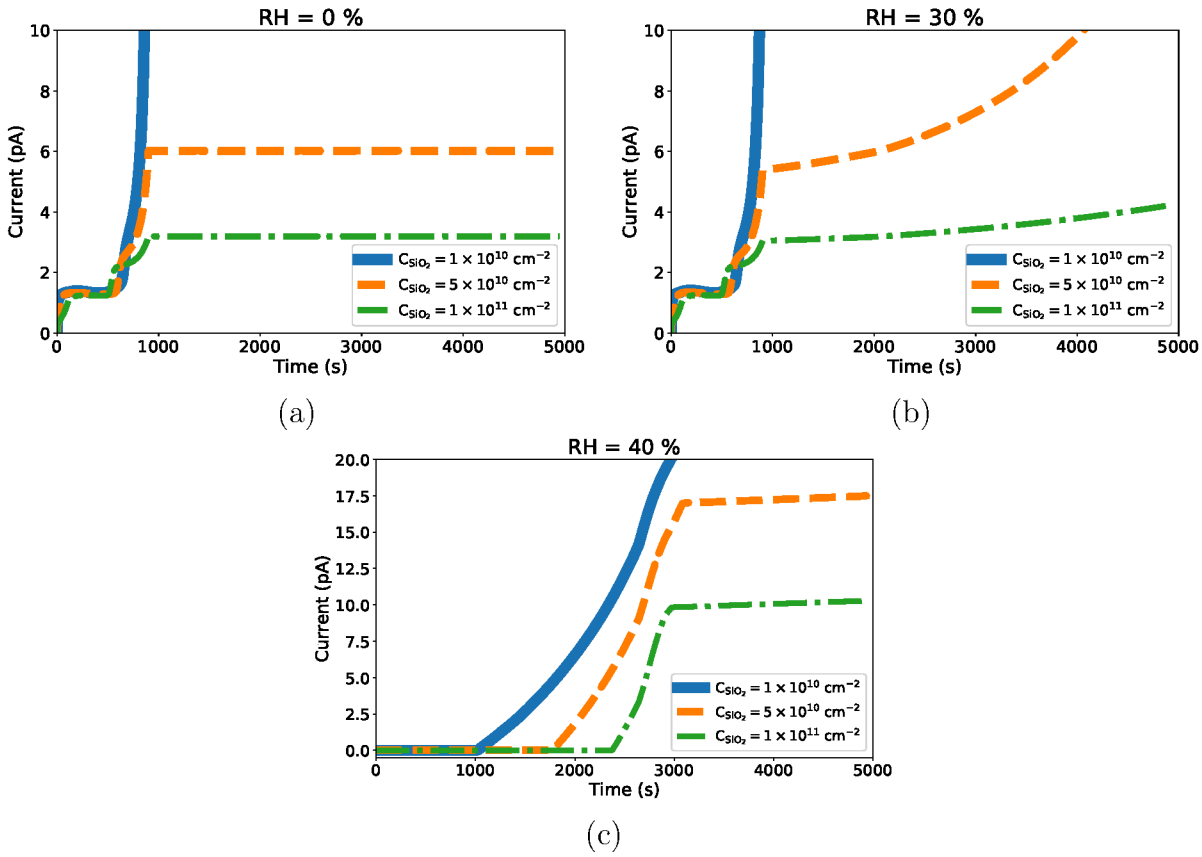

Figure 6.12: IV-const characteristics obtained for the GR at $T = 295.6\,\mathrm{K}$ as a function of Q_{ox}: $1 \cdot 10^{10}\,\mathrm{cm}^{-2}$ (with blue), $5 \cdot 10^{10}\,\mathrm{cm}^{-2}$ (with orange), and $1 \cdot 10^{11}\,\mathrm{cm}^{-2}$ (with green), for different RH values: 0 % (a), 30 % (b), and 40 % (c). The first 900 s correspond to the ramping time: $-10\,\mathrm{V}/10\,\mathrm{s}$, and afterwards the bias voltage remained constant ($-900\,\mathrm{V}$).

At $RH = 30\,\%$, the leakage current corresponding to $Q_{ox} = 5 \cdot 10^{10}\,\mathrm{cm}^{-2}$ starts to increase immediately after ramping, while the leakage current corresponding to $Q_{ox} = 1 \cdot 10^{11}\,\mathrm{cm}^{-2}$ starts to increase at $t \simeq 2000\,\mathrm{s}$.

At $RH = 40\,\%$, for $Q_{ox} = 5 \cdot 10^{10}\,\mathrm{cm}^{-2}$, the leakage current starts to increase rapidly from $t \simeq 1750\,\mathrm{s}$ until it reaches an inflection point in the $\mathcal{O}(10^{-6})\,\mathrm{A}$ at $t \simeq 3100\,\mathrm{s}$. The same behavior is present for $Q_{ox} = 1 \cdot 10^{11}\,\mathrm{cm}^{-2}$, when the leakage current starts increasing at $t \simeq 2370\,\mathrm{s}$ and it reaches an inflection point at $t \simeq 2980\,\mathrm{s}$ in the $\mathcal{O}(10^{-6})\,\mathrm{A}$.

At RH values higher than 30 %, the leakage current rise can be attributed to humidity. When $RH \leq 30\,\%$ the electron and hole accumulation inside the resistive layer on top of the passivation has a considerable impact on the electric field amplitude, such that it can generate free carriers from impact ionization. As more free carriers are produced, the leakage current increases.

6.4.2 Fixed Oxide Charge Concentration: Electric Field Cutlines

The electric field profiles at $z = 100\,\text{nm}$ along the abscissa immediately after ramping ($t = 900\,\text{s}$) at constant bias ($V_{bias} = -900\,\text{V}$) in terms of RH and Q_{ox} are presented in Fig. 6.13. Similarly to the results presented in Fig. 6.6, at $t = 900\,\text{s}$, the electric field profile at the edge of the MD8 exhibits two high electric field peaks: one at the edge of the ER at $x = 106.49\,\mu\text{m}$, and one at the edge of the GR at $x = 237.62\,\mu\text{m}$. For each Q_{ox} value, the electric field peaks have minimal variations with the increase in RH. For the same RH value, the electric field peak near the ER increases with the increase in Q_{ox}, whereas the one near the GR decreases with the increase in Q_{ox}.

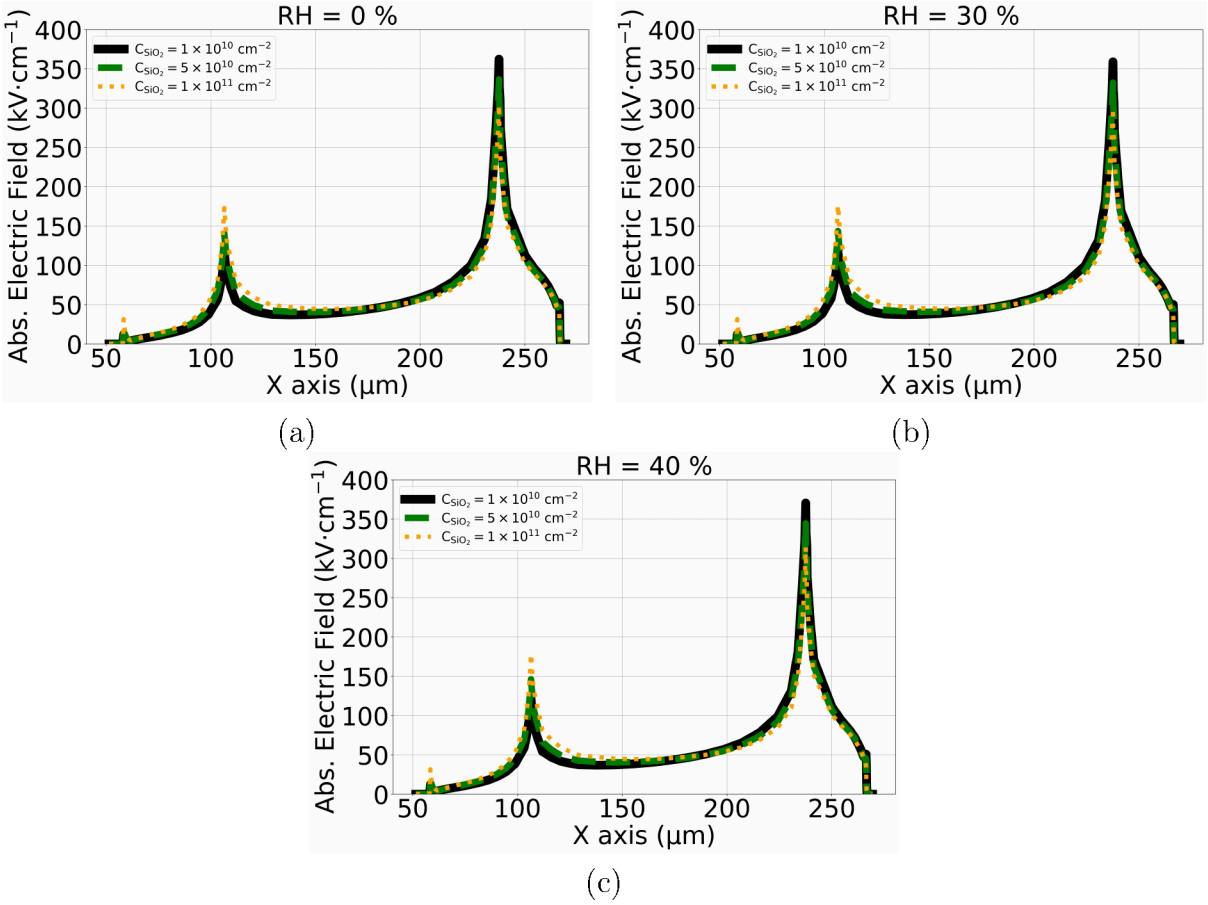

Figure 6.13: Electric field profile for $z = 100\,\text{nm}$ along the abscissa at $V_{bias} = -900\,\text{V}$ and $t = 900\,\text{s}$ as a function of Q_{ox} for different RH values: 0 % (a), 30 % (b), and 40 % (c).

It seems that a low concentration of fixed oxide charges ($1 \cdot 10^{10}\,\text{cm}^{-2}$) creates a lower electric field ($150\,\text{kV} \cdot \text{cm}^{-1}$) near the ER than at higher concentrations. In contrast, this same low concentration creates a stronger electric field near the GR compared to higher concentration values. This observation is counterintuitive since the expectation is to have an increase in the electric field amplitude for both regions. This expectation stems from the fact that for a fixed Q_{ox}, the electric field is directly proportional to the charge density [39]:

$$\mathcal{E} = \frac{Q_{ox}}{A\epsilon_{ox}}, \tag{6.18}$$

where A is the area populated by fixed oxide charges and ϵ_{ox} is the permitivity of the

oxide. It should be noted that the fixed oxide charges were implemented uniformly at the interface between Si-SiO_2, and therefore, the electric field should increase with the increase in Q_{ox}. This suggests that different effects contribute to the unexpected variations in the electric field, which have not yet been understood.

Fig. 6.14 shows the absolute electric field profile for $z = 100\,\text{nm}$ along the abscissa as a function of Q_{ox} and RH after waiting some time ($t = 3500\,\text{s}$) at constant bias voltage ($V_{bias} = -900\,\text{V}$). This timestamp was selected because variations in the electric field and carrier density were visible for $RH \geq 30\,\%$.

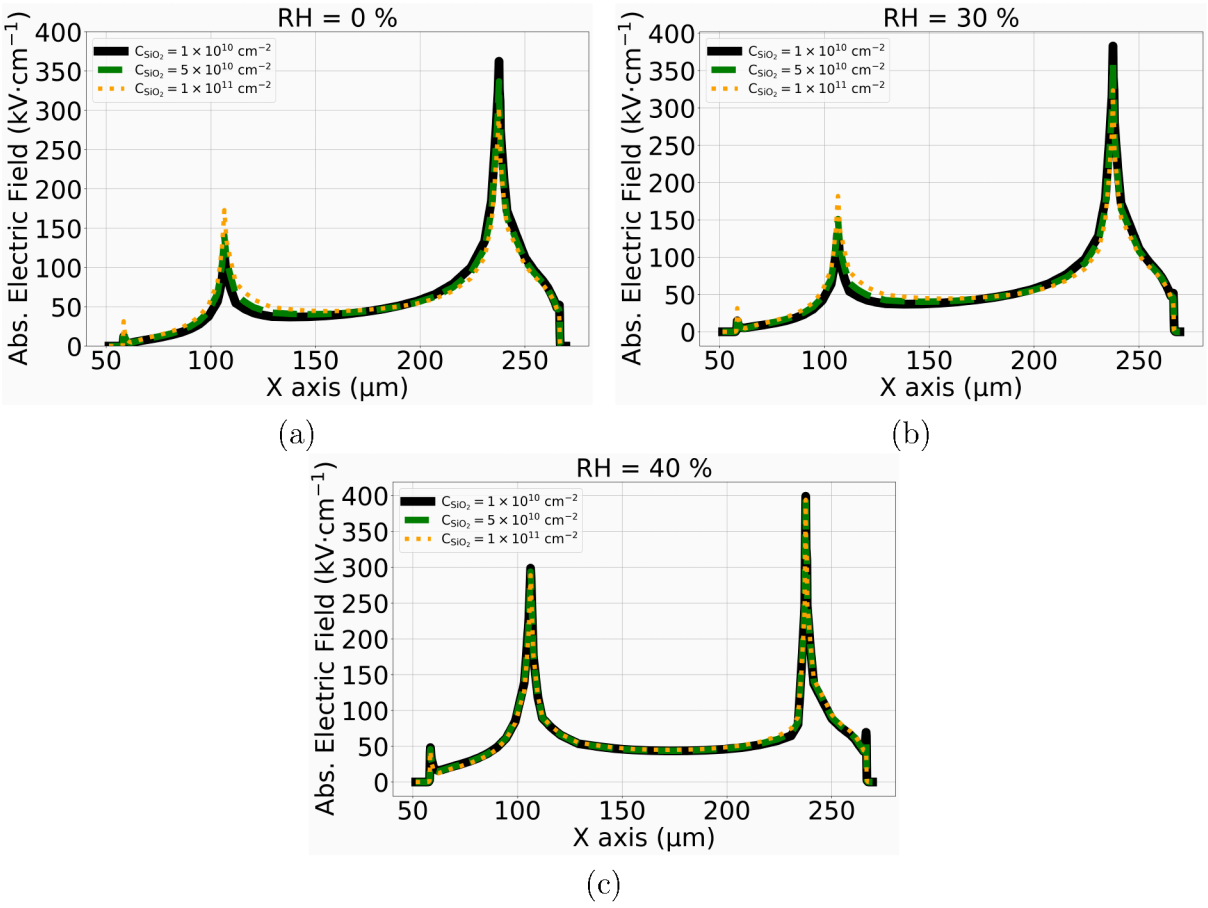

Figure 6.14: Electric field profile for $z = 100\,\text{nm}$ along the abscissa at $V_{bias} = -900\,\text{V}$ and $t = 3500\,\text{s}$ as a function of Q_{ox} for different RH values: 0 % (a), 30 % (b), and 40 % (c).

In dry conditions, the electric field profile remains the same between 900 s and 3500 s as it can be seen by comparing Fig. 6.13 (a)-6.14 (a) and Fig. 6.13 (b)-6.14 (b).

At $RH = 30\,\%$ the field peak near the GR increases with the increase in Q_{ox}, as seen in Fig. 6.14 (b). This might be explained by the electron accumulation inside the resistive layer on top of the GR, which extends past it such that it can strengthen the electric field in this region.

At $RH = 40\,\%$, the field peak near the ER increases to $300\,\text{kV} \cdot \text{cm}^{-1}$, while the field peak near the GR increases to $400\,\text{kV} \cdot \text{cm}^{-1}$ for each Q_{ox}. This could be attributed to the positive and negative charges accumulating inside the resistive layer on top of the GR and ER, respectively. The carrier separation leads to local changes in the electric field and increased amplitude.

At the same time, at $RH = 40\,\%$, the field distribution between $x = 200\,\mu\text{m}$ and $x = 237\,\mu\text{m}$ decreases to approximately $60\,\text{kV} \cdot \text{cm}^{-1}$. This might stem from the free

carriers accumulating between the two electrodes, which can have a screening effect on the electric field.

6.4.3 Fixed Oxide Charge Concentration: Electric Field

At $RH = 40\,\%$ and $t \geq 2500\,\mathrm{s}$, the amplitude of the electric field peak at $x = 237.62\,\mu\mathrm{m}$ (near the GR) is $400\,\mathrm{kV \cdot cm^{-1}}$. This value is similar across different concentrations of fixed oxide charges. Comparing the electron and hole densities when the electric field has similar values may not provide insight into what drives the increase in the electric field amplitude at low Q_{ox} values. Therefore, the figures of merit are presented for $RH = 30\,\%$ to understand better how the fixed oxide charge concentration affects the electrical behavior of the diode in conjunction with the humidity effect.

The electric field spatial distributions for an MD8 without passivation openings at constant bias voltage ($V_{bias} = -900\,\mathrm{V}$), temperature ($T = 295.6\,\mathrm{K}$), and humidity ($RH = 30\,\%$), immediately after ramping ($t = 900\,\mathrm{s}$) as a function of Q_{ox} are presented in Fig. 6.15. The color scale has been fixed similarly to the results shown in Fig. 6.8, where the minimum electric field is $0\,\mathrm{V \cdot cm^{-1}}$, and it is represented with dark blue, while the maximum electric field was set to $1.5 \cdot 10^5\,\mathrm{V \cdot cm^{-1}}$, and it is represented with red. For all Q_{ox} values, two high-field regions are present: one near the ER and one near the GR.

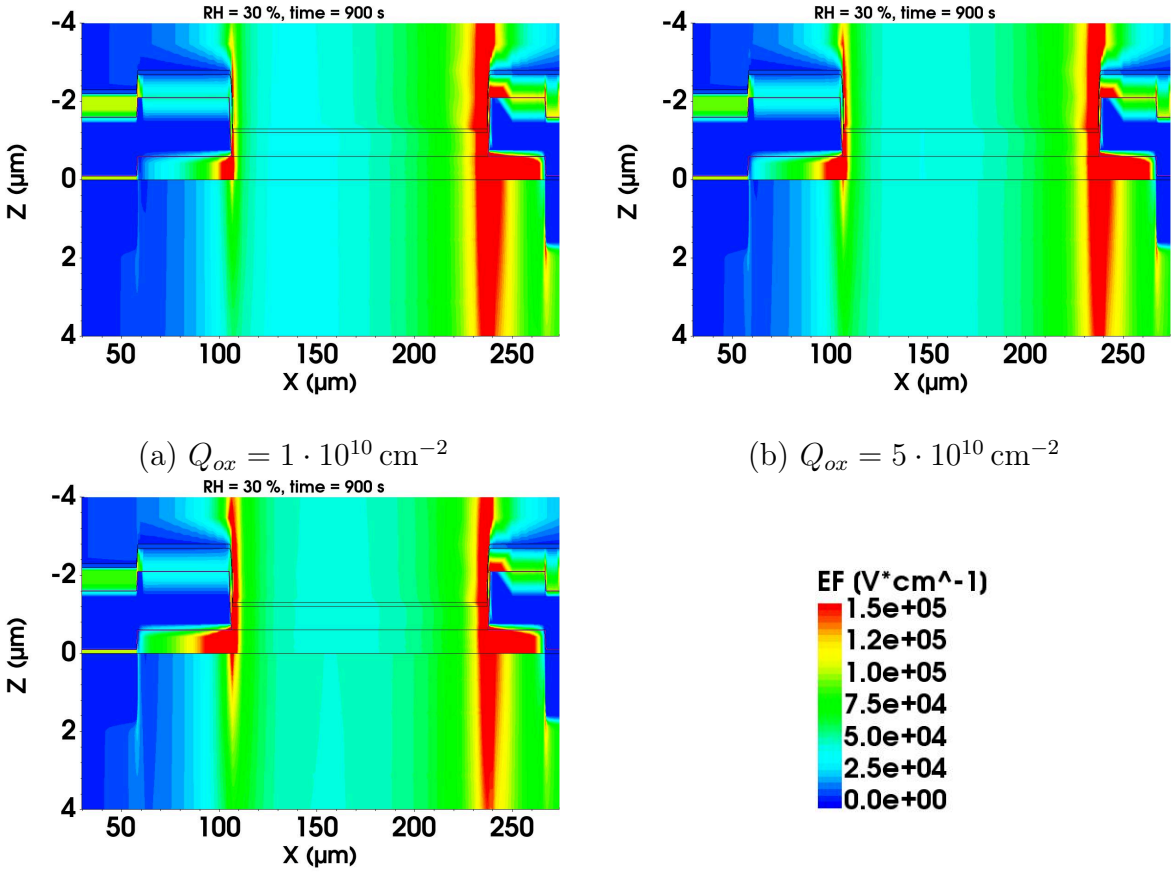

(a) $Q_{ox} = 1 \cdot 10^{10}\,\mathrm{cm^{-2}}$

(b) $Q_{ox} = 5 \cdot 10^{10}\,\mathrm{cm^{-2}}$

(c) $Q_{ox} = 1 \cdot 10^{11}\,\mathrm{cm^{-2}}$

Figure 6.15: 2D representation of the absolute electric field at $V_{bias} = -900\,\mathrm{V}$, $RH = 30\,\%$, and $t = 900\,\mathrm{s}$ for different Q_{ox} values: $1 \cdot 10^{10}\,\mathrm{cm^{-2}}$ (a), $5 \cdot 10^{10}\,\mathrm{cm^{-2}}$ (b), and $1 \cdot 10^{11}\,\mathrm{cm^{-2}}$ (c).

The electric field region near the ER is initially small for $Q_{ox} = 1 \cdot 10^{10}\,\mathrm{cm}^{-2}$, but it shows a slight lateral and longitudinal spread with the increase in Q_{ox}. In contrast, the electric field peak near the GR is initially much more prominent, showing a slight lateral decrease with the increase in Q_{ox}.

Fig. 6.16 shows the electric field spatial distribution after waiting some time at constant bias voltage and RH as a function of Q_{ox}. At $t = 3500\,\mathrm{s}$ and $Q_{ox} = 1 \cdot 10^{10}\,\mathrm{cm}^{-2}$, the electric field at $x = 106.49\,\mu\mathrm{m}$ is shielded inside the silicon. Holes accumulate inside the highly resistive layer on top of the ER, and over time, they extend beyond the electrode, shielding the electric field. This effect is less visible for $Q_{ox} \geq 5 \cdot 10^{10}\,\mathrm{cm}^{-2}$.

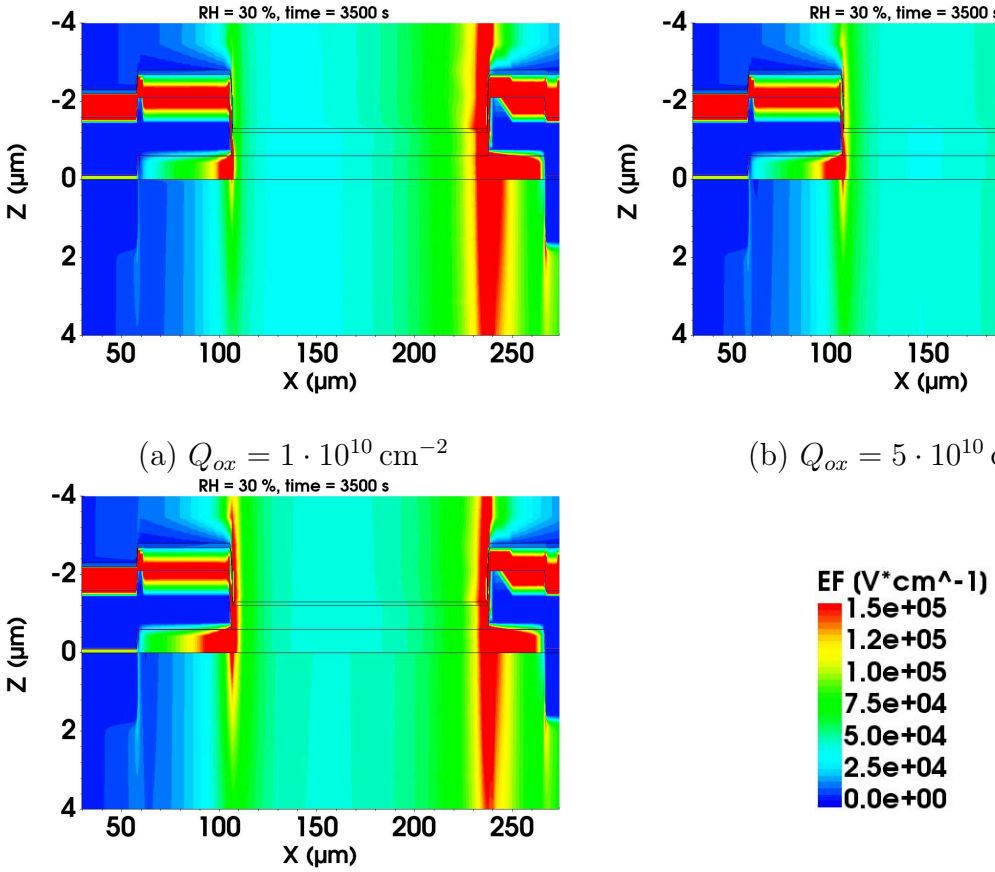

(a) $Q_{ox} = 1 \cdot 10^{10}\,\mathrm{cm}^{-2}$

(b) $Q_{ox} = 5 \cdot 10^{10}\,\mathrm{cm}^{-2}$

(c) $Q_{ox} = 1 \cdot 10^{11}\,\mathrm{cm}^{-2}$

Figure 6.16: 2D representation of the absolute electric field at $V_{bias} = -900\,\mathrm{V}$, $RH = 30\,\%$, and $t = 3500\,\mathrm{s}$ for different Q_{ox} values: $1 \cdot 10^{10}\,\mathrm{cm}^{-2}$ (a), $5 \cdot 10^{10}\,\mathrm{cm}^{-2}$ (b), and $1 \cdot 10^{11}\,\mathrm{cm}^{-2}$ (c).

6.4.4 Fixed Oxide Charge Concentration: Electron Density

The electron density 2D maps at $t = 900\,\mathrm{s}$, $V_{bias} = -900\,\mathrm{V}$ and $RH = 30\,\%$ as a function of Q_{ox} are shown in Fig. 6.17. The color map has been chosen in a similar manner to Fig. 6.9: the minimum is $10^6\,\mathrm{cm}^{-3}$, while the maximum is set to $10^{16}\,\mathrm{cm}^{-3}$. An unwanted feature that has been observed in previous plots is the low-density electron inversion layer between the ER and the GR, which is also visible in Fig. 6.17. For $Q_{ox} = 1 \cdot 10\,\mathrm{cm}^{-2}$, the inversion layer appears relatively wider as seen in Fig. 6.17 than for the other Q_{ox} values. It seems that the electron inversion layer decreases with the increase in Q_{ox}. This may be related to the same trend observed in the electric field distributions. If the electric field near the GR decreases in amplitude, then fewer electrons are accelerated in this region, gaining enough energy to create impact ionization, which leads to the generation of free carriers. As previously mentioned, it is not yet understood why the electric field near the GR decreases with the increase in Q_{ox} for $RH \leq 30\,\%$.

It should be noted that the electron accumulation inside the polysilicon layer on top of the GR is an effect of humidity, which is expected to be independent of the Q_{ox} variations.

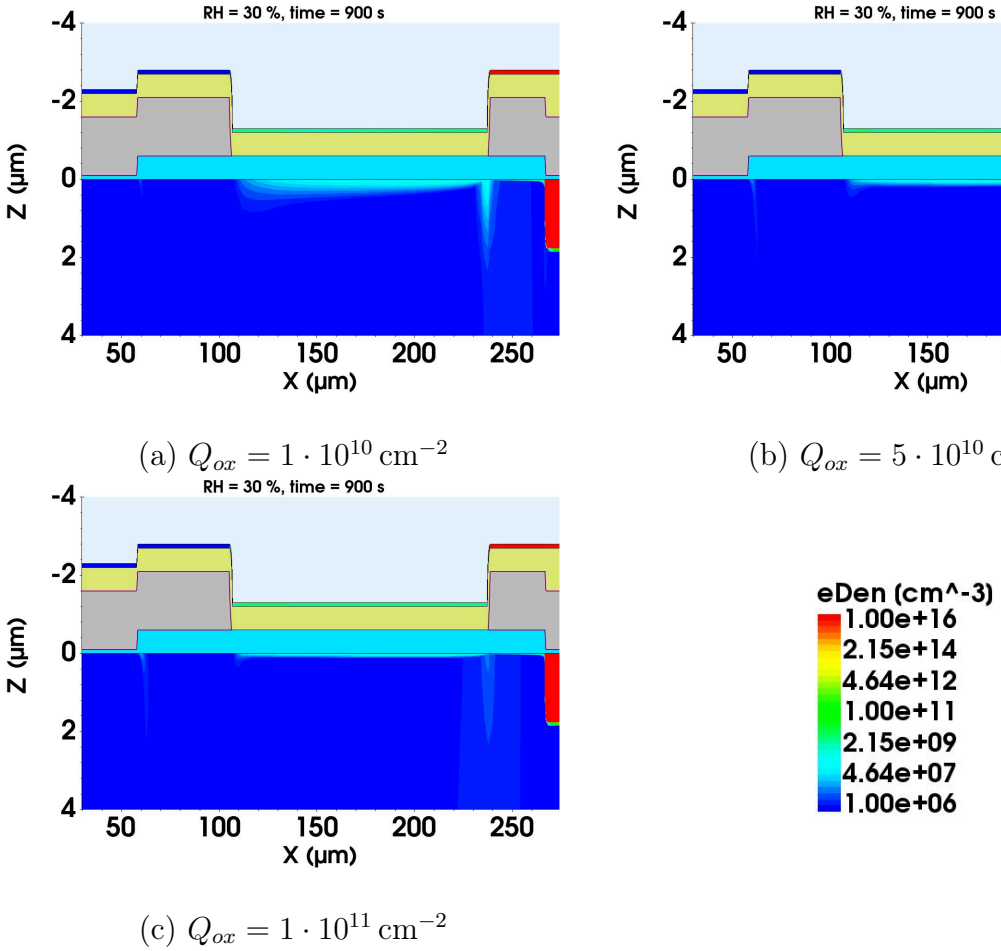

(a) $Q_{ox} = 1 \cdot 10^{10}\,\mathrm{cm}^{-2}$

(b) $Q_{ox} = 5 \cdot 10^{10}\,\mathrm{cm}^{-2}$

(c) $Q_{ox} = 1 \cdot 10^{11}\,\mathrm{cm}^{-2}$

Figure 6.17: 2D representation of the electron density at $V_{bias} = -900\,\mathrm{V}$, $RH = 30\,\%$, and $t = 900\,\mathrm{s}$ for different Q_{ox} values: $1 \cdot 10^{10}\,\mathrm{cm}^{-2}$ (a), $5 \cdot 10^{10}\,\mathrm{cm}^{-2}$ (b), and $1 \cdot 10^{11}\,\mathrm{cm}^{-2}$ (c).

Fig. 6.18 shows the electron density spatial distributions after waiting some time ($t = 3500\,\mathrm{s}$) at constant bias voltage, $V_{bias} = -900\,\mathrm{V}$ and $RH = 30\,\%$ for different Q_{ox} values. It can be seen in Fig. 6.18 (a), that for $Q_{ox} = 1 \cdot 10^{10}\,\mathrm{cm}^{-2}$ electrons have accumulated

underneath the GR with a concentration $\geq 1 \cdot 10^{11}\,\mathrm{cm}^{-3}$ and between the ER-GR region with a lower concentration. This is a result of the free electrons in the inversion layer, which were accelerated in the high electric field at the GR such that they gained enough energy to create impact ionization, leading to free carrier generation. A substantial increase of the inversion layer can be observed in Fig. 6.18 (b). No changes in the electron density near the silicon surface are observed for $Q_{ox} \geq 5 \cdot 10^{11}\,\mathrm{cm}^{-2}$.

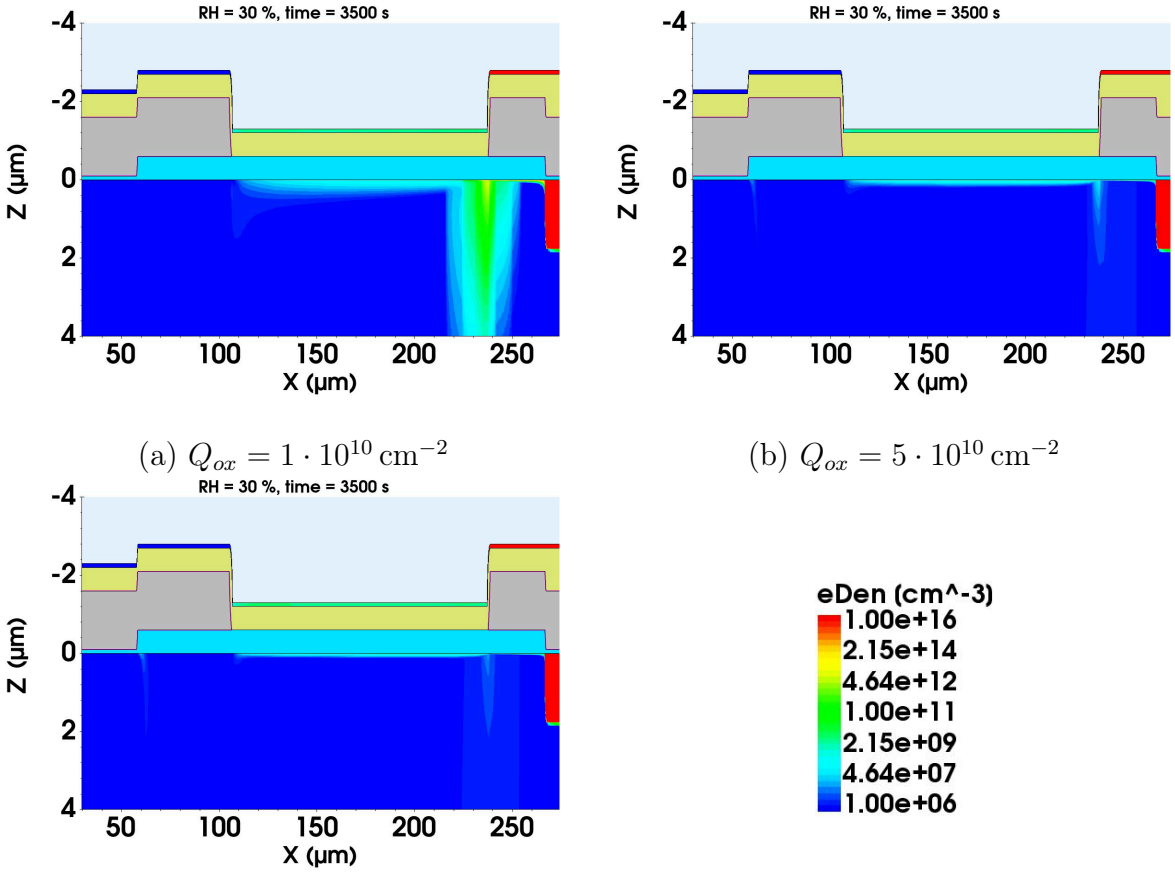

(a) $Q_{ox} = 1 \cdot 10^{10}\,\mathrm{cm}^{-2}$

(b) $Q_{ox} = 5 \cdot 10^{10}\,\mathrm{cm}^{-2}$

(c) $Q_{ox} = 1 \cdot 10^{11}\,\mathrm{cm}^{-2}$

Figure 6.18: 2D representation of the electron density at $V_{bias} = -900\,\mathrm{V}$, $RH = 30\,\%$, and $t = 3500\,\mathrm{s}$ for different Q_{ox} values: $1 \cdot 10^{10}\,\mathrm{cm}^{-2}$ (a), $5 \cdot 10^{10}\,\mathrm{cm}^{-2}$ (b), and $1 \cdot 10^{11}\,\mathrm{cm}^{-2}$ (c).

6.4.5 Fixed Oxide Charge Concentration: Hole Density

The spatial representation of the hole density immediately after ramping at $V_{bias} = -900\,\mathrm{V}$, and $RH = 30\,\%$ as a function of Q_{ox} is illustrated in Fig. 6.19. The color map is similar to the one used for the electron density: it starts at $10^6\,\mathrm{cm}^{-3}$ (dark blue) and increases up to $10^{16}\,\mathrm{cm}^{-3}$ (red). Regardless of the Q_{ox} value, a high density of holes ($\simeq 10^{16}\,\mathrm{cm}^{-3}$) has accumulated inside the resistive layer on top of the ER immediately after ramping. As previously observed, the separation of positive and negative charges within the resistive layer, along with their migration to the negatively and positively biased electrodes, is facilitated by the humidity-induced reduction in sheet resistance.

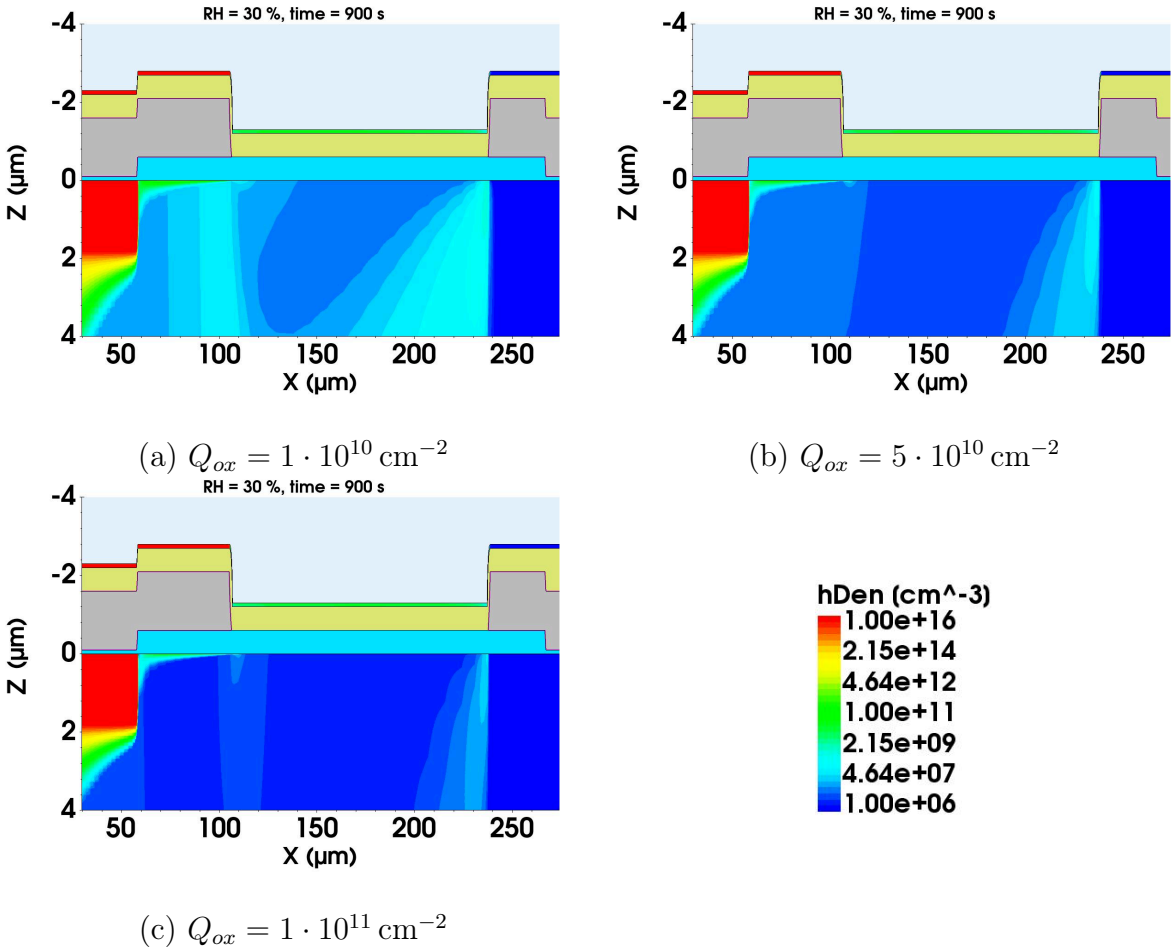

(a) $Q_{ox} = 1 \cdot 10^{10}\,\mathrm{cm}^{-2}$

(b) $Q_{ox} = 5 \cdot 10^{10}\,\mathrm{cm}^{-2}$

(c) $Q_{ox} = 1 \cdot 10^{11}\,\mathrm{cm}^{-2}$

Figure 6.19: 2D representation of the hole density at $V_{bias} = -900\,\mathrm{V}$, $RH = 30\,\%$, and $t = 900\,\mathrm{s}$ for different Q_{ox} values: $1 \cdot 10^{10}\,\mathrm{cm}^{-2}$ (a), $5 \cdot 10^{10}\,\mathrm{cm}^{-2}$ (b), and $1 \cdot 10^{11}\,\mathrm{cm}^{-2}$ (c).

For $Q_{ox} = 1 \cdot 10^{10}\,\mathrm{cm}^{-3}$, holes with a concentration $\geq 10^7\,\mathrm{cm}^{-3}$ are present between the ER and the GR immediately after the target bias voltage was reached. With the increase in Q_{ox}, the holes appear to become more dispersed, but a small accumulation remains near the edges of both electrodes. The decrease in the spatial spread of the holes with the increase of Q_{ox} is directly connected to the electric field dependence on Q_{ox}.

Fig. 6.20 shows the 2D distributions of the hole density after waiting some time at $RH = 30\,\%$ and $V_{bias} = -900\,\mathrm{V}$ for different Q_{ox} values. For $Q_{ox} = 1 \cdot 10^{10}\,\mathrm{cm}^{-2}$ the hole density in the ER and GR region increases to values $\geq 10^{11}\,\mathrm{cm}^{-3}$ after waiting some time because free carriers are generated from impact ionization. For $Q_{ox} = 5 \cdot 10^{10}\,\mathrm{cm}^{-2}$, the holes have spread laterally underneath the GR from $x = 190\,\mu\mathrm{m}$ to $x = 240\,\mu\mathrm{m}$. In

contrast, the hole density corresponding to $Q_{ox} = 1 \cdot 10^{11}\,\mathrm{cm}^{-2}$ exhibits minimal changes with time.

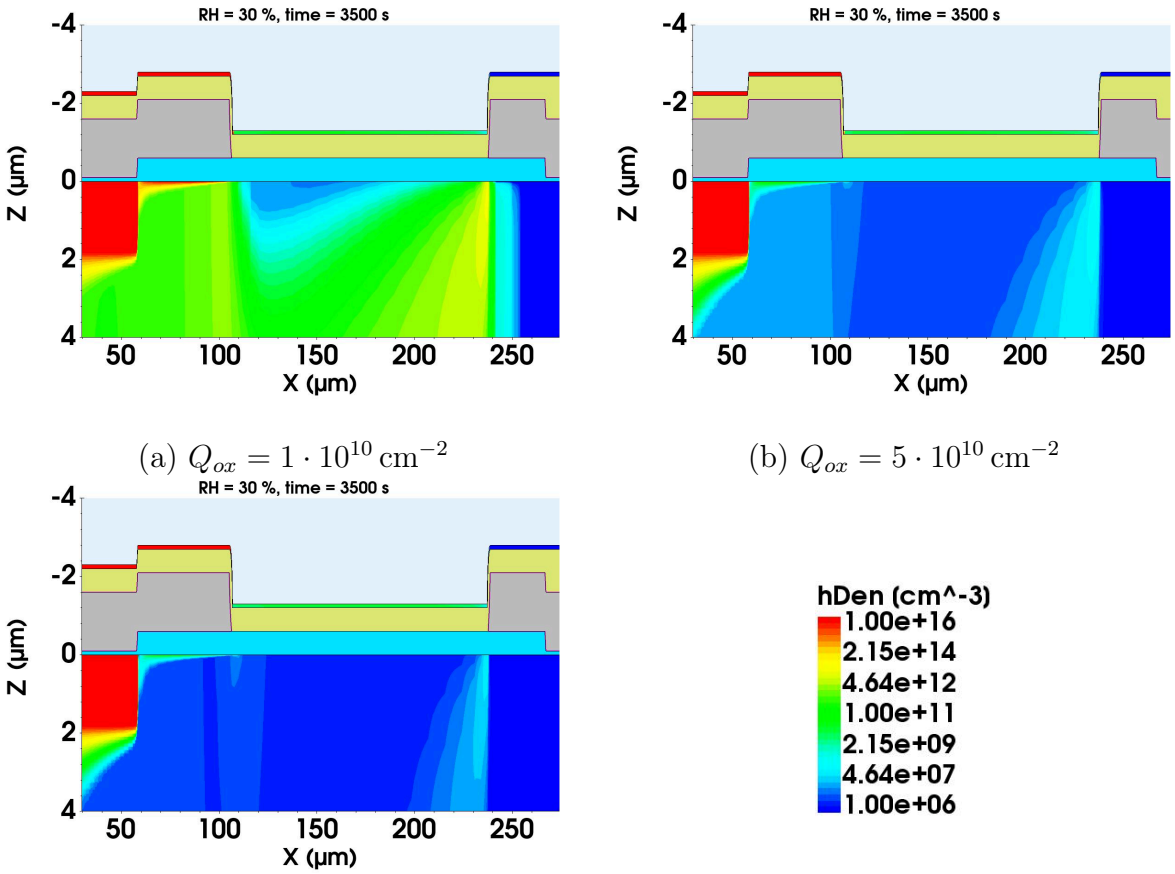

(a) $Q_{ox} = 1 \cdot 10^{10}\,\mathrm{cm}^{-2}$

(b) $Q_{ox} = 5 \cdot 10^{10}\,\mathrm{cm}^{-2}$

(c) $Q_{ox} = 1 \cdot 10^{11}\,\mathrm{cm}^{-2}$

Figure 6.20: 2D representation of the hole density at $V_{bias} = -900\,\mathrm{V}$, $RH = 30\,\%$, and $t = 3500\,\mathrm{s}$ for different Q_{ox} values: $1 \cdot 10^{10}\,\mathrm{cm}^{-2}$ (a), $5 \cdot 10^{10}\,\mathrm{cm}^{-2}$ (b), and $1 \cdot 10^{11}\,\mathrm{cm}^{-2}$ (c).

6.4.6 Fixed Oxide Charge Concentration: Impact Ionization

The 2D plots of the generation rate of free charge carriers from impact ionization at $V_{bias} = -900\,\mathrm{V}$ and RH $= 30\,\%$ immediately after ramping ($t = 900\,\mathrm{s}$) as a function of Q_{ox} are presented in Fig. 6.21. For all Q_{ox} values, there are two impact ionization regions present: one region is underneath the edge of the ER and one underneath the edge of the GR. These regions coincide with the electric field peaks seen in Fig. 6.13. The impact ionization region near the ER grows spatially with the increase in Q_{ox}, while the impact ionization region near the GR has a moderate decrease with the increase in Q_{ox}. The regions of impact ionization are expected to follow the behavior of the electric field, as it accelerates electrons, enabling them to gain sufficient energy to initiate impact ionization.

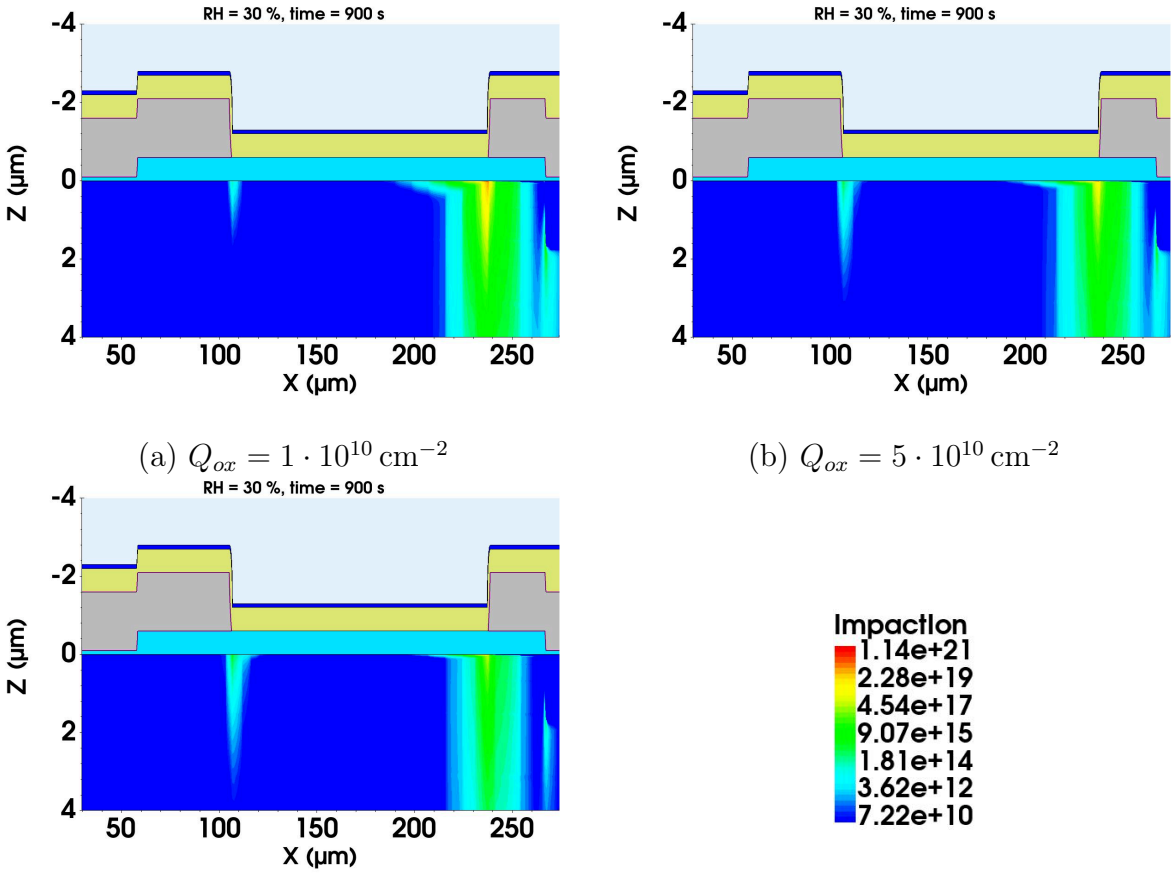

(a) $Q_{ox} = 1 \cdot 10^{10}\,\mathrm{cm}^{-2}$

(b) $Q_{ox} = 5 \cdot 10^{10}\,\mathrm{cm}^{-2}$

(c) $Q_{ox} = 1 \cdot 10^{11}\,\mathrm{cm}^{-2}$

Figure 6.21: 2D representation of the generation rate of carriers from impact ionization at $V_{bias} = -900\,\mathrm{V}$, $RH = 30\,\%$, and $t = 900\,\mathrm{s}$ for different Q_{ox} values: $1 \cdot 10^{10}\,\mathrm{cm}^{-2}$ (a), $5 \cdot 10^{10}\,\mathrm{cm}^{-2}$ (b), and $1 \cdot 10^{11}\,\mathrm{cm}^{-2}$ (c).

Fig. 6.22 shows the spatial representation of the generation rate of free charge carriers from impact ionization at constant bias voltage ($-900\,\mathrm{V}$), $t = 3500\,\mathrm{s}$ and $RH = 30\,\%$ as a function of Q_{ox}. For the lowest Q_{ox}, the impact ionization region underneath the GR extends laterally inside the silicon, and it develops a new maximum $U \geq 10^{21}\,\mathrm{cm}^{-3} \cdot \mathrm{s}^{-1}$. At the same time, the impact ionization region underneath the ER also extends on the abscissa and ordinate inside the silicon. This is directly connected to the increase in the electric field amplitude, which is high enough to accelerate electrons to the point where they gain sufficient energy to create impact ionization. Furthermore, minimal

changes occur in the impact ionization regions at the edges of the two electrodes for $Q_{ox} = 5 \cdot 10^{10}\,\mathrm{cm}^{-2}$ and $Q_{ox} = 1 \cdot 10^{11}\,\mathrm{cm}^{-2}$.

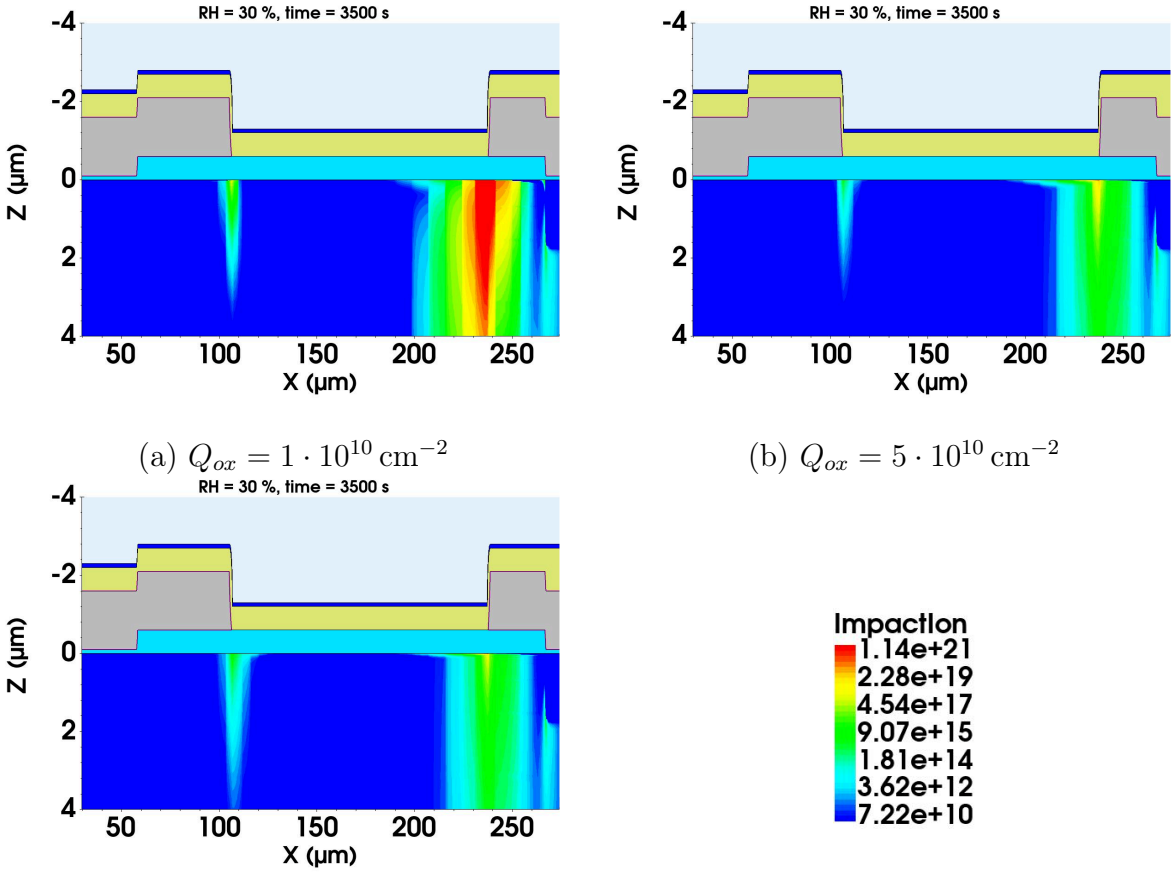

(a) $Q_{ox} = 1 \cdot 10^{10}\,\mathrm{cm}^{-2}$

(b) $Q_{ox} = 5 \cdot 10^{10}\,\mathrm{cm}^{-2}$

(c) $Q_{ox} = 1 \cdot 10^{11}\,\mathrm{cm}^{-2}$

Figure 6.22: 2D representation of the generation rate of carriers from impact ionization at $V_{bias} = -900\,\mathrm{V}$, $RH = 30\,\%$, and $t = 3500\,\mathrm{s}$ for different Q_{ox} values: $1 \cdot 10^{10}\,\mathrm{cm}^{-2}$ (a), $5 \cdot 10^{10}\,\mathrm{cm}^{-2}$ (b), and $1 \cdot 10^{11}\,\mathrm{cm}^{-2}$ (c).

It is not yet understood what phenomena strengthen the electric field value for lower Q_{ox} values. However, this observation might be an indication that higher levels of fixed oxide charges might not pose a concern in a dry atmosphere. A study focused on curing early breakdown in sensors [143] found that irradiation improves the current-voltage characteristics of silicon strip sensors. During the production phase of the ATLAS ITk strip project, it was observed that silicon strip sensors showed a lowered breakdown voltage due to mechanical damage, long-term application of voltage, humidity exposure, tasks such as gluing, etc.

For the study conducted in Reference [143], two Long Strip modules were electrically investigated. The Long Strip sensor has the same edge geometry as the strip sensor described in section 4.5 (see Fig. 4.18). The edge geometry is also identical with the MD8 diodes, with an edge ring with a p-implant, a guard ring, and a bias ring, both with n-implants.

Fig. 6.23 shows an example of an IV characteristics for a Long Strip module after assembly and after irradiation with gamma rays up to 11 krad. The breakdown voltage after module assembly is lower than the ATLAS requirement of 500 V. After irradiation,

the breakdown increased to 700 V. An improvement of the leakage current was observed after irradiation treatment for both Long Strip modules. Although the study in [143] proposes a possible treatment for sensors with lower breakdown voltage, an explanation of why irradiation improves the electrical behavior of sensors is not provided.

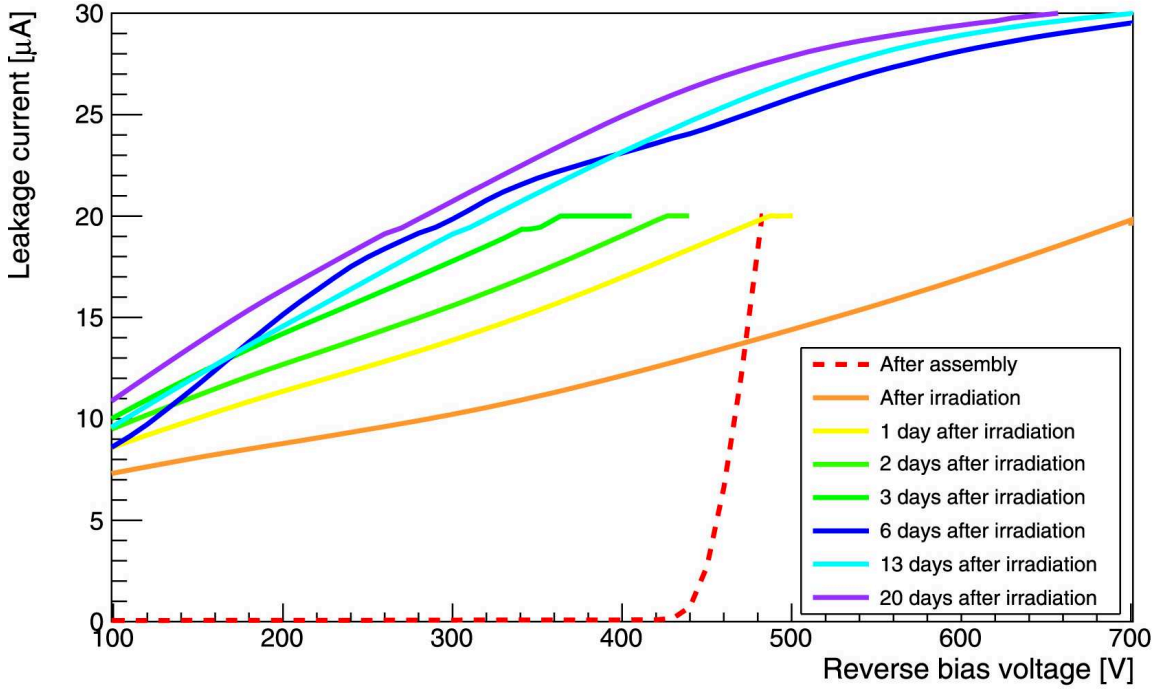

Figure 6.23: Current-Voltage measurements for an ATLAS ITk Long Strip module after assembly and after irradiation with gamma rays up to 11 krad [143].

During irradiation treatment, gamma rays can produce electron-hole pairs inside the silicon dioxide. The slow-moving holes can get trapped at the interface between silicon and silicon dioxide, increasing the concentration of fixed oxide charges. An increase in the fixed oxide concentration may improve the leakage current, as shown in the section. To verify this hypothesis, the fixed oxide concentration of the sensors before and after irradiation treatment should be measured in future studies.

Chapter 7

Discussion and Outlook

7.1 Assessment of Experimental and Simulated Data

The ATLAS detector will be upgraded to cope with the increased radiation levels resulting from the operation of the High-Luminosity Large Hadron Collider, beginning with Run 4. One of the major upgrades planned for ATLAS is the replacement of the Inner Detector (ID) with an all-silicon Inner Tracker (ITk). The new inner tracker consists of a pixel detector surrounded by a strip detector. During the prototyping phase, some of the silicon strip sensors showed signs of humidity sensitivity. When the sensors were exposed to $RH \geq 20\,\%$, some had a lower breakdown voltage. To mitigate the humidity sensitivity of sensors, they are stored and electrically tested in dry conditions $RH \leq 10\,\%$. Humidity will not pose a risk during the ATLAS operation, because the detector will operate in a dry environment. However, humidity may pose a risk if the sensors are accidentally exposed to high humidity due to a maintenance failure of the laboratory infrastructure, and then undergo electrical testing. Understanding the mechanisms that cause humidity sensitivity in silicon sensors is important for developing future detectors that can operate in harsher environments. The present research aimed to study the charge transport at the surface of n-in-p silicon diodes from the same wafer as the strip sensor in both dry and humid conditions, using the Top-Transient Current Technique (TCT) and Technology Computer-Aided Design (TCAD) simulations.

A digital microscope was used to investigate the geometry of 8 mm by 8 mm n-in-p silicon diodes (MD8) from the same wafer as the strip sensor. The dimensions of the Edge Ring (ER), Guard Ring (GR), and pad, along with their respective implants, were measured digitally based on the obtained images. These details were used to implement the edge geometry of the diode in TCAD from Synopsis.

The MD8 diodes available at DESY Zeuthen were visually inspected using a similar digital microscope. The diodes found to be free of defects were measured in humid conditions using a probe station and a Top-Transient Current Technique (Top-TCT) setup. Diodes featuring surface scratches were used to test the capabilities of the experimental setups and to observe photon emission during avalanche breakdown at the edge of the diode.

Capacitance-Voltage (CV) measurements were performed to infer the full depletion voltage, active thickness, and effective bulk doping. From Current-Voltage (IV) characteristics corresponding to the pad metal, the saturation current was obtained. Using the saturation current, the lifetime recombination of carriers was determined, which was later implemented in the simulation to obtain more realistic results.

IV measurements of MD8 diodes in dry and humid conditions were performed using a probe station setup. The sensors were tested at five relative humidity (RH) values: 10 %, 20 %, 30 %, 40 % and 50 %. The IV characteristics were done starting from the lowest RH to avoid hysteresis effects. In humid conditions, the water molecules may dissociate into positive and negative ions. The mobility of the ions appear to increase with the increase in relative humidity. If the measurements were started at high RH values, then the mobility of surface ions will be high. Even if the RH would be lowered, the surface charges would not have enough time to relax, such that their mobility would correspond to the effect of the target RH, leading to hysteresis.

An example of IV characteristics in terms of relative humidity for an MD8 was presented in Fig. 5.7. It was previously observed that for RH values lower than 40 %, the current-voltage characteristics have a similar amplitude, however for 50 %, an increase in leakage current is seen for voltage values higher than 900 V. Although the diodes tested did not show the same linear response to humidity as the strip sensor, a threshold was identified at which humidity effects start in the MD8 diodes.

Some MD8 diodes were also investigated in both dry and humid conditions using the Top-TCT setup. The Top-TCT employs a red laser to generate electron-hole pairs at the surface of the sensor. The drift of the generated charge carriers leads to the formation of the transient current, which was measured on the backside metal as a function of RH. The prompt current consists of an additional confirmation of the presence of a high electric field near the GR.

Multiple sets of measurements were done to investigate whether the system is affected by hysteresis. For this, the Top-TCT scans were performed starting from the highest RH value, $RH = 50\,\%$, and then the relative humidity was lowered in steps of 10 % until the RH reached 10 %. The charge profile and prompt current as a function of RH were found to be the same, independent of humidity, when the scans are performed from the highest target RH to the lowest, confirming that hysteresis affects the system.

A longer Top-TCT scan, consisting of scanning the laser from the edge ring toward the pad window multiple times was performed for the same conditions as the TCAD simulations, namely, $RH = 40\,\%$, $T = 295.6\,\mathrm{K}$. Further details about the simulated electric field along with the prompt current derived from Top-TCT measurements for two timestamps ($t_1 = 900\,\mathrm{s}$ and $t_2 = 2500\,\mathrm{s}$) will be discussed in the next section (7.1.1).

The edge geometry of the MD8 was implemented in TCAD from Synopsis. The electrical behavior of the diode was simulated using literature values for humidity-dependent resistive effects for three RH values (0 %, 30 % and 40 %) and for different passivation opening schemes: at the Edge Ring (ER); at the Guard Ring (GR) and pad; at the ER, GR and pad, and for no passivation openings. A passivation opening is a place on the surface of the sensor, usually on the electrodes, where there is no passivation deposited. Passivation openings are useful because they give easy access to tasks such as wirebonding. Based on the IV characteristics as a function of RH presented in Fig. 6.5, it was concluded that the diode with passivation openings at the GR and pad, and with no passivation openings exhibit a similar behavior with the results obtained in [90]: the leakage current increases with the increase in relative humidity.

Comparing the electric field at $z = 100\,\mathrm{nm}$ along the abscissa, it was observed that the diode with no passivation openings exhibits a relatively greater increase in the localized electric field maxima near the electrodes.

The sheet resistance measured on similar devices as a function of the relative humidity decreases with the increase in RH, as shown in Reference [139]. As a consequence, the

mobility of surface ions appears to increase with the increase in RH. In TCAD simulations, it was observed that positive surface charges accumulate on top of the electrode with a p-implant (ER), whereas negative surface charges accumulate on top of the electrode with an n-implant (GR). The accumulation of positive and negative charges on top of the electrodes may change the localized electric field, inducing new maxima, which can facilitate the acceleration of charge carriers, leading to secondary ionization. Charge multiplication from secondary ionization can increase the leakage current, which can lower the breakdown voltage of sensors in humid conditions. Furthermore, from the TCAD simulation, it appears that passivation openings may mitigate the effects induced by the accumulation of carriers on top of the electrodes.

The number of defects in the silicon oxide layer on top of the sensor is expected to have an impact on the sensor's performance. This is referred to as the concentration of fixed charges. The influence of the concentration of fixed charges was studied for three different values: $1 \cdot 10^{10}\,\mathrm{cm}^{-2}$, $5 \cdot 10^{10}\,\mathrm{cm}^{-2}$, and $1 \cdot 10^{11}\,\mathrm{cm}^{-2}$. It appears that $Q_{ox} = 1 \cdot 10^{10}\,\mathrm{cm}^{-2}$ induces higher electric field regions near the ER and GR with higher carrier densities in between them. This finding may indicate that higher fixed oxide charge concentrations are not an immediate concern, potentially explaining why irradiation treatments with gamma rays improve the breakdown voltage of strip sensors.

7.1.1 Prompt Current and Electric Field

Fig. 7.1 shows the simulated electric field at $z = 100$ nm along the abscissa together with the prompt current at constant bias ($V_{bias} = -900\,\mathrm{V}$) and relative humidity ($RH = 40\,\%$). The data is presented immediately after ramping up the voltage ($t_1 = 900\,\mathrm{s}$) and after waiting some time ($t_2 = 2500\,\mathrm{s}$). The simulated electric field profile corresponds to an MD8 diode with no passivation openings and $Q_{ox} = 1 \cdot 10^{11}\,\mathrm{cm}^{-2}$, which was presented in Fig. 6.6 (d) and Fig. 6.7 (d). The prompt current, derived from the measured transient current, was previously presented in Fig. 5.39. It should be noted that this side-by-side presentation aims to understand the behavior of the two figures of merit without comparing them.

It can be seen in Fig. 7.1 (a) that the electric field presents two high field regions, near the ER and GR respectively. The amplitude of the field peak at $x = 105\,\mu\mathrm{m}$ is lower than the one at $x = 237\,\mu\mathrm{m}$ at $t = 900\,\mathrm{s}$. After waiting some time ($t = 2500\,\mathrm{s}$) at constant bias and humidity, the field peak near the ER increases by 23 %, whereas the one near the GR increases by 28 %.

The prompt current increases as the laser gradually transitions from the ER to the GR region. There is no signal measured from the electrodes (for $x \leq 105\,\mu\mathrm{m}$ and $x \geq 247\,\mu\mathrm{m}$), because they are made of aluminum, which reflects the red laser. The maximum prompt current occurs at $x = 226\,\mu\mathrm{m}$. At $t = 2500\,\mathrm{s}$, it decreases by 20 %. The prompt current is directly proportional to the collected charge as presented in equation 5.15. From Fig. 5.38, it is apparent that the collected charge between the ER and the GR decreases with time. Under a high electric field and in the presence of RH, the surface states and the trap density inside the bulk might be altered, providing additional centers for carriers to recombine before reaching the collecting electrode, decreasing the collected charge.

An additional inconsistency between the two figures of merit arises from the fact that the prompt current decreases with the laser moving away from the GR towards the ER, and it is inversely proportional to RH. While the presence of a second peak in the prompt current distribution may not be a crucial feature, it suggests that there could

be a discrepancy between the geometry implemented in TCAD and the actual device. Measurements of prompt current as a function of RH show that humidity reduces the collected charge. However, the contributing factor that reduces the charge collected is still unclear.

The variations in collected charge are an indication of charge multiplication. Charge multiplication is efficient only if the concentration of charge carriers is sufficiently low not to shield the electric field peak closer to the GR shown in Fig 7.1 (a). If the applied voltage and relative humidity are high, the concentration of charge carriers in the region of the electric field peak at the GR drastically increases as illustrated in Fig. 6.10 and the width of the peak decreases as shown in Fig. 7.1 (a). When operating the sensor in humid conditions and at high bias voltage, the increase in carrier concentration at the Si-SiO_2 interface will likely lead to increased recombination and less efficient charge transport for the laser-generated charge carriers, leading to a reduced TCT signal closer to breakdown.

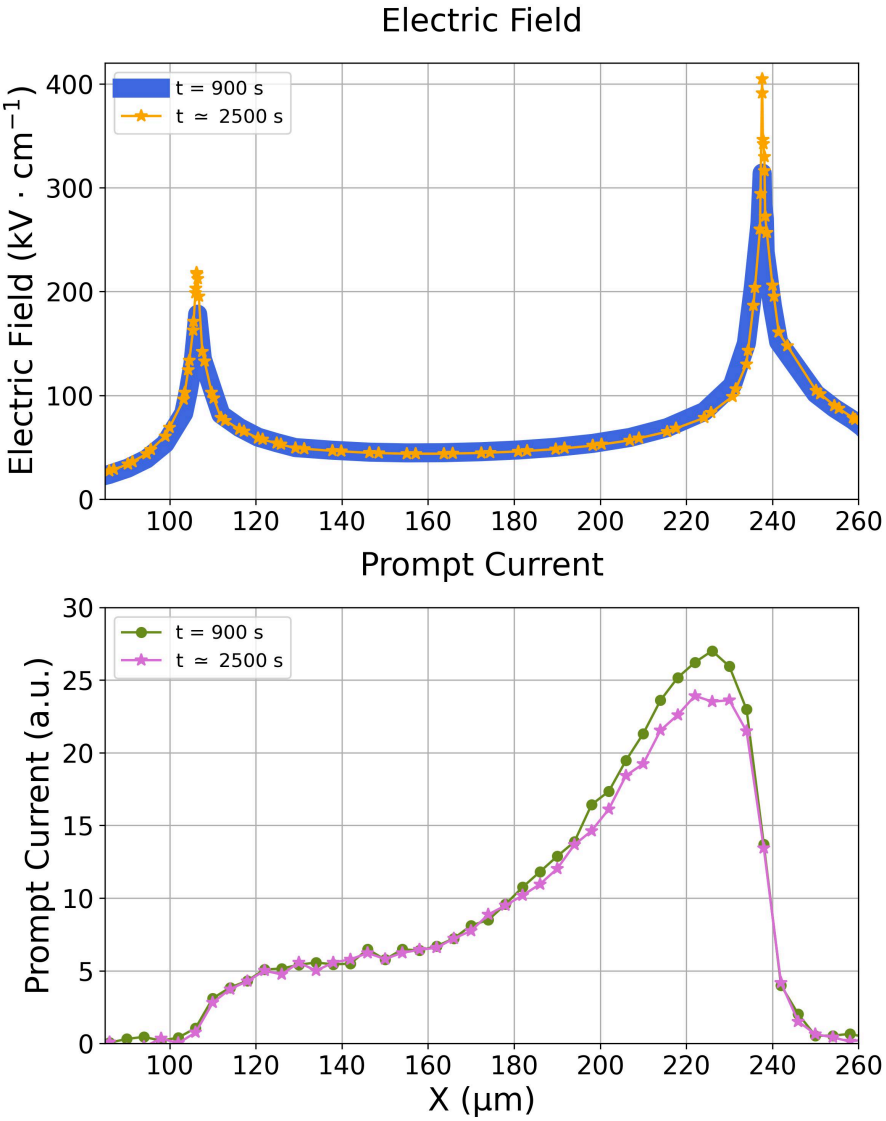

Figure 7.1: Diagram with the simulated electric field (a) and the extracted prompt current from Top-TCT scans (b) at $RH = 40\,\%$.

7.2 Outlook

The ATLAS ITk project is heading towards the production phase of the upgrade. To mitigate the effects of humidity on the strip sensors, these have been stored and tested in a dry environment ($RH \leq 10\,\%$). In a recent publication [94], it has been shown that long-term humidity exposure has no impact on the sensors' performance as long as the sensors are then operated in a dry environment. Therefore, humidity will not pose an issue as ATLAS will operate in a controlled environment. However, to plan for future detectors, it is important to fully understand their behavior in harsh conditions ($RH \geq 20\,\%$ and $V_{bias} \geq 700\,\mathrm{V}$).

The GR leakage current as a function of the bias voltage was measured with a probe station for several MD8 diodes as a function of RH. An example of IV characteristics in dry and humid conditions is presented in Fig. 5.7. The leakage current remains approximately the same for $RH \leq 40\,\%$, however at $RH = 50\,\%$, the leakage increases starting with 900 V. The leakage current, measured as a function of the biased voltage, for the large-area ATLAS ITk Strip sensor exhibits a linear dependence on the RH, as shown in [90]. The leakage current for smaller devices such as the MD8 diode does not present the same behavior when exposed to $RH \leq 40\,\%$. It was observed that smaller devices, such as diodes, are electrically more stable in humid conditions than the strip sensor. This may be related to the area of the structures. The strip sensor has a greater total edge length and a larger area where defects can appear, which could lead to earlier breakdown in humid conditions.

From Top-TCT measurements, it seems that the charge profile, together with the prompt current, is inversely proportional to the RH. This behavior is not yet fully understood. A helpful approach to understand this would be to implement the Top-TCT with the same parameters in TCAD, and simulate the transient currents as a function of RH. Using the same analysis method as described in section 5.2.4, the charge profiles and prompt currents can be obtained. This could validate the presence of charge multiplication and provide insight into the processes happening at the surface of the diode and inside the silicon bulk.

In TCAD from Synopsys, the hypothesized humidity effects on passivation were implemented using a 0.1 nm thick high-resistive layer. From laboratory measurements of the sheet resistance for similar sensors as a function of RH, it was observed that the sheet resistance changes with RH [139]. In the TCAD simulation, the sheet resistance of the resistive layer was adjusted according to literature values [139]. However, only values for the sheet resistance corresponding to $RH < 30\,\%$ were available in Reference [139]. For this reason, measurements of the sheet resistance of the MD8 diodes as a function of RH would consist of a cross-check, improving the accuracy of the simulation.

In Reference [90], sensors with different surface treatments, passivation thickness, and p-spray were tested. The sensors with thicker passivation and a p-spray addition were observed to have a breakdown voltage above the operating voltage required by ATLAS (500 V) at $RH \geq 40\,\%$. Future sensors could have thicker passivation and a p-spray addition for operation in humid conditions. An alternative to the silicon dioxide (SiO_2) and Silicon nitride (Si_3N_4) passivation could consist of Kodak Photo Resist. W. Schroen [83] reviewed the deposition of Kodak Photo Resist on a similar silicon sensor surface as a passivation method, which decreased the surface potential. In future sensors, these techniques may allow robust operation in humid conditions.

Appendix A

.1 Distribution Precision Production

The ATLAS ITk upgrade is a collective effort that spreads throughout different research institutes all over the world. To ensure that each module built meets the criteria established for the upgrade, quality control methods, together with strict assembly steps, have been created. Each module component undergoes metrology to ensure that each part has the required weight and that all components fit together properly. Visual inspection checks for debris on the surface, defects on the surface of the chip edges, defective wirebonds, etc. This is crucial for the strip sensor because oily residue can prevent wirebonding connections, conductive fibers can connect the sensor areas at different potentials, and scratches or cracks can influence the sensor performance to be outside the allowed specifications for module assembly.

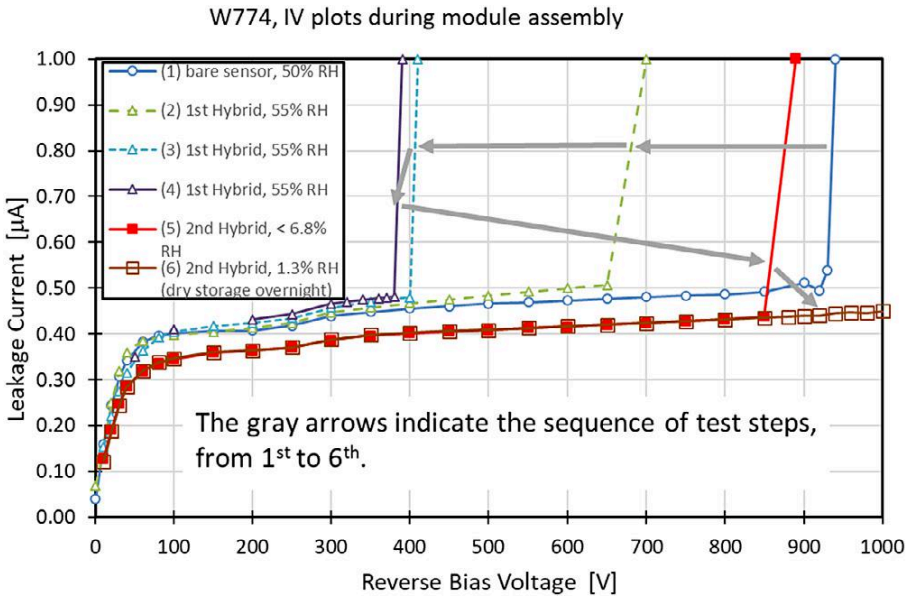

Figure 1: IV characteristic taken for one of the first modules in the prototyping program in ATLAS ITk Strips using ATLAS12 sensors. The sequence of the test and the RH value are recorded in the legend of the plot which was taken from [144].

Electrical tests are performed on the bare sensor: initial Current-Voltage (IV) and Capacitance-Voltage (CV) characteristics are taken using a probe station to ensure that the strip sensor is electrically viable and has the established full depletion and breakdown voltage. Further IVs on the strip sensor are performed after sensor gluing and after

wirebonding. Fig. 1 shows an example of initial IVs on a pre-production sensor that had a lower breakdown voltage during the assembly. This effect has been traced to the ambient humidity, and therefore, sensors are stored in a low-humidity environment and are tested only in temperature and humidity-controlled setups.

The assembly steps for modules are the same for all barrel and end-cap modules except R3-R5 because these sensors require stitching. First, the ASICs are glued onto hybrid flexes shown in Fig. 2. The quantity of glue needs to be controlled as too little glue will not offer enough support for ASICs, and too much can lead to seepage. An excess of glue can lead to unintended electrical connections, thermal and mechanical stress, and misalignment. For this reason, hybrids are weighted, while visual inspection and metrology are performed to ensure that the ASICs' alignment and the glue height are within the nominal range.

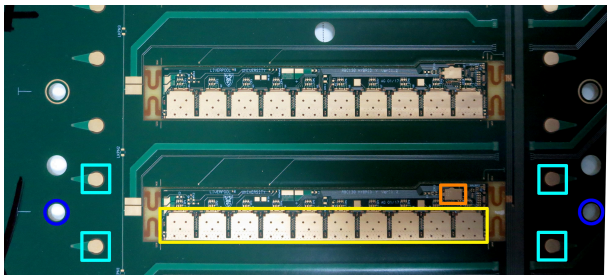

Figure 2: Image of two hybrid flexes on support panel with pads for the ABC130 chips with yellow and one for the HCC130 chip with orange. The pads with blue are used for positioning the precision tools while the pads with cyan serve as reference for the glue height. Image was taken from [145].

Following these steps, the ASICs are wire-bonded to the hybrid flex and then electrically tested according to the procedure described in [145]. ASICs are marked as good if their readout channel gain is in the range of $55 - 100\,\mathrm{mV/fC}$ and the noise is in the range of $300 - 1700\,\mathrm{ENC}$. The hybrids with good ASICs qualify for burn-in. The burn-in process is a quality control method employed to prevent infant mortality of hybrids just before installation inside the ATLAS detector. Given that 25000 hybrids will be installed in the ATLAS ITk, a cost-effective setup was designed, the hybrid burn-in crate shown in Fig. 3. The burn-in process consists of running the hybrids at $40^\circ\,\mathrm{C}$ for $100\,\mathrm{h}$ while simultaneously performing electrical tests on ASICs.

Once hybrids pass the burn-in, they can be glued to the sensor. Before this step, the sensor is placed on a vacuum jig, and the high voltage (HV) tab is attached as displayed in Fig. 4 (a). An IV measurement up to $700\,\mathrm{V}$ is taken to ensure electrical connection and to catch sensors with an early breakdown voltage. Then, the hybrids and powerboard are glued on top of the sensor. Metrology is performed to assess the glue height, the position of the hybrids, and the powerboard. The ASICs are wire-bonded to the strips, four-row bonding, and after each row, the hybrids are electrically tested. Fig. 4 (b) shows a fully assembled R0 module.

Once built, modules undergo quality control: visual inspection, metrology, and thermal cycling. Visual inspection checks for surface defects that can be detected with the naked eye or using a microscope. The most common defects are debris on the surface, defects on the surface of the chip edges, and defective wirebonds. These mechanical defects can affect the performance of the module in various ways. A defective wirebond can prevent an electrical connection between the strip and the corresponding ASIC's channel.

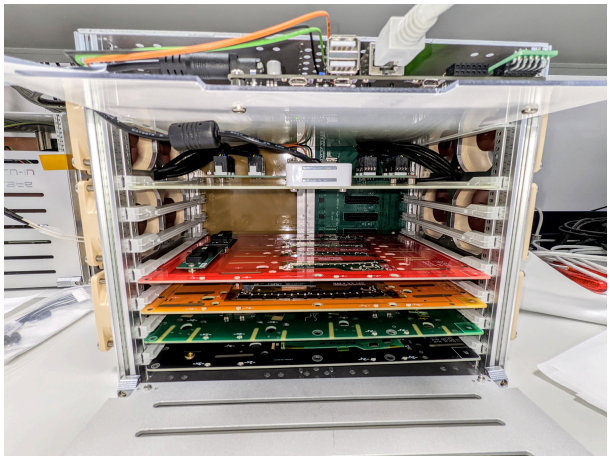

Figure 3: Front view of the hybrid burn-in crate loaded with four hybrid panels. The crate can accommodate up to six panels, which slide into the backplane. The backplane distributes power from power supplies to panels. Data lines go via backplane to a dedicated FPGA read-out board (called the Genesis G2), connected via an adapter to the crate backplane. Cooling is done via fans placed on the laterals of the crate.

(a) (b)

Figure 4: In (a), the R0 sensor is placed on a vacuum jig with a glue pattern deposited on top, and the HV tab is attached. In (b), the fully assembled R0 module at DESY Zeuthen is shown.

Module metrology checks if the sensor bowed during assembly. It is also necessary to ensure that the weight of the modules is within tolerance so that the local support structures (petals and staves) do not carry excessive weight, leading to mechanical failure. Following metrology, an IV characteristic at 550 V is measured to check the leakage current and catch early breakdown. A test to characterize the noise of the module is then performed.

The thermal cycling of modules is a quality control process performed inside a controlled setup known as the coldbox. Low temperature tests are conducted at -35° C while high temperature tests run at -40° C. The temperature variations are meant as a stress test for the integrated circuits.

.2 List of TCAD Results

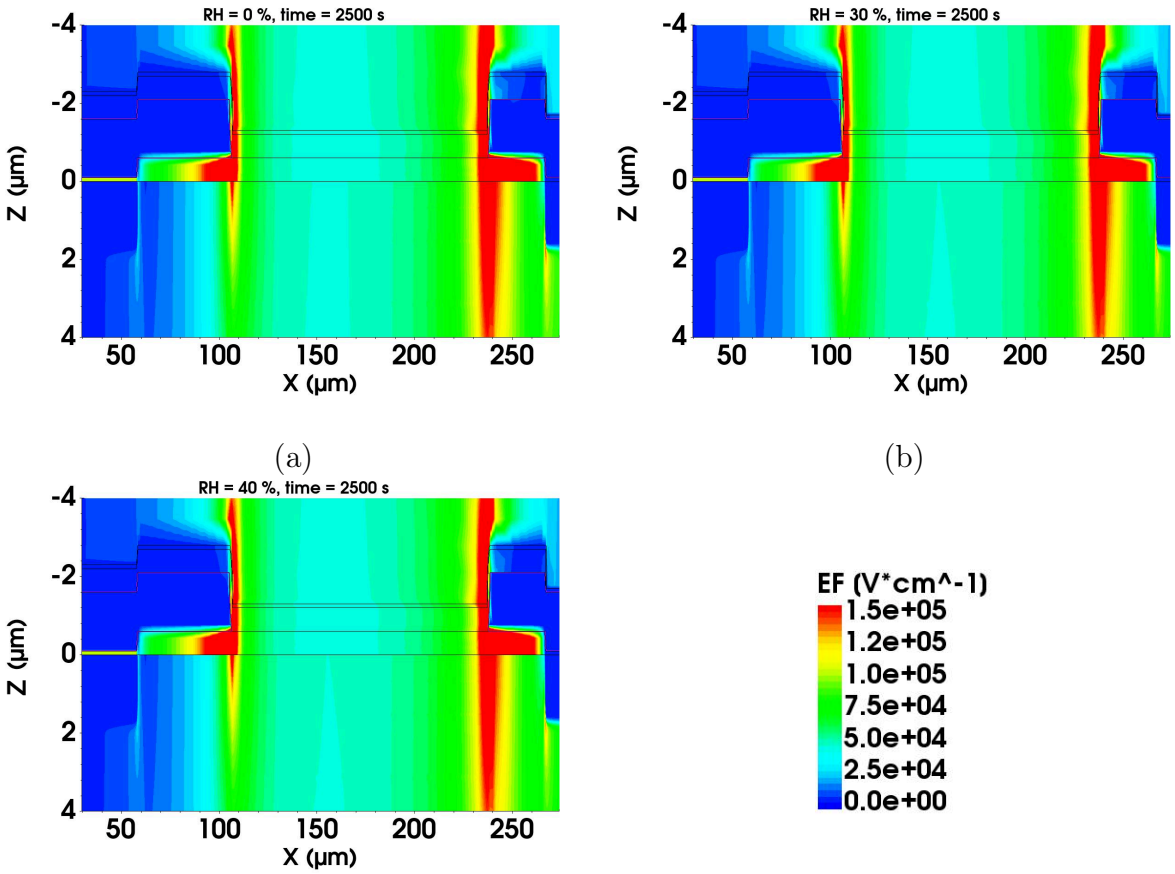

(a) (b)

(c)

Figure 5: 2D representation of the absolute electric field at $V_{bias} = -900\,\mathrm{V}$, and $t = 2500\,\mathrm{s}$ for passivation openings at the ER, GR, and pad as a function of RH: 0 % (a), 30 % (b), and 40 % .

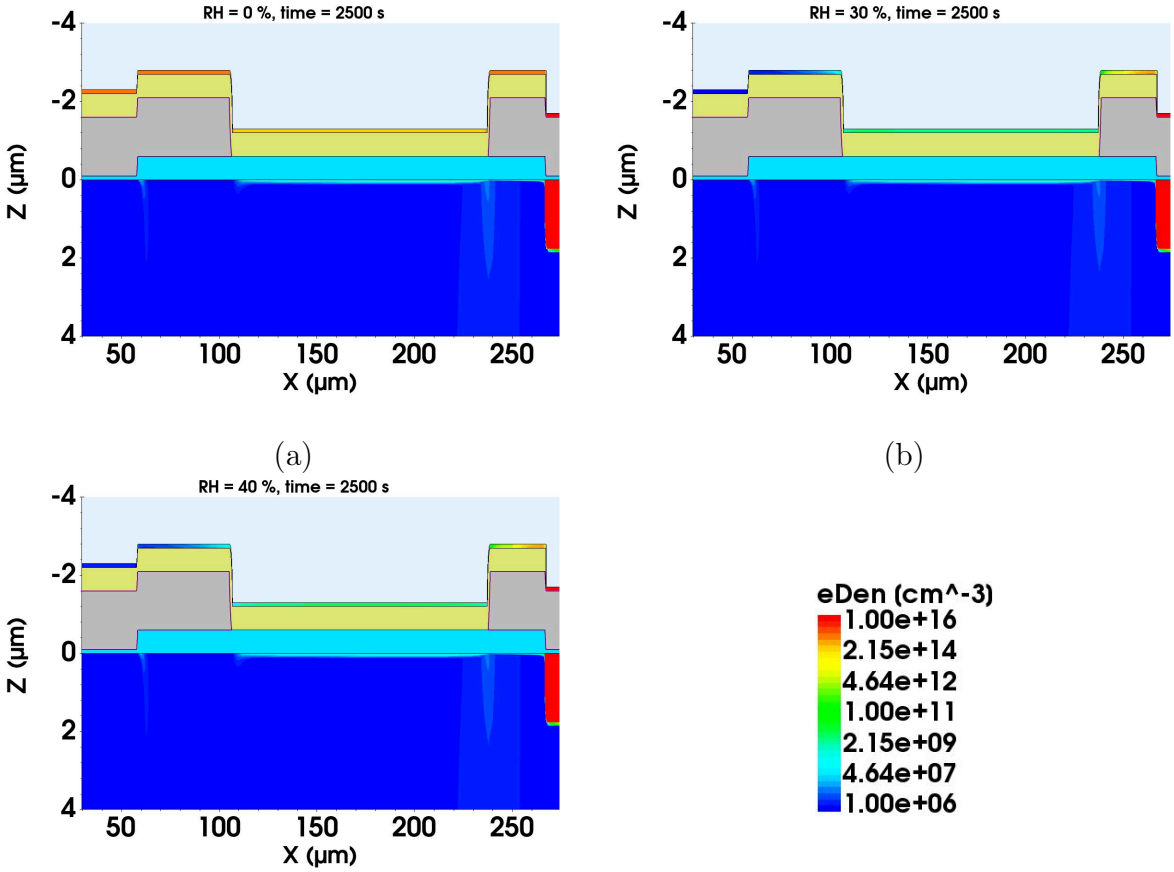

(a) (b) (c)

Figure 6: Spatial distribution of the electron density at $V_{bias} = -900\,\mathrm{V}$, and $t = 2500\,\mathrm{s}$ for passivation openings at the ER, GR, and pad as a function of RH: 0 % (a), 30 % (b), and 40 % (c).

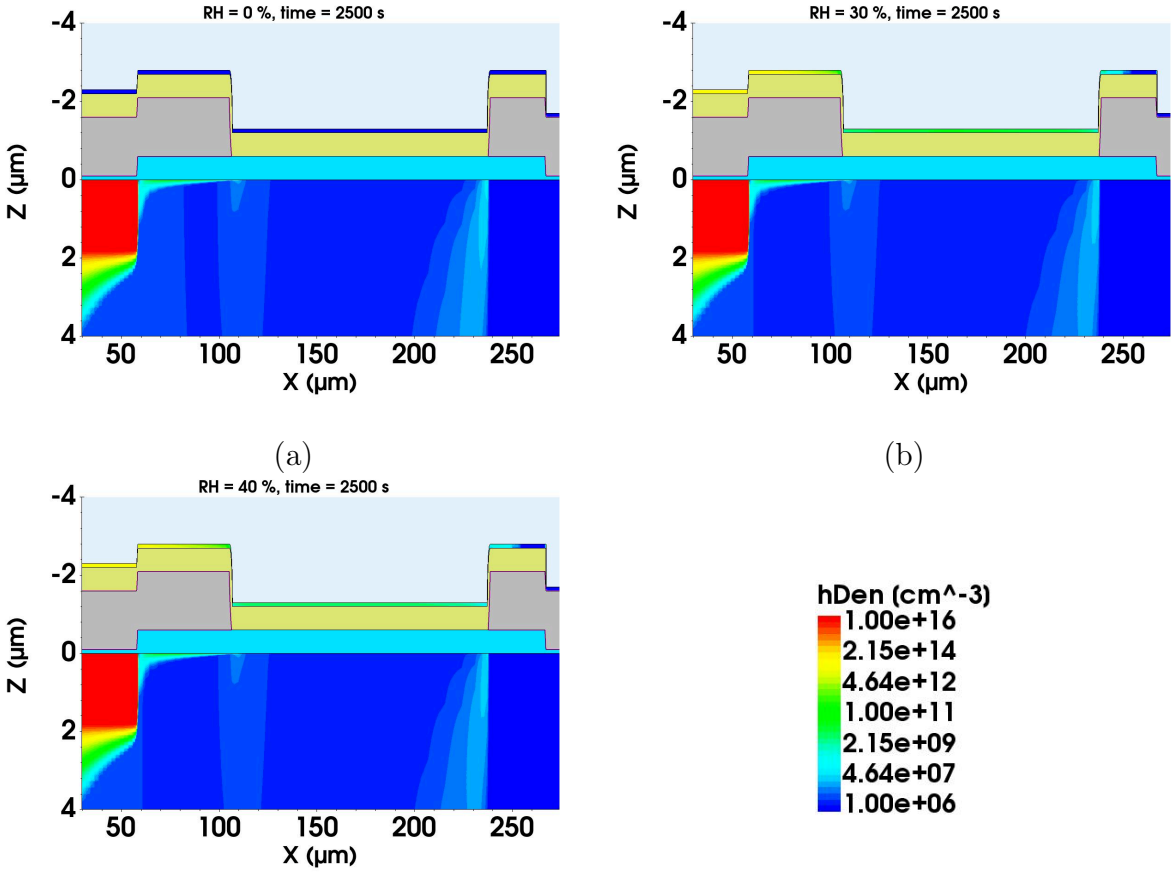

(a) (b) (c)

Figure 7: Spatial distribution of the electron density at $V_{bias} = -900\,\mathrm{V}$, and $t = 2500\,\mathrm{s}$ for passivation openings at the ER, GR, and pad as a function of RH: 0 % (a), 30 % (b), and 40 % (c).

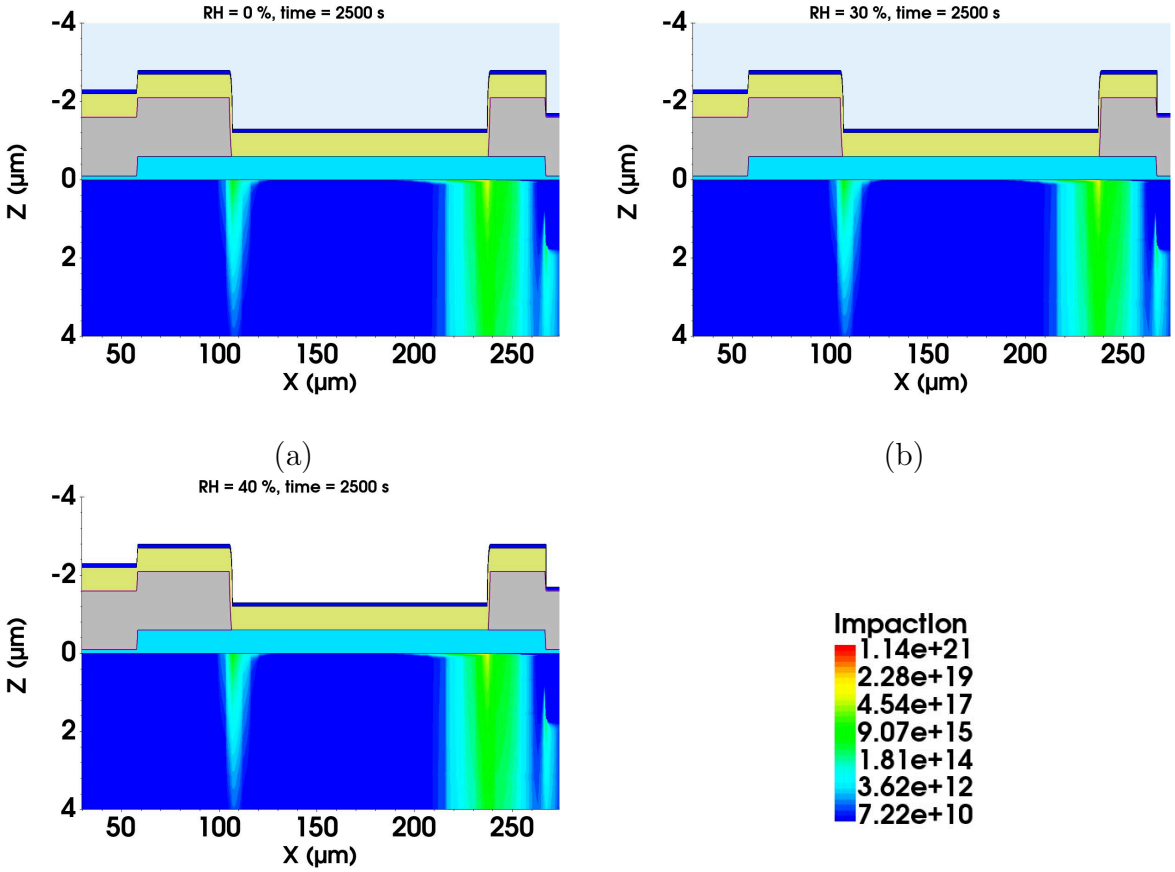

(a) (b) (c)

Figure 8: Generation rate of free charge carriers from impact ionization at $V_{bias} = -900\,\mathrm{V}$, and $t = 2500\,\mathrm{s}$ for passivation openings at the ER, GR, and pad as a function of RH: 0 % (a), 30 % (b), and 40 % (c).

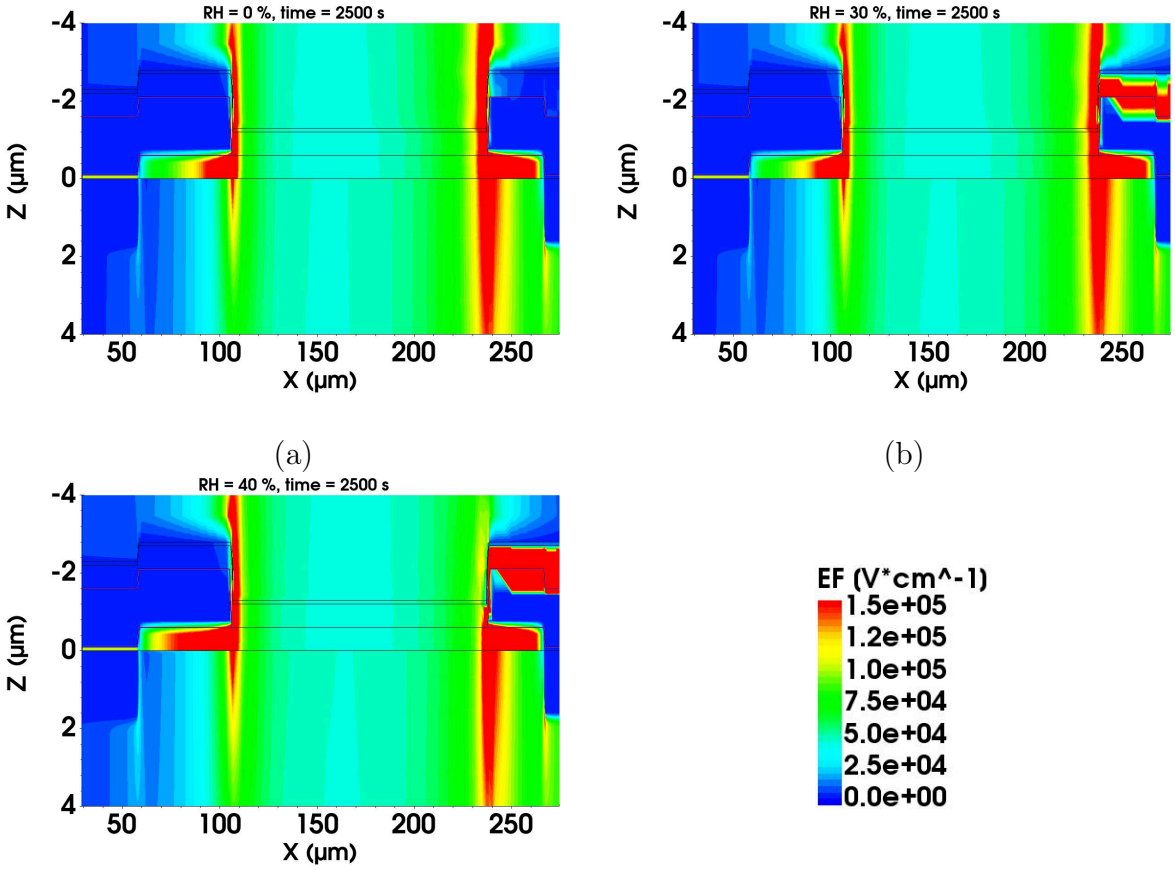

(a) (b) (c)

Figure 9: Electric field distribution at $V_{bias} = -900\,\mathrm{V}$, and $t = 2500\,\mathrm{s}$ for passivation openings only at the ER as a function of RH: 0 % (a), 30 % (b), and 40 % (c).

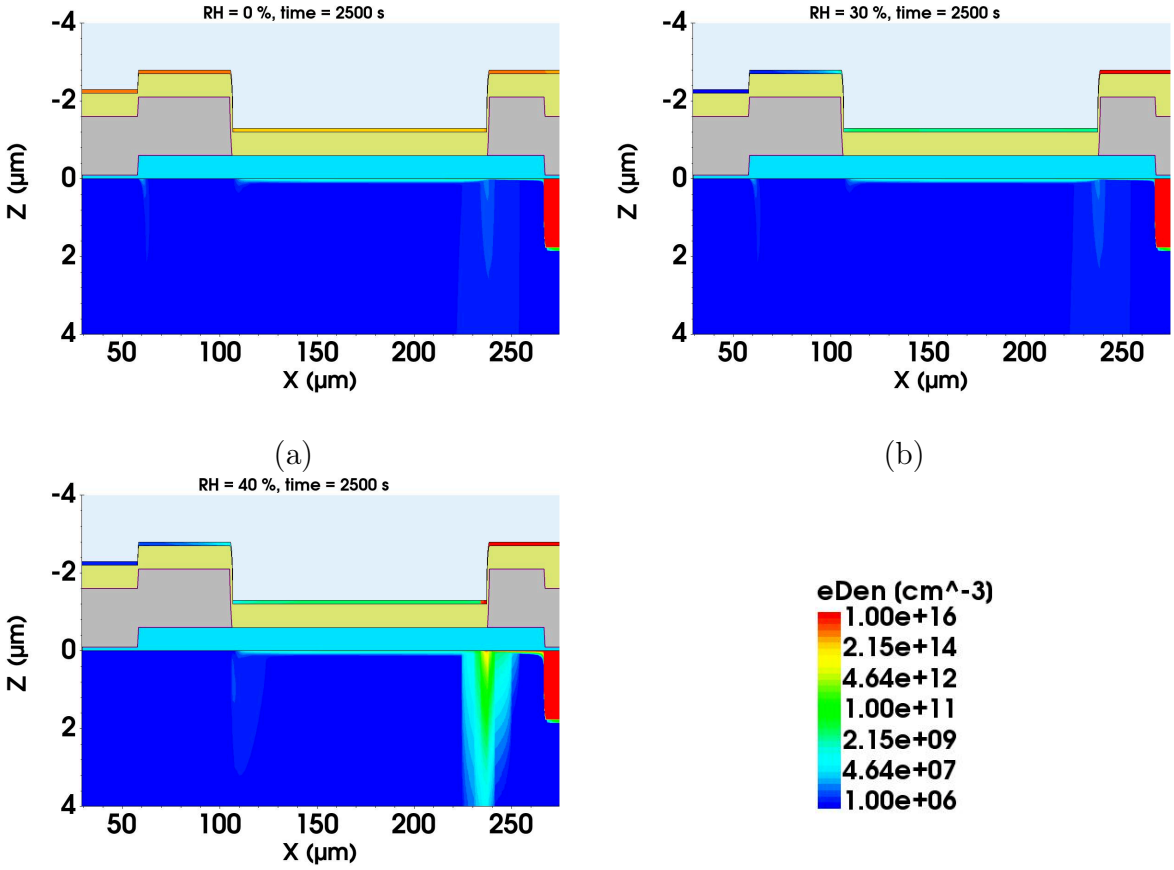

(a) (b) (c)

Figure 10: Distribution of the electron density at $V_{bias} = -900\,\mathrm{V}$, and $t = 2500\,\mathrm{s}$ for passivation openings only at the ER as a function of RH: 0 % (a), 30 % (b), and 40 % (c).

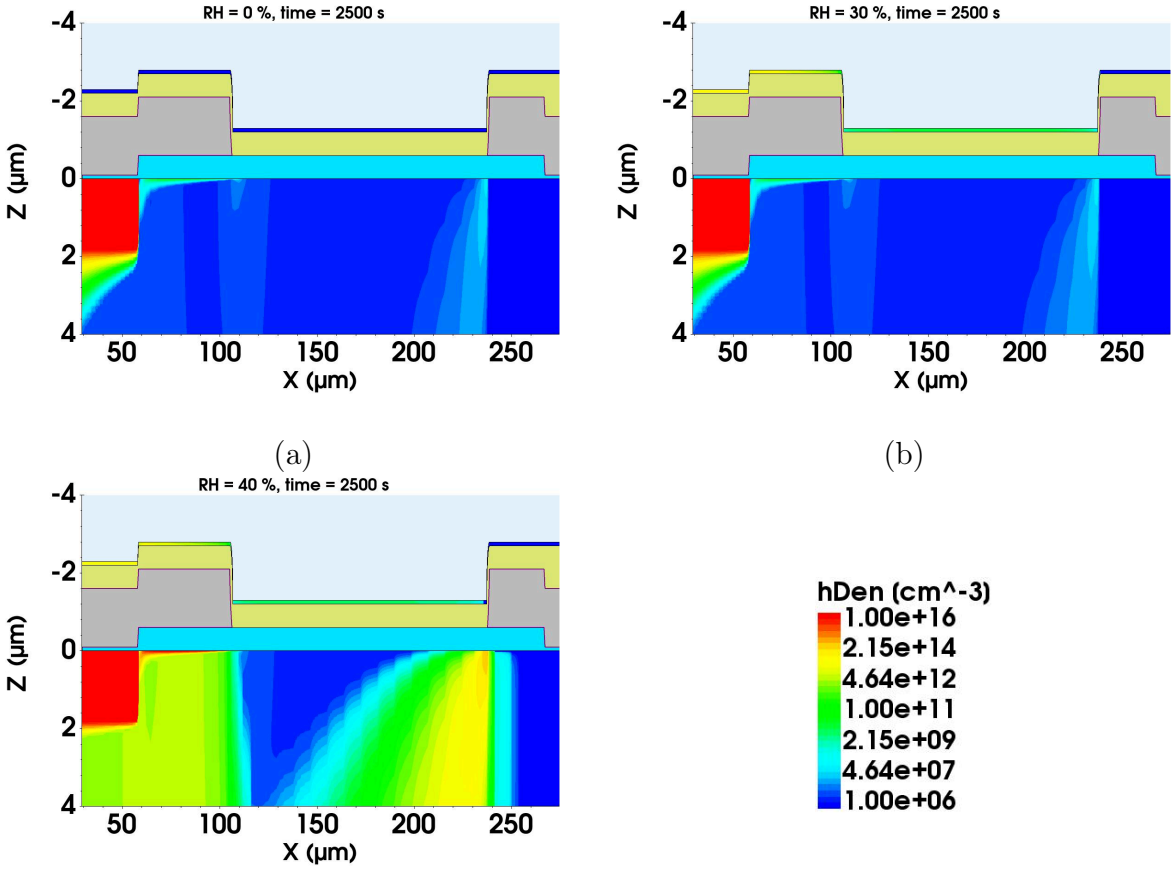

(a) (b) (c)

Figure 11: Distribution of the electron density at $V_{bias} = -900\,\mathrm{V}$, and $t = 2500\,\mathrm{s}$ for passivation openings only at the ER as a function of RH: 0 % (a), 30 % (b), and 40 % (c).

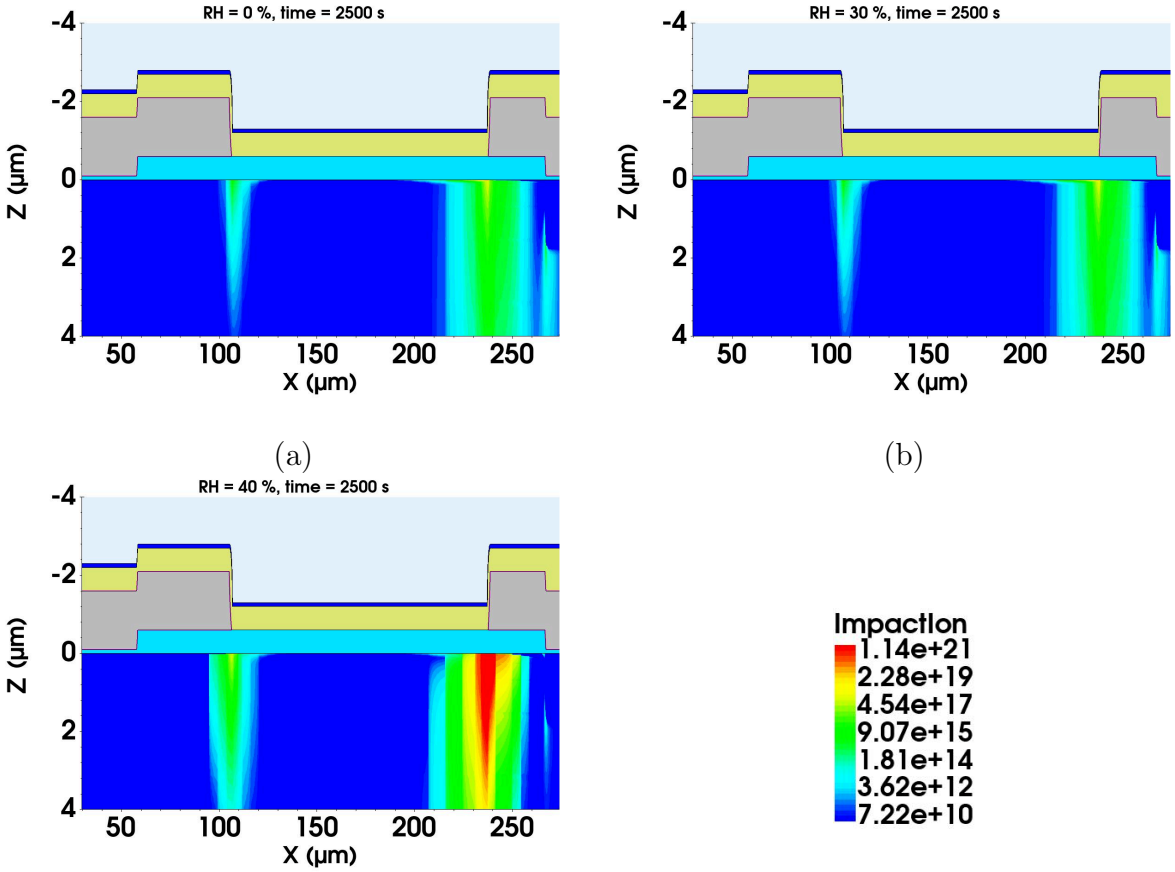

(a) (b) (c)

Figure 12: Generation rate of free charge carriers from impact ionization at $V_{bias} = -900\,\mathrm{V}$, and $t = 2500\,\mathrm{s}$ for passivation openings only at the ER as a function of RH: 0 % (a), 30 % (b), and 40 % (c).

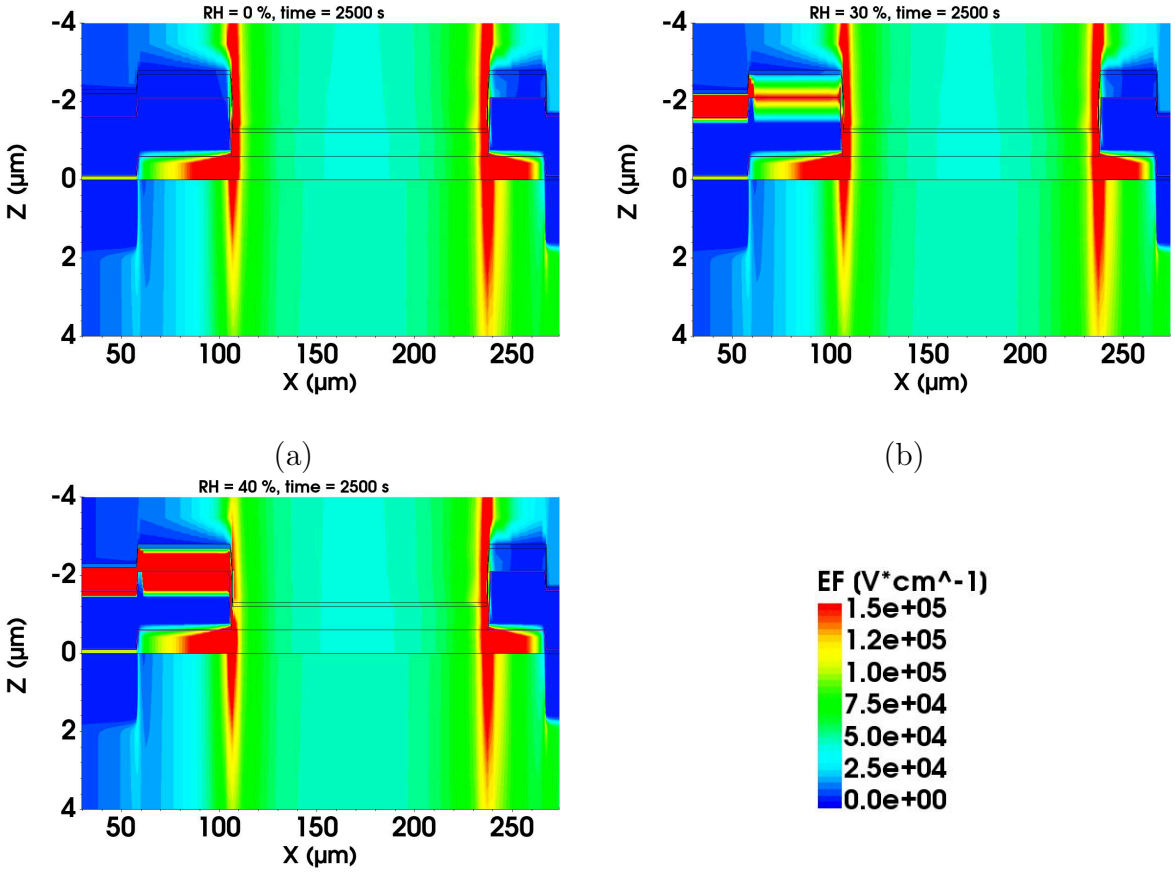

(a) (b) (c)

Figure 13: Spatial distribution of the electric field at $V_{bias} = -900\,\mathrm{V}$, and $t = 2500\,\mathrm{s}$ for passivation openings at the GR and pad as a function of RH: 0 % (a), 30 % (b), and 40 % (c).

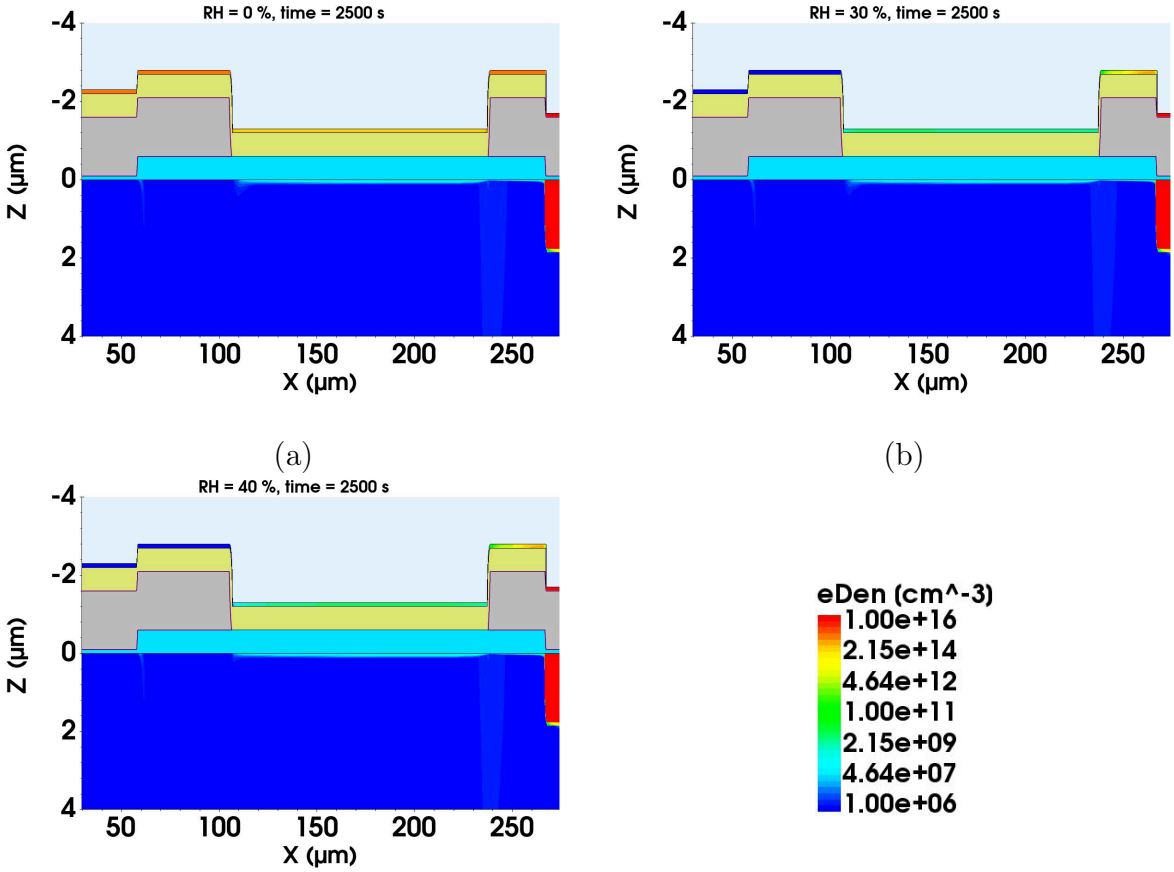

(a) (b) (c)

Figure 14: Spatial distribution of the electron density at $V_{bias} = -900\,\mathrm{V}$, and $t = 2500\,\mathrm{s}$ for passivation openings at the GR and pad as a function of RH: 0 % (a), 30 % (b), and 40 % (c).

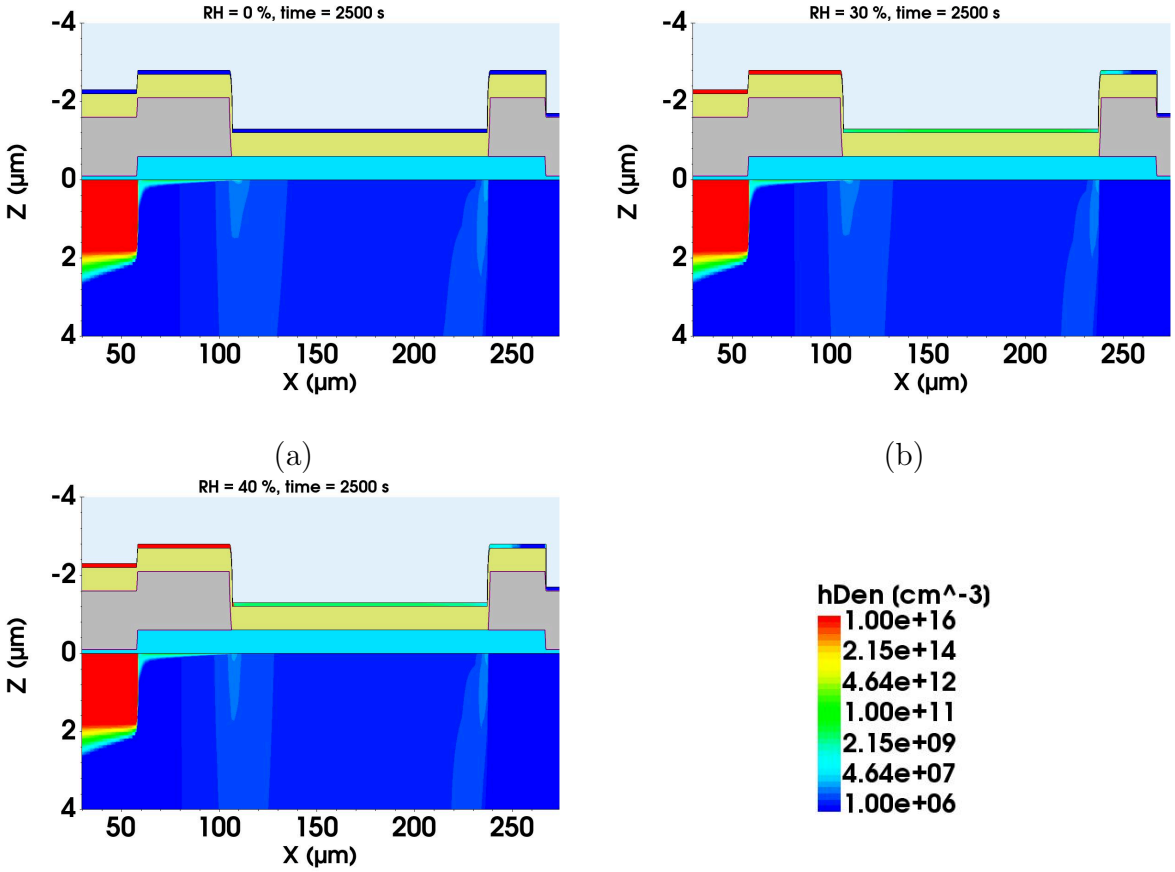

(a) (b) (c)

Figure 15: Spatial distribution of the hole density at $V_{bias} = -900\,\mathrm{V}$, and $t = 2500\,\mathrm{s}$ for passivation openings at the GR and pad as a function of RH: 0 % (a), 30 % (b), and 40 % (c).

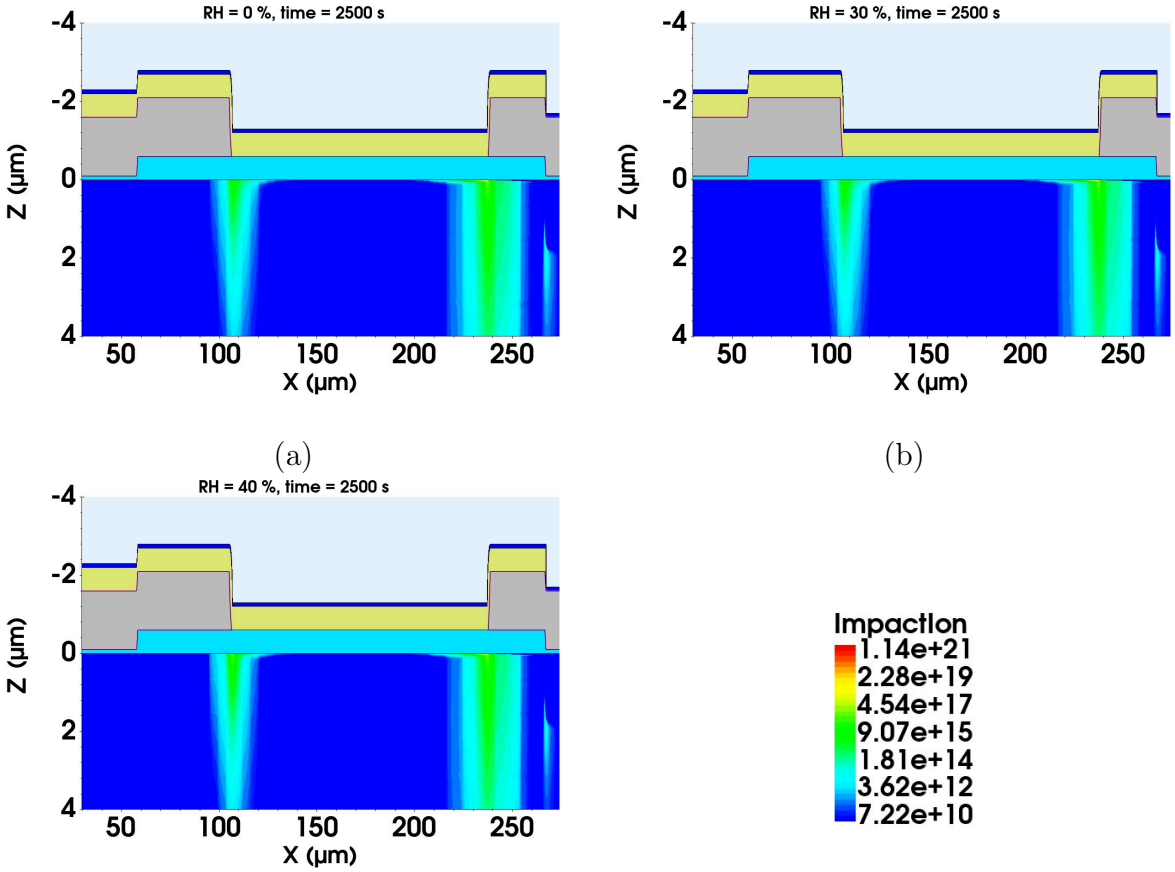

(a) (b) (c)

Figure 16: Generation rate of free carriers from impact ionization at $V_{bias} = -900\,\mathrm{V}$, and $t = 2500\,\mathrm{s}$ for passivation openings at the GR and pad as a function of RH: 0 % (a), 30 % (b), and 40 % (c).

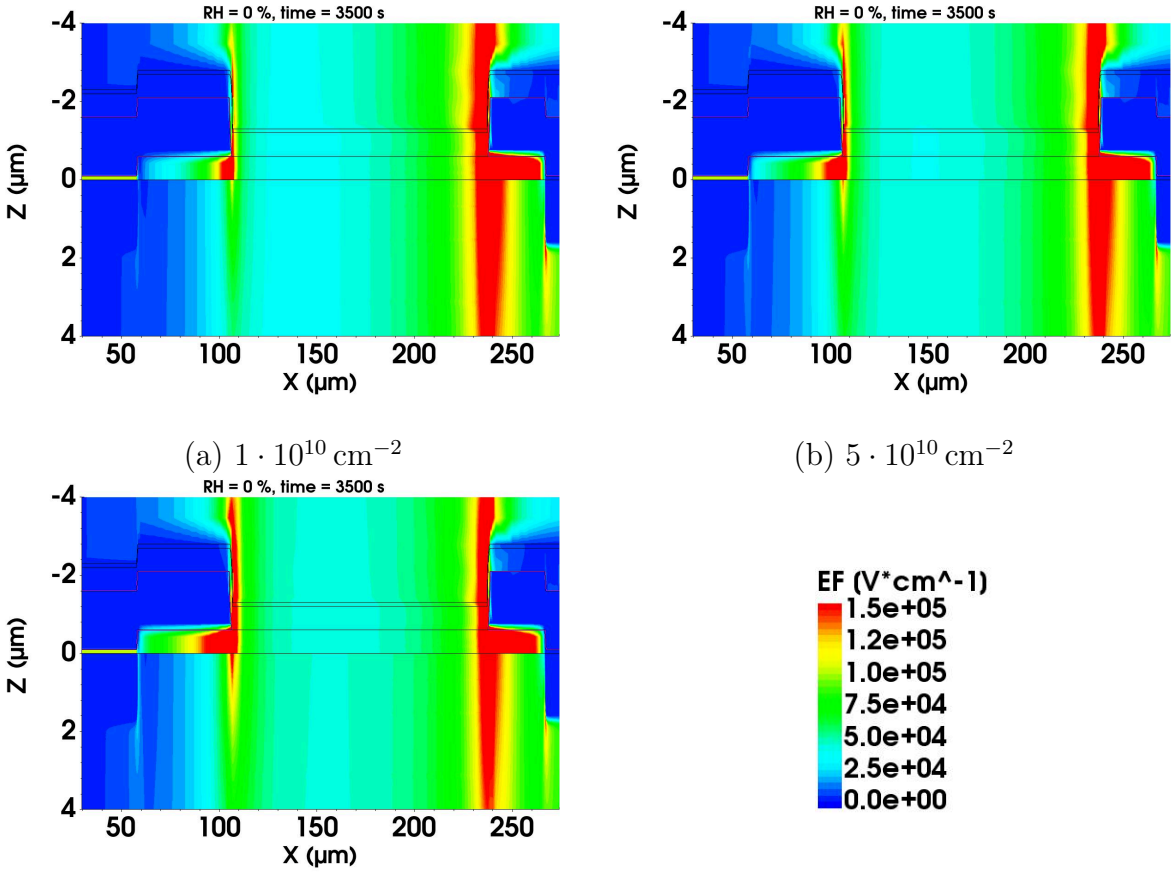

(a) $1 \cdot 10^{10}\,\mathrm{cm}^{-2}$

(b) $5 \cdot 10^{10}\,\mathrm{cm}^{-2}$

(c) $1 \cdot 10^{11}\,\mathrm{cm}^{-2}$

Figure 17: 2D representation of the absolute electric field at $V_{bias} = -900\,\mathrm{V}$, $RH = 0\,\%$, and $t = 3500\,\mathrm{s}$ for different Q_{ox} values: $1 \cdot 10^{10}\,\mathrm{cm}^{-2}$ (a), $5 \cdot 10^{10}\,\mathrm{cm}^{-2}$ (b), and $1 \cdot 10^{11}\,\mathrm{cm}^{-2}$ (c).

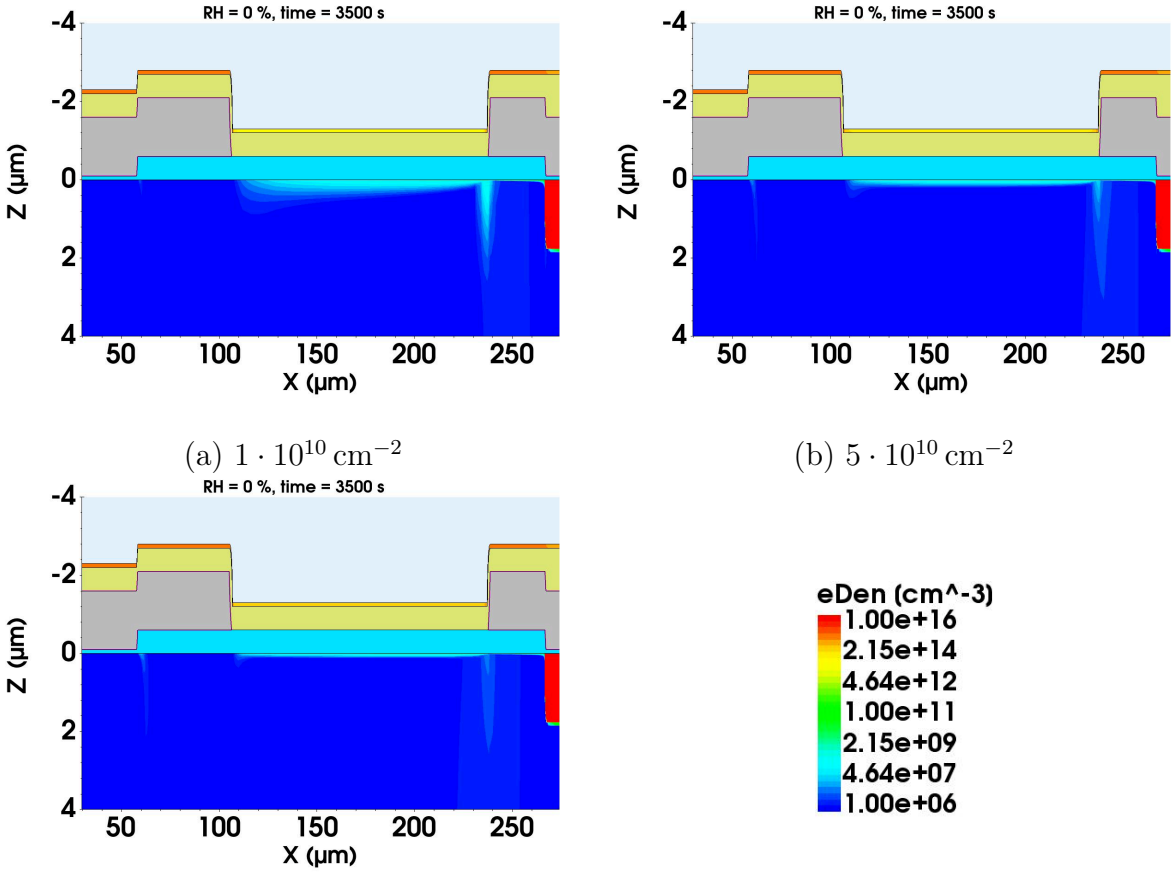

(a) $1 \cdot 10^{10}\,\mathrm{cm}^{-2}$

(b) $5 \cdot 10^{10}\,\mathrm{cm}^{-2}$

(c) $1 \cdot 10^{11}\,\mathrm{cm}^{-2}$

Figure 18: Spatial representation of the electron density at $V_{bias} = -900\,\mathrm{V}$, $RH = 0\,\%$, and $t = 3500\,\mathrm{s}$ for different Q_{ox} values: $1 \cdot 10^{10}\,\mathrm{cm}^{-2}$ (a), $5 \cdot 10^{10}\,\mathrm{cm}^{-2}$ (b), and $1 \cdot 10^{11}\,\mathrm{cm}^{-2}$ (c).

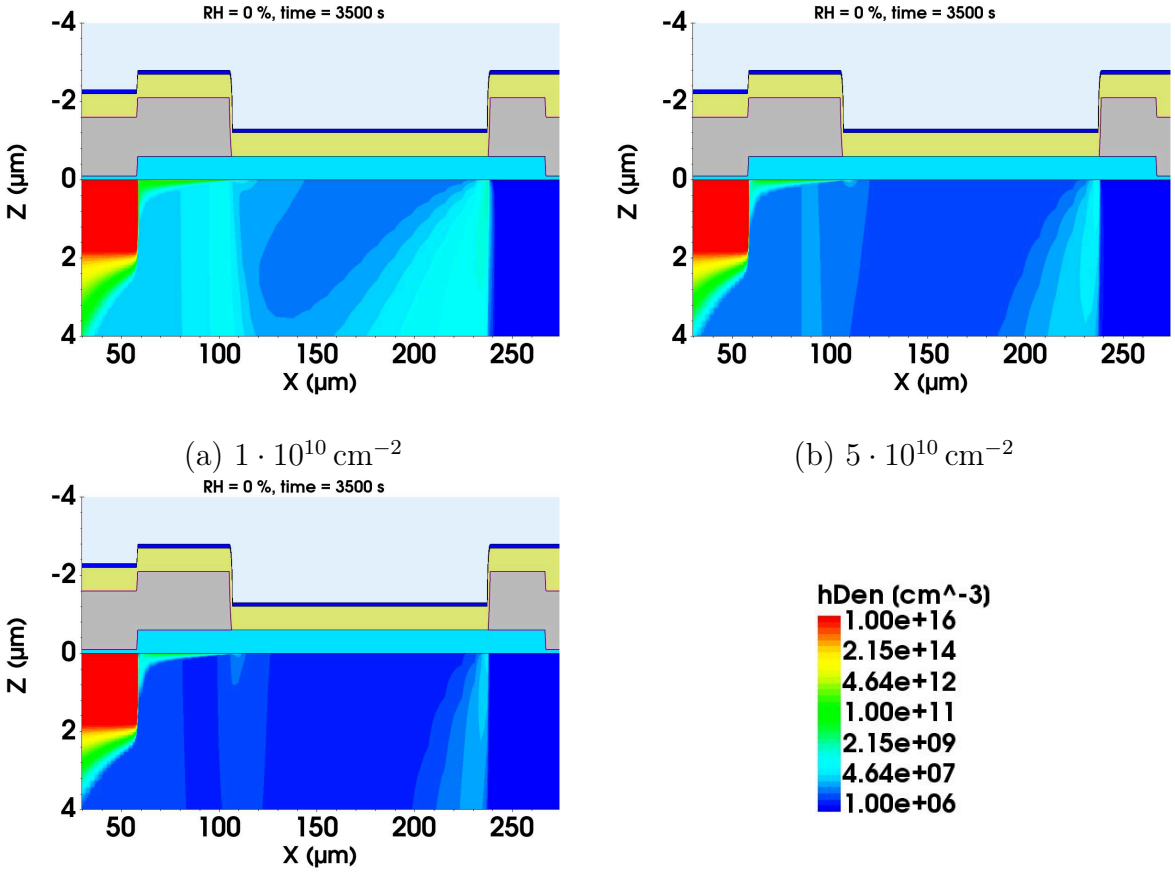

(a) $1 \cdot 10^{10}\,\mathrm{cm}^{-2}$

(b) $5 \cdot 10^{10}\,\mathrm{cm}^{-2}$

(c) $1 \cdot 10^{11}\,\mathrm{cm}^{-2}$

Figure 19: Spatial representation of the electron density at $V_{bias} = -900\,\mathrm{V}$, $RH = 0\,\%$, and $t = 3500\,\mathrm{s}$ for different Q_{ox} values: $1 \cdot 10^{10}\,\mathrm{cm}^{-2}$ (a), $5 \cdot 10^{10}\,\mathrm{cm}^{-2}$ (b), and $1 \cdot 10^{11}\,\mathrm{cm}^{-2}$ (c).

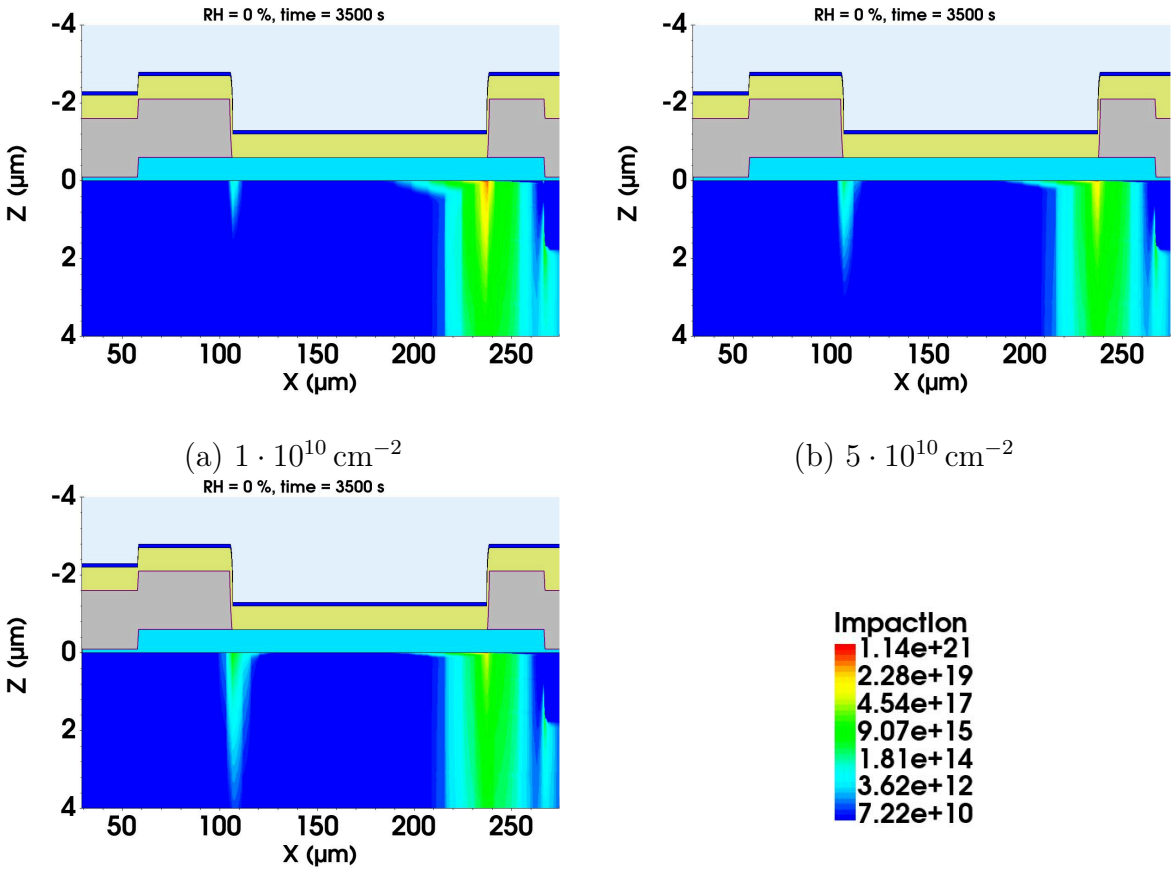

(a) $1 \cdot 10^{10}\,\mathrm{cm}^{-2}$

(b) $5 \cdot 10^{10}\,\mathrm{cm}^{-2}$

(c) $1 \cdot 10^{11}\,\mathrm{cm}^{-2}$

Figure 20: Spatial representation of the generation rate of carriers from impact ionization at $V_{bias} = -900\,\mathrm{V}$, $RH = 0\,\%$, and $t = 3500\,\mathrm{s}$ for different Q_{ox} values: $1 \cdot 10^{10}\,\mathrm{cm}^{-2}$ (a), $5 \cdot 10^{10}\,\mathrm{cm}^{-2}$ (b), and $1 \cdot 10^{11}\,\mathrm{cm}^{-2}$ (c).

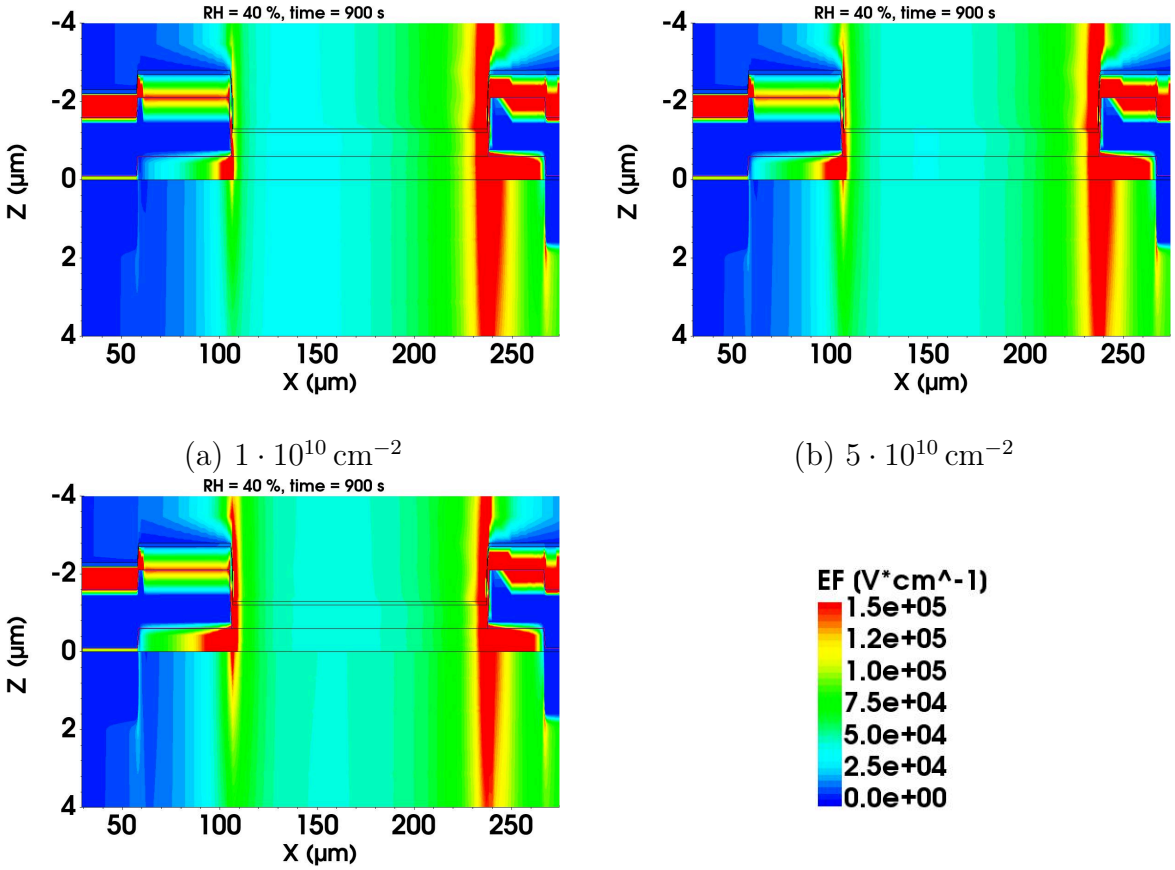

(a) $1 \cdot 10^{10}\,\mathrm{cm}^{-2}$

(b) $5 \cdot 10^{10}\,\mathrm{cm}^{-2}$

(c) $1 \cdot 10^{11}\,\mathrm{cm}^{-2}$

Figure 21: Spatial representation of the absolute electric field at $V_{bias} = -900\,\mathrm{V}$, $RH = 40\,\%$, and $t = 900\,\mathrm{s}$ for different Q_{ox} values: $1 \cdot 10^{10}\,\mathrm{cm}^{-2}$ (a), $5 \cdot 10^{10}\,\mathrm{cm}^{-2}$ (b), and $1 \cdot 10^{11}\,\mathrm{cm}^{-2}$ (c).

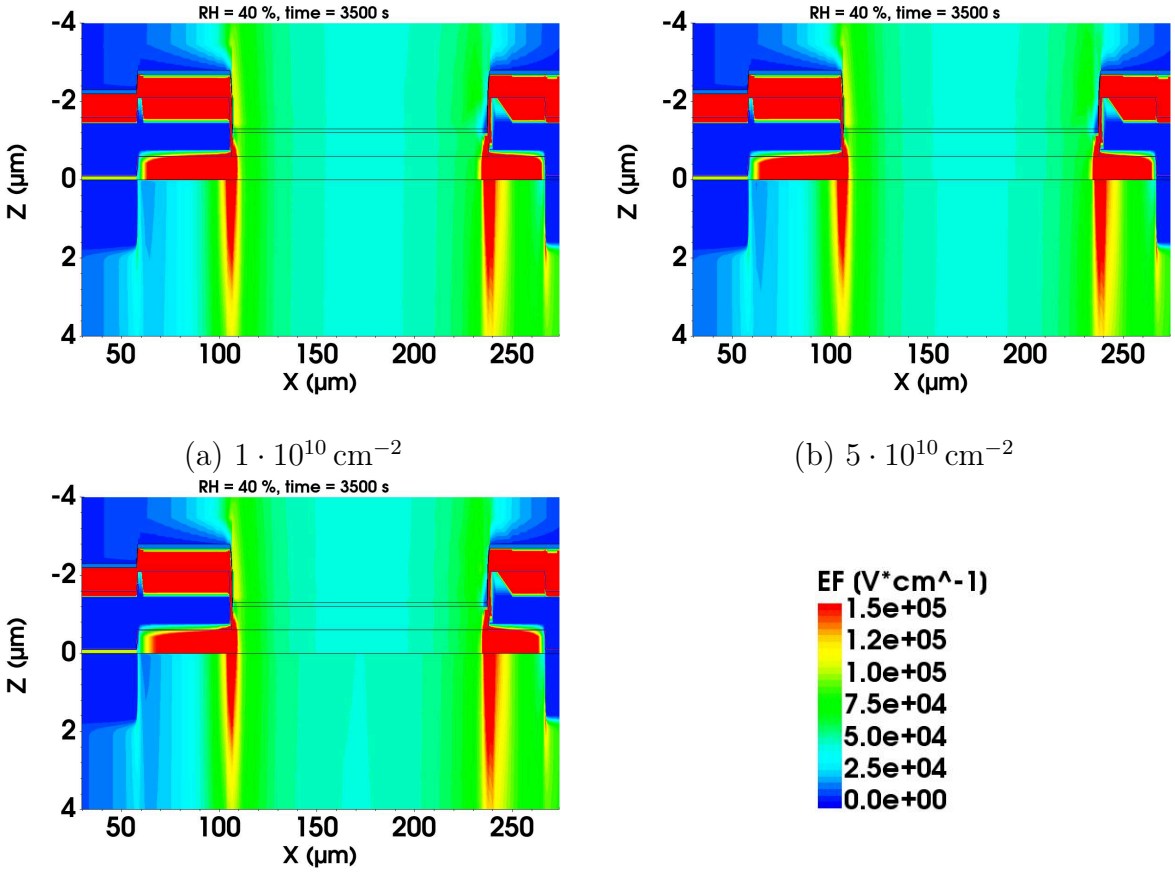

(a) $1 \cdot 10^{10}\,\mathrm{cm}^{-2}$

(b) $5 \cdot 10^{10}\,\mathrm{cm}^{-2}$

(c) $1 \cdot 10^{11}\,\mathrm{cm}^{-2}$

Figure 22: Spatial representation of the absolute electric field at $V_{bias} = -900\,\mathrm{V}$, $RH = 40\,\%$, and $t = 3500\,\mathrm{s}$ for different Q_{ox} values: $1 \cdot 10^{10}\,\mathrm{cm}^{-2}$ (a), $5 \cdot 10^{10}\,\mathrm{cm}^{-2}$ (b), and $1 \cdot 10^{11}\,\mathrm{cm}^{-2}$ (c).

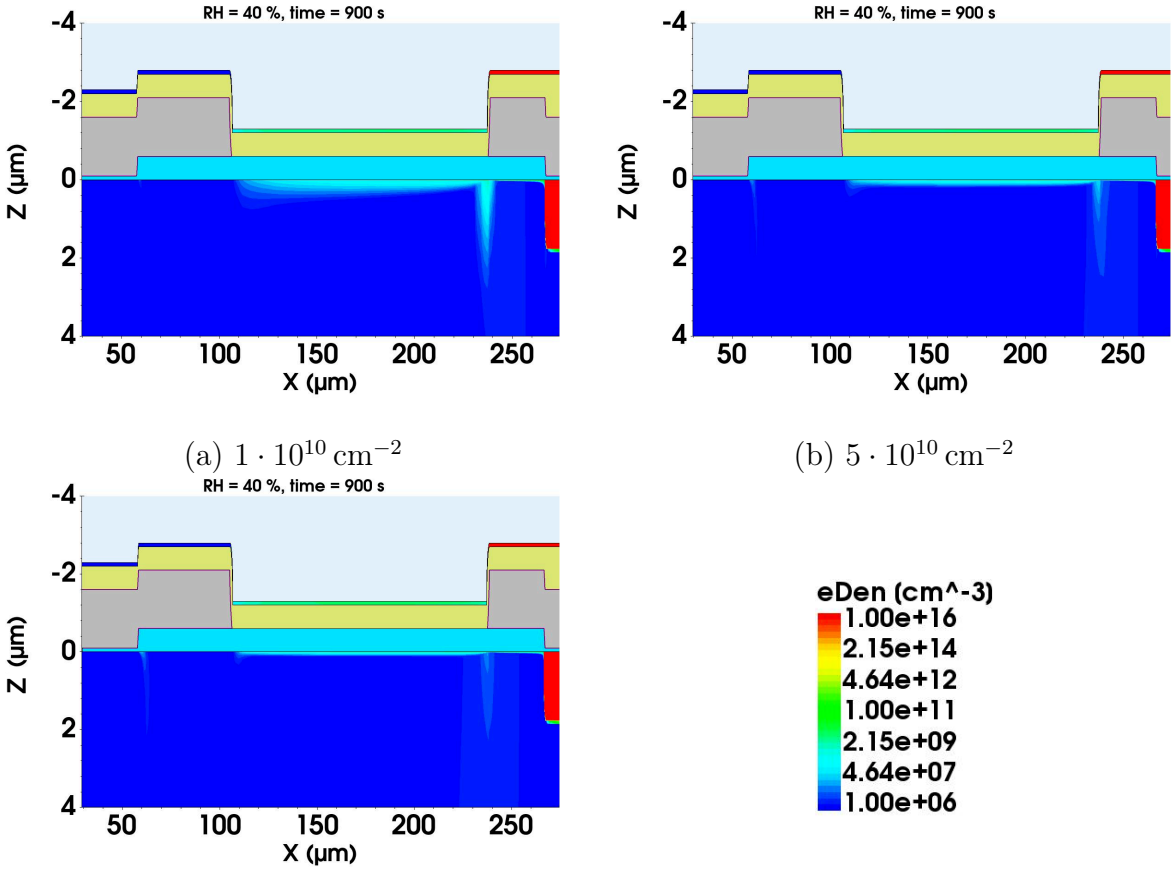

(a) $1 \cdot 10^{10}\,\mathrm{cm}^{-2}$

(b) $5 \cdot 10^{10}\,\mathrm{cm}^{-2}$

(c) $1 \cdot 10^{11}\,\mathrm{cm}^{-2}$

Figure 23: Spatial representation of the electron density at $V_{bias} = -900\,\mathrm{V}$, $RH = 40\,\%$, and $t = 900\,\mathrm{s}$ for different Q_{ox} values: $1 \cdot 10^{10}\,\mathrm{cm}^{-2}$ (a), $5 \cdot 10^{10}\,\mathrm{cm}^{-2}$ (b), and $1 \cdot 10^{11}\,\mathrm{cm}^{-2}$ (c).

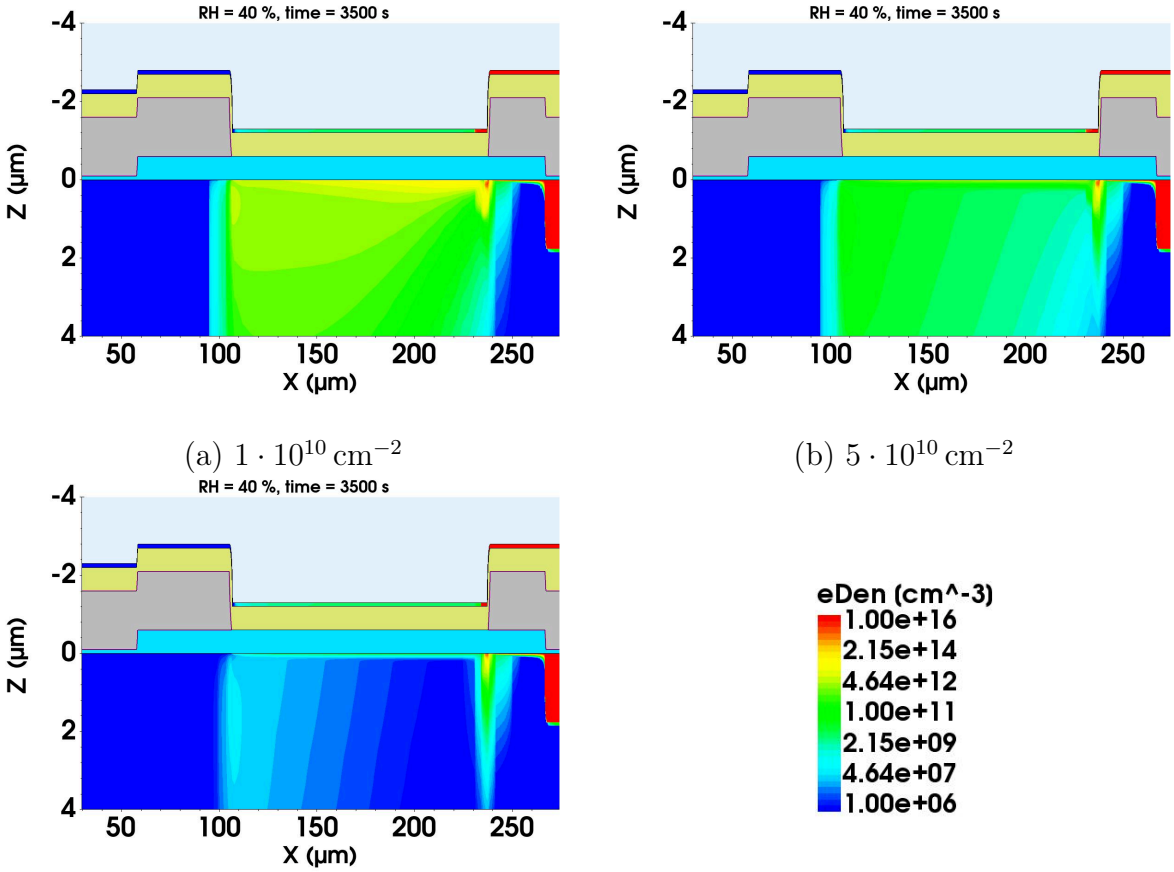

(a) $1 \cdot 10^{10}\,\mathrm{cm}^{-2}$

(b) $5 \cdot 10^{10}\,\mathrm{cm}^{-2}$

(c) $1 \cdot 10^{11}\,\mathrm{cm}^{-2}$

Figure 24: Spatial representation of the electron density at $V_{bias} = -900\,\mathrm{V}$, $RH = 40\,\%$, and $t = 3500\,\mathrm{s}$ for different Q_{ox} values: $1 \cdot 10^{10}\,\mathrm{cm}^{-2}$ (a), $5 \cdot 10^{10}\,\mathrm{cm}^{-2}$ (b), and $1 \cdot 10^{11}\,\mathrm{cm}^{-2}$ (c).

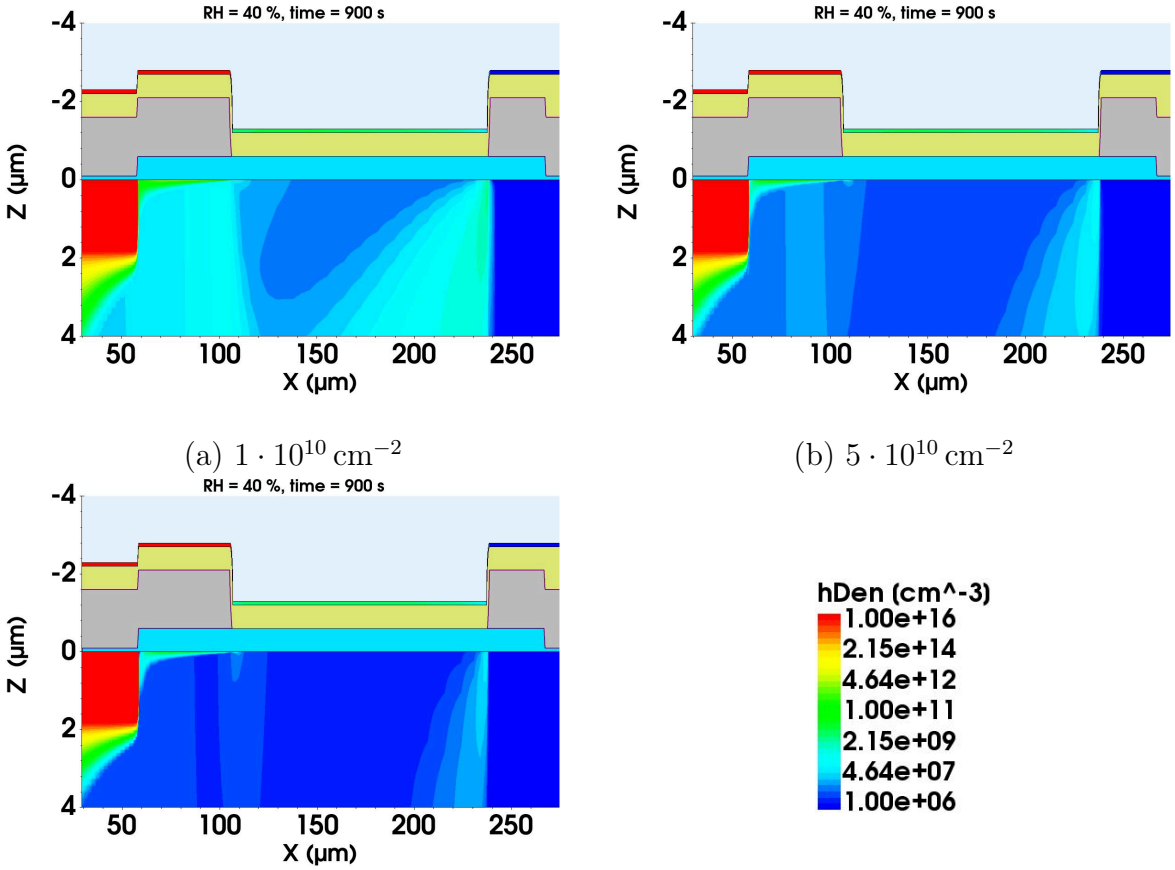

(a) $1 \cdot 10^{10}\,\mathrm{cm}^{-2}$

(b) $5 \cdot 10^{10}\,\mathrm{cm}^{-2}$

(c) $1 \cdot 10^{11}\,\mathrm{cm}^{-2}$

Figure 25: Spatial representation of the electron density at $V_{bias} = -900\,\mathrm{V}$, $RH = 40\,\%$, and $t = 900\,\mathrm{s}$ for different Q_{ox} values: $1 \cdot 10^{10}\,\mathrm{cm}^{-2}$ (a), $5 \cdot 10^{10}\,\mathrm{cm}^{-2}$ (b), and $1 \cdot 10^{11}\,\mathrm{cm}^{-2}$ (c).

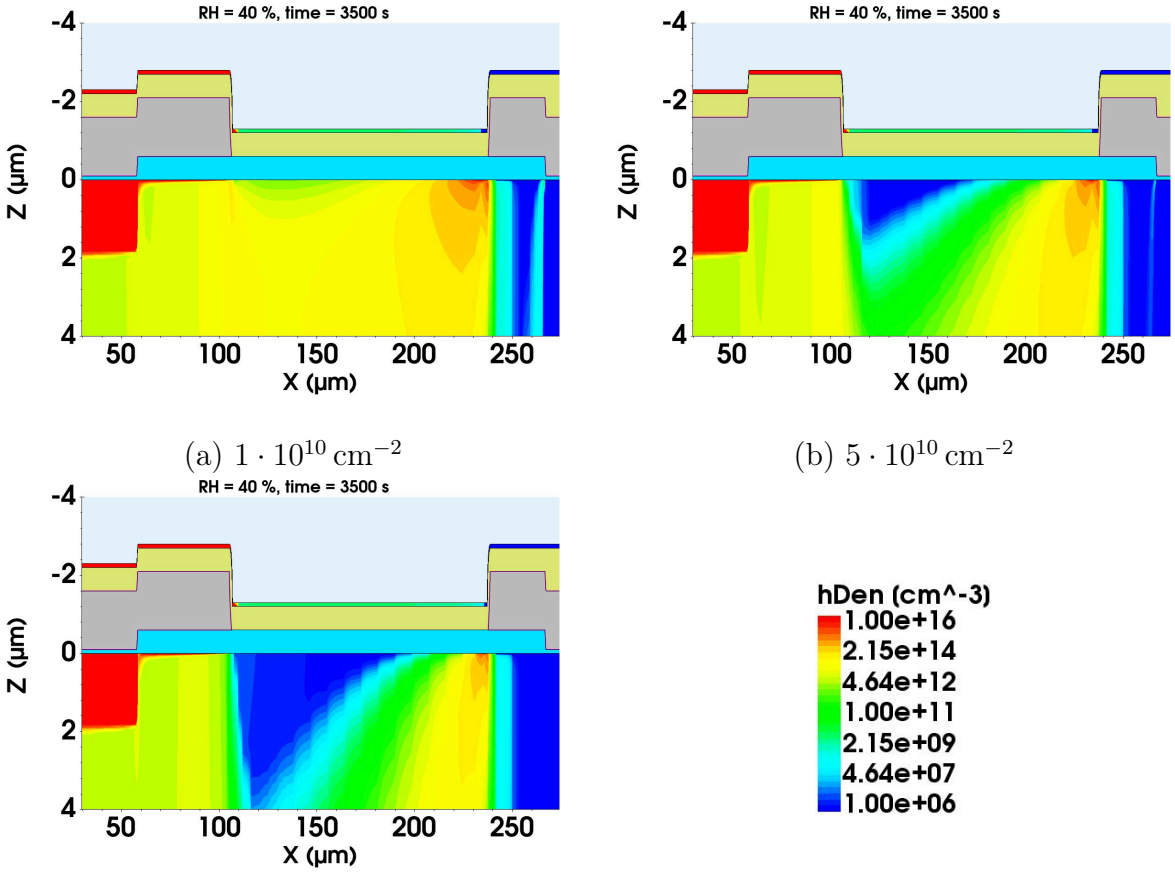

(a) $1 \cdot 10^{10}\,\mathrm{cm}^{-2}$

(b) $5 \cdot 10^{10}\,\mathrm{cm}^{-2}$

(c) $1 \cdot 10^{11}\,\mathrm{cm}^{-2}$

Figure 26: Spatial representation of the hole density at $V_{bias} = -900\,\mathrm{V}$, $RH = 40\,\%$, and $t = 3500\,\mathrm{s}$ for different Q_{ox} values: $1 \cdot 10^{10}\,\mathrm{cm}^{-2}$ (a), $5 \cdot 10^{10}\,\mathrm{cm}^{-2}$ (b), and $1 \cdot 10^{11}\,\mathrm{cm}^{-2}$ (c).

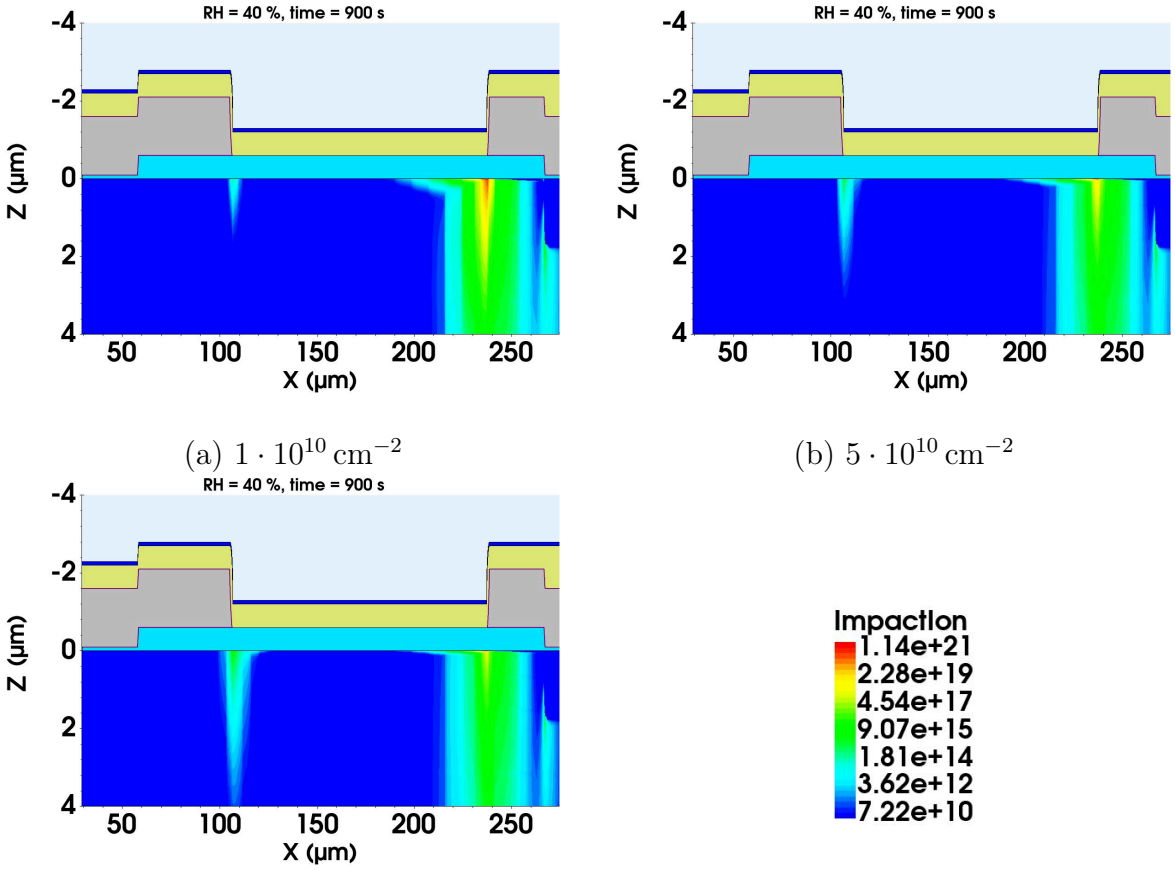

(a) $1 \cdot 10^{10}\,\mathrm{cm}^{-2}$

(b) $5 \cdot 10^{10}\,\mathrm{cm}^{-2}$

(c) $1 \cdot 10^{11}\,\mathrm{cm}^{-2}$

Figure 27: Spatial representation of generation rate of carriers from impact ionization at $V_{bias} = -900\,\mathrm{V}$, $RH = 40\,\%$, and $t = 900\,\mathrm{s}$ for different Q_{ox} values: $1 \cdot 10^{10}\,\mathrm{cm}^{-2}$ (a), $5 \cdot 10^{10}\,\mathrm{cm}^{-2}$ (b), and $1 \cdot 10^{11}\,\mathrm{cm}^{-2}$ (c).

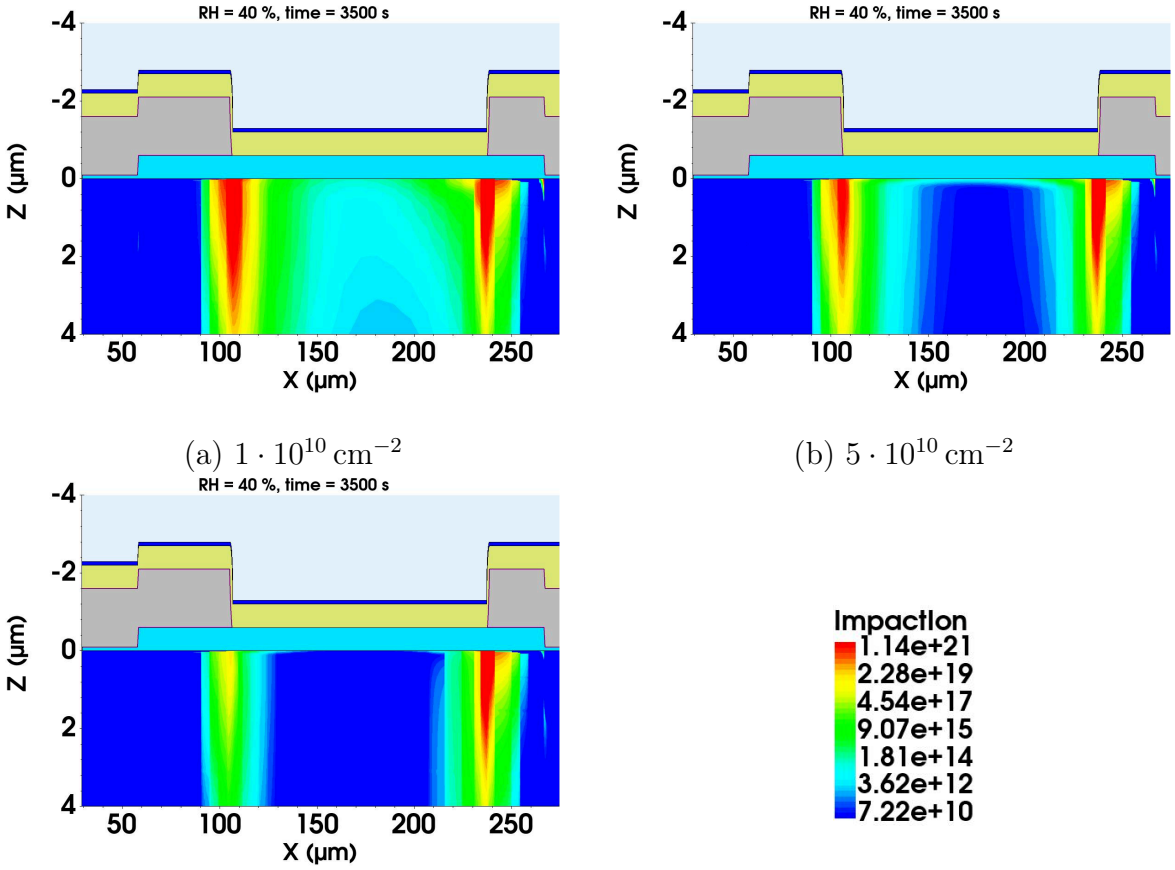

(a) $1 \cdot 10^{10}\,\mathrm{cm}^{-2}$

(b) $5 \cdot 10^{10}\,\mathrm{cm}^{-2}$

(c) $1 \cdot 10^{11}\,\mathrm{cm}^{-2}$

Figure 28: Spatial representation of generation rate of carriers from impact ionization at $V_{bias} = -900\,\mathrm{V}$, $RH = 40\,\%$, and $t = 3500\,\mathrm{s}$ for different Q_{ox} values: $1 \cdot 10^{10}\,\mathrm{cm}^{-2}$ (a), $5 \cdot 10^{10}\,\mathrm{cm}^{-2}$ (b), and $1 \cdot 10^{11}\,\mathrm{cm}^{-2}$ (c).

Acronyms

Q_{ox} fixed oxide charge concentration. XI, XIII–XV, 102–113, 133–144

RH relative humidity. VIII–XIII, XVI, 50, 54–56, 60, 61, 64–67, 72, 74–79, 81, 82, 85, 86, 90–105, 107, 113–117, 121–132

AMACStar Autonomous and Monitoring Control Star. 11

CERN European Council for Nuclear Research. 3, 4

CSC Cathode Strip Chamber. 6

CV Capacitance-Voltage. VI, VIII, 36, 58, 84, 89, 113, 118

CVD Chemical Vapor Deposition. 39

DAC Digital-to-Analog Converter. 69

DAQ Data Acquisition. 70, 72, 73

DUT Device Under Test. 67, 68

ECAL Electromagnetic Calorimeter. 6, 7

ER Edge Ring. VIII–X, XII, XIII, 53, 62, 63, 68, 72–79, 81–84, 90–94, 96, 98, 101–104, 106–109, 111, 113, 115, 116, 121–128

FWHM full width at half maximum. 71

FZ Float Zone. 9, 38, 53

GaAs gallium arsenide. V, 20

GR Guard Ring. VIII–XIII, 53, 55, 56, 58, 62–64, 66, 68, 69, 72–79, 81–84, 89–94, 96–98, 101–109, 111, 113, 115–117, 121–124, 129–132

GUI graphical user interface. 84

HCAL Hadronic Calorimeter. 7

HCCStar Hybrid Controller Chip Star. 11

HL-LHC High-Luminosity LHC. 5

HV High Voltage. 11, 68

ID Inner Detector. V, 5–9

ITk Inner Tracker. V, 9, 11, 42, 44, 87, 117

IV Current-Voltage. VI–VIII, XI, 35, 52, 54, 60–65, 72, 84, 89–91, 93, 103, 113, 114, 117–120

KPR Kodak Photo Resist. 52, 53

LAr Liquid Argon. 6

LGAD Low Gain Avalanche Diodes. 76

LHC Large Hadron Collider. V, 3–6

LS Long Strip. 9

LV Low Voltage. 11

MD8 monitor diode. VIII–XI, 56, 58, 62–64, 73–75, 78, 82, 84, 87, 90, 91, 95–104, 106, 113, 115

MDT Monitored Drift Tube. 6

MIP Minimum Ionizing Particles. 67

NIR Near-infrared. VIII, 60–62

PCB Printed Circuit Board. IX, 9, 11, 62, 63, 67, 68

PVD Physical Vapor Deposition. 39

QE Quantum Efficiency. VIII, 61

RF Radio Frequency. 37, 38

RPC Resistive Plate Chamber. 6

SCR Space Charge Region. 31, 50, 52

SCT Semiconductor Tracker. 7, 8

SDE Structure Device Editor. 84

SDevice Sentaurus Device. 84, 87

SEM Scanning Electron Microscope. VI, 40, 84

SI International System of Units. 12

Si_3N_4 Silicon nitride. 85

SiO_2 silicon dioxide. VI, VII, 26, 27, 39, 42, 44, 47–50, 52, 53, 55, 56, 85, 87, 88, 95, 102

SM Standard Model of Particle Physics. V, 3, 4

SMA SubMiniature version A. 62, 63

SNR Signal-to-Noise Ratio. 48

SRH Shockley-Read-Hall. 22, 24, 26, 27, 87, 88, 100

SS Short Strip. 9

SVisual Sentaurus Visual. 84

TCAD Technology Computer-Aided Design. IV, X, XVI, 14, 56, 73, 76, 81, 82, 84–90, 92, 95, 102, 113–117

TGC Thin Gap Chamber. 6

Top-TCT Top-Transient Current Technique. VIII, IX, XI, 56, 60, 62, 63, 66–69, 72, 74, 75, 81, 82, 113, 116, 117

TRT Transition Radiation Tracker. 8

Bibliography

[1] J. Fernandez-Tejero et al., "Humidity sensitivity of large area silicon sensors: Study and implications", *Nuclear Instruments and Methods in Physics Research Section A: Accelerators, Spectrometers, Detectors and Associated Equipment*, vol. 978, p. 164 406, 2020.

[2] ATLAS Collaboration, "Observation of an excess of events in the search for the Standard Model Higgs boson in the gamma-gamma channel with the ATLAS detector", in *Proceedings of the International Conference on High Energy Physics (ICHEP)*, ATLAS-CONF-2012-091, 2012.

[3] G. Aad *et al.*, "Observation of a new particle in the search for the Standard Model Higgs boson with the ATLAS detector at the LHC", *Physics Letters B*, vol. 716, no. 1, pp. 1–29, 2012.

[4] S. Chatrchyan *et al.*, "Observation of a new boson at a mass of 125 GeV with the CMS experiment at the LHC", *Physics Letters B*, vol. 716, no. 1, pp. 30–61, 2012.

[5] *ATLAS: technical proposal for a general-purpose pp experiment at the Large Hadron Collider at CERN*, ser. LHC technical proposal. Geneva: CERN, 1994. DOI: 10.17181/CERN.NR4P.BG9K. [Online]. Available: https://cds.cern.ch/record/290968.

[6] CMS Collaboration, *Technical Proposal*, ser. LHC Technical Proposal. Geneva: CERN, 1994. [Online]. Available: https://cds.cern.ch/record/290969.

[7] P. W. Higgs, "Broken symmetries and the masses of gauge bosons", *Physical Review Letters*, vol. 13, no. 16, p. 508, 1964.

[8] F. Englert *et al.*, "Broken symmetry and the mass of gauge vector mesons", *Physical Review Letters*, vol. 13, no. 9, p. 321, 1964.

[9] G. S. Guralnik *et al.*, "Global conservation laws and massless particles", *Physical Review Letters*, vol. 13, no. 20, p. 585, 1964.

[10] W. Pauli, "Pauli exclusion principle", *Naturwiss*, vol. 12, p. 741, 1924.

[11] H. Yukawa, "On the interaction of elementary particles. I", *Proceedings of the Physico-Mathematical Society of Japan. 3rd Series*, vol. 17, pp. 48–57, 1935.

[12] R. N. Mohapatra *et al.*, "Neutrino mass and new physics", *Annu. Rev. Nucl. Part. Sci.*, vol. 56, no. 1, pp. 569–628, 2006.

[13] *The Standard Model*. [Online]. Available: https://en.wikipedia.org/wiki/Standard_Model.

[14] *LHCb: Technical Proposal*. Geneva: CERN, 1998. [Online]. Available: https://cds.cern.ch/record/622031.

[15] *ALICE: Technical proposal for a Large Ion Collider Experiment at the CERN LHC*, ser. LHC technical proposal. Geneva: CERN, 1995. [Online]. Available: https://cds.cern.ch/record/293391.

[16] The TOTEM Collaboration, "Upgrade of the TOTEM T2 Telescope, Technical Design Report", CERN, Geneva, Tech. Rep., 2019. [Online]. Available: https://cds.cern.ch/record/2677468.

[17] O. Adriani *et al.*, *LHCf experiment: Technical Design Report*, ser. Technical design report. LHCf. Geneva: CERN, 2006. [Online]. Available: https://cds.cern.ch/record/926196.

[18] J. Pinfold *et al.*, "Technical Design Report of the MoEDAL Experiment", Tech. Rep., 2009. [Online]. Available: https://cds.cern.ch/record/1181486.

[19] H. Abreu *et al.*, "The FASER detector", *Journal of Instrumentation*, vol. 19, no. 05, P05066, 2024.

[20] A. Boyarsky *et al.*, "Searches for new physics at SND@ LHC", *Journal of High Energy Physics*, vol. 2022, no. 3, pp. 1–30, 2022.

[21] ATLAS Collaboration *et al.*, "Observation of a new χ_b state in radiative transitions to Upsilon (1S) and Upsilon (2S) at ATLAS", *arXiv preprint arXiv:1112.5154*, 2011.

[22] A. M. Sirunyan *et al.*, "Observation of a new excited beauty strange baryon decaying to Ξ b-π+ π", *Physical Review Letters*, vol. 126, no. 25, p. 252 003, 2021.

[23] R. Aaij *et al.*, "First observation of a doubly charged tetraquark and its neutral partner", *Physical Review Letters*, vol. 131, no. 4, p. 041 902, 2023.

[24] S. Chatrchyan *et al.*, "Measurement of the properties of a Higgs boson in the four-lepton final state", *Physical Review D*, vol. 89, no. 9, p. 092 007, 2014.

[25] O. Buchmueller *et al.*, "Implications of initial LHC searches for supersymmetry", *The European Physical Journal C*, vol. 71, pp. 1–13, 2011.

[26] O. Brüning *et al.*, "LHC design report(Volume I, The@ LHC main ring)", *Reports-CERN*, 2004.

[27] P. Mouche, "Overall view of the LHC. Vue d'ensemble du LHC", 2014, General Photo. [Online]. Available: https://cds.cern.ch/record/1708847.

[28] *The High Luminosity LHC*, https://home.cern/science/accelerators/high-luminosity-lhc.

[29] "Technical Design Report for the ATLAS Inner Tracker Strip Detector", CERN, Geneva, Tech. Rep., 2017. [Online]. Available: https://cds.cern.ch/record/2257755.

[30] "Technical Design Report for the ATLAS Inner Tracker Pixel Detector", CERN, Geneva, Tech. Rep., 2017. DOI: 10.17181/CERN.FOZZ.ZP3Q. [Online]. Available: https://cds.cern.ch/record/2285585.

[31] "ATLAS Liquid Argon Calorimeter Phase-II Upgrade: Technical Design Report", CERN, Geneva, Tech. Rep., 2017. DOI: 10.17181/CERN.6QIO.YGHO. [Online]. Available: https://cds.cern.ch/record/2285582.

[32] "Technical Design Report for the Phase-II Upgrade of the ATLAS Tile Calorimeter", CERN, Geneva, Tech. Rep., 2017. [Online]. Available: https://cds.cern.ch/record/2285583.

[33] "Technical Design Report for the Phase-II Upgrade of the ATLAS Muon Spectrometer", CERN, Geneva, Tech. Rep., 2017. [Online]. Available: https://cds.cern.ch/record/2285580.

[34] Joao Pequenao, "Computer generated image of the whole ATLAS detector", 2008, [Online]. Available: https://cds.cern.ch/record/1095924.

[35] J. Pequenao, "Computer Generated image of the ATLAS calorimeter", 2008, [Online]. Available: https://cds.cern.ch/record/1095927.

[36] H. Wilkens *et al.*, "The ATLAS liquid argon calorimeter: An overview", in *Journal of Physics: Conference Series*, IOP Publishing, vol. 160, 2009, p. 012 043.

[37] ATLAS Collaboration, "Performance of the ATLAS Transition Radiation Tracker in Run 1 of the LHC".

[38] M. Shochet *et al.*, "Fast TracKer (FTK) Technical Design Report", Tech. Rep., 2013. [Online]. Available: http://cds.cern.ch/record/1552953.

[39] S. M. Sze, *Semiconductor devices: physics and technology*. John Wiley & Sons, 2008.

[40] W. Miller *et al.*, *A Treatise on Crystallography*, ser. Online access with subscription: JISC Historical Texts. Printed at the Pitt Press, for J. & J.J. Deighton, 1839. [Online]. Available: https://books.google.de/books?id=_omyAAAAIAAJ.

[41] W. Bludau *et al.*, "Temperature dependence of the band gap of silicon", *Journal of Applied Physics*, vol. 45, no. 4, pp. 1846–1848, 1974.

[42] *Device User Guide Version R-2020.09*, Synopsys Inc.: San Jose, CA, USA, 2020.

[43] L. Boltzmann, "Studien uber das gleichgewicht der lebenden kraft", *Wissenschafiliche Abhandlungen*, vol. 1, pp. 49–96, 1868.

[44] P. A. M. Dirac, "On the theory of quantum mechanics", *Proceedings of the Royal Society of London. Series A, Containing Papers of a Mathematical and Physical Character*, vol. 112, no. 762, pp. 661–677, 1926.

[45] G. Lutz *et al.*, *Semiconductor radiation detectors*. Springer, 2007.

[46] A. Pais, "Einstein and the quantum theory", *Reviews of modern physics*, vol. 51, no. 4, p. 863, 1979.

[47] H. A. Lorentz, *The Theory of Electrons and Its Applications to the Phenomena of Light and Radiant Heart: A Course of Lectures Delivered in Columbia University, New York in March and April, 1906*. Teubner, 1916, vol. 29.

[48] P. Yu, *Fundamentals of semiconductors*. Springer, 2005.

[49] C. Canali et al., "Electron and hole drift velocity measurements in silicon and their empirical relation to electric field and temperature", *IEEE Transactions on Electron Devices*, vol. 22, no. 11, pp. 1045–1047, 1975.

[50] C. Kittel *et al.*, *Introduction to solid state physics*. John Wiley & Sons, 2018.

[51] A. Fick, "Ueber diffusion", *Annalen der physik*, vol. 170, no. 1, pp. 59–86, 1855.

[52] M. J. Kerr *et al.*, "General parameterization of Auger recombination in crystalline silicon", *Journal of Applied Physics*, vol. 91, no. 4, pp. 2473–2480, 2002.

[53] A. Richter *et al.*, "Improved quantitative description of Auger recombination in crystalline silicon", *Physical Review B—Condensed Matter and Materials Physics*, vol. 86, no. 16, p. 165 202, 2012.

[54] W. Shockley *et al.*, "Statistics of the recombinations of holes and electrons", *Physical review*, vol. 87, no. 5, p. 835, 1952.

[55] R. N. Hall, "Electron-hole recombination in germanium", *Physical review*, vol. 87, no. 2, p. 387, 1952.

[56] D. Fitzgerald *et al.*, "Surface recombination in semiconductors", *Surface Science*, vol. 9, no. 2, pp. 347–369, 1968.

[57] D. L. Scharfetter et al., "Large-signal analysis of a silicon read diode oscillator", *IEEE Transactions on Electron Devices*, vol. 16, no. 1, pp. 64–77, 1969.

[58] E. H. Nicollian *et al.*, *MOS (metal oxide semiconductor) physics and technology*. John Wiley & Sons, 2002.

[59] M. Ullán et al., "Quality Assurance methodology for the ATLAS Inner Tracker strip sensor production", *Nuclear Instruments and Methods in Physics Research Section A: Accelerators, Spectrometers, Detectors and Associated Equipment*, vol. 981, p. 164 521, 2020.

[60] S. M. Sze *et al.*, *Physics of Semiconductor Devices*. John Wiley & Sons, Inc., 2006. DOI: 10.1002/0470068329.

[61] G. A. M. Hurkx *et al.*, "A new recombination model for device simulation including tunneling", *IEEE Transactions on electron devices*, vol. 39, no. 2, pp. 331–338, 1992.

[62] J. Donnelly *et al.*, "The capacitance of pn heterojunctions including the effects of interface states", *IEEE Transactions on Electron Devices*, vol. 14, no. 2, pp. 63–68, 1967.

[63] J. D. Jackson, *Classical electrodynamics*. John Wiley & Sons, 2021.

[64] J. Czochralski, "Ein neues verfahren zur messung der kristallisationsgeschwindigkeit der metalle", *Zeitschrift für physikalische Chemie*, vol. 92, no. 1, pp. 219–221, 1918.

[65] W. Keller *et al.*, "Floating-zone silicon", 1981.

[66] G. Müller *et al.*, "Crystal growth, bulk: methods", 2005.

[67] T. Chen *et al.*, "Multi-label oxide classification in float-zone silicon crystal growth using transfer learning and asymmetric loss", *Journal of Intelligent Manufacturing*, pp. 1–16, 2024.

[68] D. M. Mattox, *Handbook of physical vapor deposition (PVD) processing*. William Andrew, 2010.

[69] H. Pierson, *Handbook of Chemical Vapor Deposition: Principles, Technology, and Applications*. Noyes Publications/William Andrew Publishing, 1999.

[70] S. Franssila, *Introduction to microfabrication*. John Wiley & Sons, 2010.

[71] C. Ning, *Etching Platinum using Oxford Ion Mill Tool*. [Online]. Available: https://wiki.nanofab.ucsb.edu/w/images/2/28/42-Etching_Platinum_using_Oxford_Ion_Mill_Tool-a.pdf.

[72] H. A. Bethe *et al.*, "Experimental nuclear physics", *Wiley, New York*, 1953.

[73] P. A. Cherenkov, "Visible light from clear liquids under the action of gamma radiation", *Comptes Rendus (Doklady) de l'Aeademie des Sciences de l'URSS*, vol. 2, no. 8, pp. 451–454, 1934.

[74] W. Maes *et al.*, "Impact ionization in silicon: A review and update", *Solid-State Electronics*, vol. 33, no. 6, pp. 705–718, 1990.

[75] R. Van Overstraeten et al., "Measurement of the ionization rates in diffused silicon pn junctions", *Solid-State Electronics*, vol. 13, no. 5, pp. 583–608, 1970.

[76] A. Chynoweth, "Ionization rates for electrons and holes in silicon", *Physical Review*, vol. 109, no. 5, p. 1537, 1958.

[77] E. Haug *et al.*, *The elementary process of bremsstrahlung*. World Scientific, 2004, vol. 73.

[78] G. F. Knoll, *Radiation detection and measurement*. John Wiley & Sons, 2010.

[79] P. Tandon *et al.*, "Interaction of Ionizing Radiation with Matter", in *Radiation Safety Guide for Nuclear Medicine Professionals*. Singapore: Springer Nature Singapore, 2022, pp. 21–35, ISBN: 978-981-19-4518-2. DOI: 10.1007/978-981-19-4518-2_3. [Online]. Available: https://doi.org/10.1007/978-981-19-4518-2_3.

[80] J. Yorkston *et al.*, "Interstrip surface effects in oxide passivated ion-implanted silicon strip detectors", *Nuclear Instruments and Methods in Physics Research Section A: Accelerators, Spectrometers, Detectors and Associated Equipment*, vol. 262, no. 2-3, pp. 353–358, 1987.

[81] M. Atalla *et al.*, "Stability of thermally oxidized silicon junctions in wet atmospheres", *Proceedings of the IEE-Part B: Electronic and Communication Engineering*, vol. 106, no. 17S, pp. 1130–1137, 1959.

[82] W. Shockley et al., "Mobile electric charges on insulating oxides with application to oxide covered silicon pn junctions", *Surface Science*, vol. 2, pp. 277–287, 1964.

[83] W. Schroen, "Accumulation and decay of mobile surface charges on insulating layers and relationship to reliability of silicon devices", in *Fourth Annual Symposium on the Physics of Failure in Electronics*, IEEE, 1965, pp. 291–314.

[84] L. Kelvin, "V. contact electricity of metals", *The London, Edinburgh, and Dublin Philosophical Magazine and Journal of Science*, vol. 46, no. 278, pp. 82–120, 1898.

[85] G. Calderini *et al.*, "The ATLAS ITk detector for high luminosity LHC upgrade", *Nuclear Instruments and Methods in Physics Research Section A: Accelerators, Spectrometers, Detectors and Associated Equipment*, vol. 1040, p. 167 048, 2022.

[86] C. Jessiman *et al.*, "TCAD simulation of the electrical performance of the ATLAS18 strip sensor for the HL-LHC", ATL-COM-ITK-2024-017, Tech. Rep., 2024.

[87] ZWO ASI - Astronomy Cameras, *ASI183MM Pro (mono)*. [Online]. Available: https://astronomy-imaging-camera.com/product/asi183mm-pro-mono.

[88] N. Akil et al., "A multimechanism model for photon generation by silicon junctions in avalanche breakdown", *IEEE Transactions on Electron Devices*, vol. 46, no. 5, pp. 1022–1028, 1999.

[89] J. Bude et al., "Hot-carrier luminescence in Si", *Physical Review B*, vol. 45, no. 11, p. 5848, 1992.

[90] J. Fernandez-Tejero et al., "Analysis of humidity sensitivity of silicon strip sensors for ATLAS upgrade tracker, pre-and post-irradiation", *Journal of Instrumentation*, vol. 18, no. 02, P02012, 2023.

[91] I.-S. Ninca *et al.*, "TCAD simulations of humidity-induced breakdown of silicon sensors", *Nuclear Instruments and Methods in Physics Research Section A: Accelerators, Spectrometers, Detectors and Associated Equipment*, vol. 1067, p. 169 729, 2024, ISSN: 0168-9002. DOI: https://doi.org/10.1016/j.nima.2024.169729. [Online]. Available: https://www.sciencedirect.com/science/article/pii/S0168900224006557.

[92] *Microscope picture of an MD4 in avalanche breakdown*, Private communication, 2022.

[93] Y. Unno et al., "Specifications and pre-production of n^+-in-p large-format strip sensors fabricated in 6-inch silicon wafers, ATLAS18, for the Inner Tracker of the ATLAS Detector for High-Luminosity Large Hadron Collider", *Journal of Instrumentation*, vol. 18, no. 03, T03008, 2023.

[94] V. Fadeyev *et al.*, "Long-term humidity exposure of ATLAS18 ITk strip sensors", *Nuclear Instruments and Methods in Physics Research Section A: Accelerators, Spectrometers, Detectors and Associated Equipment*, p. 169 430, 2024.

[95] P. Federičová *et al.*, "Setups for eliminating static charge of the ATLAS18 strip sensors", *Journal of Instrumentation*, vol. 19, no. 02, p. C02001, 2024.

[96] Synopsys, *TCAD - Technology Computer Aided Design*, https://www.synopsys.com/manufacturing/tcad.html.

[97] *Keithley 2400 Standard Series SMU*, Keithley Instruments, Inc.: Cleveland, Ohio, U.S.A., 2011. [Online]. Available: https://www.tek.com/en/products/keithley/source-measure-units/2400-standard-series-sourcemeter.

[98] Agilent Technologies Deutschland GmbH, *Agilent E4981A 120 Hz/1 kHz/1 MHz Capacitance Meter - User Manual*, Agilent Technologies Deutschland GmbH, 2008.

[99] F. Riemer, "Reverse current, capacitance and thermal runaway of irradiated silicon diodes", https://bib-pubdb1.desy.de/record/471495, Master's Thesis, Humboldt-Universität zu Berlin, 2021.

[100] *PSM1000 Series Microscope*, Motic Europe. [Online]. Available: https://moticeurope.com/en/microscope/serie/psm1000.

[101] *Cigar Oasis Magna 3.0 Electronic Humidifier*, Cigar Oasis. [Online]. Available: https://www.cigaroasis.com/products/cigar-oasis-magna-3-0-electronic-humidifier.

[102] *Keithley Series 6400 Picoammeters*, Keithley Instruments, Inc.: Cleveland, Ohio, U.S.A. [Online]. Available: https://www.tek.com/en/products/keithley/low-level-sensitive-and-specialty-instruments/series-6400-picoammeters.

[103] S. Christian, *Microscope picture of an n-in-p silicon diode operated in avalanche breakdown*, Private communication, Unpublished communication, 2022.

[104] J.-O. Gosewisch *et al.*, "Influence of Surface Damage and Bulk Defects on the Interstrip Isolation of p-type Silicon Strip Sensors", Tech. Rep., 2020.

[105] Particulars, *Particulars, Advanced measurement systems*, http://particulars.si/index.php.

[106] D. F. Swinehart, "The beer-lambert law", *Journal of chemical education*, vol. 39, no. 7, p. 333, 1962.

[107] *Particulars Laser – Hardware Manual*, Particulars, Advanced Measurement Systems. [Online]. Available: http://particulars.si/downloads/ParticularsLaserHardware-UserGuideV2.0.pdf.

[108] *Particulars Lasers - User Manual*. [Online]. Available: http://particulars.si/downloads/ParticularsLaserHardware-UserGuideV2.0.pdf.

[109] *F220FC-850 Fiber Collimator*, Thorlabs Inc. [Online]. Available: https://www.thorlabs.de/thorproduct.cfm?partnumber=F220FC-850.

[110] *GBE15-B - 15X Achromatic Galilean Beam Expander*, Thorlabs Inc. [Online]. Available: https://www.thorlabs.de/thorproduct.cfm?partnumber=GBE15-B.

[111] *8MT175 - Motorized Linear Stages*, Standa Ltd. [Online]. Available: https://www.standa.lt/products/catalog/motorised_positioners?item=60.

[112] *Minichiller 300 OLÉ*, Huber Inc. [Online]. Available: https://www.huber-online.com/produkte/umwaelzkuehler/umwaelzkuehler-bis-25-kw/minichiller/minichiller-300-ole.

[113] *8MTF - Motorized XY Scanning Stage*, Standa Ltd. [Online]. Available: https://www.standa.lt/products/catalog/motorised_positioners?item=311.

[114] *6517B Electrometer/High Resistance Meter*, Keithley Instruments, Inc.: Cleveland, Ohio, U.S.A. [Online]. Available: https://www.tek.com/de/datasheet/6517b-electrometer-high-resistance-meter.

[115] *Particulars HV Filter*, Particulars, Advanced Measurement Systems. [Online]. Available: http://particulars.si/downloads/ParticularsHVFilter-Manuals.pdf.

[116] *Particulars Bias-T*, Particulars, Advanced Measurement Systems. [Online]. Available: http://particulars.si/downloads/ParticularsBias-T-Manuals.pdf.

[117] M. A. Green, "Self-consistent optical parameters of intrinsic silicon at 300 K including temperature coefficients", *Solar Energy Materials and Solar Cells*, vol. 92, no. 11, pp. 1305–1310, 2008.

[118] *RS®RTO1000 Digitales Oszilloskop*, Rohde and Schwarz. [Online]. Available: https://www.rohde-schwarz.com/de/produkte/messtechnik/oszilloskope/rs-rto1000-digitales-oszilloskop_63493-191808.html.

[119] A. M. S. Particulars, *Particulars Wide Band Current Amplifiers*. [Online]. Available: http://particulars.si/downloads/ParticularsAmps-Manuals.pdf.

[120] *Particulars Lasers – Software Manual*, Particulars, Advanced Measurement Systems. [Online]. Available: http://particulars.si/downloads/ParticularsLaserControl-UserGuide.pdf.

[121] *Particulars - Laser pulse*. [Online]. Available: http://particulars.si/downloads/Particulars-Procedures-LaserPulse.pdf.

[122] H. J. Eichler *et al.*, "Lasers: Basics, advances and applications", 2018.

[123] N. Potters, "Investigation of irradiated silicon strip sensors using the edge transient current technique", Master's Thesis, University of Heidelberg, 2021.

[124] *Scanning TCT data acqusition software*, Particulars, Advanced Measurement Systems. [Online]. Available: http://particulars.si/downloads/ScanTCT_DAQ-V1.81.pdf.

[125] *Particulars - Finding the focus*. [Online]. Available: http://particulars.si/downloads/Particulars-Procedures-FocusFind.pdf.

[126] E. Currás et al., "Gain reduction mechanism observed in low gain avalanche diodes", *Nuclear Instruments and Methods in Physics Research Section A: Accelerators, Spectrometers, Detectors and Associated Equipment*, vol. 1031, p. 166 530, 2022.

[127] F. Feindt, "Edge-TCT for the investigation of radiation damaged silicon strip sensors", Deutsches Elektronen-Synchrotron (DESY), Tech. Rep., 2017.

[128] Particle Data Group, *Particle Physics Booklet*. 2012. [Online]. Available: http://pdg.lbl.gov.

[129] M. Tanabashi *et al.*, "Review of Particle Physics: particle data groups", *Physical Review D*, vol. 98, no. 3, pp. 1–1898, 2018.

[130] W. Shockley, "Currents to conductors induced by a moving point charge", *Journal of applied physics*, vol. 9, no. 10, pp. 635–636, 1938.

[131] S. Ramo, "Currents induced by electron motion", *Proceedings of the IRE*, vol. 27, no. 9, pp. 584–585, 1939.

[132] G. Kramberger et al., "Investigation of irradiated silicon detectors by edge-TCT", *IEEE Transactions on Nuclear Science*, vol. 57, no. 4, pp. 2294–2302, 2010.

[133] K. G. McKay, "Avalanche Breakdown in Silicon", *Phys. Rev.*, vol. 94, pp. 877–884, 4 May 1954. DOI: 10.1103/PhysRev.94.877. [Online]. Available: https://link.aps.org/doi/10.1103/PhysRev.94.877.

[134] T. Kuwano *et al.*, "Systematic study of micro-discharge characteristics of ATLAS barrel silicon microstrip modules", *Nuclear Instruments and Methods in Physics Research Section A: Accelerators, Spectrometers, Detectors and Associated Equipment*, vol. 579, no. 2, pp. 782–787, 2007.

[135] *Sentaurus Structure Editor User Guide R-2020.09*, Synopsys Inc.: San Jose, CA, USA, 2020.

[136] *Sentaurus Visual User Guide R-2020.09*, Synopsys Inc.: San Jose, CA, USA, 2020.

[137] E. Staats et al., "Evaluation of MOS and Gated Diode Devices of the ATLAS ITk Test Chip", ATL-COM-ITK-2021-044, Tech. Rep., 2021.

[138] D. Brueske et al., "Investigation of the insulator layers for segmented silicon sensors before and after X-ray irradiation", in *IEEE Nuclear Science Symposium and Medical Imaging Conference (NSS/MIC)*, 2014, pp. 1–5. DOI: 10.1109/NSSMIC.2014.7431261.

[139] J. Schwandt *et al.*, "Surface effects in segmented silicon sensors", *Nuclear Instruments and Methods in Physics Research Section A: Accelerators, Spectrometers, Detectors and Associated Equipment*, vol. 845, pp. 159–163, 2017.

[140] D. M. Caughey *et al.*, "Carrier mobilities in silicon empirically related to doping and field", *Proceedings of the IEEE*, vol. 55, no. 12, pp. 2192–2193, 1967.

[141] M. A. Green, "Intrinsic concentration, effective densities of states, and effective mass in silicon", *Journal of Applied Physics*, vol. 67, no. 6, pp. 2944–2954, 1990.

[142] C. T. Klein, "Investigation of performance and the influence of environmental conditions on strip detectors for the ATLAS Inner Tracker Upgrade", PhD thesis, University of Cambridge, 2019. DOI: 10.17863/CAM.45814. [Online]. Available: https://doi.org/10.17863/CAM.45814.

[143] L. Poley *et al.*, "Curing early breakdown in silicon strip sensors with radiation", *Nuclear Instruments and Methods in Physics Research Section A: Accelerators, Spectrometers, Detectors and Associated Equipment*, vol. 1064, p. 169 405, 2024.

[144] C. Helling *et al.*, "Strip sensor performance in prototype modules built for ATLAS ITk", *Nuclear Instruments and Methods in Physics Research Section A: Accelerators, Spectrometers, Detectors and Associated Equipment*, vol. 978, p. 164 402, 2020, ISSN: 0168-9002. DOI: https://doi.org/10.1016/j.nima.2020.164402. [Online]. Available: https://www.sciencedirect.com/science/article/pii/S0168900220307993.

[145] L. Poley *et al.*, "The ABC130 barrel module prototyping programme for the ATLAS strip tracker", *Journal of instrumentation*, vol. 15, no. 09, P09004, 2020.